

# Electroweak Processes in the Standard Model and Beyond: Backgrounds to Higgs Physics and Semileptonic Decay Modes

Zur Erlangung des akademischen Grades eines  
DOKTORS DER NATURWISSENSCHAFTEN

von der Fakultät für Physik des  
Karlsruher Instituts für Technologie (KIT)

genehmigte

DISSERTATION

von

Dipl.-Phys. Bastian Feigl  
aus Mutlangen

Tag der mündlichen Prüfung: 15. November 2013

Referent: Prof. Dr. D. Zeppenfeld  
Korreferentin: Prof. Dr. M. Mühlleitner



# Abstract

This thesis describes several aspects of electroweak processes at the Large Hadron Collider (LHC). In the first part an analysis of supersymmetry (SUSY) induced backgrounds to the production of a SM-like Higgs boson in the Minimal Supersymmetric Extension of the Standard Model (MSSM) is performed. In this study the  $h \rightarrow \tau\tau$  and  $h \rightarrow WW$  decay modes of Higgs boson production in vector boson fusion are considered as signal processes. Substantial SUSY backgrounds arise only for low SUSY particle masses. For SUSY particle masses compatible with current LHC exclusion limits the SUSY background in these channels is under good control.

The possible influence of BSM effects on the data-driven determination of non-BSM backgrounds is discussed in the second part of this thesis. Taking the early-2012 LHC analyses of the  $h \rightarrow WW$  search channel as an example, it is shown that contributions from MSSM processes could have lead to a significantly modified prediction of the  $WW$  continuum background.

Finally, the implementation of semileptonic decay modes for processes involving several electroweak gauge bosons is discussed. The transition from fully leptonic to semileptonic weak boson decays has an impact on the tagging jet definition. Additionally, the real emission contributions of next-to-leading order QCD cross sections are enhanced in the semileptonic case, when cuts on final-state particles are applied.

# Zusammenfassung

In dieser Arbeit werden verschiedene Aspekte von elektroschwachen Prozessen im Hinblick auf den Large Hadron Collider (LHC) am CERN beleuchtet. Im ersten Teil wird eine Analyse von möglichen Untergründen zur Higgsbosonsuche durch die Produktion supersymmetrischer (SUSY) Teilchen vorgestellt. Als Signalprozesse werden die Zerfallskanäle  $h \rightarrow WW$  und  $h \rightarrow \tau\tau$  der Produktion eines standardmodellartigen Higgs-Bosons in Vektorbosonfusion in der Minimalen Supersymmetrischen Erweiterung des Standardmodells untersucht. Beträchtliche SUSY-Untergründe treten nur bei der Annahme sehr leichter SUSY-Teilchen auf. Mit den Einschränkungen aufgrund der neuesten SUSY-Suchen am LHC ist der Beitrag der SUSY-Untergründe deutlich kleiner als die erwarteten Ereignisraten der Signalprozesse.

Im zweiten Teil der Arbeit wird untersucht, ob Effekte aufgrund Physik jenseits des Standardmodells auch die Bestimmung von anderen Untergrundbeiträgen beeinflussen können, wenn diese direkt aus experimentellen Daten ermittelt werden. Am Beispiel der  $h \rightarrow WW$  Analysen am LHC vom März 2012 wird gezeigt, dass SUSY-Prozesse die  $WW$ -Untergrundsbestimmung soweit beeinflussen können, dass der Beitrag des Signalprozesses nennenswert unterschätzt wird.

Zu guter Letzt wird die Implementierung semileptonischer Zerfälle in ein Programm zur Berechnung von Wirkungsquerschnitten für Prozesse mit mehreren Vektorbosonen vorgestellt. Es zeigt sich, dass in diesem Fall eine andere Definition für die sogenannten „Tagging Jets“ in Vektorbosonfusionsprozessen gewählt werden muss. Außerdem wird der Anteil der realen Emission bei Berechnungen in nächst-führender Ordnung QCD verstärkt, sofern Phasenraumschnitte an die Endzustandsteilchen angelegt werden.



---

# Contents

---

<b>1</b>	<b>Introduction</b>	<b>1</b>
<b>2</b>	<b>Theoretical Concepts</b>	<b>5</b>
2.1	The Standard Model of Particle Physics . . . . .	5
2.1.1	Field Content of the SM . . . . .	6
2.1.2	EWSB in the SM: The Higgs Sector . . . . .	8
2.2	Supersymmetry . . . . .	10
2.2.1	The Minimal Supersymmetric Extension of the Standard Model	11
2.2.2	SUSY Breaking in the MSSM . . . . .	13
2.2.3	The Higgs Sector of the MSSM . . . . .	16
2.3	Collider Physics at Hadron Colliders . . . . .	18
2.3.1	Cross Sections at Hadron Colliders . . . . .	18
2.3.2	Background Determination . . . . .	21
<b>3</b>	<b>SUSY Background to Neutral MSSM Higgs Boson Searches</b>	<b>25</b>
3.1	Introduction . . . . .	25
3.2	SUSY Scenarios and Relevant Processes . . . . .	27
3.2.1	SUSY scenario construction . . . . .	28
3.2.2	The Signal Processes $h \rightarrow WW$ and $h \rightarrow \tau\tau$ in VBF . . . . .	31
3.2.3	Irreducible Background Contributions . . . . .	32
3.2.4	Theoretical Precision of Signal and Background Estimation . . . . .	36
3.2.5	Reducible Background Contributions . . . . .	37
3.3	Analysis Procedure . . . . .	39
3.3.1	Overview . . . . .	39
3.3.2	Analysis Tool-Chain . . . . .	40
3.3.3	Validation . . . . .	43
3.3.4	Particle and Event Selection . . . . .	45
3.4	LHC Results for the $h \rightarrow WW$ Channel at 14 TeV . . . . .	48

3.4.1	SPS1a-like Scenario SPS1amod . . . . .	48
3.4.2	SUSY Background in a Scenario with a Heavier Higgs Boson (Scenario SPS1amod2) . . . . .	62
3.4.3	Sparticle Mass Dependence . . . . .	63
3.4.4	Scenario with an Inverted Slepton Hierarchy . . . . .	69
3.5	LHC Results for the $h \rightarrow \tau\tau$ Channel at 14 TeV . . . . .	73
3.5.1	SPS1a-like Scenario . . . . .	73
3.5.2	Scenario with an Inverted Slepton Hierarchy . . . . .	80
3.6	LHC Results at 7 TeV Center-of-Mass Energy . . . . .	82
3.6.1	SPS1a-like Scenario . . . . .	82
3.6.2	Light Sleptons with Higher Squark Masses . . . . .	84
3.6.3	Scenario with a Higgs Boson Mass of about 125 GeV . . . . .	86
3.7	Additional Aspects of SUSY Background Processes . . . . .	87
3.7.1	Effect of a Light LSP . . . . .	87
3.7.2	Effect of Small Mass Differences in the SUSY Particle Decay Chain . . . . .	88
3.7.3	Effect of a Central Jet Veto on QCD Radiation in SUSY Back- ground Processes . . . . .	89
3.8	Conclusion . . . . .	91
<b>4</b>	<b>New Physics Effects in Background Determination</b>	<b>93</b>
4.1	Introduction . . . . .	93
4.2	Analysis Setup . . . . .	94
4.2.1	SUSY Scenario . . . . .	94
4.2.2	Analysis Tools . . . . .	96
4.2.3	Event Selection . . . . .	97
4.3	Results . . . . .	99
4.3.1	SUSY Background Contribution in the “Base” Scenario . . . . .	100
4.3.2	Effects of Varying the Chargino, Slepton and LSP Mass . . . . .	102
4.3.3	SUSY Background Contribution in the “Worst Case” Scenario . . . . .	105
4.3.4	SUSY Background Contribution in Scenarios with Modified Chargino Parameters . . . . .	107
4.4	Conclusion . . . . .	109
<b>5</b>	<b>Multiboson Production with Semileptonic Decays</b>	<b>111</b>
5.1	Introduction . . . . .	111
5.2	Implementation of Semileptonic Vector Boson Decays in VBFNLO . . . . .	113
5.2.1	Overview and Process List . . . . .	113
5.2.2	Implementation Details . . . . .	117
5.2.3	Tests and Comparisons . . . . .	130
5.3	Phenomenological Aspects . . . . .	134
5.3.1	Tagging-Jet Definitions . . . . .	134
5.3.2	Interpretation of Inclusive NLO Cross Sections for the Semilep- tonic Processes . . . . .	138
5.3.3	Anomalous Gauge Boson Couplings . . . . .	140
5.4	Conclusion . . . . .	143

---

<b>6 Summary</b>	<b>145</b>
<b>A SUSY Spectra</b>	<b>147</b>
A.1 Scenarios for “SUSY Background to Neutral MSSM Higgs Boson Searches”	147
A.2 Scenarios for “New Physics Effects in Background Determination” . . .	153
<b>B List of VBFNLO Changes for Semileptonic Decays</b>	<b>157</b>
<b>Bibliography</b>	<b>159</b>
<b>Acknowledgments</b>	<b>179</b>



# CHAPTER 1

---

## Introduction

---

In the last decades tremendous accomplishments have been achieved in the field of elementary particle physics. The understanding of the smallest building blocks of our universe and their interactions has been completely revamped by the introduction of the concepts of quantum mechanics and relativistic quantum field theories. They form the foundation of the current Standard Model (SM) of elementary particle physics. It covers three of the four fundamental interactions, the strong, the weak and the electromagnetic force and two types of matter particles, the leptons which are only affected by the electromagnetic and weak interactions and the quarks, which additionally participate in the strong interaction. The strong interaction is described by quantum chromodynamics (QCD) [1–3]. The weak and the electromagnetic interaction are jointly described by the Glashow-Weinberg-Salam theory of electroweak (EW) interactions [4–6], which includes the Higgs mechanism [7–10] in order to be able to describe the masses of the gauge bosons of the weak force without violating the SM gauge symmetries. Additionally, the scalar particle arising from the Higgs mechanism, the Higgs boson, unitarizes the electroweak gauge boson scattering at high energies. The Higgs sector furthermore allows for the introduction of fermion masses into the SM by means of Yukawa interactions between the fermion fields and the scalar Higgs field in the ground state. Since these interactions give rise to a mixing of the three quark generations, parametrized in the CKM matrix [11, 12], they introduce direct  $CP$ -violation into the SM.

The experimental success of the SM is remarkable. Already before the start of the CERN Large Hadron Collider (LHC) almost all constituents have been observed. Several of these particles, like the top-quark [13, 14] and the W boson [15, 16], have not been included into the SM after their discovery, but instead they have been predicted by this theory. Furthermore, the global SM fit to various precision measurements shows

a very good agreement [17]. Direct  $CP$ -violation due to CKM effects has been confirmed experimentally as well [18]. Since the top-quark discovery in 1995 the last sector of the SM that craved for experimental confirmation was the Higgs sector. With the observation of a scalar boson by the LHC in 2012 [19,20] this last building block seems to have been found: so far all measurements are compatible with this boson being the SM Higgs boson.

However, for various reasons the SM cannot be the ultimate theory. The most obvious one is the fact that the SM does not include the gravitational force. This leads to an upper bound of  $\mathcal{O}(10^{19}$  GeV) on the validity at high energies, the Planck scale. At this point a theory of quantum gravity would have to take over. There are also several hints for New Physics effects setting in at much lower energies. The observed shape of the rotation curves of galaxies [21–23] for example cannot be explained by the visible matter alone if Newton's laws are assumed to be valid. A highly favored explanation for the observed curves is the existence of so-called (cold) dark matter. Unfortunately, the SM does not include a viable dark matter candidate. Additionally, the amount of  $CP$ -violation inherent in the SM is not enough to explain the substantial matter-antimatter asymmetry of the universe. From a theoretical point of view a large amount of fine-tuning as it occurs in the Higgs sector is unsatisfactory. Furthermore, the SM offers no explanation for the huge mass differences of several orders of magnitude in the fermion sector.

Therefore, despite the great success of the SM, it still offers plenty of room for physics beyond the Standard Model (BSM Physics). As it has been mentioned before, the Higgs sector, i.e. the mechanism of electroweak symmetry breaking (EWSB) in the SM, is only at the beginning of its experimental examination. Therefore, since investigations of the EWSB sector and the search for New Physics are carried out simultaneously, they naturally influence each other. Two different aspects of this interplay will be discussed in this thesis for the case of the Minimal Supersymmetric Extension of the Standard Model (MSSM) [24–33] (for a review see e.g. [34]) as an example for a BSM theory. The MSSM is a representative of the class of supersymmetric theories [24–33, 35–40]. They are considered as promising examples of New Physics theories, since they can solve for example the dark matter issue and the fine-tuning puzzle of the SM. The first aspect discussed in this work is the question, whether supersymmetry (SUSY) induced processes could yield a sizable contribution to the background for the search of a SM-like Higgs boson in vector boson fusion within the MSSM. Up to now, SUSY backgrounds have only been considered in MSSM Higgs boson analyses that involve SUSY cascade decays in the signal process, but not in SM-type search channels. The second topic of this thesis is the question, whether SUSY processes, or in general BSM processes, could interfere with the data-driven determination of other backgrounds in the Higgs analyses, leading to an erroneous estimation of the rate of the signal process. This has been studied for the determination of the continuum  $WW$  production background to the ( $h \rightarrow WW$ ) channels with zero or one additional jet via a control region.

Further aspects of the SM which can be tested experimentally for the first time at the LHC due to the achieved large center-of-mass energies are the quartic gauge boson

---

self couplings. Since there exist no stringent experimental bounds on these couplings so far there might be residual effects of BSM physics at higher scales encoded in the quartic interactions. At the LHC they are probed in a model-independent way using an effective Lagrangian with higher-dimensional operators contributing to the gauge boson vertices [41]. Additionally, the quartic gauge boson couplings are linked to the Higgs sector, since a description of longitudinal vector boson scattering at high energies in the SM relies on the existence of a relatively light SM Higgs boson with a mass below  $\mathcal{O}(1 \text{ TeV})$ . Therefore, measurements of the high-energy tail of vector boson scattering and triple vector boson production may lead to new insights on the nature of the recently found scalar boson. Due to the very small cross sections of these electroweak processes not only the fully leptonic vector boson decay modes should be considered experimentally, but also the cases in which one vector boson decays hadronically. The implementation of such semileptonic vector boson decay modes into a parton-level Monte Carlo program is the third project presented in this thesis.

The organization of the thesis is as follows: Chapter 2 gives a brief introduction into the SM, the MSSM and the calculation of cross sections for hadron colliders. Additionally, several methods of data-driven background determination are sketched. In Chapter 3 the SUSY background to the production of a SM-like Higgs boson in vector boson fusion is discussed in detail for a variety of MSSM scenarios. The impact of SUSY processes on the  $WW$  background to the  $h \rightarrow WW$  channel is illustrated in Chapter 4. The implementation of semileptonic decays into a parton-level Monte Carlo program for several processes involving multiple electroweak bosons is described in Chapter 5. Finally, Chapter 6 briefly summarizes the results of Chapters 3–5.



# CHAPTER 2

---

## Theoretical Concepts

---

This chapter presents a brief introduction into the models of elementary particle physics which are relevant for this thesis. The electroweak sector of the Standard Model and in particular the electroweak symmetry breaking mechanism are discussed. Chapters 3 and 4 are devoted to effects of physics beyond the Standard Model, with the Minimal Supersymmetric Extension of the Standard Model as a representative of a BSM model. Therefore the MSSM will be sketched as well. Finally, a few words on the signal and background determination at hadron colliders will follow.

### 2.1 The Standard Model of Particle Physics

Over the last decades the Standard Model of Particle Physics, a relativistic Quantum Field Theory, has been established. It combines the electroweak theory from Glashow, Weinberg and Salam [4–6] with quantum chromodynamics [1–3], the theory of strong interactions. Since explicit mass terms in the Lagrangian would break gauge invariance, the mass terms of elementary particles in the Standard Model are generated by spontaneous symmetry breaking of the electroweak sector. In the SM, EWSB is implemented via the Higgs mechanism [7–10]. The SM agrees extremely well with the experimental data. Since 1995 all constituents of the SM have been experimentally confirmed, except for the Higgs boson connected to the mechanism of EWSB. However, in 2012 a new particle with properties compatible with the SM Higgs boson has been observed at the LHC [19, 20], which presumably completes the SM. Nevertheless, the SM cannot be the ultimate theory, since e.g. gravity as fourth elementary force is not included and the existence of dark matter as well as the size of the baryon asymmetry cannot be explained by the SM. Therefore, searches for BSM physics are ongoing, with efforts

from both the theoretical and the experimental side. One promising class of BSM models involves supersymmetry, which is able to solve some theoretical limitations of the SM, like the fine tuning of the Higgs boson mass. The MSSM, which is the minimal supersymmetric extension of the SM, will be briefly discussed in the next section.

### 2.1.1 Field Content of the SM

The SM is based on the gauge group  $SU(3)_c \times SU(2)_L \times U(1)_Y$ , with  $SU(3)_c$  as the gauge group of QCD and  $SU(2)_L \times U(1)_Y$  being the symmetry group of the electroweak sector before EWSB.

The elementary matter fields can be grouped into quarks, which carry color charge as triplets under  $SU(3)_c$  and are therefore affected by strong interactions, and colorless leptons. Leptons and quarks are chiral fermions, carrying spin- $\frac{1}{2}$ . Left- and right-handed components of quark and lepton fields, with

$$\Psi_{L/R} = \frac{1 \mp \gamma_5}{2} \Psi, \quad (2.1)$$

transform differently under the weak symmetry group  $SU(2)_L$ . Here and in the following all fermion fields are commonly denoted by  $\Psi$ . Only the left-handed fermion components are affected by the weak force. They form a doublet under the weak isospin, while the right-handed components are a singlet under  $SU(2)_L$ . This leads to the vector minus axial vector ( $V - A$ ) coupling structure [42, 43] of W bosons to fermions. In the quark case each doublet combines two kinds of quark fields, an up-type and a down-type one. The weak isospin doublets of the lepton sector combine a lepton and the corresponding neutrino. Finally, the quantum number of the  $U(1)$  symmetry is called weak hypercharge, which can be expressed through the electric charge  $Q$  and the third component of the weak isospin  $T_3$  by  $Y = Q - T_3$ . A right-handed neutrino would be a singlet under all SM gauge groups and is therefore not included.

All quarks and leptons occur in three generations with identical SM quantum numbers, i.e. the SM forces are generation blind. Normal (stable) matter is built from quarks and leptons of the first generation, since the heavier second and third generation fermions decay rapidly into their lightest representatives. Furthermore, since the potential of QCD rises with increasing distance between two color-charged particles, only color-singlet states can exist as free particles. Therefore quarks always confine into bound states of at least two quarks. All matter constituents of the SM and their quantum numbers are listed in Table 2.1. Additionally, for each of these left-handed (right-handed) particles a corresponding right-handed (left-handed) antiparticle exists, with flipped signs for all quantum numbers.

The interactions between the matter fields are mediated by spin-1 gauge fields. Strong interactions are transmitted by the gluon fields  $G_\mu^a$ , which form an octet under  $SU(3)_c$  and correspond to the eight generators of this group. One possible representation of these generators is given by  $\frac{1}{2}\lambda^a$ , with  $a = 1, \dots, 8$  and  $\lambda^a$  being the Gell-Mann matrices. The  $W_\mu^i$  fields, with  $i = 1, 2, 3$ , are responsible for the weak force and correspond to

type	particle generation			quantum numbers		
	1st	2nd	3rd	$SU(3)_c$	$T_3 [SU(2)_L]$	$Y [U(1)_Y]$
quarks	$\begin{pmatrix} u_L \\ d_L \end{pmatrix}$	$\begin{pmatrix} c_L \\ s_L \end{pmatrix}$	$\begin{pmatrix} t_L \\ b_L \end{pmatrix}$	<b>3</b>	$+\frac{1}{2}$	$+\frac{1}{6}$
	$u_R$	$c_R$	$t_R$	<b>3</b>	$-\frac{1}{2}$	$+\frac{1}{6}$
	$d_R$	$s_R$	$b_R$	<b>3</b>	0	$+\frac{2}{3}$
				<b>3</b>	0	$-\frac{1}{3}$
leptons	$\begin{pmatrix} \nu_{e,L} \\ e_L^- \end{pmatrix}$	$\begin{pmatrix} \nu_{\mu,L} \\ \mu_L^- \end{pmatrix}$	$\begin{pmatrix} \nu_{\tau,L} \\ \tau_L^- \end{pmatrix}$	<b>1</b>	$+\frac{1}{2}$	$-\frac{1}{2}$
	$e_R^-$	$\mu_R^-$	$\tau_R^-$	<b>1</b>	$-\frac{1}{2}$	$-\frac{1}{2}$
				<b>1</b>	0	-1

Table 2.1: Matter content of the Standard Model.

interaction	gauge group	gauge field	quantum numbers		
			$SU(3)_c$	$SU(2)_L$	$Y [U(1)_Y]$
strong	$SU(3)_c$	$g$	<b>8</b>	<b>1</b>	0
weak	$SU(2)_L$	$W_\mu^a$	<b>1</b>	<b>3</b>	0
hypercharge	$U(1)$	$B_\mu$	<b>1</b>	<b>1</b>	0

Table 2.2: Gauge fields of the Standard Model before EWSB.

the generators of the  $SU(2)_L$  group, which have  $\frac{1}{2}\sigma^i$  as one possible representation. Here  $\sigma^i$  denotes the  $2 \times 2$  Pauli matrices. Since  $SU(3)_c$  and  $SU(2)_L$  are Yang-Mills theories [44] the  $W_\mu^i$  and  $G_\mu^a$  fields carry weak isospin and color, respectively, and are therefore interacting with themselves. The  $B_\mu$  field corresponds to the generator  $Y$  of the abelian  $U(1)_Y$  group. As it does not carry weak hypercharge no self-couplings exist. The gauge fields and their quantum numbers are summarized in Table 2.2.

The coupling between gauge fields  $G_\mu^a/W_\mu^a/B_\mu$  and matter fields  $\Psi_{L/R}$  is described by covariant derivatives, which are given by

$$D_\mu \Psi_L = \left( \partial_\mu - \underbrace{i\frac{g_s}{2} G_\mu^a \lambda^a}_{\text{only for quarks}} - i\frac{g}{2} W_\mu^i \sigma^i - i\frac{g'}{2} B_\mu \right) \Psi_L, \quad (2.2)$$

$$D_\mu \Psi_R = \left( \partial_\mu - \underbrace{i\frac{g_s}{2} G_\mu^a \lambda^a}_{\text{only for quarks}} - i\frac{g'}{2} B_\mu \right) \Psi_R, \quad (2.3)$$

with  $g_s$ ,  $g$  and  $g'$  denoting the  $SU(3)_c$ ,  $SU(2)_L$  and  $U(1)_Y$  coupling constants, respectively. The field strength tensors of the three gauge fields can be written as

$$G_{\mu\nu}^a = \partial_\mu G_\nu^a - \partial_\nu G_\mu^a + g_s f^{abc} G_\mu^b G_\nu^c \quad (2.4)$$

$$W_{\mu\nu}^i = \partial_\mu W_\nu^i - \partial_\nu W_\mu^i + g \epsilon^{ijk} W_\mu^j W_\nu^k \quad (2.5)$$

$$B_{\mu\nu} = \partial_\mu B_\nu - \partial_\nu B_\mu, \quad (2.6)$$

where  $f^{abc}$  and  $\epsilon^{ijk}$  are the structure constants of the  $SU(3)_c$  and the  $SU(2)_L$ , respectively ( $a, b, c = 1, \dots, 8$ ;  $i, j, k = 1, 2, 3$ ).

With these constituents the Lagrangian of the SM without EWSB can be written as

$$\begin{aligned} \mathcal{L}_{\text{SM}'} = & -\frac{1}{4}G_{\mu\nu}^a G^{a\mu\nu} - \frac{1}{4}W_{\mu\nu}^i W^{i\mu\nu} - \frac{1}{4}B_{\mu\nu}B^{\mu\nu} \\ & + i\bar{\Psi}_{L,k} D_\mu \gamma^\mu \Psi_{L,k} + i\bar{\Psi}_{R,k} D_\mu \gamma^\mu \Psi_{R,k} \end{aligned} \quad (2.7)$$

The first row describes the kinetic terms of the gauge fields and their self-couplings, while the second row includes the kinetic terms of the matter fields and their interactions with the gauge bosons. The index  $k$  denotes the different fermion fields. As mentioned before, the direct inclusion of mass terms into the Lagrangian would break gauge invariance. However, masses for the elementary particles can be included consistently by means of an EWSB sector. The EWSB mechanism of the SM is the Higgs mechanism [7–10] which will be introduced in the next subsection and generates the masses for the weak gauge bosons. Masses of quarks and leptons are then included by the addition of Yukawa interactions between the fermions and the Higgs field.

## 2.1.2 EWSB in the SM: The Higgs Sector

The brief introduction of the Higgs mechanism in the SM is based on Ref. [45], which offers a very detailed introduction into the SM Higgs sector. In the Higgs mechanism mass terms for gauge bosons are generated by introducing a new scalar field in the Lagrangian

$$\mathcal{L}_S = (D^\mu \Phi)^\dagger (D_\mu \Phi) + V(\Phi^\dagger \Phi) = (D^\mu \Phi)^\dagger (D_\mu \Phi) - \mu^2 \Phi^\dagger \Phi - \lambda (\Phi^\dagger \Phi)^2 \quad (2.8)$$

with a special choice for the parameters of the potential  $V(\Phi^\dagger \Phi)$ . With  $\mu^2 < 0$  and  $\lambda > 0$  the famous mexican-hat type potential is obtained which features a minimum at  $\langle \Phi^\dagger \Phi \rangle = -\frac{\mu^2}{2\lambda}$ .

In the SM case the minimal choice for the scalar field is a complex weak isospin doublet

$$\Phi = \begin{pmatrix} \phi^+ \\ \phi^0 \end{pmatrix} \quad \text{with} \quad Y = \frac{1}{2}, \quad (2.9)$$

which has 4 degrees of freedom; enough to give mass to the three weak gauge bosons. With the covariant derivative

$$D_\mu \Phi = \left( \partial_\mu - i\frac{g}{2}W_\mu^i \sigma^i - i\frac{g'}{2}B_\mu \right) \Phi \quad (2.10)$$

the Lagrangian  $\mathcal{L}_S$  is invariant under the SM group  $SU(3)_c \times SU(2)_L \times U(1)_Y$ . However, the ground state is no longer invariant under this group. Instead,  $SU(2)_L \times U(1)_Y$  is broken due to the non-vanishing vacuum expectation value (vev)  $v$ ,

$$\langle \Phi \rangle_0 = \begin{pmatrix} 0 \\ \frac{v}{\sqrt{2}} \end{pmatrix} \quad \text{with} \quad v = \sqrt{\frac{-\mu^2}{\lambda}}, \quad (2.11)$$

where the vev has been chosen solely in the neutral  $\Phi$  component in order to still maintain the  $U(1)$  symmetry of quantum electrodynamics (QED). This effect, that a Lagrangian respects a certain symmetry which the ground state does not, is called “spontaneous symmetry breaking”. The scalar field can now be expanded around the vev by introducing the four real fields  $\phi_{1,2,3}(x)$  and  $H(x)$ . If additionally a special gauge, the unitary gauge, is chosen, only the physical Higgs field  $H(x)$  survives,

$$\Phi = \left( \begin{array}{c} \phi_2 + i\phi_1 \\ \frac{1}{\sqrt{2}}(v + H) - i\phi_3 \end{array} \right) \xrightarrow{\text{unitary gauge}} \frac{1}{\sqrt{2}} \left( \begin{array}{c} 0 \\ (v + H) \end{array} \right). \quad (2.12)$$

Inserting this expression into the kinetic term of Eq. (2.8) yields

$$(D^\mu \Phi)^\dagger (D_\mu \Phi) = \frac{1}{2}(\partial_\mu H)^2 + \frac{1}{8}g(v + H)^2 |W_\mu^1 + iW_\mu^2|^2 + \frac{1}{8}(v + H)^2 |gW_\mu^3 - g'B_\mu|^2. \quad (2.13)$$

By introducing the physical  $W^\pm$ ,  $Z$  and photon fields as

$$W^\pm = \frac{1}{\sqrt{2}}(W_\mu^1 \mp iW_\mu^2), \quad Z = c_W W_\mu^3 - s_W B_\mu \quad \text{and} \quad A = s_W W_\mu^3 + c_W B_\mu, \quad (2.14)$$

with the sine and the cosine of the electroweak mixing angle  $\theta_W$  defined by

$$s_W = \sin \theta_W = \frac{g'}{\sqrt{g^2 + g'^2}} \quad \text{and} \quad c_W = \cos \theta_W = \frac{g}{\sqrt{g^2 + g'^2}}, \quad (2.15)$$

the bilinear terms of Eq. (2.13) yield masses for the  $W$  and  $Z$  bosons,

$$M_W = \frac{gv}{2} \quad \text{and} \quad M_Z = \frac{gv}{2 \cos \theta_W}, \quad (2.16)$$

while the photon remains massless. Additionally, Eq. (2.13) introduces couplings between the physical Higgs field  $H$  and the massive gauge bosons, with the trilinear couplings being proportional to the gauge boson masses,  $g_{HVV} = \frac{2M_V^2}{v}$ . Since the photon is massless it does not couple directly to the Higgs boson, but only through loops of electrically charged massive particles. Proving that the newly discovered scalar boson exhibits this coupling structure is an important step for establishing this boson as the true SM Higgs boson and a major task for the LHC in the near future. The Higgs boson itself is also massive. From the potential of Eq. (2.8) follows

$$M_H^2 = 2\lambda v^2 = -2\mu^2. \quad (2.17)$$

The value of the vev can be obtained from Eq. (2.16), yielding  $v \approx 246$  GeV. However, since the values of  $\mu^2$  and  $\lambda$  are not predicted by the SM, the Higgs boson mass is a free parameter of the theory. Additionally, the potential gives rise to triple and quartic Higgs boson self couplings.

So far, only the gauge bosons have acquired mass. However, the scalar field of Eqs. (2.8) and (2.9) allows additionally for a gauge invariant formulation of fermion mass terms in the SM Lagrangian. The introduction of so-called Yukawa interactions of fermions and scalars, with coupling constants  $\lambda_f$ ,

$$\mathcal{L}_F = -\lambda_f \bar{\Psi}_L \Phi \Psi_R + \text{h.c.}, \quad (2.18)$$

lead to fermion mass terms due to the non-zero vev. Again, couplings between the fermions and the Higgs field are introduced, with coupling constants proportional to the fermion mass.

The Yukawa interactions introduce a mixing of different fermion generations into the SM, since the couplings in the Yukawa terms of Eq. (2.18) are in general not diagonal in the generations, but are non-diagonal  $3 \times 3$  matrices. Thus the mass eigenstates and the interaction eigenstates of the weak force are no longer the same. The conversion from interaction to mass eigenstates in the quark sector can be parametrized by the CKM-matrix [11, 12]. Furthermore, the mixing of three quark generations yields a non-vanishing phase in the CKM-matrix, which introduces  $CP$ -violation into the Standard Model. However, the amount of  $CP$ -violation from this mechanism is not large enough to describe the observed matter-antimatter asymmetry of the universe. The generation mixing in the quark sector is very small, especially for the mixing of the third generation with the other two. Therefore, and since the CKM-effects are not important for the analyses described in the following, the CKM-matrix is assumed to be diagonal throughout this thesis.

## 2.2 Supersymmetry

As mentioned before, the SM is an extremely successful theory. Nevertheless, observations of phenomena like dark matter imply that it cannot be the ultimate theory. From a theoretical point of view, a theory with the unification of all three forces of the SM at a high energy scale, the Grand Unified Theory (GUT) scale, would yield an elegant high-energy completion of the SM. However, when considering only the SM in the renormalization group evolution of the coupling constants, they do not meet at a common energy scale as it would be desirable [46, 47]. Another theoretical shortcoming of the SM are the huge radiative corrections to the Higgs boson mass. The bare Higgs boson mass of the unrenormalized Lagrangian receives large corrections from massive fermion and gauge boson loops. These corrections depend quadratically on the cut-off scale  $\Lambda$ , which defines the scale up to which the SM is expected to be valid. It may be as high as the GUT scale or the Planck scale if no New Physics is found at lower energies. A physical Higgs boson mass of  $\mathcal{O}(100 \text{ GeV})$  therefore requires an extreme fine-tuning of the unrenormalized parameter. Additionally, the SM offers no explanation, why the difference between the Planck scale and the electroweak scale is several orders of magnitude. The latter one is the so-called hierarchy problem of the SM.

These problems can be solved by including an additional symmetry into the theory, which predicts a bosonic partner for each fermionic degree of freedom of the theory, and vice versa. The SUSY transformation, generated by the operator  $Q$  therefore yields

$$Q|\text{Boson}\rangle = |\text{Fermion}\rangle \quad Q|\text{Fermion}\rangle = |\text{Boson}\rangle . \quad (2.19)$$

In an unbroken SUSY all quantum numbers of these partners are equal, except for the spin difference of one half. Since in the SM no suitable counterparts for the bosons

and fermions exist, this implies the introduction of new particles, the so-called superpartners, into the theory.

In an exact SUSY theory the radiative corrections to the Higgs boson mass cancel exactly, due to the relative minus sign in fermionic and bosonic loops. Therefore the Higgs boson mass is protected by a symmetry, which is a natural solution for the hierarchy problem. If SUSY is broken, i.e. the SM particles and their superpartners differ in mass, the dependence on the cut-off scale still reduces from a quadratic to a logarithmic dependence. The amount of fine-tuning needed in order to cancel these corrections is modest, as long as the mass splitting of the SM particle and the corresponding superpartner is not larger than  $\mathcal{O}(1 \text{ TeV})$ . The additional particle content of a SUSY theory with appropriate mass ranges can lead to a much better coupling unification than in the pure SM case [46, 47]. The postulation of another symmetry [36], which forbids baryon and lepton number violating couplings, is well motivated by e.g. the non-observation of a proton decay [48]. This  $R$ -parity allows for the classification of the particle content into SM particles and Higgs bosons with even  $R$ -parity and the new superpartners due to SUSY with odd  $R$ -parity. The latter ones are called supersymmetric particles (SUSY particles) in the following. Due to  $R$ -parity vertices with an odd number of supersymmetric particles are not allowed. This leads to a stable lightest supersymmetric particle (LSP), which, therefore, can serve as a viable dark matter candidate.

### 2.2.1 The Minimal Supersymmetric Extension of the Standard Model

In the following, the minimal SUSY model embedding the SM shall be discussed. This Minimal Supersymmetric Extension of the Standard Model is the theoretical basis of the studies presented in Chapter 3 and 4. A detailed review of the MSSM can be found e.g. in Ref. [34]. This short introduction into the MSSM follows Ref. [49].

In the Lagrangian of a SUSY theory the SM fields and their corresponding superpartners are combined into superfields. The left-handed fermion fields of the SM and their superpartners form a chiral superfield, which consists of a complex scalar field with two degrees of freedom and one two-component Weyl spinor. The right-handed SM fermion fields and the corresponding SUSY particles are cast into chiral superfields as well, by considering them as left-handed antiparticles. The scalars associated to the SM quarks and leptons are denoted as “scalar quarks” and “scalar leptons”, or short as “squarks” and “sleptons”. For the superpartners of the SM bosons the ending “-ino” is appended to the name of the SM particle, e.g. the gluino  $\tilde{g}$  is the partner of the gluon  $g$ . The Higgs fields and the corresponding Higgsinos are again organized in chiral superfields. In contrast to the SM at least two Higgs doublets with opposite hypercharge are needed in a SUSY extension, in order to cancel chiral anomalies arising due to the new fermionic Higgsinos with non-zero hypercharge. Additionally, both Higgs doublets are needed in order to give mass to up-type and down-type fermions simultaneously. The spin-1 gauge bosons of the SM and the associated gauginos are combined into

superfield	field content		quantum numbers		
	$R = +1$	$R = -1$	$SU(3)_c$	$SU(2)_L$	$U(1)_Y$
$\widehat{Q}$	$(u_L, d_L)$	$(\widetilde{u}_L, \widetilde{d}_L)$	<b>3</b>	<b>2</b>	$+\frac{1}{6}$
$\widehat{U}^c$	$\bar{u}_R$	$\widetilde{u}_R^*$	$\bar{\mathbf{3}}$	<b>1</b>	$-\frac{2}{3}$
$\widehat{D}^c$	$\bar{d}_R$	$\widetilde{d}_R^*$	$\bar{\mathbf{3}}$	<b>1</b>	$+\frac{1}{3}$
$\widehat{L}$	$(\nu_{e,L}, e_L)$	$(\widetilde{\nu}_{e,L}, \widetilde{e}_L)$	<b>1</b>	<b>2</b>	$-\frac{1}{2}$
$\widehat{E}^c$	$\bar{e}_R$	$\widetilde{e}_R^*$	<b>1</b>	<b>1</b>	$+1$
$\widehat{H}_u$	$(H_u^+, H_u^0)$	$(\widetilde{H}_u^+, \widetilde{H}_u^0)$	<b>1</b>	<b>2</b>	$+\frac{1}{2}$
$\widehat{H}_d$	$(H_d^0, H_d^-)$	$(\widetilde{H}_d^0, \widetilde{H}_d^-)$	<b>1</b>	<b>2</b>	$-\frac{1}{2}$
$\widehat{G}_a$	$G_a^\mu$	$\widetilde{G}_a$	<b>8</b>	<b>1</b>	0
$\widehat{W}_i$	$W_i^\mu$	$\widetilde{W}_i$	<b>1</b>	<b>3</b>	0
$\widehat{B}$	$B^\mu$	$\widetilde{B}$	<b>1</b>	<b>1</b>	0

Table 2.3: Chiral and vector superfields of the MSSM. For the quark and lepton superfields only the first of three generations is shown.

vector superfields [25], which consist of a massless gauge field and a two-component Weyl spinor.

The general MSSM is defined by the following minimality requirements:

- **Minimal gauge group:** The MSSM is based on the same gauge group as the SM,  $SU(3)_c \times SU(2)_L \times U(1)_Y$ . The gauge superfields of the MSSM are given in Table 2.3.
- **Minimal particle content:** The only new matter fields with respect to the SM are the additional Higgs doublet and one superpartner for each degree of freedom of this two Higgs doublet model. The chiral superfields of the MSSM, which comprise all matter fields of the MSSM are listed in Table 2.3. More details on the MSSM Higgs sector will follow in Section 2.2.3.
- **Minimal Yukawa interactions due to  $R$ -parity conservation:** Demanding  $R$ -parity conservation excludes Yukawa terms which are possible in a SUSY model, but are not mandatory for a viable theory.
- **SUSY has to be broken “soft”:** The criteria described above define a fully working SUSY theory. However, the SUSY particles would have the same mass as the SM particles. As no SUSY particles have been observed so far such a model with an exact SUSY is excluded. Soft SUSY breaking is a breaking mechanism which does not introduce new quadratic divergences into the theory. It will be discussed in Section 2.2.2.

After EWSB several of the SUSY particles have the same quantum numbers, i.e. the same electric charge,  $R$ -parity, spin and color, and can therefore mix with each other forming the following mass eigenstates: the neutral Higgsinos, the neutral Wino and

name	spin	color	el. charge	gauge eigenstates	mass eigenstates
squarks	0	<b>3</b>	$+\frac{2}{3}$	$\tilde{u}_L, \tilde{u}_R, \tilde{c}_L, \tilde{c}_R$	$\tilde{u}_L, \tilde{u}_R, \tilde{c}_L, \tilde{c}_R$
			$-\frac{1}{3}$	$\tilde{d}_L, \tilde{d}_R, \tilde{s}_L, \tilde{s}_R$	$\tilde{d}_L, \tilde{d}_R, \tilde{s}_L, \tilde{s}_R$
			$+\frac{2}{3}$	$\tilde{t}_L, \tilde{t}_R$	$\tilde{t}_1, \tilde{t}_2$
			$-\frac{1}{3}$	$\tilde{b}_L, \tilde{b}_R$	$\tilde{b}_1, \tilde{b}_2$
sleptons	0	<b>1</b>	-1	$\tilde{e}_L, \tilde{e}_R, \tilde{\mu}_L, \tilde{\mu}_R$	$\tilde{e}_L, \tilde{e}_R, \tilde{\mu}_L, \tilde{\mu}_R$
			0	$\tilde{\nu}_{e,L}, \tilde{\nu}_{\mu,L}$	$\tilde{\nu}_{e,L}, \tilde{\nu}_{\mu,L}$
			-1	$\tilde{\tau}_L, \tilde{\tau}_R$	$\tilde{\tau}_1, \tilde{\tau}_2$
			0	$\tilde{\nu}_{\tau,L}$	$\tilde{\nu}_{\tau,L}$
neutralinos	$\frac{1}{2}$	<b>1</b>	0	$\tilde{B}^0, \tilde{W}^0, \tilde{H}_u^0, \tilde{H}_d^0$	$\chi_1^0, \chi_2^0, \chi_3^0, \chi_4^0$
charginos	$\frac{1}{2}$	<b>1</b>	+1	$\tilde{W}^+, \tilde{H}_u^+$	$\chi_1^+, \chi_2^+$
			-1	$\tilde{W}^-, \tilde{H}_d^-$	$\chi_1^-, \chi_2^-$
gluino	$\frac{1}{2}$	<b>8</b>	0	$\tilde{g}$	$\tilde{g}$

Table 2.4: Mass eigenstates and the corresponding gauge eigenstates of the MSSM SUSY particles. The stops, sbottoms, staus, neutralinos and charginos are sorted by increasing mass.

the Bino give rise to four neutralinos  $\chi_i^0$  ( $i = 1, 2, 3, 4$ ). In many MSSM scenarios the lightest neutralino serves as LSP. The charged Higgsinos and the charged Winos mix into two charginos  $\chi_j^\pm$  ( $j = 1, 2$ ). In the squark and slepton sector large mixing only occurs in the third generation. For the first two generations the mixing is very small due to the small Yukawa couplings and therefore mixing effects are usually neglected. The resulting SUSY particle mass eigenstates of the MSSM are summarized in Table 2.4.

### 2.2.2 SUSY Breaking in the MSSM

So far SUSY particles have not been observed, therefore SUSY has to be broken. It is assumed that SUSY is spontaneously broken by an unknown mechanism in a “hidden sector”. Since the exact model of SUSY breaking is unknown, the SUSY breaking is parametrized by the introduction of explicit SUSY breaking terms in the Lagrangian and the determination of the breaking mechanism has yet to be performed once SUSY particles have been discovered. However, a few ansatzes for SUSY breaking mechanisms exist, e.g. gauge mediated SUSY breaking (see e.g. Ref. [50]) or gravity mediated SUSY breaking. A widely used model of the latter class is minimal supergravity (mSUGRA) [51–55] based SUSY breaking. Due to a small number of parameters it has a large predictive power.

In order to avoid quadratic divergences in the higher-order corrections of the Higgs boson mass the SUSY breaking has to be “soft” [56]. For the MSSM, the condition of

only soft SUSY breaking is fulfilled by mass terms for gauginos and sfermions, mass and bilinear terms for the Higgs bosons and trilinear couplings between sfermions and Higgs bosons. The soft SUSY breaking mass terms for the Higgs fields are part of the Higgs potential and SUSY breaking is mandatory in order to get a potential that leads to EWSB in the MSSM [49].

Without any restrictions on these additional terms the unconstrained MSSM has 105 new free parameters on top of the 19 parameters from the SM. However, certain phenomenologically well motivated assumptions lead to a much smaller parameter set:

- all soft SUSY breaking terms are real. Therefore  $CP$ -violation arises solely due to CKM effects.
- the sfermion mass matrices and the trilinear coupling matrices are diagonal, excluding tree-level flavor changing neutral currents.
- First and second generation SUSY breaking masses and trilinear couplings are the same at the SUSY scale, which is motivated by e.g. constraints from  $K^0 - \bar{K}^0$  mixing.

These constraints reduce the input parameters from 105 to the following 22, comprising the “phenomenological MSSM” or pMSSM [57]:

- $M_1, M_2, M_3$ : the Bino, Wino and gluino mass parameters
- $A_u = A_c, A_d = A_s, A_e = A_\mu$ : the first- and second-generation trilinear couplings
- $A_t, A_b, A_\tau$ : the third-generation trilinear couplings
- $m_{H_u}^2, m_{H_d}^2$ : the Higgs mass parameters squared
- $M_{eL} = M_{\mu L}$ : the mass parameter of the left-handed first- and second-generation slepton/sneutrino
- $M_{eR} = M_{\mu R}$ : the mass parameter of the right-handed selectron and smuon
- $M_{\tau L}$ : the mass parameter of the left-handed stau and tau-sneutrino
- $M_{\tau R}$ : the mass parameter of the right-handed stau
- $M_{q_1 L} = M_{q_2 L}$ : the mass parameter of the left-handed first- and second-generation squarks
- $M_{uR} = M_{cR}, M_{dR} = M_{sR}$ : the mass parameters of the right-handed first- and second-generation squarks
- $M_{q_3 L}$ : the mass parameter of the left-handed third-generation squarks
- $M_{tR}, M_{bR}$ : the mass parameters of the right-handed stop and sbottom
- $\tan \beta$ : the ratio of the vevs of the two Higgs doublets

With the assumption of a specific SUSY breaking mechanism the number of free parameters can still be reduced significantly. A well-known example of such a model is the already mentioned SUSY breaking via mSUGRA. Here only 4 continuous parameters

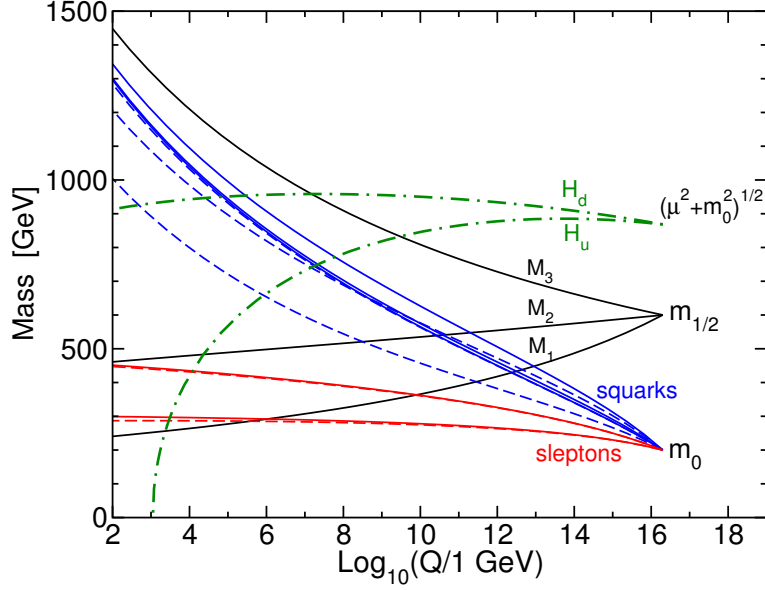


Figure 2.1: Visualization of the RGE running of the soft SUSY breaking parameters in an mSUGRA scenario with  $m_0 = 200$  GeV,  $m_{\nu_2} = -A_0 = 600$  GeV,  $\tan\beta = 10$ ,  $\text{sign}(\mu) = +1$  at the high scale. The negative value for  $(\mu^2 + m_{H_u}^2)$  provides the EWSB. This figure is taken from Ref. [34].

and one sign remain at the GUT scale  $M_U \approx 2 \cdot 10^{16}$  GeV, at which the communication of the SUSY breaking in the “hidden sector” is transmitted to the “visible sector” by universal gravitational interactions. The unification conditions of mSUGRA are the following:

- universal gaugino masses:

$$M_1(M_U) = M_2(M_U) = M_3(M_U) \equiv m_{\nu_2} \quad (2.20)$$

- universal scalar masses:

$$\begin{aligned} m_{H_u}(M_U) &= m_{H_d}(M_U) = \\ M_{eL}(M_U) &= M_{\mu L}(M_U) = M_{eR}(M_U) = M_{\mu R}(M_U) = \\ M_{\tau L}(M_U) &= M_{\tau R}(M_U) = M_{q_1 L}(M_U) = M_{q_2 L}(M_U) = \\ M_{uR}(M_U) &= M_{cR}(M_U) = M_{dR}(M_U) = M_{sR}(M_U) = \\ M_{q_3 L}(M_U) &= M_{tR}(M_U) = M_{bR}(M_U) \equiv m_0 \end{aligned} \quad (2.21)$$

- universal trilinear couplings:

$$\begin{aligned} A_u(M_U) &= A_c(M_U) = A_d(M_U) = A_s(M_U) = A_e(M_U) = A_\mu(M_U) = \\ A_t(M_U) &= A_b(M_U) = A_\tau(M_U) \equiv A_0 \end{aligned} \quad (2.22)$$

Two more parameters are necessary for the description of the SUSY sector in an mSUGRA model, the ratio of the two Higgs doublet vevs  $\tan\beta$  and the sign of the

Higgs/Higgsino mass parameter  $\mu$ ,  $\text{sign}(\mu)$ . Therefore, the SUSY parameters of an mSUGRA MSSM scenario at the GUT scale are

$$m_0, \quad m_{1/2}, \quad A_0, \quad \tan\beta, \quad \text{sign}(\mu). \quad (2.23)$$

The soft SUSY breaking parameters at the low (SUSY) scale are obtained from these due to running by renormalization group equations (RGEs). One example of the evolution of the soft SUSY breaking terms in mSUGRA is depicted in Figure 2.1.

The SUSY models discussed in Chapters 3 and 4 are based on an mSUGRA scenario, which gives rise to a set of pMSSM parameters, which are then further modified in order to achieve models with certain phenomenological characteristics.

### 2.2.3 The Higgs Sector of the MSSM

The last part of the MSSM which is important for the analyses of Chapters 3 and 4 is the EWSB sector. It has been mentioned before that the MSSM has to contain two Higgs doublets of opposite hypercharge,

$$H_u = \begin{pmatrix} H_u^+ \\ H_u^0 \end{pmatrix} \quad \text{with} \quad Y_{H_u} = +\frac{1}{2}, \quad H_d = \begin{pmatrix} H_d^0 \\ H_d^- \end{pmatrix} \quad \text{with} \quad Y_{H_d} = -\frac{1}{2}, \quad (2.24)$$

in order to be able to give mass to up-type and down-type quarks and to obtain an anomaly-free [58, 59] theory.

Like in the SM the neutral components of the two Higgs fields get a vacuum expectation value,

$$\langle H_d^0 \rangle = \frac{v_d}{\sqrt{2}} \quad \text{and} \quad \langle H_u^0 \rangle = \frac{v_u}{\sqrt{2}}, \quad (2.25)$$

with

$$v_u^2 + v_d^2 = v^2 \approx (246 \text{ GeV})^2. \quad (2.26)$$

Since only the ratio of the two vevs is unknown one defines

$$\tan\beta = \frac{v_u}{v_d} = \frac{v \sin\beta}{v \cos\beta}. \quad (2.27)$$

The five physical Higgs bosons  $h$ ,  $H$ ,  $A$ ,  $H^\pm$  and the three Goldstone modes, which give rise to longitudinal degrees of freedom of the massive gauge bosons, can again be obtained in the expansion of the scalar fields around the vacuum,

$$H_u = \frac{1}{\sqrt{2}} \begin{pmatrix} H_u^+ \\ v_u + H_u^0 + iP_u^0 \end{pmatrix}, \quad H_d = \frac{1}{\sqrt{2}} \begin{pmatrix} v_d + H_d^0 + iP_d^0 \\ H_d^- \end{pmatrix}, \quad (2.28)$$

followed by the diagonalization of the resulting mass matrices.

The light  $CP$ -even Higgs boson  $h$  and the corresponding heavy one  $H$  are given by a rotation

$$\begin{pmatrix} H \\ h \end{pmatrix} = \begin{pmatrix} \cos \alpha & \sin \alpha \\ -\sin \alpha & \cos \alpha \end{pmatrix} \begin{pmatrix} H_d^0 \\ H_u^0 \end{pmatrix}, \quad (2.29)$$

with

$$\alpha = \frac{1}{2} \arctan \left( \tan 2\beta \frac{M_A^2 + M_Z^2}{M_A^2 - M_Z^2} \right), \quad -\frac{\pi}{2} \leq \alpha \leq 0, \quad (2.30)$$

where  $M_A$  is the mass of the  $CP$ -odd Higgs boson and will be given below.

The neutral  $CP$ -odd Higgs boson  $A$  and the charged Higgs bosons  $H^\pm$  are obtained by

$$\begin{pmatrix} G^0 \\ A \end{pmatrix} = \begin{pmatrix} \cos \beta & \sin \beta \\ -\sin \beta & \cos \beta \end{pmatrix} \begin{pmatrix} P_d^0 \\ P_u^0 \end{pmatrix} \quad (2.31)$$

and

$$\begin{pmatrix} G^\pm \\ H^\pm \end{pmatrix} = \begin{pmatrix} \cos \beta & \sin \beta \\ -\sin \beta & \cos \beta \end{pmatrix} \begin{pmatrix} H_d^\pm \\ H_u^\pm \end{pmatrix}. \quad (2.32)$$

Here  $H_u^-$  and  $H_d^+$  are defined by  $H_u^- = H_u^{+*}$  and  $H_d^+ = H_d^{-*}$ , respectively, and  $G^0, G^\pm$  denote the Goldstone modes.

The tree-level masses of the Higgs bosons are given by [34]

$$\begin{aligned} M_A^2 &= 2|\mu|^2 + m_{H_u}^2 + m_{H_d}^2 \\ M_{H^\pm}^2 &= M_A^2 + M_W^2 \\ M_{h,H}^2 &= \frac{1}{2} \left( M_A^2 + M_Z^2 \mp \sqrt{(M_A^2 - M_Z^2)^2 + 4M_A^2 M_Z^2 \sin^2 2\beta} \right). \end{aligned} \quad (2.33)$$

In contrast to a general two Higgs doublet model the spectrum is severely constrained, since only two free parameters, e.g.  $M_A$  and  $\tan \beta$ , are sufficient to determine the Higgs sector at tree level. Additionally, the masses of the Higgs bosons are restricted as well,

$$\begin{aligned} M_h &\leq \min(M_A, M_Z) \cdot |\cos 2\beta| \leq M_Z \\ M_H &> \max(M_A, M_Z) \\ M_{H^\pm} &> M_W. \end{aligned} \quad (2.34)$$

With the inclusion of higher-order corrections the upper bound on  $M_h$  can be weakened [60–62], yielding roughly [49]

$$M_h \lesssim 140 \text{ GeV}. \quad (2.35)$$

However, these corrections involve other sectors of the MSSM, in particular, the stop is important [63–68]. Therefore experimental constraints on the Higgs sector can also have a significant impact on MSSM parameters beyond the pure Higgs sector.

There are furthermore many constraints on the couplings of Higgs bosons. Of particular interest for Chapters 3 and 4 are the couplings of the neutral  $CP$ -even Higgs bosons to vector bosons. Relative to the SM Higgs to vector boson coupling, they read

$$\begin{aligned} g_{hVV} &= \sin(\beta - \alpha) \cdot g_{HVV}^{\text{SM}} \\ g_{HV^\pm} &= \cos(\beta - \alpha) \cdot g_{HV^\pm}^{\text{SM}}. \end{aligned} \quad (2.36)$$

The couplings  $g_{hVV}$  and  $g_{HVV}$  are therefore complementary, with

$$g_{hVV}^2 + g_{HVV}^2 = (g_{HVV}^{\text{SM}})^2. \quad (2.37)$$

Thus, for a wide parameter range of the MSSM one of the neutral  $CP$ -even Higgs bosons couples to the vector bosons like the SM Higgs boson. In the SUSY scenarios discussed in Chapters 3 and 4 the light neutral  $CP$ -even Higgs boson  $h$  will be SM-like with a mass exceeding the Large Electron Positron Collider (LEP) limit of  $m_h \geq 114.4$  GeV [69, 70].

## 2.3 Collider Physics at Hadron Colliders

At present and in the foreseeable future the LHC will be the most powerful machine for high-energy particle physics. Since the results of this thesis are merely theoretical predictions for the LHC, in the following the constituents of cross section calculations at hadron colliders will be introduced briefly. Furthermore, given that the estimation of background processes is a crucial task for LHC analyses, a short overview on background determination methods will follow. Possible effects of BSM physics on such a background determination method will be discussed in detail in Chapter 4.

### 2.3.1 Cross Sections at Hadron Colliders

In a hadron-hadron collision usually one parton<sup>1</sup> from the first hadron interacts with one parton from the other hadron. Each parton carries a fraction  $x$  of the hadron momentum  $p$ . In the following the colliding hadrons are assumed to be protons, since the LHC is used as a proton-proton collider most of the time. The initial state partons considered for a proton-proton collider usually include quarks, antiquarks and the gluon. For QED-induced processes or corrections the photon is considered as well. Figure 2.2 sketches the production of a  $W^+$  boson with subsequent decay into a charm-quark and an anti-strange-quark in a proton-proton-collision. In this particular subprocess two proton constituents, the up-quark from proton 1 and the anti-down-quark from proton 2, are the two partons which actually interact with each other. Under the assumption that the factorization theorems of QCD [71] hold a hard collision at a hadron collider can be split into a process independent part, the extraction of a parton from each hadron, and the partonic process, which is  $u\bar{d} \rightarrow W^+ \rightarrow c\bar{s}$  in this example. A full description of  $pp \rightarrow W^+ \rightarrow c\bar{s}$  then has to include a sum over all possible subprocesses, where  $u$  and  $\bar{d}$  are replaced by the other proton constituents.

The splitting of the cross section for the general process  $pp \rightarrow f_1, \dots, f_n$  with  $n$  final state particles into a process-independent part, the *parton distribution functions* (PDFs), and the partonic process  $ab \rightarrow f_1, \dots, f_n$  introduces a new parameter, the factorization scale  $\mu_F$ . This parameter defines the scale that separates the long-distance

---

<sup>1</sup>The “parton model” has been introduced by R. Feynman.

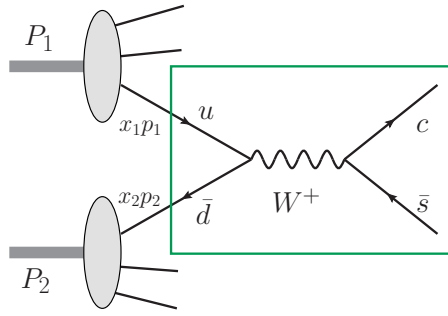


Figure 2.2: Sketch of  $W^+$  production with subsequent decay into an  $c\bar{s}$  pair in a proton-proton collision, in which an up-quark and an anti-down-quark constitute the primary interaction. The hard process is highlighted by the green box.

and non-perturbative QCD effects which are included in the PDFs, and the short-distance QCD effects which are counted towards the partonic process. The PDF  $f_a(x_a, \mu_F^2)$  gives the probability to find a parton  $a$  with momentum fraction  $x$  at  $\mu_F$  in the proton. The expression for the hadronic cross section finally reads

$$\sigma^{pp \rightarrow f_1, \dots, f_n} = \sum_{a,b} \int dx_a dx_b f_a(x_a, \mu_F^2) f_b(x_b, \mu_F^2) \hat{\sigma}^{ab \rightarrow f_1, \dots, f_n}. \quad (2.38)$$

The partonic cross section for the process  $ab \rightarrow f_1, \dots, f_n$  is given by the integration of the hard matrix element squared over all possible momentum configurations for the two initial and  $n$  final state partons, multiplied by the flux factor of the incoming partons:

$$\hat{\sigma}^{ab \rightarrow f_1, \dots, f_n} = \frac{1}{4 x_1 P_1 \cdot x_2 P_2} \int d\Phi_n(x_1, x_2; p_{f_1}, \dots, p_{f_n}) |\mathcal{M}|^2(ab \rightarrow f_1, \dots, f_n). \quad (2.39)$$

For sufficiently high energies  $\hat{\sigma}^{ab \rightarrow f_1, \dots, f_n}$  can be calculated perturbatively. In the case of QCD the expansion in the strong coupling constant  $\alpha_s$  is given by

$$\hat{\sigma} = \hat{\sigma}_0 + \hat{\sigma}_1 \alpha_s + \hat{\sigma}_2 \alpha_s^2 + \dots, \quad (2.40)$$

where  $\hat{\sigma}_0$  contains the matrix element with the smallest powers of strong and electroweak coupling constants,  $\alpha_s$  and  $\alpha$ , respectively, yielding the desired final state.

In the simplest case,  $\hat{\sigma}_{\text{LO}} = \hat{\sigma}_0$ , the hard matrix element can be described by leading-order (LO) Feynman diagrams. The LO diagram of the process  $u\bar{d} \rightarrow W^+ \rightarrow c\bar{s}$  is depicted in Figure 2.2, highlighted by the green box. There exist reliable tools which can generate LO matrix elements, the Born contribution, as long as the leading order does not involve any loops.<sup>2</sup> Examples for automated matrix element generators that can handle  $2 \rightarrow n$  processes with  $n = \mathcal{O}(10)$  are MadGraph/MadEvent [72, 73], WHIZARD/Omega [74, 75] and Sherpa/AMEGIC++ [76, 77].

<sup>2</sup>The  $gg \rightarrow H$  process for example features a heavy-quark loop already at Born level.

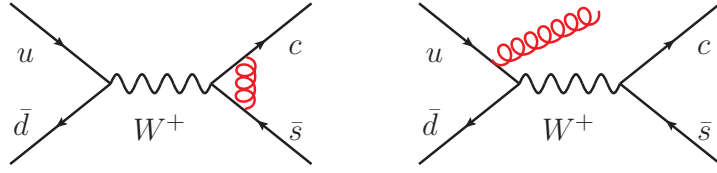


Figure 2.3: Feynman diagrams for the parton-level process  $u\bar{d} \rightarrow W^+ \rightarrow c\bar{s}$ . The left plot shows an exemplary diagram of a one-loop contribution, while the right plot depicts a diagram for the real emission of one additional gluon.

A next-to-leading order (NLO) QCD calculation includes the LO contributions and additionally all terms with one additional factor of  $\alpha_s$  in the matrix element,

$$\hat{\sigma}_{\text{NLO}} = \hat{\sigma}_{\text{LO}} + \hat{\sigma}_{\text{virt}} + \hat{\sigma}_{\text{real}}. \quad (2.41)$$

The first part of the NLO QCD contributions are the virtual corrections,  $\sigma_{\text{virt}}$ , which contain the interference of the one-loop matrix element with the Born matrix element  $|2 \cdot \mathcal{M}_{\text{virt}}^* \cdot \mathcal{M}_{\text{LO}}|$ . The real emission of an additional parton makes up the second part of the NLO QCD contributions,  $\sigma_{\text{real}}$ . Exemplary Feynman diagrams for the one-loop and real-emission contributions of the process  $u\bar{d} \rightarrow W^+ \rightarrow c\bar{s}$  are shown in Figure 2.3.

In contrast to the LO case the fully automated generation of matrix elements at NLO QCD is still at the very beginning. It has been achieved for rather simple  $2 \rightarrow 2$  processes, for example in the `aMC@NLO` [78] or the `GoSam` [79] framework. However, it is currently not feasible to get competitive results for arbitrary processes (e.g.  $2 \rightarrow 6$ ) in a fully automated way.

Colored partons in the final state of the hard scattering process, e.g. the  $c$  and  $\bar{s}$  of Figure 2.2, again undergo non-perturbative interactions. They lead to stable or at least long-living color-singlet states which can be measured in the detector. This hadronization usually yields collimated jets of hadrons. It is carried out in phenomenological models like the cluster model [80] of `Herwig++` [81] or the “Lund string fragmentation framework” [82] in case of `PYTHIA 8` [83]. The connection of the hard scale from the matrix element down to the non-perturbative regime of hadronization is usually established by parton showers [84, 85], which are part of Monte Carlo event generators like `Herwig++` or `PYTHIA 8` as well. The parton-shower uses an all-order approximation to describe additional (soft) QCD radiation, which cannot be handled by fixed-order calculations. Additionally, the parton shower can also describe further radiation from initial-state partons. However, parton-shower and hadronization effects will be neglected in this thesis. Instead, “partonic jets” will serve as an approximation to the hadronic jets. These objects are built up from the final-state partons. Especially for hard partons the partonic jet and the resulting hadronic jet coincide in direction and energy, allowing for a good description of the underlying physics of the hard process.

### 2.3.2 Background Determination

At the LHC the searches for new phenomena have to cope with a huge background of SM processes. The background is made up of contributions from processes besides the signal process that pass the selection criteria of the analysis. Additionally, background contributions can arise from particle mis-identification, e.g. a jet may be identified as a lepton in the detector.

Secondary interactions of the proton remnants (see Figure 2.2), lead to additional activity in the detector, the underlying event (UE) [86]. It is usually estimated from minimum-bias measurements, i.e. measurements with as loose trigger settings as possible in low-luminosity runs, and modeled within the Monte Carlo event generators. Additionally, collisions of other protons in the same bunch, so-called pile-up collisions, produce further activity in the detector. Experimentally, however, this contribution can be identified by the reconstruction of primary interaction vertices.

Coming back to the “real” background processes, especially the searches for electroweak processes face a QCD-induced background which is much higher than the signal process. It is therefore inevitable to have a detailed knowledge of all possible background contributions to the signal process under investigation.

In case of very precisely known background processes, i.e. the remaining theoretical and systematic uncertainty on the contribution is much smaller than the expected signal size, the background process can be estimated from LO or NLO Monte Carlos, maybe normalized to inclusive higher-order cross section calculations where available. This background additionally undergoes the same simulation steps as the signal, i.e. parton shower, hadronization and detector simulation. The resulting contribution can then be subtracted from the experimental event yield. This method is widely used, either for all or a subset of the relevant background contributions of an analysis. The differential  $H \rightarrow \gamma\gamma$  study of Ref. [87] is one example in which the estimation of all background contributions completely relies on simulations.

However, by far not all background contributions can be determined with sufficient precision for a background estimation based solely on Monte Carlo simulations. Additionally, this method demands a precise knowledge of detector efficiencies and a good detector simulation in general, especially for fake backgrounds arising from particle mis-identification. In these cases a background determination which at least partly relies on measured data, the so-called data-driven background determination, can help to reduce these theoretical and systematical uncertainties. A selection of data-driven background determination methods will be sketched in the following. This list is not intended to be complete, since different LHC analyses may have special requirements on background identification and suppression, which leads to a large variety of background determination methods (see e.g. Refs. [88–90]).

**Background Normalization in a Control Region:** Here, Monte Carlo simulations at LO or NLO QCD are used for the determination of a background contribution,

but the simulation is normalized to data in a control region. This region has to fulfill two conditions: on the one hand no signal contribution has to be expected and on the other hand the considered background contributions have to account for a large fraction of the total rate in this region. Given that the shape of distributions can be described well by Monte Carlo and only the normalization of the simulation has a large error, this method can improve the background determination significantly. Still, the composition of the control region must be modeled correctly by Monte Carlo simulations in order to give a reliable prediction on the normalization. This method is used e.g. for the  $WW$  continuum background determination in the zero- and one-jet channels of the  $H \rightarrow WW$  search [91–93].

**Sideband Analysis:** If the signal contribution is expected to show up as a narrow resonance on top of a smooth background in a certain variable, e.g. the invariant mass  $m_{\gamma\gamma}$  in the  $H \rightarrow \gamma\gamma$  search, the background contribution right at the peak can be inferred from the sidebands of the peak. This method is used for example in the  $H \rightarrow \gamma\gamma$  analysis of CMS [20, 94].

**Factorization/“ABCD” Method:** A background contribution can be determined with this method, if two uncorrelated observables  $x$  and  $y$  can be found, which can be split into four regions  $A$  ( $x < x_c, y > y_c$ ),  $B$  ( $x < x_c, y < y_c$ ),  $C$  ( $x > x_c, y > y_c$ ) and  $D$  ( $x > x_c, y < y_c$ ) by choosing  $x_c$  and  $y_c$  such, that the following requirements are met:

- the signal is located in region  $C$ , with negligible contributions to the other regions.
- variable  $x$  has no discriminative power on the background
- the background can be measured in the regions  $A$ ,  $B$  and  $D$ .

In this case the background contribution  $N_C$  in the signal region  $C$  is given by

$$N_C = N_D \cdot \frac{N_A}{N_B}. \quad (2.42)$$

This method is used in several CMS analyses, e.g. in inclusive W and Z boson cross section measurements [95] or in BSM searches for opposite-sign dilepton events [96].

**Replacement/Removal:** The method of replacing or removing certain particles allows a transfer from a well-measured and understood process to a background process which cannot be assessed directly in data. One example of such a process is  $(Z \rightarrow \nu\bar{\nu}) + \text{jets}$  as a background to the jets +  $\cancel{p}_T$  search of SUSY [97, 98]. The  $(Z \rightarrow \nu\bar{\nu}) + \text{jets}$  contribution cannot be extracted directly from data, since it matches the signal signature exactly. However,  $(Z \rightarrow \ell^+\ell^-) + \text{jets}$ , with  $\ell^+\ell^- = e^+e^-(\mu^+\mu^-)$ , can be determined in an experimental analysis. The measured events with  $Z \rightarrow \ell^+\ell^-$  can then be used for the  $Z \rightarrow \nu\bar{\nu}$  background after the removal of the two leptons

from the  $Z$  boson decay and a recalculation of the missing transverse momentum. Additionally, the contribution has to be corrected for the different branching ratio of the  $Z \rightarrow \ell^+\ell^-$  and the  $Z \rightarrow \nu\bar{\nu}$  decay and the detector acceptance of the  $\ell^+\ell^-$  pair.

**Tag-and-Probe Method:** Backgrounds due to mis-measured particles can be eliminated for example with the tag-and-probe method. It is used for example in the  $H^\pm \rightarrow \tau^\pm\nu$  search [90] for the determination of the fake rate due to electrons which are identified as  $\tau$  jets. Here,  $Z \rightarrow e^+e^-$  events are used, with one electron<sup>3</sup> satisfying a tight electron selection. This is the so-called tag electron. Since the other final-state particle, the probe, has to be an electron as well (which can be ensured by checking the two-particle invariant mass) the fake rate can be determined from the fraction of events in which the probe electron is reconstructed as a muon.

While these methods prove to be successful in reducing the error on background determination, they might introduce new errors into the analysis, since for example effects of BSM physics might remain unrecognized and can spoil the background determination. An example of such a situation will be discussed in detail in Chapter 4.

---

<sup>3</sup>Here, no distinction shall be made between electrons and positrons.



## CHAPTER 3

---

# SUSY Background to Neutral MSSM Higgs Boson Searches

---

The work described in this chapter has been published in *Eur.Phys.J. C72 (2012) 1903* [99] and *Eur.Phys.J. C73 (2013) 2564* [100].

### 3.1 Introduction

When the Large Hadron Collider started operating at a center-of-mass energy of 7 TeV in 2010, major goals were to shed light on the mechanism of electroweak symmetry breaking and additionally search for physics beyond the Standard Model. Well motivated models for BSM physics are based on supersymmetry, with the Minimal Supersymmetric Extension of the Standard Model as its simplest representative. The most promising mechanism for EWSB, in the meantime strongly supported by the results of the LHC experiments [19, 20], is the Higgs mechanism, which is part of the Standard Model (SM) and of the MSSM. Pre-LHC data from colliders and electroweak precision measurements suggested that a SM-like Higgs boson would have a mass slightly above the exclusion limit from the Large Electron Positron Collider of 114.4 GeV [69, 70]. At the same time electroweak precision measurements [101] and theory considerations (see Chapter 2.2) hinted towards SUSY particle masses below or around 1 TeV.

While the SM incorporates a minimal Higgs sector with only one Higgs doublet, leading to one physical Higgs boson, the Higgs sector of the MSSM consists of two Higgs doublets, resulting in five physical Higgs bosons after EWSB: two neutral  $\mathcal{CP}$ -even bosons  $h$  and  $H$ , one neutral  $\mathcal{CP}$ -odd one  $A$  and a charged Higgs boson pair  $H^\pm$ . For a wide parameter range in the MSSM, one of the neutral  $\mathcal{CP}$ -even Higgs bosons couples

to vector bosons like the SM Higgs boson. Therefore, this MSSM Higgs boson can be searched for using strategies of SM Higgs analyses. A general overview on Higgs boson studies within the SM and the MSSM at the LHC can be found in Refs. [102, 103].

An important Higgs boson production channel at the LHC, both in the SM and the MSSM, is vector boson fusion (VBF, see Figure 3.1) [104–108]. Although having a production cross section much smaller than the gluon fusion production mode, it is very important both in discovery and coupling measurements due to the distinct features of the two accompanying jets, which are called tagging jets: they are usually in the forward and backward direction of the detector, and their large rapidity separation and high invariant mass allows for a good separation from the QCD background (see e.g. [106, 109]).

The work presented in this chapter focuses on the production of a SM-like light MSSM Higgs boson  $h$  in VBF (Figure 3.1). The allowed mass range, not considering LHC data, starts at the LEP bound ( $m_h > 114.4 \text{ GeV}$ ) [69, 70] and reaches up to roughly 140 GeV, the upper limit on the mass of the light Higgs boson in the MSSM [49]. Two Higgs decay modes will be studied, the decay into tau leptons and into W bosons, including subsequent leptonic decays:

$$\begin{aligned} h &\rightarrow \tau^+\tau^- && \rightarrow \ell^+\ell^- \nu_\ell\bar{\nu}_\ell\nu_\tau\bar{\nu}_\tau \\ h &\rightarrow W^+W^- && \rightarrow \ell^+\ell^- \nu_\ell\bar{\nu}_\ell, \end{aligned} \quad (3.1)$$

with  $\ell = \{e, \mu\}$ . The  $h \rightarrow \tau\tau$  decay mode in VBF was considered a promising discovery channel for a Higgs boson in the previously mentioned mass range, both in the MSSM [107] and in the SM [105]. The  $h \rightarrow WW$  channel faces low branching ratios at Higgs boson masses below 130 GeV, but still was considered valuable for discovery [108]. Recently, CMS published first results for the latter channel in a dedicated analysis, considering the full 7+8 TeV dataset [110]. ATLAS analyzed the VBF-dominated 2-jet channel together with the 0-jet and 1-jet channel in a single analysis [111, 112]. Additionally, both channels can be important for coupling measurements [113].

The signature of these two Higgs boson search channels consists of two opposite-charged leptons, missing energy/missing transverse momentum  $\cancel{p}_T$  from the neutrinos and two jets from the two quarks,

$$\ell^+\ell^- jj + \cancel{p}_T. \quad (3.2)$$

Major SM background processes include top quark pair production (plus jets), W boson pair production plus two jets, tau lepton pair production plus two jets and Z boson pro-

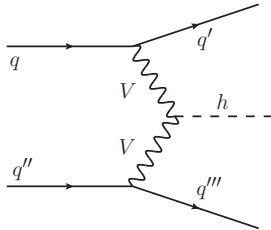


Figure 3.1: Feynman diagram for  $h$  production in vector boson fusion, with  $V = W, Z$ .

duction plus two jets. Within the MSSM additional background processes are possible, involving the production of SUSY partners of SM particles. Their influence on SM-like processes has been studied for calibration processes [114]. For the Higgs boson searches SUSY processes have been discussed as background for Higgs boson production within the decay cascades of SUSY particles [103, 115, 116]. Additionally, SUSY background contributions have been considered for the production of heavy Higgs bosons, which decay into a chargino/neutralino pair with subsequent cascade decays [117]. However, first [118, 119] and also more recent [120, 121] MSSM Higgs boson searches with SM-like signal topologies at the LHC did not include potential background contributions arising from SUSY processes.

In this chapter background processes originating from SUSY particle production to the production of  $h$  in VBF will be studied for the two decay channels listed in Eq. (3.1). Within the discussed scenarios, which include  $R$ -parity conservation and the lightest neutralino as lightest supersymmetric particle, the following processes give rise to the same final state signature as the Higgs boson production and therefore contribute to the irreducible background: chargino pair production plus two jets, lightest plus next-to-lightest neutralino production plus two jets and slepton pair production plus two jets. In subsequent decays each chargino and slepton gives rise to one lepton plus missing energy, the next-to-lightest neutralino leads to a lepton pair plus missing energy and the stable lightest neutralino directly contributes to the missing energy. Several other chargino and neutralino combinations, which produce additional leptons or jets, are feasible, possibly accompanied by jets. Those processes contribute to the reducible background, as the additional particles might not be detected in the experiment.

The main goal of this work is to check whether the SUSY processes give any notable contribution to the background for Higgs boson production, or if they are already sufficiently suppressed by the cuts necessary for SM background suppression. The starting point will be a very conservative scenario with masses not far above the LEP and Tevatron exclusion limits. This scenario can be excluded with LHC data, but still serves very well as an upper limit on SUSY contributions to the background given that SUSY particle production cross sections generally decrease with increasing SUSY particle masses. Later on also scenarios with larger squark and gluino masses, the particles with the strongest constraints from the LHC, will be studied. Furthermore, additional scenarios with distinct features will be discussed.

## 3.2 SUSY Scenarios and Relevant Processes

The details of MSSM phenomenology significantly depend on the parameter choice in the SUSY breaking sector (see Chapter 2.2). Therefore the MSSM parameters and their phenomenological implications will be discussed in Section 3.2.1. Afterwards the relevant background processes giving rise to the signature  $\ell^+ \ell^- j j + \cancel{p}_T$  can be identified.

### 3.2.1 SUSY scenario construction

The scenarios discussed include  $R$ -parity conservation, with the lightest neutralino being the LSP. The starting point for this analysis is provided by the scenario SPS1a [122], a scenario widely discussed in the pre-LHC era. For this scenario the SUSY breaking is implemented following the mSUGRA assumptions [51, 52, 123, 124], which imply that the parameters unify to only 4 parameters and a sign at the Grand Unified Theory scale (roughly at  $10^{16}$  GeV). For the scenario SPS1a the parameters at the high scale are

$$M_0 = 100 \text{ GeV}, \quad M_{1/2} = 250 \text{ GeV}, \quad A_0 = -100 \text{ GeV}, \quad \tan \beta = 10, \quad \mu > 0. \quad (3.3)$$

They are then evolved down to the SUSY scale, chosen as 1 TeV, using renormalization group equations (RGEs)<sup>1</sup>. The resulting masses of the SUSY particles are rather small, between 500 GeV and 600 GeV for squarks and for the gluino. Neutralinos and charginos are even lighter, namely

$$m_{\chi_1^\pm} = 181 \text{ GeV}, \quad m_{\chi_2^0} = 182 \text{ GeV} \quad \text{and} \quad m_{\chi_1^0} = 98 \text{ GeV}. \quad (3.4)$$

This leads to high cross sections for the SUSY particle production modes, which are still in agreement with the pre-LHC collider constraints from SUSY searches for SPS1a [125–128]. While the masses of the SUSY particles fulfill these constraints, this is not the case for the mass of the light neutral Higgs boson  $h$ . For this SM-like Higgs boson the scenario SPS1a predicts a mass of  $m_h \approx 112$  GeV, which is below the previously mentioned LEP bound. Therefore the trilinear coupling  $A_t$  at the low (SUSY) scale is not taken from the SPS1a value after RGE running, but a value of  $A_t = -733$  GeV is assumed, according to the  $m_h^{\text{max}}$  scenario [129]. The resulting new scenario will be called “*SPS1amod*”, predicting a Higgs boson mass of  $m_h \approx 118$  GeV, clearly above the LEP exclusion bound and within the range where the  $h \rightarrow \tau\tau$  and  $h \rightarrow WW$  search channels can be important for a SM-like Higgs boson [105, 107, 108, 113]. In summary, the scenario SPS1amod serves well in giving an upper bound on the SUSY contribution to the background of SM-like Higgs boson searches in VBF.

Particularly interesting features concerning the scope of this analysis are the branching ratios and the kinematics of SUSY particle decays leading to final-state leptons and missing energy, which play a crucial role in the signal signature. For both SPS1a and SPS1amod the light chargino  $\chi_1^\pm$  decays predominantly into the light tau slepton  $\tilde{\tau}_1$  ( $m_{\tilde{\tau}_1} = 133$  GeV) and a neutrino. The tau slepton subsequently always decays into a tau lepton and the LSP. The other (heavier) sleptons either decay into a lepton and the LSP or into the light chargino. Additionally, the next-to-lightest neutralino always decays into a lepton pair and an LSP. The relevant background processes, which involve the production of charginos, neutralinos and sleptons, will be listed in the following sections (Sections 3.2.3 and 3.2.5). More details about branching ratios and masses of the SPS1amod scenario can be found in Appendix A.

<sup>1</sup>A visualization of the RGE running in mSUGRA is given in Figure 2.1, taken from Ref. [34].

As the cross section of the  $h \rightarrow WW$  channel below the  $WW$  threshold heavily depends on the Higgs boson mass, the effect of larger Higgs boson masses is discussed as well. Therefore the base scenario SPS1amod has been altered in the third generation squark sector, which has a big influence on the light Higgs boson mass due to radiative corrections [63–68]. The parameters which have been set to higher values at the low scale are  $M_{q_3L} = 881$  GeV,  $M_{tR} = 808$  GeV and  $A_t = -1833$  GeV. This gives a Higgs boson mass of  $m_h \approx 124$  GeV, which is in the vicinity of the mass of the SM-Higgs-like boson discovered at the LHC [19, 20]. The resulting scenario is called “*SPS1amod2*”.

Besides the upper limit estimation on the SUSY background contribution in the scenario SPS1amod, the dependence on the squark and gluino masses is of particular interest: as the LHC is a hadron collider, the cross sections of color-charged particles are comparatively large and these SUSY particles are the first ones with significantly rising exclusion limits due to LHC data [96, 130–132]. In order to study the squark/gluino mass dependence, the soft SUSY breaking mass terms at the low scale which control the masses of the squarks and of the gluino have been varied in a series of scenarios.

- For final states containing only quarks of the first and second generation,  $M_{q_1L}$ ,  $M_{q_2L}$ ,  $M_{uR}$ ,  $M_{dR}$ ,  $M_{cR}$  and  $M_{sR}$  are modified by a factor  $(1 + \xi)$  with  $0 \leq \xi \leq 2$ .  $M_3$  will be modified accordingly to ensure that the gluino is always heavier than the squarks. This leads to average squark masses between 553 and 1581 GeV.
- For the case with at least one b-quark in the final state, the mass of the stop has a large impact on the cross section. Therefore the parameters which influence the third generation squark masses,  $M_{q_3L}$ ,  $M_{tR}$ ,  $M_{bR}$ ,  $A_t$ ,  $A_b$  and  $M_3$ , will be varied separately by a factor  $(1 + \rho)$  with  $0 \leq \rho \leq 1$ . Varying these parameters changes the Higgs boson mass as well. It increases from  $m_h \approx 118$  GeV for  $\rho = 0$  up to  $m_h \approx 123$  GeV for  $\rho = 1$ .

As not only squarks and gluinos will be constrained by the LHC with increasing energy and integrated luminosity, but also the other SUSY particles will be probed, another scenario has been investigated where all SUSY particle masses are roughly 30% larger than in SPS1amod. This has been achieved by not starting with SPS1a, but instead choosing parameters from the SPS1a slope [122] with

$$M_0 = -A_0 = 130 \text{ GeV}, \quad M_{1/2} = 2.5 \cdot M_0, \quad (3.5)$$

where  $M_0$  is 30% larger than at SPS1a and the other parameters are changed accordingly. After the RGE evolution the parameters  $A_t$ ,  $M_{tL}$  and  $M_{tR}$  are changed like in SPS1amod2 to fulfill the requirements of the  $m_h^{\max}$  scenario [129]. This scenario will be denoted as “*SPS1a-slope*”.

In mSUGRA scenarios the lightest slepton is usually one of the third generation sleptons. As the mechanism of SUSY breaking is not determined so far, this restriction can also be dropped and the phenomenological implications of heavier third generation sleptons will be discussed. Heavier stau leptons, with masses above  $m_{\chi_1^\pm}$  and  $m_{\chi_2^0}$  are of particular interest when considering processes with lepton production from SUSY cascade decays. Heavier stau leptons are achieved by increasing the parameters  $M_{\tau L}$  and

$M_{\tau R}$ . Additionally,  $M_{eL}$  and  $M_{\mu L}$  are lowered to get the left-handed and right-handed selectrons and smuons close in mass. The mass hierarchy is therefore

$$m_{\chi_1^0} < m_{\tilde{e}_L} = m_{\tilde{\mu}_L} \approx m_{\tilde{e}_R} = m_{\tilde{\mu}_R} < m_{\{\chi_1^\pm/\chi_2^0\}} < m_{\tilde{\tau}_{1/2}}. \quad (3.6)$$

The full list of relevant masses and branching ratios of the SUSY particles, as well as all SM and MSSM input parameters can be found in Appendix A. For this type of scenarios the dominant decay chain of  $\chi_1^\pm$  and  $\chi_2^0$  no longer involves tau leptons, but first and second generation (s)leptons are produced directly. Therefore the rate of leptons visible in the detector (electrons and muons) is enhanced, as the tau lepton decay with a rather low branching ratio of  $BR(\tau \rightarrow \nu_\tau \ell \bar{\nu}_\ell) \approx 0.35$ , with  $\ell = \{e, \mu\}$ , is avoided. Additionally, this also leads to harder leptons compared to the decay chain with tau leptons. Three different examples of scenarios with this slepton mass hierarchy have been considered:

- The first scenario has squark and gluino masses corresponding to  $\xi = \rho = 0$  and will be called “*light sleptons*” scenario.
- The squark and gluino masses of the second scenario corresponding to  $\xi = \rho = 1$ , giving the “*light sleptons with high  $m_{\tilde{q}}, m_{\tilde{g}}$* ” scenario.
- With  $\xi = 1.5$ ,  $M_{q_3L} = 1058$  GeV,  $M_{tR} = 898$  GeV and  $A_t = -1950$  GeV, a scenario with rather heavy squarks of 1328 GeV, a light stop mass of 816 GeV and a Higgs boson mass of  $m_h = 124.4$  GeV, compatible within the theoretical and experimental errors on  $m_h$  with the Higgs boson search results of Refs. [19, 20], is obtained. This scenario will be denoted “*light sleptons with LHC-like Higgs*”. It has been used only in the  $h \rightarrow WW$  7 TeV analysis.

Finally, two scenarios with special kinematic features within the decay chains are discussed:

- The first scenario is a modified version of SPS1amod with an almost massless LSP and a  $\tilde{\tau}_1$  mass which is about half of the chargino mass. While this is no longer a genuine MSSM scenario it can illustrate the effect of much harder leptons on the cut acceptance of the SUSY background processes.
- The last scenario shows the effect of mother and daughter particles within the decay chain with a very small mass splitting. This is discussed within an mSUGRA scenario which differs from SPS1a in the value of  $A_0$ , which is set to  $A_0 = -750$  GeV instead of  $A_0 = -100$  GeV for SPS1a. This gives a small light stau lepton mass of 108 GeV, quite close to the LSP mass, which is at 99 GeV.

An SLHA file [133, 134] containing the mass spectrum, the widths and the branching ratios of the SUSY particles has been generated in the following way for all discussed SUSY scenarios:

- The RGE running from the GUT scale down to the SUSY scale for the mSUGRA input parameters has been done using the spectrum calculator `SuSpect` [135] from SUSYHIT 1.3 [135–138].

- The low-scale parameters obtained from the RGE running have then been modified according to the prescript discussed in this section and fed back into SUSYHIT.
- A cross check using the spectrum calculator `SPheno 3.0 beta` [139] instead of SUSYHIT gave comparable results, within theory uncertainties.
- The resulting SLHA file has been finally processed with the program `FeynHiggs 2.6.5` [140–143] to obtain precise values of the Higgs boson masses, including higher-order corrections.

The resulting file has then been used as input for the Monte Carlo programs that will be described in the next section.

### 3.2.2 The Signal Processes $h \rightarrow WW$ and $h \rightarrow \tau\tau$ in VBF

The signal process for which the SUSY background contributions are discussed is the production of a light MSSM Higgs boson in VBF. The Feynman graph for this process at leading order is depicted in Figure 3.1. At LO this is a pure electroweak process, therefore no QCD renormalization scale dependence arises. For the factorization scale the momentum transfer of the exchanged vector boson is used, which is a good choice for VBF processes [144]. The total cross section at the LHC with only very basic cuts on the two jets,

$$p_{T,j} > 20 \text{ GeV}, \quad |\eta_j| < 4.5, \quad \text{and} \quad \Delta R_{jj} > 0.8, \quad (3.7)$$

at a center-of-mass energy of 14 TeV is 2.8 pb, calculated with VBFNLO [145–147]. Here,  $\eta_i$  denotes the rapidity of particle  $i$ , while the  $R$ -separation of the particles  $i$  and  $j$  is defined as  $\Delta R_{ij} = \sqrt{(\Delta\eta_{ij})^2 + (\Delta\phi_{ij})^2}$ , with  $\Delta\eta_{ij}$  and  $\Delta\phi_{ij}$  representing the rapidity separation and azimuthal angle difference between  $i$  and  $j$ , respectively.

Besides graphs with  $t$ -channel exchange of a vector boson also graphs with  $s$ -channel vector boson resonances contribute to quark-induced Higgs boson plus two jet production. These contributions belong to another Higgs boson production process, called Higgs-Strahlung [109]. They are eliminated up to a negligible contribution by the cuts on the invariant jet pair mass (usually a few hundred GeV are requested in VBF analyses) and on the rapidity separation (mainly between three and slightly above four), which are applied for the Higgs boson searches in the VBF channels. Therefore these contributions can be dropped already from the start. The general  $hjj$  signal consists not only of the VBF-dominated quark-induced channels, but there is an additional contribution from double-real radiation to the Higgs boson production in gluon fusion. Before the application of VBF-specific cuts the gluon fusion contribution is larger than the genuine VBF production process, but it is efficiently suppressed by the cuts used in VBF Higgs boson analyses and reduced to values well below the VBF rate [148]. For the scenario SPS1amod the gluon fusion contribution, which is not included in the analysis, accounts for roughly 30% of the VBF cross section (calculated with VBFNLO [145–147] for the final cuts in the  $h \rightarrow WW$  analysis). Interference effects between VBF and gluon fusion have been found to be very small [149, 150].

The full signal process includes not only the production of the Higgs boson, but also its decay. As the light MSSM Higgs boson is a scalar particle with an extremely narrow width  $\Gamma$ , with a width to mass ratio  $\frac{\Gamma}{m} \approx \mathcal{O}(10^{-5})$ , the Narrow Width Approximation (NWA) can be applied to factorize production and decay. Two decay modes of the Higgs boson are discussed, the decay into a tau lepton pair and into a W boson pair with subsequent decays of the tau lepton and W boson into electrons or muons and corresponding neutrinos. The complete signal processes (production and decay) are:

$$\begin{aligned} qq \rightarrow qq h \rightarrow qq \tau^+ \tau^- &\rightarrow qq \ell^+ \ell^- \nu_\ell \bar{\nu}_\ell \nu_\tau \bar{\nu}_\tau \\ qq \rightarrow qq h \rightarrow qq W^+ W^- &\rightarrow qq \ell^+ \ell^- \nu_\ell \bar{\nu}_\ell, \end{aligned} \quad (3.8)$$

with  $q = \{d, u, s, c, \bar{d}, \bar{u}, \bar{s}, \bar{c}\}$  and  $\ell = \{e, \mu\}$ . The cross sections for  $m_h = 118.2 \text{ GeV}$  within the cuts of Eq. (3.7) are 11.5 fb for the  $h \rightarrow WW$  case and 26.4 fb for the  $h \rightarrow \tau\tau$  channel, including decays into electrons and muons.

### 3.2.3 Irreducible Background Contributions

For the scenario SPS1amod the processes

$$pp \rightarrow \chi_1^+ \chi_1^- jj \rightarrow \ell^+ \chi_1^0 \nu_\ell \ell^- \chi_1^0 \bar{\nu}_\ell jj \quad (3.9)$$

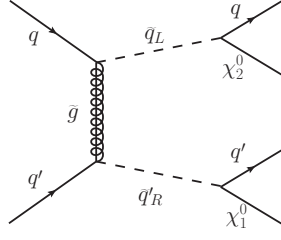
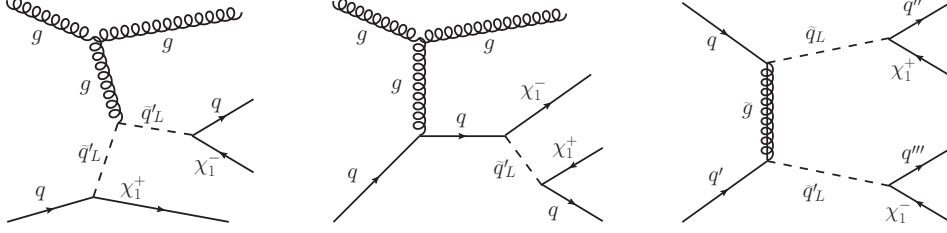
$$pp \rightarrow \chi_1^0 \chi_2^0 jj \rightarrow \chi_1^0 \ell^+ \ell^- \chi_1^0 jj, \quad (3.10)$$

with  $\ell = \{e, \mu, \tau\}$ , give the largest background contribution to the exact signature of VBF Higgs production with the two decay modes of Eq. (3.1), namely two jets, two opposite charged leptons and missing energy. Here,  $p$  denotes the incoming protons with quarks and anti-quarks of the first and second generation as well as the gluon considered as incoming partons. Outgoing jets at parton level are labeled  $j$ , where  $j = \{d, u, s, c, \bar{d}, \bar{u}, \bar{s}, \bar{c}, g\}$ . For the case of a tau lepton in the final state, the decay  $\tau \rightarrow \nu_\tau \ell' \bar{\nu}_{\ell'}$ , with  $\ell' = \{e, \mu\}$  will occur with a branching ratio  $BR \approx 0.35$ , where electrons and muons are directly detected in the experiments. Like the Higgs boson, the SUSY particles have very small widths compared to their masses, and the widths are also small compared to the mass differences of mother and daughter particles in the decay chains. Therefore the NWA can be applied [151] and the processes can be separated into on-shell production and decay of the charginos and neutralinos. The effect of the neglected spin correlation between production process and decay will be estimated in the next section. It turns out to be small for the processes of Eqs. (3.9) and (3.10).

Within SPS1amod the  $\chi_1^+ \chi_1^- jj$  production cross section at the 14 TeV LHC is 2.6 pb,<sup>2</sup> with only very basic jet cuts from Eq. (3.7). For  $\chi_2^0 \chi_1^0 jj$  production the production cross section is 1.4 pb.

The dominant contribution to  $\chi_2^0 \chi_1^0 jj$  production originates from squark pair production with subsequent decay into neutralinos. The corresponding Feynman diagram

<sup>2</sup>All SUSY particle production cross sections given in this and the next section have been calculated with MadGraph/MadEvent [72, 73].

Figure 3.2: Dominant Feynman graph for  $\chi_1^0 \chi_2^0 jj$  production in the SPS1amod scenario.Figure 3.3: Dominant Feynman graphs for  $\chi_1^+ \chi_1^- jj$  production in the SPS1amod scenario.

with the largest contribution is depicted in Figure 3.2. As the relevant scale for the initial state partons and for the QCD part of this process is determined by the underlying hard process of squark pair production, the factorization scale  $\mu_F$  and renormalization scale  $\mu_R$  are chosen to be of the order of the squark masses. For the scenario SPS1amod and the other scenarios with the same squark masses the numerical value for these quantities is chosen as

$$\mu_F = \mu_R = 550 \text{ GeV}. \quad (3.11)$$

The most relevant Feynman diagrams for  $\chi_1^+ \chi_1^- jj$  production are shown in Figure 3.3. Here not only squark pair production, but also other production modes like initial-state radiation from  $\chi_1^\pm \tilde{q} j$  production contribute. These additional diagrams are additionally enhanced in the interesting part of the phase space concerning VBF Higgs production. For higher squark masses they additionally gain in relative importance. In this case the factorization scale is chosen as

$$\mu_F^2 = p_{T,j1} \cdot p_{T,j2} \quad (3.12)$$

and the strong coupling constant squared  $\alpha_s^2$  is calculated as

$$\alpha_s^2 = \alpha_s(p_{T,j1}) \cdot \alpha_s(p_{T,j2}). \quad (3.13)$$

Here,  $p_{T,ji}$  denotes the the transverse momentum  $p_T = \sqrt{p_x^2 + p_y^2}$  of the  $i$ -th jet, with the jets sorted by decreasing  $p_T$ . This choice takes the different scales for  $\chi_1^+ \chi_1^- jj$  production into account: if the jet stems directly from  $t$ -channel production, the jet  $p_T$  is the scale governing the momentum transfer between the QCD vertices, while for jets from squark decays the  $p_T$  is usually large and  $p_T \approx m_{\tilde{q}}/2$  becomes the effective scale.

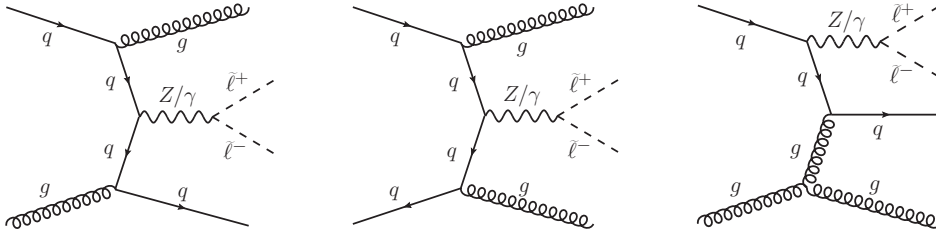


Figure 3.4: Dominant Feynman graphs for  $\tilde{\ell}^+ \tilde{\ell}^- jj$  production in SPS1amod scenario.

Subleading contributions to the background for SPS1amod come from direct slepton pair production accompanied by two jets, followed by a subsequent decay into leptons and invisible particles

$$pp \rightarrow \tilde{e}_{L,R}^+ \tilde{e}_{L,R}^- jj \rightarrow \ell^+ \chi_1^0 \ell^- \chi_1^0 jj + \cancel{p}_T \quad (3.14)$$

$$pp \rightarrow \tilde{\mu}_{L,R}^+ \tilde{\mu}_{L,R}^- jj \rightarrow \ell^+ \chi_1^0 \ell^- \chi_1^0 jj + \cancel{p}_T \quad (3.15)$$

$$pp \rightarrow \tilde{\tau}_{1,2}^+ \tilde{\tau}_{1,2}^- jj \rightarrow \ell^+ \chi_1^0 \ell^- \chi_1^0 jj + \cancel{p}_T. \quad (3.16)$$

The right-handed sleptons  $\tilde{e}_R$ ,  $\tilde{\mu}_R$  and  $\tilde{\tau}_1$  decay directly into the corresponding lepton and the LSP. The left-handed sleptons  $\tilde{e}_L$ ,  $\tilde{\mu}_L$  and  $\tilde{\tau}_2$  are heavier than the chargino. Therefore the decay into a chargino is possible and occurs roughly for every fourth slepton. The chargino subsequently decays into a lepton, a neutrino and the LSP. All processes of Eqs. (3.14)–(3.16) combined will be called  $\tilde{\ell}^+ \tilde{\ell}^- jj$  production in the rest of this chapter. The combined production cross section of the slepton channels with the minimal cuts of Eq. (3.7) is 0.085 pb, which is a factor of 50 smaller than the combined cross section for  $\chi_1^+ \chi_1^- jj$  and  $\chi_2^0 \chi_1^0 jj$ . However, when considering the decay of the SUSY particles, the fraction of the slepton induced background becomes larger, as the decay of  $\tilde{e}_R$  and  $\tilde{\mu}_R$  directly produces detectable electrons and muons. The charginos and next-to-lightest neutralinos on the other hand are the initial particles in a cascade decay: the major part of the contribution includes one or two leptonic tau decays, which reduce the relative contribution of the chargino and next-to-lightest neutralino contributions significantly. With the additional cuts from the Higgs boson analysis the slepton contribution adds roughly 15% to the irreducible SUSY background, and for higher squark and gluino masses the slepton contributions can even become larger than the chargino and next-to-lightest neutralino channels. This will be discussed in detail in Chapters 3.4.1 and 3.4.3. The Feynman diagrams leading to the dominant contribution for slepton pair production are displayed in Figure 3.4. No squarks are involved, and the relevant scale for the QCD part is again given by the transverse momentum of the jets. Therefore the scales from Eqs. (3.12) and (3.13) are also used for the slepton pair production processes.

So far no processes with b-quarks in the initial or final state have been discussed. This process class can be split into two subclasses:

- Contributions with at least one b-quark in the initial state and none in the final state are very small and can be neglected.

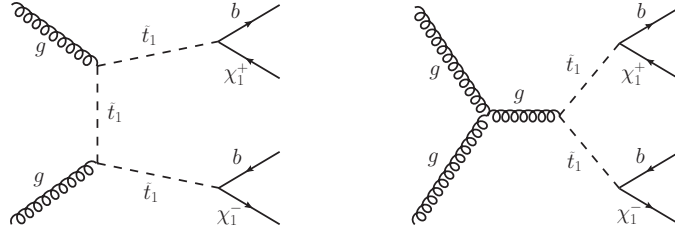


Figure 3.5: Dominant Feynman graphs in the scenario SPS1amod for  $\chi_1^+ \chi_1^- jj$  production with at least one  $b/\bar{b}$  quark in the final state.

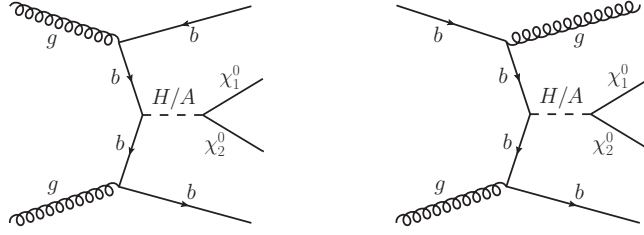


Figure 3.6: Additional Feynman graphs in the scenario SPS1amod for  $\chi_2^0 \chi_1^0 jj$  production with at least one  $b/\bar{b}$  quark in the final state.

- Processes with at least one b-quark in the final state are treated separately. In this case b-quarks are allowed to appear in the initial state as well. These processes will be called “b-quark contributions”.

The b-quark contributions to  $\chi_1^+ \chi_1^- jj$  at the production level have a cross section of 3.0 pb, which is of the same order as the contribution without b-quarks (again within the cuts of Eq. (3.7)). The dominant b-quark contributions, depicted in Figure 3.5, result from the production of a pair of light stops  $\tilde{t}_1$ , with two gluons in the initial state and subsequent decay  $\tilde{t}_1 \rightarrow b \chi_1^+$ . Renormalization and factorization scale are chosen as for chargino pair production without b-quark contributions, i.e.  $\mu_F^2 = p_{T,j1} \cdot p_{T,j2}$  and  $\alpha_s^2 = \alpha_s(p_{T,j1}) \cdot \alpha_s(p_{T,j2})$ .

For  $\chi_2^0 \chi_1^0 jj$  production the b-quark contributions are much smaller at production level, they account for a cross section of only 0.150 pb within the cuts of Eq. (3.7). Squark production plays a minor role for the b-quark contribution in this process for several reasons:

- Bottom squarks are the relevant squarks for this process, which are heavier than the light  $\tilde{t}_1$ .
- The branching ratios for  $\tilde{b}_1$  and  $\tilde{b}_2$  into a bottom quark and a neutralino are much smaller than the corresponding stop decays.
- Additionally, the analogous Feynman graph to the dominant graphs of chargino production is not allowed: for the contribution to the irreducible background the production of one lightest neutralino and one next-to-lightest neutralino is needed. As one of the sbottoms decays preferably into  $\chi_1^0$ , while the other one has a tendency to decay into a  $\chi_2^0$ , a  $g\text{-}\tilde{b}_1\text{-}\tilde{b}_2$  coupling would be necessary for a

large squark contribution from initial state gluons. This coupling does not exist and the contribution from  $\tilde{b}_1 \tilde{b}_1$  or  $\tilde{b}_2 \tilde{b}_2$  production is much smaller.

As squarks give only small contributions here, additional graphs like the ones depicted in Figure 3.6 play a major role for the b-quark contribution of  $\chi_2^0 \chi_1^0 jj$  production. Therefore the squark mass, which was used to set the scales in the non-b contributions, is no longer a reasonable scale for the process. Instead,  $\mu_F$  and  $\mu_R$  have been set according to Eqs. (3.12) and (3.13).

For  $\tilde{\ell}^+ \tilde{\ell}^- jj$  production the b-quark contribution accounts for only 3% of the non-b-quark contribution with the final set of cuts as given in Section 3.4.1.1. Therefore the b-quark contribution for slepton pair production can be neglected.

### 3.2.4 Theoretical Precision of Signal and Background Estimation

The renormalization and factorization scale uncertainty is a widely used measure for the estimation of the theoretical error inherent in calculations carried out in a truncated perturbative expansion. Table 3.1 lists the cross sections for  $\chi_1^+ \chi_1^- jj$ ,  $\chi_2^0 \chi_1^0 jj$ ,  $\tilde{\ell}^+ \tilde{\ell}^- jj$  and the  $h \rightarrow WW$  signal process in VBF with subsequent decays into leptons for the central scales as defined before, and for twice and half of this central scale. These cross sections have been obtained with the analysis setup described in Section 3.3.2.

For the SUSY processes the typical leading-order  $\alpha_s^2$  scale dependence is apparent. Therefore a precise cross section prediction would have to incorporate the next-to-leading-order QCD corrections. Unfortunately the QCD corrections are only available for a subset of the relevant topologies in the discussed SUSY processes (for example the diagram in Fig. 3.2). Typical  $K$ -factors (the ratio of NLO vs. LO cross section) for these  $2 \rightarrow 2$  processes in the scenario SPS1amod are in the range from 1.25 for  $\tilde{q}\tilde{q}$  production up to 1.5 for  $\tilde{q}\tilde{q}$  production (obtained with `Prospino2` [152, 153] for  $\mu_F = \mu_R = m_{\tilde{q}}$ ). However, for topologies like the first two diagrams of Figure 3.3 the QCD corrections do not exist in the literature. Therefore rescaling the LO results by the NLO  $K$ -factor is not possible. Nevertheless, the range given by the scale variation of the LO results covers the size of the known NLO corrections for the topologies involving squark pair production. Therefore no exceptional effects are expected at NLO QCD and the LO precision is good enough for an estimation of the SUSY background.

The signal process  $h \rightarrow WW$  in VBF has a much smaller scale dependence as it is a pure electroweak process without  $\mu_R$ -dependence at LO. For this process higher-order corrections have been known for quite some time. They are typically small: the NLO QCD corrections are of the order of 10% [144, 154–158], the NLO EW corrections are of the same order, they account for 5 – 10% of the LO cross section [157–159]. Within the MSSM also the SUSY QCD and SUSY EW corrections have been studied. The SUSY QCD corrections turn out to be negligible [159–161] and the SUSY EW corrections are small (usually of the order 1% or less) [159, 161]. The gluon-induced VBF-process [162], which is formally of next-to-next-to-leading order (NNLO) in QCD,

	$\zeta = 0.5$	$\zeta = 1.0$	$\zeta = 2.0$
$\chi_1^+ \chi_1^- jj$	1.71 fb	1.21 fb	0.88 fb
$\chi_2^0 \chi_1^0 jj$	1.37 fb	1.04 fb	0.82 fb
$\tilde{\ell}^+ \tilde{\ell}^- jj$	1.74 fb	1.23 fb	0.91 fb
$h \rightarrow WW$	3.03 fb	2.91 fb	2.79 fb

Table 3.1: Scale dependence for  $\chi_1^+ \chi_1^- jj$ ,  $\chi_2^0 \chi_1^0 jj$ ,  $\tilde{\ell}^+ \tilde{\ell}^- jj$  and  $h \rightarrow WW$  cross sections without b-quarks in the final state (basic jet and lepton cuts plus  $\Delta\eta_{jj} \geq 4.2$  and  $\eta_{j,min} \leq \eta_\ell \leq \eta_{j,max}$  are applied, see Eqs. (3.39), (3.40)). The scales used are  $\mu_R = \mu_F = \zeta \cdot \mu_0$ . For the SUSY processes  $\mu_0$  has been defined in Eqs. (3.11)–(3.13). The signal has no  $\mu_R$  dependence, the default factorization scale is chosen as specified in Section 3.2.2.

as well as an approximative NNLO calculation of the VBF process in the structure-function approach [163] have been studied and the NNLO effect in both cases turned out to be very small. The  $K$ -factors for the Higgs boson production process with the minimal jet cuts of Eq. (3.7), calculated with VBFNLO [145–147], are  $K_{\text{QCD}} = 1.10$  for the NLO QCD corrections and  $K_{\text{EW}} = 0.95$  for the NLO EW corrections. Although the NLO corrections are available for the signal process, in the following only LO predictions will be used in order to match the calculation of the SUSY processes. In any case, the main theoretical uncertainty of this analysis can be attributed to the large scale dependence of the SUSY background processes.

### 3.2.5 Reducible Background Contributions

Besides the previously discussed SUSY processes, which contribute to the exact signature  $\ell^+ \ell^- jj + \cancel{p}_T$  of the Higgs boson signal processes, several processes produce additional jets and/or leptons. If these additional particles are detectable, these processes do not give rise to a background for the Higgs boson production. However, the additional particles could end up in the region close to the beam axis, which is not covered by the detector, or they could be too soft for detection. Additionally, leptons could “hide” in a jet, i.e. the lepton is too close to the jet for a separate detection of the jet and the lepton, or two quarks could form a single jet. Furthermore, a veto on additional jet activity is not always used. Additional leptons on the other hand can be identified quite well.

In the SPS1amod scenario the SUSY particle production processes that give the dominant contribution to the reducible background are:

$$pp \rightarrow \chi_1^+ \chi_2^0 jj \quad (3.17)$$

$$pp \rightarrow \chi_1^- \chi_2^0 jj \quad (3.18)$$

$$pp \rightarrow \chi_2^0 \chi_2^0 jj. \quad (3.19)$$

For these processes it is no longer one specific final state that contributes to the background, but several final states from different decay chains add up to the reducible background. For example the chargino plus next-to-lightest neutralino production from Eq. (3.17) can lead to a trilepton final state, when both the  $\chi_1^+$  and the  $\chi_2^0$  decay via a stau lepton and the resulting tau leptons again decay leptonically:

$$\begin{aligned}
pp &\rightarrow \left( \chi_1^+ \rightarrow \left( \tilde{\tau}_1^+ \rightarrow \left( \tau^+ \rightarrow e^+ \nu_e \bar{\nu}_\tau \right) \chi_1^0 \right) \nu_\tau \right) \\
&\quad \left( \chi_2^0 \rightarrow \left( \tilde{\tau}_1^+ \rightarrow \left( \tau^+ \rightarrow e^+ \nu_e \bar{\nu}_\tau \right) \chi_1^0 \right) \left( \tau^- \rightarrow \mu^- \bar{\nu}_\mu \nu_\tau \right) \right) jj \\
&\rightarrow e^+ \nu_e \bar{\nu}_\tau \nu_\tau \chi_1^0 e^+ \nu_e \bar{\nu}_\tau \mu^- \bar{\nu}_\mu \nu_\tau \chi_1^0 jj.
\end{aligned} \tag{3.20}$$

The chargino could also decay into a W boson, which leads to the same signature if the W boson subsequently decays leptonically. On the other hand, additional jets could occur from hadronic tau lepton or W boson decays:

$$\begin{aligned}
pp &\rightarrow \left( \chi_1^+ \rightarrow \left( \tilde{\tau}_1^+ \rightarrow \left( \tau^+ \rightarrow j_\tau \bar{\nu}_\tau \right) \chi_1^0 \right) \nu_\tau \right) \\
&\quad \left( \chi_2^0 \rightarrow \left( \tilde{\tau}_1^+ \rightarrow \left( \tau^+ \rightarrow e^+ \nu_e \bar{\nu}_\tau \right) \chi_1^0 \right) \left( \tau^- \rightarrow \mu^- \bar{\nu}_\mu \nu_\tau \right) \right) jj \\
&\rightarrow j_\tau \bar{\nu}_\tau \nu_\tau \chi_1^0 e^+ \nu_e \bar{\nu}_\tau \mu^- \bar{\nu}_\mu \nu_\tau \chi_1^0 jj,
\end{aligned} \tag{3.21}$$

where  $j_\tau$  stands for the jet stemming from a hadronic tau decay. In all these cases one additional jet (or possibly two in case of the hadronic W decay) or lepton is produced that has to evade detection.

Besides the processes from Eqs. (3.17)–(3.19) several other processes can give rise to the reducible background of VBF Higgs boson production, but their contribution turns out to be much smaller than the three processes mentioned above. The list of additional SUSY particle production processes that have been considered for the reducible background in this analysis is

$$pp \rightarrow \chi_1^\pm \chi_2^0 j \tag{3.22}$$

$$pp \rightarrow \chi_2^0 \chi_2^0 (j) \tag{3.23}$$

$$pp \rightarrow \chi_3^0 \chi_1^0 jj \tag{3.24}$$

$$pp \rightarrow \chi_4^0 \chi_1^0 jj \tag{3.25}$$

$$pp \rightarrow \chi_4^0 \chi_2^0 jj \tag{3.26}$$

$$pp \rightarrow \chi_1^\pm \chi_2^\mp jj \tag{3.27}$$

$$pp \rightarrow \chi_2^+ \chi_2^- jj \tag{3.28}$$

$$pp \rightarrow \chi_2^\pm \chi_2^0 jj \tag{3.29}$$

$$pp \rightarrow \chi_2^+ \chi_1^0 jj \tag{3.30}$$

$$pp \rightarrow \tilde{g} \chi_1^0 (j)(j). \tag{3.31}$$

The  $j$  in parentheses indicates that this process is generated separately with and without the additional jet, e.g.  $pp \rightarrow \chi_2^0 \chi_2^0 (j)$  stands for the two processes  $pp \rightarrow \chi_2^0 \chi_2^0$  and  $pp \rightarrow \chi_2^0 \chi_2^0 j$ . While the processes of Eqs. (3.17)–(3.19) will be discussed in detail in Sections 3.4.1 - 3.4.4, the contribution of the sub-dominant processes of Eqs. (3.22)–(3.31) will only be briefly summarized in Section 3.4.1. A few additional combinations of heavier charginos and neutralinos are possible but have been neglected. As can be inferred from the processes which have been calculated, their contribution is very small. The process  $pp \rightarrow \chi_2^+ \chi_1^0 jj$  of Eq. (3.30) for example gives an extremely tiny contribution to the background. As the charge-conjugated process is expected to be even smaller for a  $pp$  collider it has been neglected.

The topologies contributing to the cross section of the processes involved in the reducible background are similar to the ones of chargino pair production plus two jets (see Figure 3.3). The only exception is next-to-lightest neutralino pair production plus two jets, where Feynman diagrams with primary squark pair production play a more important role. As the topologies are very similar to the  $\chi_1^+ \chi_1^- jj$  production process, the renormalization and factorization scales are set in the same way, according to Eqs. (3.12) and (3.13).

## 3.3 Analysis Procedure

After the introduction of all discussed signal and background processes and all considered MSSM scenarios, the analysis method will be presented in the following. The general analysis features will be given first, followed by the description of the programs used and of the cross-checks performed. Finally, peculiarities in the particle and event selection for the reducible background processes will be discussed.

### 3.3.1 Overview

The study of the SUSY background to Higgs boson production in VBF is based on a parton-level analysis at leading order, carried out mainly with the programs MadGraph/MadEvent [72, 73], VBFNLO [145–147] and Herwig++ [81]. A detailed description of the technical setup will be presented in Section 3.3.2.

The main discussion of the SUSY background processes is done for the LHC running at a center-of-mass energy of 14 TeV, as the VBF processes will be most important at this energy due to their small cross sections. The effect of an energy reduction to 7 TeV on signal and SUSY background will be discussed afterwards.

As this is a parton-level analysis, hadronization effects and detection efficiencies are not taken into account. Parton shower effects are neglected as well, but the effect of a central jet veto (CJV) on additional jets from QCD radiation is estimated in Section 3.7.3 for selected processes in the exponentiation model of Refs. [164, 165]. The effects of a finite energy resolution in the detector for jets and leptons have been checked, modeling the effect by a Gaussian smearing of the parton energies. The distributions of the discussed processes are only slightly affected as they do not show any sharp peaks. Therefore the detector effects in the energy measurement are neglected, except for the reconstructed tau pair mass  $m_{\tau\tau}$  for the  $h \rightarrow \tau\tau$  signal. This reconstruction is very sensitive to fake missing transverse energy, which can be parametrized by a Gaussian distribution [166] with

$$\sigma(E_x^{miss}, E_y^{miss}) = 0.41 \cdot \sqrt{\sum E_T}. \quad (3.32)$$

Therefore the mis-measurement effects from Eq. (3.32) for the missing transverse momentum will be considered for the tau pair mass reconstruction. The amount of fake

missing transverse energy depends on the total transverse energy deposit  $\sum E_T$  in the hadronic calorimeters of the detector. Besides including the  $\sum E_T$  from the hard process, additional underlying event (UE) contributions are considered as well. Pileup effects on the other hand will be neglected. The UE contribution to  $\sum E_T$  for a center-of-mass energy of  $\sqrt{s} = 7 \text{ TeV}$  within the pseudorapidity range  $-4.5 < \eta < 4.5$  can be estimated to approximately 100 GeV [167]. Considering ATLAS measurements at 900 GeV [167], Tevatron measurements at 1.96 TeV [168] and modeling of the UE activity [169], the UE activity at 14 TeV can be extrapolated to approximately 130 GeV. An UE measurement published after the completion of this study, taking into account a larger rapidity range and a larger event sample [170], suggests a larger UE contribution, especially in events with harder jets. However, as the effect of a larger UE fraction of the transverse energy deposit on the SUSY background results is very small<sup>3</sup>, the original value has been kept.

### 3.3.2 Analysis Tool-Chain

There are several tools publicly available which in principle allow for a parton-level analysis at leading order of arbitrary processes both in the SM and in the MSSM. `MadGraph/MadEvent` [72, 73], `WHIZARD/Omega` [74, 75], `Sherpa/AMEGIC++` [76, 77] and `CalcHEP/CompHEP` [171–173] are among the most popular representatives of these automated parton-level event generators. Additionally, the Monte Carlo event generators `Herwig++` [81, 174, 175] and `PYTHIA 8` [83, 176] as well as their FORTRAN predecessors [177–179] have all possible  $2 \rightarrow 2$  MSSM processes included, along with arbitrary cascade decays of the produced SUSY particles.

However, using a single program for the whole process, which consists of the SUSY particle pair production and subsequent decay down to electrons and muons did not seem feasible: the automated parton-level event generators cannot handle the large number of final state particles<sup>4</sup> and the huge number of Feynman diagrams in the considered SUSY processes. `Herwig++` and `PYTHIA 8` on the other hand can handle the SUSY decay chains very efficiently, but several topologies which are important for the SUSY background processes are not included in the hard matrix elements: while diagrams like the one in Figure 3.2 are available, which basically represent  $2 \rightarrow 2$  processes with subsequent decay, e.g. the first two topologies of Figure 3.3 are not included.

By combining the hard matrix element from a parton-level event generator with a Monte Carlo event generator, these limitations can be avoided: As it has already been mentioned in the discussion of the relevant SUSY processes, the NWA can be applied and the SUSY processes can be separated into production and decay of the SUSY particles. `MadGraph/MadEvent` has been used for the production stage of this

<sup>3</sup>The effect of a 50% increase of the UE contribution to  $\sum E_T$  on the  $h \rightarrow \tau\tau$  cross section with all cuts is only  $\approx 4\%$ . For the SUSY background processes the changes are negligible as there is no sharp peak in the  $m_{\tau\tau}$  distribution for these processes.

<sup>4</sup>The process from Eq. (3.20) for example leads to 14 final state particles.

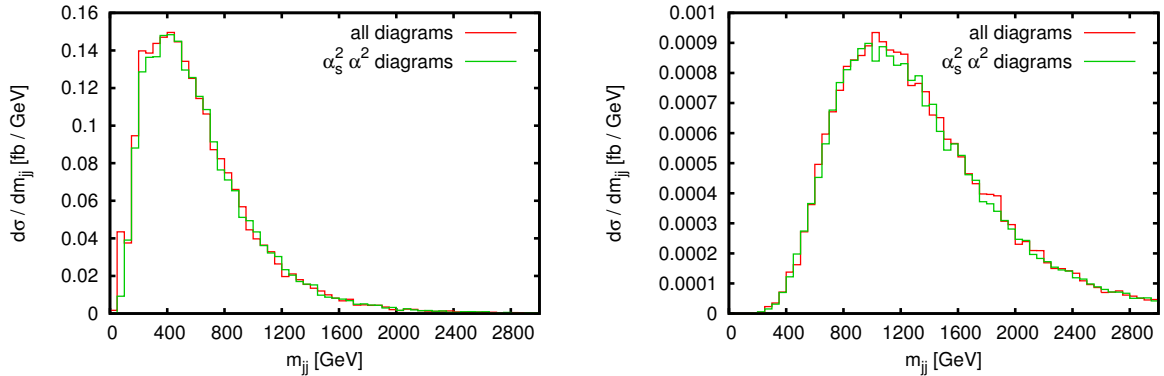


Figure 3.7: Comparison of the full process vs. the approximation for  $\chi_2^0\chi_1^0jj$  production with minimal jet cuts (left) and an additional rapidity separation cut of  $\Delta\eta \geq 4.2$  (right) in the dijet mass.

analysis, interfaced via Les Houches event files [180] to *Herwig++*, which handles the decay of the SUSY particles and the tau leptons. This method has one drawback: while *Herwig++* preserves the spin correlation within the decay chain [181], no spin information is transferred from the production process to the decay part. However, as will be discussed in the next section, the effect of this simplification is small for the SUSY processes considered here.

Another simplification has been used for the production process  $pp \rightarrow \chi_2^0\chi_1^0jj$ . Here only the  $\mathcal{O}(\alpha_s^2\alpha^2)$  contributions are taken into account, while the  $\mathcal{O}(\alpha^4)$  diagrams are not considered in the calculation. This leads to a significant speed-up in the event generation, as the number of Feynman diagrams decreases from 38112 to 8256 in the *MadGraph* 4 way of counting. Using only the restricted set of diagrams is a reasonable approximation, as the difference compared to the full process is very small. In addition, the events neglected in this approximation have a fairly small invariant jet pair mass  $m_{jj}$ , as can be seen in the left plot of Figure 3.7. The tagging jets in the discarded events furthermore have a small rapidity separation, which is shown in the right plot of Figure 3.7: with an additional cut requiring a minimal rapidity separation of  $\Delta\eta > 4.2$  the difference between the full process and the  $\mathcal{O}(\alpha_s^2\alpha^2)$  contributions vanishes. Since the VBF Higgs boson analyses include cuts on  $\Delta\eta$  and on  $m_{jj}$ , there is no significant difference between the full process and the approximation concerning the background for Higgs boson production in VBF.

All SUSY particle production processes except for slepton pair production have been generated with *MadGraph/MadEvent* V4 in the versions 4.4 and 4.5 [72], while the slepton pair production processes have been calculated with *MadGraph/MadEvent* 5.1.3 [73]. Afterwards the parton-level events from *MadGraph/MadEvent* have been fed into *Herwig++* 2.4.2 [81] for the SUSY particle decays. The parton shower and hadronization modules of *Herwig++* have not been active, so the quarks and gluons are left unchanged. For the *MadGraph/MadEvent* runs, the basic jet cuts from Eq. (3.7) have been applied in order to get finite cross sections. The CTEQ611 [182] parton distribution functions have been chosen for all *MadGraph/MadEvent* simulations. More

stringent analysis cuts have been enforced after the **Herwig++** run in an analysis program written in FORTRAN. For the irreducible background processes with very powerful analysis cuts applied, a mild cut on the rapidity separation between the two jets has already been used within **MadGraph/MadEvent** for a more efficient event generation.

The complete list of SUSY particle production processes generated with **MadGraph/MadEvent** is

$$\begin{array}{lll}
pp \rightarrow \chi_1^+ \chi_1^- j j & pp \rightarrow \chi_1^\pm \chi_2^0 j (j) & pp \rightarrow \chi_1^\pm \chi_2^\mp j j \\
pp \rightarrow \chi_2^0 \chi_1^0 j j & pp \rightarrow \chi_2^0 \chi_2^0 (j) (j) & pp \rightarrow \chi_2^+ \chi_2^- j j \\
pp \rightarrow \tilde{e}_{L,R}^+ \tilde{e}_{L,R}^- j j & pp \rightarrow \chi_3^0 \chi_1^0 j j & pp \rightarrow \chi_2^\pm \chi_2^0 j j \quad (3.33) \\
pp \rightarrow \tilde{\mu}_{L,R}^+ \tilde{\mu}_{L,R}^- j j & pp \rightarrow \chi_4^0 \chi_1^0 j j & pp \rightarrow \chi_2^+ \chi_1^0 j j \\
pp \rightarrow \tilde{\tau}_{1,2}^+ \tilde{\tau}_{1,2}^- j j & pp \rightarrow \chi_4^0 \chi_2^0 j j & pp \rightarrow \tilde{g} \chi_1^0 (j) (j),
\end{array}$$

with  $p = j = \{d, u, s, c, \bar{d}, \bar{u}, \bar{s}, \bar{c}, g\}$ . The first column lists the processes contributing to the irreducible background from Eqs. (3.9), (3.10) and (3.14)–(3.16). All processes giving rise to the reducible background, originally given in Eqs. (3.17)–(3.19) and (3.22)–(3.31), are listed in the second and third column.

The SUSY processes with at least one b-quark in the final state have been generated separately. These b-quark contributions will be studied for all SUSY processes except for  $pp \rightarrow \chi_1^\pm \chi_2^0 j$ ,  $pp \rightarrow \chi_1^\pm \chi_2^0 j j$ ,  $pp \rightarrow \tilde{\ell}^+ \tilde{\ell}^- j j$  and the gluino processes. The first process has no b-quark contributions (a b-quark in the final state of this process would require a top-quark in the initial state), while for the other ones they are small compared to the non-b-quark contributions and can be neglected. For the processes with at least one b-quark in the final state b-quarks are allowed in the initial state as well, so here  $p$  and  $j$  consist of  $\{d, u, s, c, b, \bar{d}, \bar{u}, \bar{s}, \bar{c}, \bar{b}, g\}$ , and the list of considered processes reads

$$\begin{array}{lll}
pp \rightarrow \chi_1^+ \chi_1^- j b/\bar{b} & pp \rightarrow \chi_2^0 \chi_2^0 (j) b/\bar{b} & pp \rightarrow \chi_1^\pm \chi_2^\mp j b/\bar{b} \\
pp \rightarrow \chi_2^0 \chi_1^0 j b/\bar{b} & pp \rightarrow \chi_3^0 \chi_1^0 j b/\bar{b} & pp \rightarrow \chi_2^+ \chi_2^- j b/\bar{b} \\
pp \rightarrow \chi_2^0 \chi_1^0 j b/\bar{b} & pp \rightarrow \chi_4^0 \chi_1^0 j b/\bar{b} & pp \rightarrow \chi_2^\pm \chi_2^0 j b/\bar{b} \\
pp \rightarrow \chi_4^0 \chi_2^0 j b/\bar{b} & & pp \rightarrow \chi_2^+ \chi_1^0 j b/\bar{b}. \quad (3.34)
\end{array}$$

As for the irreducible background processes, contributions with b-quarks in the initial state but none in the final state can be neglected for the reducible ones as well. The only exceptions are the processes  $pp \rightarrow \chi_2^0 \chi_2^0$  and  $pp \rightarrow \chi_2^0 \chi_2^0 j$ .

For the interface between **Herwig++** and the analysis program, which performs the cuts and generates the histograms, a substantially modified version of the **Herwig++** analysis module **RootSimple v.1.00** [183] has been used. Originally, this code writes out each final **Herwig++** event into a ROOT [184] data structure. The modified version instead writes out all information relevant for this analysis in a Les Houches event file. Additionally, this routine already dismisses events where the SUSY decays did

not produce at least two leptons and two jets. This can happen as `Herwig++` always generates all possible decays according to the given branching ratios in the SLHA file.

The event files for the signal processes  $h \rightarrow WW$  and  $h \rightarrow \tau\tau$  of Eq. (3.8) are generated at LO with the parton-level Monte Carlo program `VBFNLO 2.6.2` [145–147]. This program is optimized for the VBF processes and can calculate the signal processes very fast and efficiently, both within the SM and the MSSM. For the  $h \rightarrow WW$  process the subsequent decay into electrons and muons is treated within `VBFNLO`, while the tau lepton decay of the  $h \rightarrow \tau\tau$  process is again performed using `Herwig++`.

### 3.3.3 Validation

Several checks have been done to ensure the correctness of the analysis described in the last section.

The `MadGraph/MadEvent V4` results for the processes  $\chi_1^+ \chi_1^- jj$  and  $\chi_2^0 \chi_1^0 jj$  have been checked against `WHIZARD 2.0` [74, 75]. The results agree for total cross sections as well as for distributions with and without SUSY particle decay (performed by `Herwig++`). Some distributions for both processes including a decay into tau leptons via a stau lepton are shown in Figure 3.8. The process  $pp \rightarrow \tilde{e}_L^+ \tilde{e}_L^- jj$  as an example of a `MadGraph/MadEvent 5` process has been checked against `WHIZARD` as well.

The validity of the SUSY particle decays generated by `Herwig++`, according to the branching ratios from the SLHA spectrum and decay file, has been tested against `MadGraph/MadEvent` using its decay chain syntax [185]. The main purpose of this test is to check whether the missing spin information transfer between production and decay of the spin- $\frac{1}{2}$  particles, charginos and neutralinos, changes the lepton distributions significantly.

Therefore one specific decay chain for the chargino process

$$pp \rightarrow \chi_1^+ \chi_1^- jj \rightarrow \tilde{\tau}_1^+ \nu_\tau \tilde{\tau}_1^- \bar{\nu}_\tau jj \rightarrow \chi_1^0 \chi_1^0 \tau^- \bar{\nu}_\tau \tau^+ \nu_\tau jj \quad (3.35)$$

and for the neutralino process

$$pp \rightarrow \chi_1^0 \chi_2^0 jj \rightarrow \chi_1^0 \tilde{\tau}_1^\pm \tau^\mp jj \rightarrow \chi_1^0 \chi_1^0 \tau^\pm \tau^\mp jj \quad (3.36)$$

has been studied, where the chargino or next-to-lightest neutralino decays into a tau slepton, followed by a subsequent decay into a tau lepton. For these decay chains the computation with `MadGraph/MadEvent` has been done up to the  $\tilde{\tau}$ -level. At this stage the SUSY particles are scalars. Therefore `Herwig++` can take over and perform the last decay  $\tilde{\tau}_1^\pm \rightarrow \chi_1^0 \tau^\pm$  without losing any spin information. Comparing this result with the one where `Herwig++` performs the full chargino/next-to-lightest neutralino decay provides a good estimate on the impact of spin correlation between production and decay.

The results for both calculations of the chargino decay agree very well, except for some small differences in the tau lepton  $p_T$  distributions: In the full calculation of

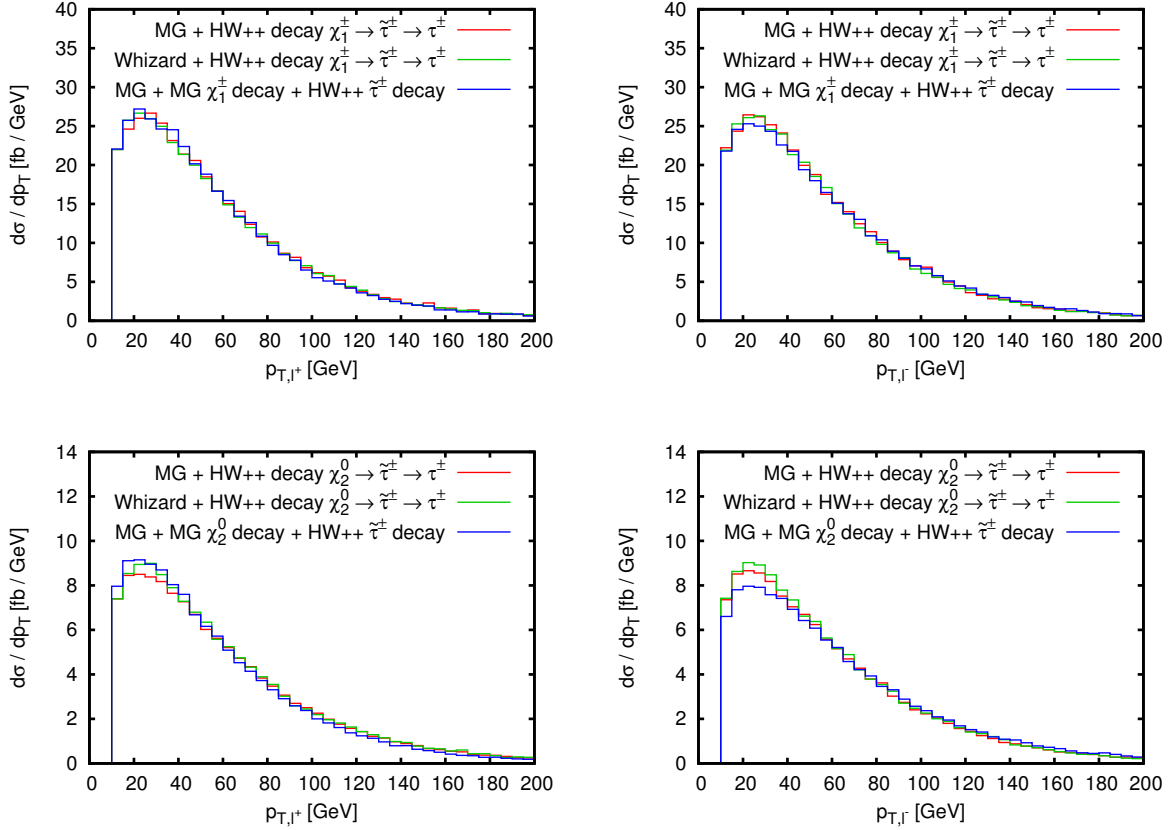


Figure 3.8: Comparison of MadGraph/MadEvent and WHIZARD calculating the production process from Eq. (3.35) and Eq. (3.36), with Herwig++ generating the decay chain. The third curve shows the same processes, but MadGraph/MadEvent generates the production process and the  $\chi_1^\pm / \chi_2^0$  decay, while Herwig++ calculates the second part of the SUSY decay chain, the  $\tilde{\tau}_1$  decay. Fixed scales are used, with  $\mu_F = \mu_R = M_Z$ . The  $p_T$  distributions of  $\tau^+$  and  $\tau^-$  are shown in the left and right column, respectively.

the decay chain with Herwig++ the shapes of the two tau leptons match each other. For the case where MadGraph/MadEvent generates the chargino decay there is a small asymmetry. Both curves are shown in Figure 3.8. The results for the next-to-lightest neutralino case, again depicted in Figure 3.8, are similar to the chargino decay, except that the asymmetry in the tau lepton  $p_T$  distributions is slightly enhanced. As the cuts on positively and negatively charged leptons within this analysis are identical, neglecting the asymmetry still gives a reasonable result, which is precise enough for this LO analysis.

The VBFNLO results for the  $h \rightarrow \tau\tau$  signal process have been verified in two ways: the Higgs boson production part has been checked against MadGraph/MadEvent, with agreement at the sub-per-cent level. The Higgs boson decay to tau leptons has been verified with Herwig++: the results of both programs agree within a few per-mil.

The  $h \rightarrow WW$  process has been checked against the full  $WW$  production process in VBF, restricting the invariant  $WW$  mass to be very close to the Higgs boson mass.

Therefore the full  $WW$  process is vastly dominated by the Higgs boson production graphs and the two processes should give the same result. Indeed the two results agree within one per-cent for the cuts of Eqs. (3.39)–(3.41), which is within the statistical errors of the test run.

Finally, the FORTRAN analysis routine, which handles the cuts, histograms and also the jet finding algorithm needed for the reducible background contributions, has been checked against an independent implementation written by a co-author of Ref. [99].

### 3.3.4 Particle and Event Selection

For the irreducible background processes the particle selection in the analysis is straightforward: concerning visible objects, two jets and two opposite-charged leptons are required for the signal process. The irreducible background processes produce exactly two quarks/gluons and two leptons, so there is no ambiguity in the selection. Each quark/gluon has to form a separate jet, and both leptons have to be visible to match the desired signature. Therefore it is sufficient to apply some cuts on minimal transverse momentum, maximal pseudorapidity and a minimal separation between the particles to identify each particle with a detector signal. As soon as at least one particle of an event does not fulfill a cut requirement, the desired signal signature cannot be achieved and the event can be discarded.

This approach is no longer valid for the processes contributing to the reducible background. The additional particles are allowed to be soft, outside the detector, or even close to another particle. For example a lepton which is close to a jet will be counted as part of the jet. If there are still two oppositely charged leptons in the event passing all cuts this event can still contribute to the SUSY background. Additionally, the hadronic tau lepton decays become important, as now events with more than two (tau) leptons are possible. The full details of the particle selection for all considered reducible background processes will be discussed in the following.

At first, the `Herwig++` analysis routine that produces the Les Houches event files has to be extended to support “partonic tau jets”, as the hadronic tau decay in `Herwig++` directly produces hadrons instead of partons. These particles do not match the parton stage used in the rest of the analysis. Therefore the `Herwig++` analysis routine collects all visible hadronic tau decay products and combines their momenta into one single object, which will be called a “partonic tau jet”. Afterwards, the same cuts as for the other partons are applied to that object. This method allows for the contribution of events with additional soft tau decay jets evading detection. Additionally, hard tau jets can serve as tagging jets.

The event generation for the reducible background processes with `MadGraph/MadEvent` itself is very similar to the generation for irreducible background processes. Again, the minimal jet cuts of Eq. (3.7) are applied to render the cross sections finite. After the decay step performed by `Herwig++` the event contains up to two partons already generated by `MadGraph/MadEvent`, at least two leptons of opposite charge, and additional

partons (for example from hadronic W boson and tau lepton decays) plus several invisible particles from the SUSY decay chains. The extended final state with respect to the irreducible background processes leads to a slightly more complicated missing energy definition: for the irreducible background processes it was sufficient to just take the absolute value of the negative vectorial sum of the transverse momenta of identified jets and leptons as missing energy. This prescription is no longer valid, instead, all particles depositing energy in the calorimeter should be taken into account. Therefore,  $\cancel{p}_T$  is determined as the absolute value of the negative vectorial sum of the transverse momenta of all light partons, tau jets and electrons up to  $|\eta| < 4.5$  and of muons up to  $|\eta| < 2.5$ . However, particles are only considered if their  $p_T$  is above the threshold of  $p_T > 3 \text{ GeV}$ .

Jets are defined according to the anti- $k_T$  clustering algorithm [186] with a distance parameter of  $\Delta R = 0.4$ . Leptons which are close to a jet, with a  $R$ -separation  $\Delta R_{jl} \leq 0.3$ , are counted as part of the jet. Resulting jets and leptons are defined as visible if they fulfill

$$p_{T,j} > 20 \text{ GeV}, \quad |\eta_j| < 4.5 \quad (3.37)$$

and

$$p_{T,\ell} > 10 \text{ GeV}, \quad |\eta_\ell| < 2.5, \quad (3.38)$$

respectively. Events are kept, if the final state at the end consists of at least two visible jets and exactly one positively and one negatively charged lepton. Afterwards, the usual analysis cuts as described in the next sections will be applied.

In some cases events of the reducible background processes have to be discarded in order to get a well-defined cross section. Due to limitations of the analysis setup, events have to be thrown away if one of the following criteria is met:

- If one of the partons generated by **MadGraph/MadEvent** does not end up in a tagging jet, but instead a parton from the SUSY particle decay chain serves as tagging jet. The case of two **MadGraph/MadEvent** partons forming a single jet is problematic as well, but this situation is already excluded by the basic jet cuts from Eq. (3.7) used in the generation.
- If a parton generated by **MadGraph/MadEvent** and a parton from a subsequent decay form a single jet.

These problems can be explained by looking at the origins of the **MadGraph/MadEvent** partons. There are two different production modes, one being a QCD splitting as shown in Figure 3.4. The other source of partons is from the decay of a heavy particle, with a sample diagram shown in Figure 3.2. In a full matrix element, with all diagrams combined, these two contributions of course cannot be separated. However, the distinction of the two production modes assists the illustration of the problems in handling **MadGraph/MadEvent** jets in the reducible background case. Two problems are apparent, the second one being explicitly linked to the fact that the two parton types cannot be separated:

- A parton generated by `MadGraph/MadEvent` which originates from a QCD splitting can be considered as part of the real-emission contribution of the corresponding `MadGraph/MadEvent` level process with one quark/gluon less in the final state. Unfortunately the real-emission contribution alone is not infrared (IR) safe, but diverges for small  $p_T$  of the extra parton. Only the full NLO corrections would yield an IR finite result. Therefore any final state selection which allows the parton from the QCD splitting to receive an arbitrary low  $p_T$  value leads to a cross section which is no longer well defined.

Within this analysis setup the IR divergence is regularized by the minimal  $p_T$  cut of 20 GeV set already at the `MadGraph/MadEvent` level. This arbitrary cut has no effect and is therefore justified, as long as each `MadGraph/MadEvent` parton is part of a different jet consisting only of this single parton, all these jets serve as tagging jets, and the analysis cuts are not weaker than the `MadGraph/MadEvent` event generation cuts.

In addition, the contribution from e.g.  $\chi_2^0\chi_2^0jj$  with one `MadGraph/MadEvent` parton ending up untagged is already included in the process  $\chi_2^0\chi_2^0j$ . Considering both contributions thus would result in a double-counting of this part.

- Another problem occurs for partons produced already by `MadGraph/MadEvent`: if they are produced in the decay of a heavy particle and are recombined with another hard parton, originating e.g. from a hadronic W boson decay, they should be allowed to become arbitrarily soft. However, the contribution from “decay” partons up to the  $p_T$  cut of 20 GeV is not included in the calculation due to the cut set already at the `MadGraph/MadEvent` generation level.

The error caused by discarding events where the partons from `MadGraph/MadEvent` do not form pure tagging jets can be estimated requiring  $p_{T,j} > 20$  GeV for all partons and investigating how large the contribution of the neglected events is in that sample: for the first case, where the `MadGraph/MadEvent` partons do not end up in a tagging jet at all, the neglected contribution accounts for 1-3% of the total cross section, after applying the rapidity separation cut for the two tagging jets, which is part of the analysis cuts. For the mixed jets of the second case, where a `MadGraph/MadEvent` parton is recombined with another parton, the contribution which is rejected can be estimated to be below 1%. Both contributions can be considered small with respect to the desired precision of this LO analysis.

## 3.4 LHC Results for the $h \rightarrow WW$ Channel at 14 TeV

Several processes that involve the production of charginos, neutralinos and sleptons can give rise to the background of VBF Higgs boson production. The discussion of the background contribution from these processes to the  $h \rightarrow WW$  and  $h \rightarrow \tau\tau$  modes of the VBF Higgs boson production will be split into three parts: this section is dedicated to the effect on the Higgs boson search in the  $WW$  channel for the LHC running at 14 TeV center-of-mass energy. Although the signatures in the detector are the same for the  $h \rightarrow WW$  and  $h \rightarrow \tau\tau$  signal processes they feature different characteristics in their distributions. Therefore the  $h \rightarrow \tau\tau$  case will be discussed separately in the next section. Afterwards, both Higgs boson channels will be discussed in the context of the LHC running at 7 TeV center-of-mass energy, which was used during the 2011 run.

The 14 TeV  $h \rightarrow WW$  analysis itself is separated into the discussion of the SPS1a-like scenario SPS1amod, the scenario with a heavier Higgs boson SPS1amod2, the analysis of the squark and gluino mass dependence, and the examination within scenarios showing an inverted slepton hierarchy. The cuts necessary for a suppression of the SM background are taken from Ref. [108], where the  $H \rightarrow WW$  channel in VBF was discussed for a relatively light SM Higgs boson, starting at  $m_H = 115$  GeV.

### 3.4.1 SPS1a-like Scenario SPS1amod

The discussion of the SPS1a-like scenario SPS1amod is done separately for the processes contributing to the irreducible and reducible background, respectively, as the additional particles occurring in the latter case present some additional aspects compared to the processes that match the signal signature exactly.

#### 3.4.1.1 Irreducible Background in the Scenario SPS1amod

The SUSY processes contributing to the irreducible background for Higgs boson production with subsequent Higgs decay into W bosons, which themselves decay into leptons, are  $pp \rightarrow \chi_1^+ \chi_1^- jj$ ,  $pp \rightarrow \chi_2^0 \chi_1^0 jj$  and  $pp \rightarrow \tilde{\ell}^+ \tilde{\ell}^- jj$ . As mentioned before, the contributions with final-state b-quarks will be considered separately in the following. With some basic cuts on the produced jets and leptons, which mostly account for detector acceptance (close to the basic cuts in Ref. [108])

$$\begin{aligned}
 p_{T,j} &\geq 20 \text{ GeV} & p_{T,\ell} &\geq 10 \text{ GeV} \\
 |\eta_j| &\leq 4.5 & |\eta_\ell| &\leq 2.5 \\
 \Delta R_{jj} &\geq 0.8 & \Delta R_{j\ell} &\geq 1.7 \\
 m_{\ell\ell} &\geq 10 \text{ GeV} , & &
 \end{aligned}
 \tag{3.39}$$

the background contributions from the SUSY processes are very large compared to the signal. This is shown in the left panels of Figures 3.9 and 3.10. The cross sections are

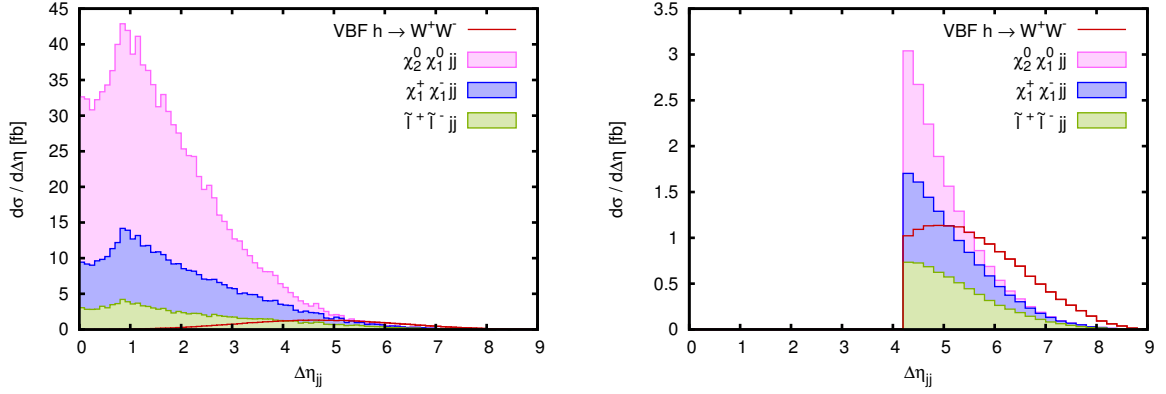


Figure 3.9: Rapidity separation for the irreducible SUSY background processes and the  $h \rightarrow WW$  signal with basic cuts, Eq. (3.39), (left) and additional  $\Delta\eta$  plus “leptons inside rapidity gap” cuts, Eq. (3.40) (right).

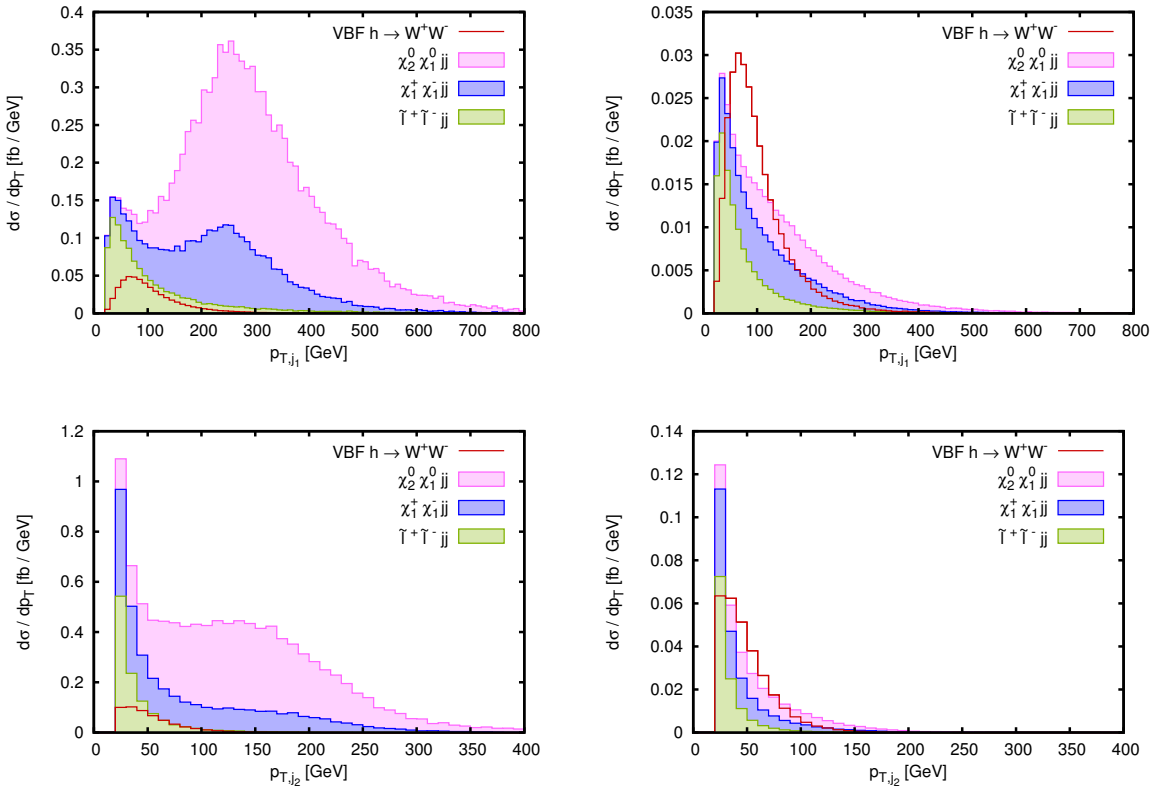


Figure 3.10: Transverse momentum of the harder (upper plots) and softer (lower plots) tagging jet for the irreducible SUSY background processes and the  $h \rightarrow WW$  signal with basic cuts, Eq. (3.39), (left) and additional  $\Delta\eta$  plus “leptons inside rapidity gap” cuts, Eq. (3.40) (right).

Processes	basic cuts	+ rapidity gap	+ $m_{inv},$ $p_T^{\min}, \phi_{\ell\ell}$	+ $M_T(WW)$	+ $p_T^{\max}$
	Eq. (3.39)	+ (3.40)	+ (3.41)	+ (3.43)	+ (3.44)
$\chi_1^+ \chi_1^- j j$	25.97 fb	1.21 fb	0.148 fb	0.113 fb	0.073 fb
$\chi_2^0 \chi_1^0 j j$	66.79 fb	1.04 fb	0.537 fb	0.146 fb	0.081 fb
$\tilde{\ell}^+ \tilde{\ell}^- j j$	11.55 fb	1.23 fb	0.080 fb	0.031 fb	0.028 fb
VBF $h \rightarrow WW$	5.09 fb	2.91 fb	1.46 fb	1.37 fb	1.33 fb

Table 3.2: Total cross sections for  $\chi_1^+ \chi_1^- j j$ ,  $\chi_2^0 \chi_1^0 j j$ ,  $\tilde{\ell}^+ \tilde{\ell}^- j j$  and VBF  $h \rightarrow WW$  at various cut levels for the scenario SPS1amod, without b-quark contributions.

listed in Table 3.2. In Eq. (3.39),  $m_{\ell\ell}$  denotes the invariant mass of the dilepton system. In the distributions of the rapidity separation between the two tagging jets,  $\Delta\eta_{jj}$ , and the transverse momenta of the tagging jets, massive differences between the VBF Higgs process and the SUSY background processes become visible: the signal shows the typical VBF shape, with two forward jets, giving a large separation in rapidity, and rather small transverse momenta of the jets. The SUSY processes on the other hand do not exhibit this large separation in rapidity, but show the normal distribution of QCD initiated processes. For the next-to-lightest neutralino process both jets additionally have a much larger transverse momentum, as both jets originate from the decay of comparatively heavy squarks. For the chargino process both jets again have a high- $p_T$  component, but especially the second jet also has a large contribution at low  $p_T$ . This is due to the different production modes, with the high- $p_T$  jets arising from a squark decay (third diagram in Figure 3.3), while the low- $p_T$  jets originate from QCD radiation (first two diagrams in Figure 3.3). For the slepton case the first and second hardest jets are rather soft, as QCD radiation is largely responsible for both jets in this case (see Figure 3.4).

Looking closely at the left diagram in Figure 3.9, it becomes apparent that the behavior of the individual SUSY processes in the  $\Delta\eta_{jj}$  distribution is slightly different: While the steepness for the next-to-lightest neutralino process is even more pronounced than for the chargino case, the slepton curve has a slightly bigger tail at large rapidity separations. This is due to the fact that hard jets from heavy particle decays have a tendency to be produced in more central regions of the detector, given that the partonic energy has to be larger in this case. Therefore, after the application of a cut on the rapidity separation

$$\Delta\eta_{jj} \geq 4.2 \quad \eta_{j1} \cdot \eta_{j2} < 0 \quad \eta_{j,min} + 0.6 \leq \eta_{\ell} \leq \eta_{j,max} - 0.6, \quad (3.40)$$

which is obviously extremely efficient considering the reduction of the SUSY background, all three SUSY processes contribute more or less equally to the background. The  $\Delta\eta_{jj}$  cut is combined with two other cuts, which further exploit the production mechanism of vector boson fusion: as both jets are directed in the forward direction, they end up in opposite detector hemispheres, while the Higgs boson decay products

end up in the central region. The total cross sections are again listed in Table 3.2. With the cuts from Eq. (3.40) the jet- $p_T$  shapes of the SUSY processes and the VBF signal process approach each other (see right plots in Figure 3.10).

Several additional cuts are used in the  $h \rightarrow WW$  analysis for VBF [108] to suppress the SM background:

$$\begin{aligned} \not{p}_T &\geq 30 \text{ GeV} & m_{jj} &\geq 600 \text{ GeV} \\ m_{\ell\ell} &\leq 60 \text{ GeV} & \phi_{\ell\ell} &\leq 140^\circ \approx 2.44 \text{ rad} \\ m_{\tau\tau,rec} &\leq M_Z - 25 \text{ GeV} . \end{aligned} \quad (3.41)$$

The cut on a minimal amount of missing transverse momentum  $\not{p}_T$  is useful for the SM background reduction, but does not reduce the cross sections of the SUSY background processes, as they include several invisible particles. The cut on the reconstructed invariant tau pair mass  $m_{\tau\tau,rec}$  reduces the  $Z \rightarrow \tau\tau$  background.<sup>5</sup> The remaining cuts are particularly useful in both SM and SUSY background reduction. The cut on the invariant jet pair mass  $m_{jj}$ , which is part of the typical VBF cuts, improves the signal to background ratio for the sleptons, as  $m_{jj}$  is rather small compared to the other SUSY processes and the signal process (see upper plot of Figure 3.11). The azimuthal angle difference for the two leptons,  $\phi_{\ell\ell}$ , depicted in the lower left plot of Figure 3.11, shows quite some difference for the slepton and chargino process on the one hand and the next-to-lightest neutralino and VBF  $h \rightarrow WW$  process on the other hand: For chargino and slepton pair production the two leptons arise from two different decay chains of heavy particles. Therefore they tend to move in opposite directions. The leptons for both of the other two processes are usually close in their azimuthal angle, but for different reasons. In the next-to-lightest neutralino process the two leptons come from the decay of one rather heavy next-to-lightest neutralino, which again is produced in the decay of a much heavier squark. Therefore already the neutralino is significantly boosted, and the two leptons move into the same direction. For the  $h \rightarrow WW$  signal, the two leptons having a small opening angle is linked to the spin-0 state of the Higgs boson and the coupling structure of the W boson to fermions [187]. The invariant mass of the two leptons,  $m_{\ell\ell}$ , is quite small for the Higgs boson, which is again specific for the  $h \rightarrow WW$  channel [188]. This quantity is also rather small for the  $\chi_2^0\chi_1^0jj$  process, as it is bounded from above by the mass difference  $m_{\chi_2^0} - m_{\chi_1^0}$ . For  $\chi_1^+\chi_1^-jj$  and  $\tilde{\ell}^+\tilde{\ell}^-jj$  the invariant lepton mass can acquire values which are only limited by the partonic center-of-mass energy, therefore the cut on  $m_{\ell\ell}$  very efficiently reduces these two contributions, especially the slepton pair production part. To summarize, the cuts from Eq. (3.41) particularly effect the background contribution due to slepton and chargino production, while the next-to-lightest neutralino process does not receive a stronger suppression than the  $h \rightarrow WW$  signal. In total, the size of the discussed SUSY background at this cut level is roughly half of the  $h \rightarrow WW$  signal size.

<sup>5</sup>Reconstructing the  $m_{\tau\tau}$  mass is only possible for some events in the  $h \rightarrow WW$  case, as the electrons and muons in fact do not arise from the decay chain  $X \rightarrow \tau\tau \rightarrow \ell\ell + \not{p}_T$  assumed in the reconstruction formula. More details concerning this cut in the  $h \rightarrow WW$  analysis can be found in Ref. [108]. The use of the  $m_{\tau\tau}$  reconstruction in the  $h \rightarrow \tau\tau$  channel will be discussed in Section 3.5.

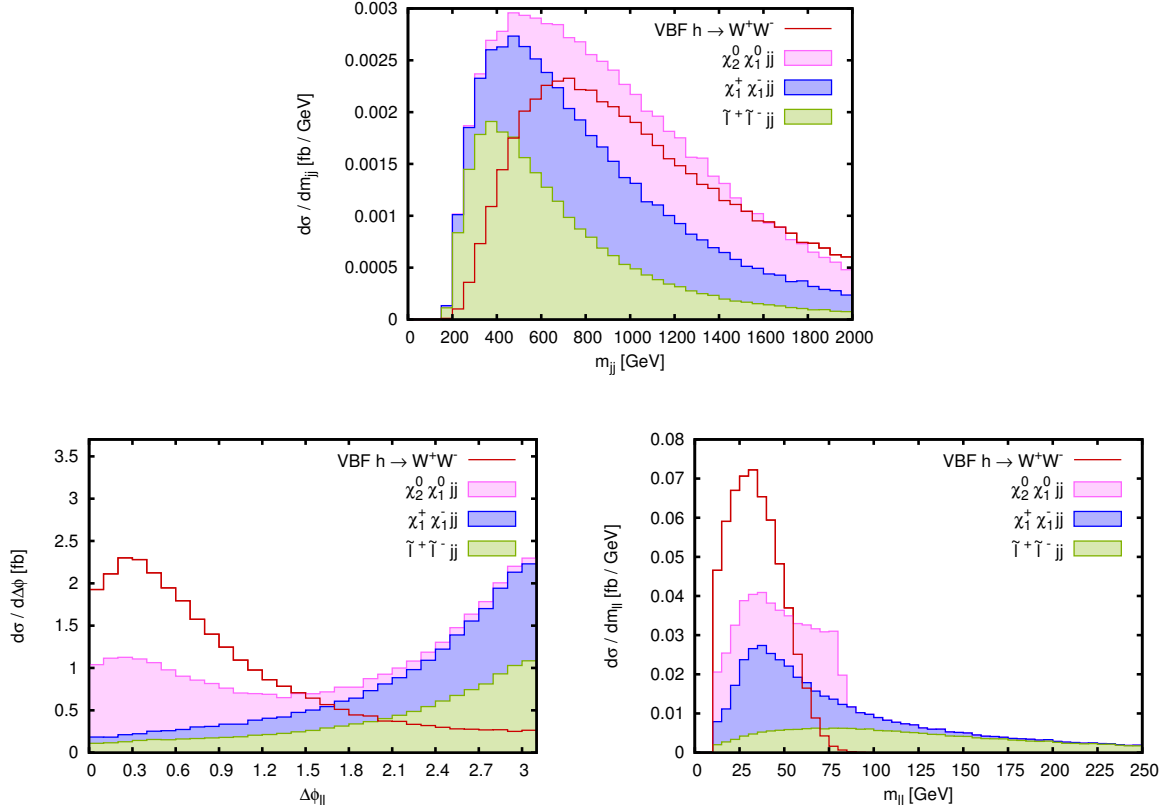


Figure 3.11: The upper plot shows the invariant mass of the two tagging jets, the lower row features the azimuthal angle between the leptons (left) and the invariant mass of both leptons (right) for the irreducible SUSY background processes and the  $h \rightarrow WW$  signal with the cuts from Eqs. (3.39)–(3.40) and Eq. (3.43).

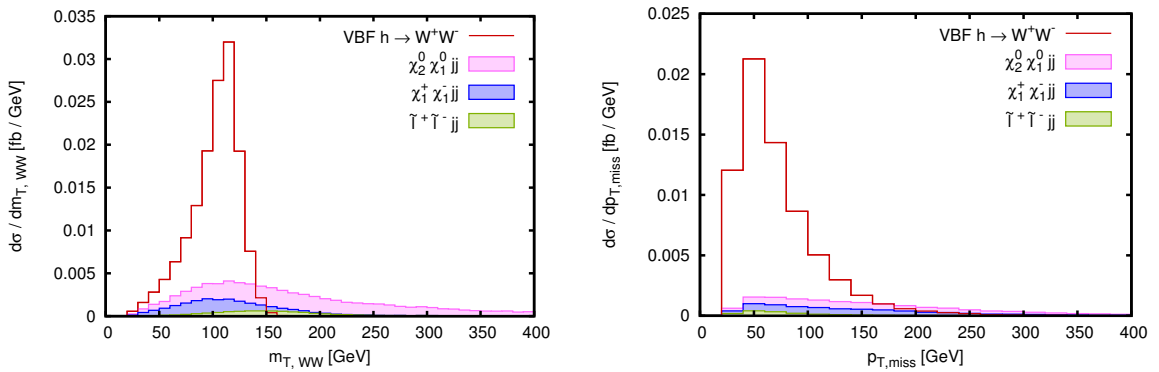


Figure 3.12: Left panel: Transverse  $WW$  mass distribution with cuts (3.39)–(3.41). Right panel:  $p_T$  distribution for the irreducible SUSY background contributions and the  $h \rightarrow WW$  signal with the cuts from Eqs. (3.39)–(3.41) and Eq. (3.43).

A reconstruction of the Higgs boson mass from the final state particles would be very helpful in the Higgs boson search. Especially as the light Higgs boson is extremely narrow, a new sharp resonance would be a clear signal of a possible Higgs boson. Unfortunately, a full reconstruction of the Higgs boson mass in the  $h \rightarrow WW$  decay is not possible due to the neutrinos in the leptonic W boson decay. However, it is possible to define the transverse  $WW$  mass as [108]

$$M_T(WW) = \sqrt{(\cancel{E}_T + E_{T,\ell\ell})^2 - (\cancel{\mathbf{p}}_T + \mathbf{p}_{T,\ell\ell})^2}, \quad (3.42)$$

with  $E_{T,\ell\ell} = \sqrt{\mathbf{p}_{T,\ell\ell}^2 + m_{\ell\ell}^2}$  and  $\cancel{E}_T = \sqrt{\cancel{\mathbf{p}}_T^2 + m_{\ell\ell}^2}$ . In this definition of  $M_T(WW)$  the experimentally inaccessible quantity  $m_{\nu\nu}^2$  in  $\cancel{E}_T$  has been replaced by  $m_{\ell\ell}^2$ . For the signal process, the  $M_T(WW)$  distribution peaks nicely around the Higgs boson mass of  $m_h \approx 118$  GeV, as depicted in the left diagram of Figure 3.12. The chargino process shows a broader peak, centered roughly at  $m_h$ , while the next-to-lightest neutralino process and the slepton pair production process exhibit significantly larger  $M_T(WW)$  values. Therefore the cut

$$50 \text{ GeV} < M_T(WW) < m_h + 20 \text{ GeV}, \quad (3.43)$$

proposed in Ref. [108], reduces the next-to-lightest neutralino background by 75%, the slepton background by 60% and the chargino background by 25%, while the signal reduction is less than 10%.

Finally, as the SUSY processes incorporate more sources of missing transverse momentum  $\cancel{p}_T$  (see right diagram of Figure 3.12), a cut of

$$\cancel{p}_T \leq 170 \text{ GeV} \quad (3.44)$$

again reduces the SUSY background significantly, but leaves the signal almost unaffected. After the application of all cuts the three processes  $\chi_1^+ \chi_1^- jj$ ,  $\chi_2^0 \chi_1^0 jj$  and  $\tilde{\ell}^+ \tilde{\ell}^- jj$  generate a background contribution that accounts for 14% of the VBF  $h \rightarrow WW$  cross section. This is an enormous reduction with respect to the background level with basic cuts, where the sum of the SUSY processes was about 20 times larger than the signal.

### b-Quark Contributions

So far, Feynman diagrams with b-quarks in the initial or final state have not been considered. As mentioned before, the contributions with at least one  $b/\bar{b}$  in the initial state, but none in the final state have been checked to be very small. Therefore they will be neglected in the following discussion. Instead, the focus will be on the subprocesses with at least one  $b/\bar{b}$  in the final state and no restrictions on the initial state. These subprocesses will be called “b-quark contributions”. In tables, the corresponding b-quark contributions to the process  $X jj$  will be denoted as  $X j b/\bar{b}$ .

For the chargino pair production process, the b-quark contributions within basic cuts are of the same order as the process without b-quarks: the b-quarks add a cross section

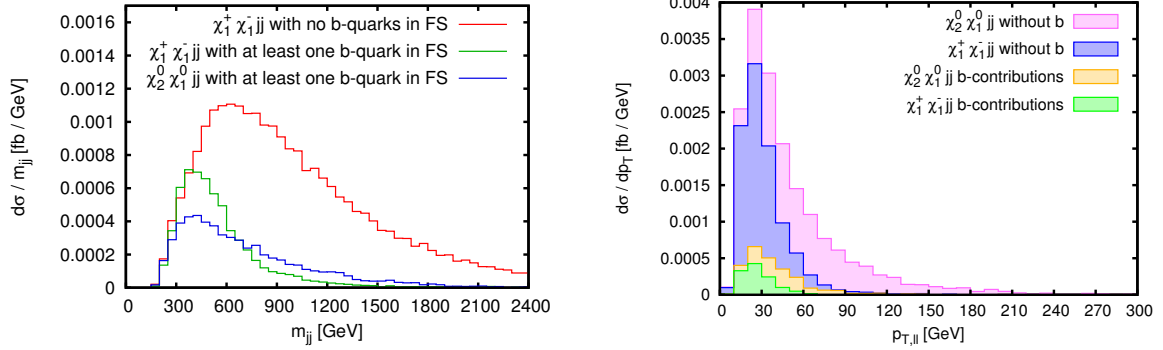


Figure 3.13: Left panel: Dijet mass distribution of  $\chi_1^+ \chi_1^- jj$ ,  $\chi_1^+ \chi_1^- j b \bar{b}$  and  $\chi_2^0 \chi_1^0 j b \bar{b}$  with the cuts from Eqs. (3.39) + (3.40). Right panel: Dilepton transverse momentum distribution for  $\chi_1^+ \chi_1^- jj$  and  $\chi_2^0 \chi_1^0 jj$  including b-quark contributions, with the cuts from Eqs. (3.39)–(3.41), (3.43)–(3.44) and the b-quark veto from Eq. (3.45).

Processes	basic cuts	+ rap. gap	+ $m_{inv}, \cancel{p}_T,$ $\phi_{\ell\ell}, M_T(WW)$	+ b-tagging
	Eq. (3.39)	+ (3.40)	+ (3.41), (3.43), (3.44)	+ (3.45)
$\chi_1^+ \chi_1^- jj$	25.97 fb	1.21 fb	0.073 fb	0.073 fb
$\chi_1^+ \chi_1^- j b \bar{b}$	14.50 fb	0.31 fb	0.022 fb	0.012 fb
$\chi_2^0 \chi_1^0 jj$	66.79 fb	1.04 fb	0.081 fb	0.080 fb
$\chi_2^0 \chi_1^0 j b \bar{b}$	7.65 fb	0.29 fb	0.022 fb	0.014 fb
$\tilde{\ell}^+ \tilde{\ell}^- jj$	11.55 fb	1.23 fb	0.028 fb	0.028 fb
$\sum_{irred}^{SUSY}$	126.46 fb	4.08 fb	0.226 fb	0.207 fb
VBF $h \rightarrow WW$	5.09 fb	2.91 fb	1.33 fb	1.32 fb

Table 3.3: Total cross sections for  $\chi_1^+ \chi_1^- jj$ ,  $\chi_2^0 \chi_1^0 jj$ ,  $\tilde{\ell}^+ \tilde{\ell}^- jj$ , including b-quark contributions  $\chi_1^+ \chi_1^- j b \bar{b}$  and  $\chi_2^0 \chi_1^0 j b \bar{b}$ , and VBF  $h \rightarrow WW$  at various cut levels for the scenario SPS1amod.

of 14.5 fb to the non-b-quark cross section of 26.0 fb. The by far largest fraction of the b-quark contributions comes from the production of a light stop pair  $\tilde{t}_1$ , with two gluons in the initial state. Due to the much lighter  $\tilde{t}_1$ , compared to the squarks of the first two generations, the invariant dijet mass of these events is much smaller than for the non-b-quark contribution, as can be seen in the left diagram of Figure 3.13. Additionally, the rapidity separation  $\Delta\eta_{jj}$  is also smaller, and therefore the cuts from Eqs. (3.40) and (3.41) are much more efficient than in the non-b-quark case. So after applying all cuts from Eqs. (3.39)–(3.41), (3.43) and (3.44), the b-quark contributions add 25% to the previously discussed chargino process. This can still be reduced by requesting a b-jet veto. According to Refs. [102, 189, 190], the assumption

$$P_{\text{b-tag}} = 0.6, \quad \text{yielding} \quad P_{\text{mistag}} = 0.01 \quad \text{for} \quad |\eta_b| \leq 2.5, \quad (3.45)$$

is a reasonable choice with a low mistag rate, which is included in the following results as well. Here,  $P_{\text{b-tag}}$  is the probability to positively detect a b-quark jet, while  $P_{\text{mistag}}$  gives the probability that a light jet without b-quarks will be erroneously identified as a b-quark jet. At the LHC detectors, b-tagging is only possible in the central region ( $|\eta| \lesssim 2.5$ ), which is in conflict with the cut on the large rapidity separation, yielding rather forward jets. However, as most of the events contain a  $b\bar{b}$  pair, there is a good chance that at least one of the two b-jets falls into the region of the detector where b-tagging can be applied. Including the b-jet veto with the tagging efficiency from Eq. (3.45), the b-quark contribution from charginos drops to 13% of the chargino cross section with the final set of cuts (see the right plot of Figure 3.13). Details on the cross sections at the discussed cut levels can be found in Table 3.3.

For the next-to-lightest neutralino process the cross section of the b-quark contributions with inclusive cuts is smaller than in the chargino case (see Table 3.3). As discussed in Section 3.2.3, the squark-induced contributions, which play a dominant role for the b-quark contributions in the chargino process, are very small in this case. However, the additional analysis cuts are not as effective as for the chargino case, given that e.g. the  $m_{jj}$  distribution is shifted to higher values. This leads to a b-quark contribution for the next-to-lightest neutralino process that is comparable to the one for the chargino process.

The b-quark contribution to the slepton process is very small: with all cuts it accounts for only 3% of the already small slepton cross section. Therefore they have not been considered for this study.

In total, and after applying all cuts including the b-quark veto, the discussed b-quark contributions add roughly 15% to the irreducible SUSY background for the scenario SPS1amod.

### 3.4.1.2 Reducible Background in the Scenario SPS1amod

So far the processes from Section 3.2.3 have been discussed, which lead to exactly the same visible particles in the final state as those in the signal process  $h \rightarrow WW$ . In the

Processes	basic cuts Eq. (3.39)	+ rap. gap + (3.40)	+ $m_{inv}, \not{p}_T, \phi_{\ell\ell},$ $M_T(WW)$ , b-tag + (3.41),(3.43)–(3.45)	+ CJV on $j_{decay}$ + (3.46)
$\chi_1^+ \chi_2^0 j j$	100.8 fb	3.94 fb	0.403 fb	0.275 fb
$\chi_1^- \chi_2^0 j j$	63.22 fb	2.20 fb	0.222 fb	0.144 fb
$\chi_2^0 \chi_2^0 j j$	46.40 fb	1.35 fb	0.149 fb	0.059 fb
$\chi_2^0 \chi_2^0 j b/\bar{b}$	5.02 fb	0.168 fb	0.010 fb	0.006 fb
$\sum_{red}^{SUSY}$	215.4 fb	7.66 fb	0.784 fb	0.484 fb
VBF $h \rightarrow WW$	5.09 fb	2.91 fb	1.32 fb	1.32 fb

Table 3.4: Total cross sections for the reducible background contributions  $\chi_1^\pm \chi_2^0 j j$  and  $\chi_2^0 \chi_2^0 j j$ , including b-quark contributions  $\chi_2^0 \chi_2^0 j b/\bar{b}$ , and VBF  $h \rightarrow WW$  at various cut levels for the scenario SPS1amod.

following, the focus will be on the processes that lead to additional detectable particles. In principle, these processes could be eliminated by a veto on particles that are not needed for the signal signature. However, a full veto is not possible: the superfluous particles can be too soft for detection or they could travel into a direction not covered by the detector. Especially the veto on additional hadronic activity at a hadron collider is far from being perfect.

The discussion features the processes  $\chi_1^\pm \chi_2^0 j j$  and  $\chi_2^0 \chi_2^0 j j$  which give the dominant contribution to the reducible background. The b-quark contributions to  $\chi_1^\pm \chi_2^0 j j$  can be neglected as they are tiny and within the error of the Monte Carlo integration for the process without b-quarks. The event selection for the reducible background is not as trivial as it is for the irreducible background processes, which has already been addressed in Section 3.3.4.

The total cross sections of the processes giving the dominant contribution to the reducible background for the  $h \rightarrow WW$  channel are listed in Table 3.4 for different cut levels. All given numbers include a veto on additional visible<sup>6</sup> electrons and muons. The cuts of Eqs. (3.39)–(3.41) and Eqs. (3.43)–(3.45) have been discussed in detail for the irreducible background processes. They, of course, have to be applied to the reducible background processes as well. In events with three or more jets, the two jets with largest  $p_T$  have been identified with the tagging jets, and the jet cuts in Eqs. (3.39)–(3.41) have been applied on these two hardest jets. As before, the cross sections of the background processes are very large before the application of the rapidity separation cut from Eq. (3.40). With the final set of cuts from the irreducible background discussion, the contribution from the reducible background is smaller than the signal, but still significantly larger than the irreducible background. The impact

<sup>6</sup>A visible lepton has been defined in Eq. (3.38) by demanding  $p_{T,\ell} > 10$  GeV and  $|\eta_\ell| < 2.5$ .

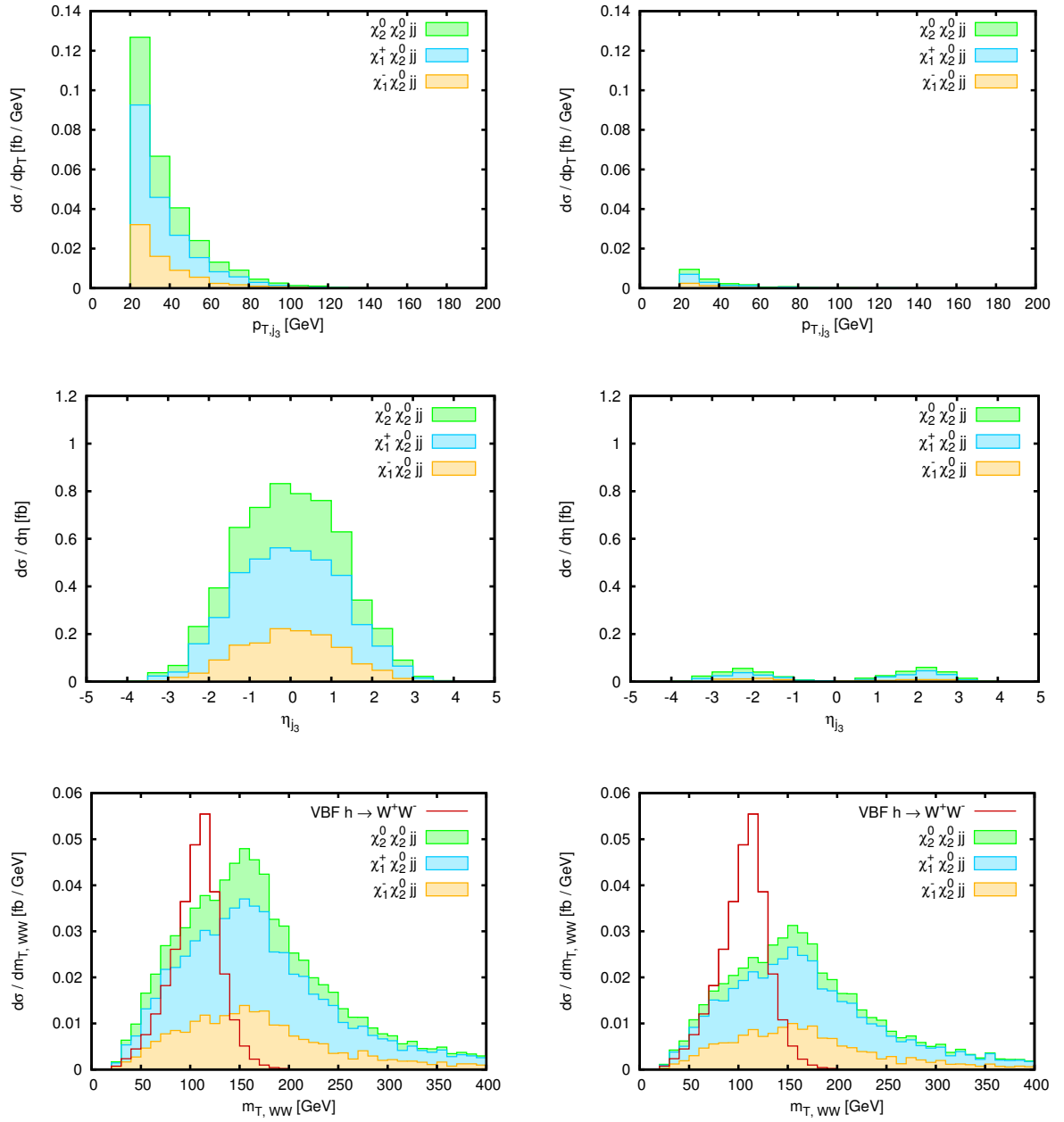


Figure 3.14: Transverse momentum (top row) and rapidity (middle row) of the third jet occurring in  $\chi_1^\pm \chi_2^0 jj$  and  $\chi_2^0 \chi_2^0 jj$ , including b-quark contributions for the latter process. The bottom row shows the transverse  $WW$  mass distribution of these processes. Since the  $h \rightarrow WW$  signal has no third jet at LO and it is only included in the transverse mass plots. Cuts for the left column are from Eqs. (3.39) - (3.40); the plots in the right column also include the veto from Eq. (3.46). Distributions are shown for the scenario SPS1amod.

of the processes with additional jets in their final state can be reduced by a veto on additional visible<sup>7</sup> and central jets

$$\eta_{j_{tag,min}} < \eta_{j_{decay}} < \eta_{j_{tag,max}} \quad \text{with} \quad p_{T,j_{decay}} > 20 \text{ GeV}, \quad |\eta_{j_{decay}}| < 4.5, \quad (3.46)$$

where central is defined as being within the rapidity of the jets, taking the two tagging jets as boundary. It has to be noted, however, that this jet veto affects only additional jets from the decay of a heavy particle. As no parton shower has been used for this analysis, the effect of the jet veto on additional jets from QCD radiation is not included. The question, whether a veto on these additional radiated jets will improve the signal over SUSY background ratio will be discussed later on in Section 3.7.3. In an experimental analysis the discrimination between the two jet types is, of course, not possible. Therefore an experimental jet veto would act on jets from QCD radiation as well as on jets from a heavy particle decay.

The effect of the central jet veto from Eq. (3.46) is shown in Figure 3.14. The left hand side shows distributions with the basic cuts from Eq. (3.39) and with the VBF-type rapidity cuts from Eq. (3.40). The plots on the right hand side include the central jet veto from Eq. (3.46). The  $p_T$  and  $\eta$  distributions of the additional third visible jet show that the events with three or more visible jets are eliminated efficiently. However, a large part of the contribution from reducible background processes remains, due to additional jets and leptons which are too soft for detection or are outside detector coverage. This is depicted in the last row of Figure 3.14, which shows the transverse  $WW$  mass. It is apparent from that distribution, and also from Table 3.4, that in particular the  $\chi_2^0\chi_2^0jj$  process, which can yield up to four jets, has a large fraction of events with an additional visible jet and therefore is significantly reduced by the jet veto. The signal process does not have any three-jet contributions as long as QCD radiation is not considered. Therefore it is not affected at all by the jet veto. Finally, even after the central jet veto, the contribution from the processes  $\chi_1^\pm\chi_2^0jj$ ,  $\chi_2^0\chi_2^0jj$  and  $\chi_2^0\chi_2^0jb/\bar{b}$  is larger than the one of the processes contributing to the irreducible background.

### 3.4.1.3 Summary for the Scenario SPS1amod

After a detailed separate discussion of the dominant irreducible and reducible SUSY background to the  $h \rightarrow WW$  channel in VBF in the scenario SPS1amod, the results are shortly summarized. Additionally, the cross section ratio of signal over SUSY background  $S/B^{SUSY}$  from the dominant irreducible and reducible contributions is calculated. Finally, several sub-dominant processes are also listed and briefly discussed.

Table 3.5 lists all previously discussed processes, giving the largest contributions to the SUSY background for VBF Higgs boson production. The processes listed there are also depicted in Figure 3.15, which shows once again the rapidity separation between the two hardest jets. The left plot is done with only basic cuts, while the right plot shows

<sup>7</sup>A jet has been declared as visible in Eq. (3.37) by the requirements  $p_{T,j} > 20 \text{ GeV}$  and  $|\eta_\ell| < 4.5$ .

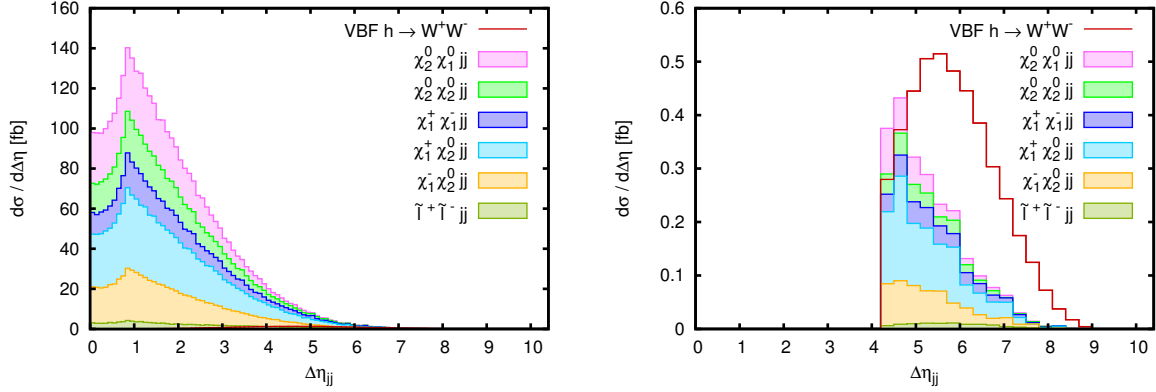


Figure 3.15: Rapidity separation for the SUSY background processes including relevant b-quark contributions and the  $h \rightarrow WW$  signal in the scenario SPS1amod. The left plot is for minimal cuts from Eq. (3.39). The right plot includes all discussed cuts from Eqs. (3.39) - (3.41), (3.43) - (3.46).

Processes	basic cuts	+ rap. gap	+ $m_{inv}, \cancel{p}_T, \phi_{\ell\ell},$	+ CJV on
	Eq. (3.39)	+ (3.40)	$M_T(WW),$ b-tag	$j_{decay}$
			+ (3.41),(3.43)–(3.45)	+ (3.46)
$\chi_1^+ \chi_1^- jj$	25.97 fb	1.21 fb	0.073 fb	0.073 fb
$\chi_1^+ \chi_1^- jj b/\bar{b}$	14.50 fb	0.31 fb	0.012 fb	0.012 fb
$\chi_2^0 \chi_1^0 jj$	66.79 fb	1.04 fb	0.080 fb	0.080 fb
$\chi_2^0 \chi_1^0 jj b/\bar{b}$	7.65 fb	0.29 fb	0.014 fb	0.014 fb
$\tilde{\ell}^+ \tilde{\ell}^- jj$	11.55 fb	1.23 fb	0.028 fb	0.028 fb
$\chi_1^+ \chi_2^0 jj$	100.8 fb	3.94 fb	0.403 fb	0.275 fb
$\chi_1^- \chi_2^0 jj$	63.22 fb	2.20 fb	0.222 fb	0.144 fb
$\chi_2^0 \chi_2^0 jj$	46.40 fb	1.35 fb	0.149 fb	0.059 fb
$\chi_2^0 \chi_2^0 jj b/\bar{b}$	5.02 fb	0.168 fb	0.010 fb	0.006 fb
$\Sigma B^{SUSY}$	341.9 fb	11.74 fb	0.991 fb	0.700 fb
VBF $h \rightarrow WW$	5.09 fb	2.91 fb	1.32 fb	1.32 fb
$S/B^{SUSY}$	0.015	0.25	1.3	1.9

Table 3.5: Total cross sections of the SUSY background contributions dominant at low squark masses and the VBF  $h \rightarrow WW$  signal for the scenario SPS1amod.

the same distributions with the final set of cuts used in the analysis. The corresponding cross sections are given in the first and last column of Table 3.5, respectively. The effect of the analysis cuts on the SUSY background processes is huge: while their cross section with basic cuts is almost 70 times larger than the signal cross section, the signal to background ratio improves to

$$S/B^{SUSY} = 1.3, \quad (3.47)$$

including all cuts except the central jet veto from Eq. (3.46). Here and in the following,  $B^{SUSY}$  includes all processes from Table 3.5. With the application of this jet veto on the jets arising from heavy-particle decays the signal to SUSY background ratio improves to

$$S/B^{SUSY} = 1.9. \quad (3.48)$$

The processes with only sub-dominant contributions to the SUSY background are listed in Table 3.6. The cross section of each process in this list is very small, given that all analysis cuts are applied. In total their cross sections sum up to less than 7% of the whole contribution from the dominant processes listed in Table 3.5.

The sub-dominant SUSY processes from Table 3.6 can be split into three classes. Processes of each class feature different reasons for the smallness of the contribution to the background for VBF Higgs boson production:

- The first class includes the processes from Table 3.5, but with fewer light jets at matrix element level, i.e. jets which are already generated by `MadGraph/MadEvent`.

For these processes, one (or two for  $\chi_2^0 \chi_2^0$  production) of the tagging jets in the event have to be produced in a hadronic tau lepton or W boson decay. These tau leptons and W bosons arise from the chargino or next-to-lightest neutralino decay. The contributions with less than two matrix-element jets are much smaller than the two-jet contributions, given that resonant squark pair production which produces fairly hard jets is not possible here. The “tau jets” on the other hand are rather soft. Additionally, the rapidity separation between the two tagging jets is smaller for this process class which leads to an increased efficiency of the rapidity gap cut from Eq. (3.40).

- The second process class consists of processes involving gluinos.

With the basic cuts from Eq. (3.39), the cross sections of the gluino processes are reasonably large. However, the jets from the gluino decay are very close in rapidity, which leads to an even larger impact of the rapidity gap cut, with respect to the other processes, especially for the processes with zero or one jet at matrix element level. For the process  $\tilde{g} \chi_1^0$ , which has no jets except from the gluino decay, the rapidity gap cut leads to a cross section reduction of more than three orders of magnitude. The gluino process with two jets at matrix-element level on the other hand produces many hard jets, which makes the jet veto very efficient.

Processes	basic cuts	+ rap. gap	+ $m_{inv}, \cancel{p}_T, \phi_{\ell\ell},$	+ CJV on
	Eq. (3.39)	+ (3.40)	$M_T(WW),$ b-tag + (3.41),(3.43)–(3.45)	$j_{decay}$ + (3.46)
$\chi_1^+ \chi_2^0 j$	15.96 fb	0.230 fb	0.008 fb	0.007 fb
$\chi_1^- \chi_2^0 j$	8.93 fb	0.115 fb	0.004 fb	0.003 fb
$\chi_2^0 \chi_2^0 j$	7.76 fb	0.052 fb	0.003 fb	0.002 fb
$\chi_2^0 \chi_2^0 b/\bar{b}$	0.95 fb	0.010 fb	$\ll 0.001$ fb	$\ll 0.001$ fb
$\chi_2^0 \chi_2^0$	0.25 fb	$\ll 0.001$ fb	$\ll 0.001$ fb	$\ll 0.001$ fb
$\chi_2^0 \chi_2^0$ b-contr.	0.15 fb	$\ll 0.001$ fb	$\ll 0.001$ fb	$\ll 0.001$ fb
$\tilde{g} \chi_1^0 j j$	54.33 fb	3.15 fb	0.117 fb	< 0.01 fb
$\tilde{g} \chi_1^0 j$	64.98 fb	0.54 fb	0.046 fb	0.007 fb
$\tilde{g} \chi_1^0$	0.32 fb	$\ll 0.001$ fb	$\ll 0.001$ fb	$\ll 0.001$ fb
$\chi_1^+ \chi_2^- j j$	2.03 fb	0.074 fb	0.003 fb	0.002 fb
$\chi_1^+ \chi_2^- j b/\bar{b}$	0.67 fb	0.028 fb	< 0.001 fb	< 0.001 fb
$\chi_1^- \chi_2^+ j j$	2.06 fb	0.095 fb	0.005 fb	0.003 fb
$\chi_1^- \chi_2^+ j b/\bar{b}$	0.69 fb	0.029 fb	< 0.001 fb	< 0.001 fb
$\chi_2^+ \chi_2^- j j$	0.27 fb	0.021 fb	< 0.001 fb	< 0.001 fb
$\chi_2^+ \chi_2^- j b/\bar{b}$	0.11 fb	0.002 fb	$\ll 0.001$ fb	$\ll 0.001$ fb
$\chi_3^0 \chi_1^0 j j$	0.33 fb	0.009 fb	< 0.001 fb	< 0.001 fb
$\chi_3^0 \chi_1^0 j b/\bar{b}$	0.14 fb	0.002 fb	$\ll 0.001$ fb	$\ll 0.001$ fb
$\chi_4^0 \chi_1^0 j j$	1.76 fb	0.041 fb	< 0.001 fb	< 0.001 fb
$\chi_4^0 \chi_1^0 j b/\bar{b}$	0.24 fb	0.004 fb	$\ll 0.001$ fb	$\ll 0.001$ fb
$\chi_4^0 \chi_2^0 j j$	2.40 fb	0.066 fb	0.005 fb	0.003 fb
$\chi_4^0 \chi_2^0 j b/\bar{b}$	0.34 fb	0.003 fb	$\ll 0.001$ fb	$\ll 0.001$ fb
$\chi_2^+ \chi_2^0 j j$	1.97 fb	0.061 fb	0.005 fb	0.002 fb
$\chi_2^+ \chi_2^0 j b/\bar{b}$	0.06 fb	< 0.001 fb	$\ll 0.001$ fb	$\ll 0.001$ fb
$\chi_2^- \chi_2^0 j j$	1.83 fb	0.041 fb	0.004 fb	0.002 fb
$\chi_2^- \chi_2^0 j b/\bar{b}$	0.04 fb	< 0.001 fb	$\ll 0.001$ fb	$\ll 0.001$ fb
$\chi_2^+ \chi_1^0 j j$	0.68 fb	0.013 fb	< 0.001 fb	< 0.001 fb
$\chi_2^+ \chi_1^0 j b/\bar{b}$	0.01 fb	$\ll 0.001$ fb	$\ll 0.001$ fb	$\ll 0.001$ fb
$\Sigma$ further processes	169.3 fb	4.59 fb	0.207 fb	< 0.048 fb

Table 3.6: Total cross sections of further SUSY background processes to the VBF  $h \rightarrow WW$  channel for the scenario SPS1amod.

- The processes with two jets at matrix element level, but with other chargino and neutralino combinations than the processes from Table 3.5, form the third process class present in Table 3.6.

The heavier charginos and neutralinos in this process class lead to much smaller production cross sections compared to the other processes. In addition, their branching ratios into particles relevant for the  $h \rightarrow WW$  process in VBF are substantially smaller compared to the branching ratios of the light chargino and the next-to-lightest neutralino.

### 3.4.2 SUSY Background in a Scenario with a Heavier Higgs Boson (Scenario SPS1amod2)

After discussing the SUSY background contribution in the VBF  $h \rightarrow WW$  channel for the base scenario SPS1amod, the effect of several modifications to this scenario will be reviewed in the following subsections.

The scenario SPS1amod2 has been designed with the goal of achieving a heavier Higgs boson mass of  $m_h \approx 124$  GeV with as few modifications as possible with respect to SPS1amod, which features  $m_h \approx 118$  GeV. Table 3.7 lists the cross sections of the dominant SUSY processes and the  $h \rightarrow WW$  signal. The change of the SUSY breaking parameters  $M_{q3L}$ ,  $M_{tR}$  and  $A_t$  with respect to SPS1amod modifies the stop sector, which has a big influence on  $m_h$ , but leaves the other SUSY masses and branching ratios almost unchanged. Therefore at production level the cross sections for the processes without contributions from stops or sbottoms are nearly unaffected. However, due to higher-order corrections the masses and branching ratios of the other SUSY particles can also change slightly. The next-to-lightest neutralino for example decays slightly more often into a stau than for SPS1amod. Due to the additional tau decay compared to a direct neutralino decay into selectrons or smuons, the contributions from processes with a next-to-lightest neutralino slightly decrease. On the other hand, the processes  $\chi_1^+ \chi_1^- jj$  and  $\tilde{\ell}^+ \tilde{\ell}^- jj$  are not affected by the scenario changes since the relevant branching ratios remain the same. The b-quark contribution to chargino production is drastically reduced, as the main part here arises from  $\tilde{t}_1 \tilde{t}_1$  production and the  $\tilde{t}_1$  mass almost doubles. Finally, the b-quark contribution to the neutralino processes is not affected that much, given that the  $\tilde{b}_1$  mass does not change as much as the  $\tilde{t}_1$  mass. Additionally, the squark-induced part is not as large as for the chargino process.

In summary, the total SUSY process contribution is a bit reduced with respect to the SPS1amod scenario. The  $h \rightarrow WW$  signal on the other hand benefits from the larger Higgs boson mass and increases by more than 60%. Therefore the signal to background ratio with all cuts improves from  $S/B^{SUSY} = 1.9$  (SPS1amod) to

$$S/B^{SUSY} = 3.6 \tag{3.49}$$

in the scenario SPS1amod2.

Processes	basic + rapidity	+ $m_{inv}, \cancel{p}_T, \phi_{\ell\ell},$	+ CJV on $j_{decay}$
	gap cuts	$M_T(WW),$ b-tag	
	Eqs. (3.39), (3.40)	+ (3.41), (3.43)–(3.45)	+ (3.46)
$\chi_1^+ \chi_1^- j j$	1.20 fb	0.069 fb	0.069 fb
$\chi_1^+ \chi_1^- j b/\bar{b}$	0.053 fb	0.004 fb	0.004 fb
$\chi_2^0 \chi_1^0 j j$	0.85 fb	0.071 fb	0.071 fb
$\chi_2^0 \chi_1^0 j b/\bar{b}$	0.196 fb	0.009 fb	0.009 fb
$\tilde{\ell}^+ \tilde{\ell}^- j j$	1.26 fb	0.028 fb	0.028 fb
$\chi_1^+ \chi_2^0 j j$	3.46 fb	0.361 fb	0.241 fb
$\chi_1^- \chi_2^0 j j$	1.88 fb	0.197 fb	0.125 fb
$\chi_2^0 \chi_2^0 j j$	1.24 fb	0.156 fb	0.063 fb
$\chi_2^0 \chi_2^0 j b/\bar{b}$	0.104 fb	0.007 fb	0.004 fb
$\Sigma B^{SUSY}$	10.24 fb	0.902 fb	0.614 fb
VBF $h \rightarrow WW$	4.96 fb	2.19 fb	2.19 fb
$S/B^{SUSY}$	0.48	2.4	3.6

Table 3.7: Total cross sections of the SUSY background contributions dominant at low squark masses and the VBF  $h \rightarrow WW$  signal for the scenario with a higher Higgs boson mass SPS1amod2.

### 3.4.3 Sparticle Mass Dependence

A very important aspect of MSSM scenarios are the masses of squarks and gluinos, as the sensitivity of a proton-proton collider on colored particles is much better than on weakly coupled particles. Therefore the first question addressed in this section is the SUSY background dependence on the masses of the squarks of the first two generations. It has already been mentioned in Section 3.2.1, that the gluino mass will be changed accordingly to the squark masses, in order to keep the characteristics of the original scenario. Otherwise, if the gluino mass would be lighter than the squarks, with  $m_{\tilde{g}} < m_{\tilde{q}} - m_q$ , the squark decay channel  $\tilde{q} \rightarrow q\tilde{g}$  would open up, leading to final states with less contribution to the VBF Higgs boson production signature. As the third generation squarks have a quite different phenomenology than the squarks of the first two generations, and in addition influence only the b-quark contributions, their mass dependence is studied separately. Finally, the scenario SPS1a-slope will be studied, which has SUSY particles which are in general about 30% heavier than in the scenario SPS1amod. For the sparticle mass dependence the dominant SUSY processes identified in the last section will be discussed.

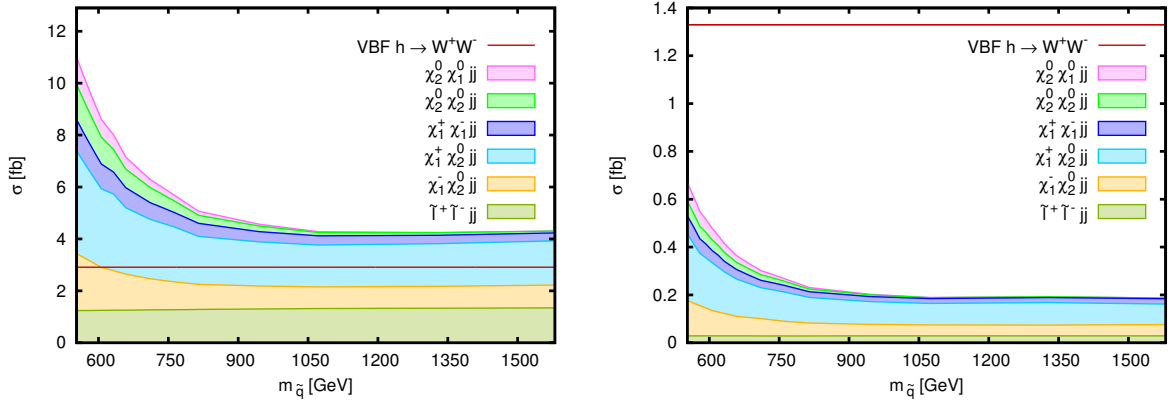


Figure 3.16: Squark and gluino mass dependence for the SUSY-background as a function of the average squark mass without b-quark contributions. Left panel: with cuts from Eqs. (3.39) + (3.40). Right panel: with additional cuts from Eqs. (3.41), (3.43), (3.44) and (3.46).

### 3.4.3.1 Squark and Gluino Mass Dependence

Modifying the SUSY breaking parameters dominantly contributing to the squark and gluino masses as described in Section 3.2.1 leads to average squark masses between  $m_{\tilde{q}} = 553$  GeV and  $m_{\tilde{q}} = 1581$  GeV. The gluino masses are always a few per-cent larger than the squark masses. Those changes mostly influence the non-b-quark contributions, which are depicted in Figure 3.16 for two different sets of cuts. The left plot takes into account only the basic cuts from Eq. (3.39) and the rapidity gap cuts from Eq. (3.40), while the right plot is done for all analysis cuts, except for the b-quark veto, which has no effect here.

Starting from  $m_{\tilde{q}} \approx 550$  GeV, a strong suppression of the background contribution can be seen, especially for the processes containing two neutralinos. These are the processes which largely contain squark pair production as primary production mechanism. Especially for  $\chi_2^0 \chi_1^0 j j$ , even at high squark masses, the dominant production process is via squark pair production with the exchange of a t-channel gluino. This production mode therefore depends both on the squark mass and on the gluino mass. It has been checked both for the  $\mathcal{O}(\alpha_s^2 \alpha^2)$  approximation described in Section 3.3.2 and for the full process, that this production mode is dominant at low and high squark / gluino masses.

The processes involving charginos have a non-negligible contribution with charginos and neutralinos being produced via the decay of a virtual vector boson. As these contributions are independent of squark and gluino masses, their cross sections do not decrease as fast with rising squark/gluino masses, and from roughly  $m_{\tilde{q}} \approx 1$  TeV on the squark contributions are dominated by the other production modes, leading to no further squark mass dependence at higher values.

The slepton processes, finally, do not involve any squarks and gluinos and are therefore not affected by their mass variation, except for very small effects due to higher-order

Processes	basic + rapidity gap cuts Eqs. (3.39), (3.40)	+ $m_{inv}, \cancel{p}_T, \phi_{\ell\ell},$ $M_T(WW)$ , b-tag + (3.41), (3.43)–(3.45)	+ CJV on $j_{decay}$ + (3.46)
$\chi_1^+ \chi_1^- j j$	0.353 fb	0.020 fb	0.020 fb
$\chi_1^+ \chi_1^- j b/\bar{b}$	0.227 fb	0.010 fb	0.010 fb
$\chi_2^0 \chi_1^0 j j$	0.032 fb	0.001 fb	0.001 fb
$\chi_2^0 \chi_1^0 j b/\bar{b}$	0.228 fb	0.010 fb	0.010 fb
$\tilde{\ell}^+ \tilde{\ell}^- j j$	1.311 fb	0.028 fb	0.028 fb
$\chi_1^+ \chi_2^0 j j$	1.611 fb	0.122 fb	0.090 fb
$\chi_1^- \chi_2^0 j j$	0.836 fb	0.061 fb	0.046 fb
$\chi_2^0 \chi_2^0 j j$	0.128 fb	0.011 fb	0.004 fb
$\chi_2^0 \chi_2^0 j b/\bar{b}$	0.137 fb	0.008 fb	0.004 fb
$\sum B^{SUSY}$	4.86 fb	0.271 fb	0.213 fb
VBF $h \rightarrow WW$	2.91 fb	1.32 fb	1.32 fb
$S/B^{SUSY}$	0.60	4.9	6.2

Table 3.8: Total cross sections of the SUSY background contributions dominant at low squark masses and the VBF  $h \rightarrow WW$  signal for average squark masses of 1.1 TeV.

Processes	basic + rapidity gap cuts Eqs. (3.39),(3.40)	+ $m_{inv}, \cancel{p}_T, \phi_{\ell\ell},$ $M_T(WW)$ , b-tag + (3.41),(3.43)–(3.45)	+ CJV on $j_{decay}$ + (3.46)
$\chi_1^+ \chi_2^0 j$	0.350 fb	0.013 fb	0.012 fb
$\chi_1^- \chi_2^0 j$	0.168 fb	0.004 fb	0.004 fb
$\chi_2^0 \chi_2^0 j$	0.012 fb	0.001 fb	< 0.001 fb
$\tilde{g} \chi_1^0 j j$	0.038 fb	0.001 fb	< 0.001 fb
$\tilde{g} \chi_1^0 j$	0.008 fb	$\ll$ 0.001 fb	$\ll$ 0.001 fb
$\chi_1^+ \chi_2^- j j$	0.016 fb	< 0.001 fb	< 0.001 fb
$\chi_1^- \chi_2^+ j j$	0.015 fb	< 0.001 fb	< 0.001 fb
$\chi_4^0 \chi_2^0 j j$	0.013 fb	< 0.001 fb	< 0.001 fb
$\chi_2^+ \chi_2^0 j j$	0.012 fb	< 0.001 fb	$\ll$ 0.001 fb
$\chi_2^- \chi_2^0 j j$	0.007 fb	< 0.001 fb	$\ll$ 0.001 fb
$\sum$ further processes	0.639 fb	< 0.024 fb	< 0.021 fb

Table 3.9: Total cross sections of further SUSY background processes to the VBF  $h \rightarrow WW$  channel for average squark masses of 1.1 TeV.

corrections in the SUSY particle mass and branching ratio calculations. The same holds also for the Higgs boson production process: as the squark masses of the first two generations have almost no effect on the Higgs boson mass, the signal cross section remains unchanged with respect to the scenario SPS1amod. The VBF  $h \rightarrow WW$  cross sections are  $\sigma = 2.91$  fb for the cuts of the left plot in Figure 3.16 and  $\sigma = 1.33$  fb for the settings used in the right plot.

For average squark masses of 1.1 TeV (corresponding to  $\xi = 1.0$ , see Section 3.2.1) it has been checked, whether the processes dominating at small squark masses still give the largest contributions to the SUSY background at higher masses. The cross sections for this mass configuration of the dominant SUSY contributions from Table 3.5 are listed in Table 3.8. The cross sections of all additional processes from Table 3.6 with not completely negligible cross sections at low squark masses are listed in Table 3.9. Most of the processes in the latter table also show a reduced cross section with respect to the results at lower squark masses. The only exception is for  $\chi_1^\pm \chi_2^0 j$ , which has a somewhat larger cross section at high squark masses than in the scenario SPS1amod. This is due to interference effects between graphs with and without squarks. But still, the processes from Table 3.9 add only a few per-cent to the SUSY background for the  $h \rightarrow WW$  channel in VBF.

To summarize, for higher squark and gluino masses the process  $\chi_1^\pm \chi_2^0 j j$  gives the largest contribution to the SUSY background, with a total signal to SUSY background ratio of

$$S/B^{SUSY} = 6.2 \quad (3.50)$$

for average squark masses of 1.1 TeV. Increasing the squark masses to even higher values while keeping the electroweak gaugino and slepton masses light hardly changes anything.

### 3.4.3.2 Stop/Sbottom Mass Dependence of b-Quark Contributions

The masses of the first two squark generations are not important for the b-quark contributions to the SUSY background. Instead, they include stops and sbottoms as intermediate particles and therefore they show a dependence on their mass. Again, the relevant SUSY breaking parameters have been varied as described in Section 3.2.1. The resulting light stop masses vary between  $m_{\tilde{t}_1} = 346$  GeV and  $m_{\tilde{t}_1} = 768$  GeV, while the light sbottom masses start at  $m_{\tilde{b}_1} = 518$  GeV and reach up to  $m_{\tilde{b}_1} = 1003$  GeV.

Since the b-quark contributions to chargino pair production are dominated by  $\tilde{t}_1$  pair production as primary process, they exhibit a quite strong dependence on the stop mass variation. This mass dependence is depicted in Figure 3.17. However, small contributions from the production of heavy Higgs bosons with a subsequent decay into charginos exist as well. Therefore a small chargino contribution remains even at high stop masses. The minor increase in the cross section at low stop mass values in the right plot of Figure 3.17 is due to the applied  $m_{jj}$  cut, which cuts away a smaller cross section fraction for larger stop masses.

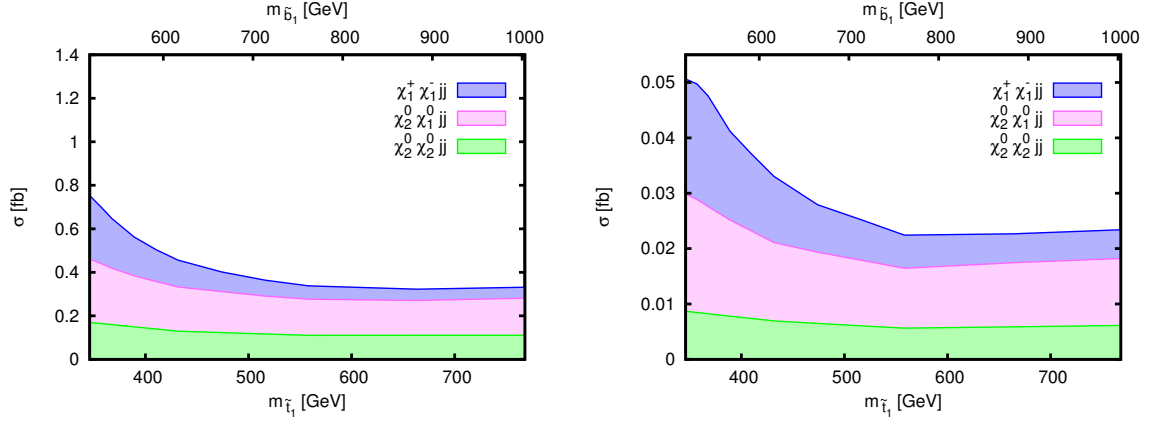


Figure 3.17: Third generation squark mass dependencies for the b-quark contributions of the SUSY-background processes as a function of the  $\tilde{t}_1$ -mass. Left panel: with cuts from Eqs. (3.39) + (3.40). Right panel: with additional cuts from Eqs. (3.41), (3.43), (3.44) and (3.46).

The next-to-lightest neutralino plus lightest neutralino production has a smaller contribution from squarks, with  $\tilde{b}_1$  being the relevant squark for this process. Several reasons for the small squark contribution have been given in Section 3.2.3. These minor  $\tilde{b}_1$  contributions become completely negligible at high  $\tilde{b}_1$  masses, where only the contributions from heavy Higgs boson decays into neutralinos remain. Starting at  $m_{\tilde{b}_1} \approx 750$  GeV, after a significant cross section reduction, the contribution from  $\chi_2^0 \chi_1^0 j j$  starts to slowly grow again. This is due to minor changes in the masses and branching ratios of the heavy Higgs bosons and the next-to-lightest neutralino.

The mass dependence of the b-quark contributions to  $\chi_2^0 \chi_2^0 j j$  is very similar to  $\chi_2^0 \chi_1^0 j b/\bar{b}$ , given that the same Feynman graph topologies lead to relevant contributions in both processes.

In contrast to the mass dependence of first and second generation squarks, the stop mass variation has a sizable influence on the Higgs boson mass. It increases from  $m_h = 118$  GeV for  $m_{\tilde{t}_1} = 346$  GeV up to  $m_h = 123$  GeV for  $m_{\tilde{t}_1} = 768$  GeV. Due to the larger  $h \rightarrow WW$  branching ratio at higher Higgs boson masses, this leads to higher cross sections for the VBF  $h \rightarrow WW$  channel. At low stop masses the cross section for the final set of cuts accounts for  $\sigma = 1.33$  fb, while for high stop masses the cross section is  $\sigma = 1.98$  fb.

### 3.4.3.3 Scenario SPS1a-slope

So far, only the dependence on the squark mass variation has been checked. In order to test the effect of overall larger SUSY particle masses, the SUSY background processes have been calculated for the scenario SPS1a-slope (see Section 3.2.1). This scenario features SUSY particle masses, which are generally 30% larger than the masses in the base scenario. The cross sections for the scenario SPS1a-slope are listed in Table 3.10.

Processes	basic + rapidity gap cuts Eqs. (3.39), (3.40)	+ $m_{inv}, \cancel{p}_T, \phi_{\ell\ell},$ $M_T(WW)$ , b-tag + (3.41), (3.43)–(3.45)	+ CJV on $j_{decay}$ + (3.46)
$\chi_1^+ \chi_1^- j j$	0.60 fb	0.032 fb	0.032 fb
$\chi_1^+ \chi_1^- j b/\bar{b}$	0.03 fb	0.002 fb	0.002 fb
$\chi_2^0 \chi_1^0 j j$	0.25 fb	0.013 fb	0.013 fb
$\chi_2^0 \chi_1^0 j b/\bar{b}$	0.03 fb	0.001 fb	0.001 fb
$\tilde{\ell}^+ \tilde{\ell}^- j j$	0.81 fb	0.010 fb	0.010 fb
$\chi_1^+ \chi_2^0 j j$	1.12 fb	0.069 fb	0.039 fb
$\chi_1^- \chi_2^0 j j$	0.58 fb	0.040 fb	0.023 fb
$\chi_2^0 \chi_2^0 j j$	0.39 fb	0.027 fb	0.011 fb
$\chi_2^0 \chi_2^0 j b/\bar{b}$	0.03 fb	0.001 fb	0.001 fb
$\sum B^{SUSY}$	3.84 fb	0.195 fb	0.132 fb
VBF $h \rightarrow WW$	5.32 fb	2.37 fb	2.37 fb
$S/B^{SUSY}$	1.4	12	18

Table 3.10: Total cross sections of the SUSY background processes dominant at low squark masses and the VBF  $h \rightarrow WW$  signal for the scenario SPS1a-slope.

They should be compared to the results for the scenario SPS1amod2 (see Table 3.7), given that the same steps have been performed to increase the Higgs boson mass.

The SUSY process results in this scenario are as expected: the cross sections are much smaller compared to the case where only the squark masses have been increased. While increasing the first and second generation squark masses by 30% in the last chapter gave a reduction of the non-b-contributions by roughly 55% (excluding the slepton contribution, which is not affected by the squark mass variation), the total cross section of these processes decreases by roughly 80% for higher squark, chargino, and neutralino masses. Additionally, the slepton contributions suffer from the increased slepton masses, giving slepton process cross sections which are roughly 65% smaller than in the scenario SPS1amod2. Finally, the Higgs boson masses in SPS1a-slope and SPS1amod2 are very similar: they differ only by 0.1 GeV, which is clearly not significant. Therefore, the  $h \rightarrow WW$  partial widths are very much alike, their difference is less than 1%. Still, the  $h \rightarrow WW$  branching ratio is 15% instead of 14% for SPS1amod2, due to smaller  $h \rightarrow f\bar{f}$  partial widths. This leads to an increase in the signal cross section of a few per cent.

In total, the signal to background ratio increases strongly, from  $S/B^{SUSY} = 3.6$  for the scenario SPS1amod2, to

$$S/B^{SUSY} = 18 \quad (3.51)$$

for the scenario SPS1a-slope.

### 3.4.4 Scenario with an Inverted Slepton Hierarchy

The sleptons play a key role in the decay of the light chargino and the next-to-lightest neutralino. In many (mSUGRA) MSSM scenarios, and also in the modified SPS1a-like scenarios, the lightest slepton is one of the tau sleptons, due to the large mixing in the third generation. Therefore, a large fraction of  $\chi_1^\pm$  and  $\chi_2^0$  decays via tau sleptons, and a large fraction of the electrons and muons from SUSY processes arises from a  $\tilde{\tau}^\pm \rightarrow \tau^\pm \chi_1^0 \rightarrow e^\pm/\mu^\pm \nu \bar{\nu}' \chi_1^0$  decay. Thus, a leptonic tau decay is involved, which has a fairly low branching ratio of  $BR \approx 0.35$ . Larger effects from SUSY particles to the background for the  $h \rightarrow WW$  channel in VBF can be expected in scenarios where selectrons and smuons are the dominant chargino and next-to-lightest neutralino decay channels. Such scenarios will be discussed in the following.

#### 3.4.4.1 Squark / Gluino Masses like in SPS1amod

The first “light sleptons” scenario discussed features SUSY particle masses comparable to the ones of the scenario SPS1amod, except for the sleptons and the sneutrinos. The staus have been chosen heavier than the chargino and the next-to-lightest neutralino, while the masses of the left-handed selectrons and smuons have been lowered, taking roughly the same masses as their right-handed counterparts. The masses of the left-handed sleptons are correlated with the sneutrino masses. Therefore these changes also lead to lighter sneutrinos, which now have masses significantly below the chargino/next-to-lightest neutralino masses as well. The modifications have been carried out by changing the soft SUSY breaking mass terms. As all SUSY masses except for the slepton masses remain unchanged, the  $h \rightarrow WW$  signal process remains unaffected by the changes. More details on this “light sleptons” scenario can be found in Section 3.2.1.

In this scenario, 100% of the charginos decay to a lepton, neutrino and the LSP

$$\chi_1^\pm \rightarrow \left\{ \begin{array}{l} \tilde{\ell}^\pm \nu_\ell \\ \tilde{\nu}_\ell \ell^\pm \end{array} \right\} \rightarrow \ell^\pm \nu_\ell \chi_1^0, \quad (3.52)$$

either via a slepton or a sneutrino. With chargino masses of 180 GeV, slepton masses of about 142 GeV, sneutrino masses of 119 GeV and an LSP mass of 97 GeV, there is a reasonable amount of kinetic energy available for the lepton in both decay chains. For the next-to-lightest neutralino decay the branching ratio of decays leading to direct electron and muon production, without a tau lepton involved, increases as well with respect to the scenario SPS1amod. However, more than 60% of the next-to-lightest neutralinos decay completely invisibly into a sneutrino and a neutrino, due to the light sneutrino masses. As the sneutrino itself always decays invisibly into a neutrino and the LSP, this leads to no visible particles at all

$$\chi_2^0 \rightarrow \left\{ \begin{array}{l} \tilde{\ell}^\pm \ell^\mp \rightarrow \ell^\pm \ell^\mp \chi_1^0 \\ \tilde{\nu}_\ell \bar{\nu}_\ell \rightarrow \nu_\ell \bar{\nu}_\ell \chi_1^0 \end{array} \right\}. \quad (3.53)$$

More details on the branching ratios in the “light sleptons” scenario can be found in Appendix A.

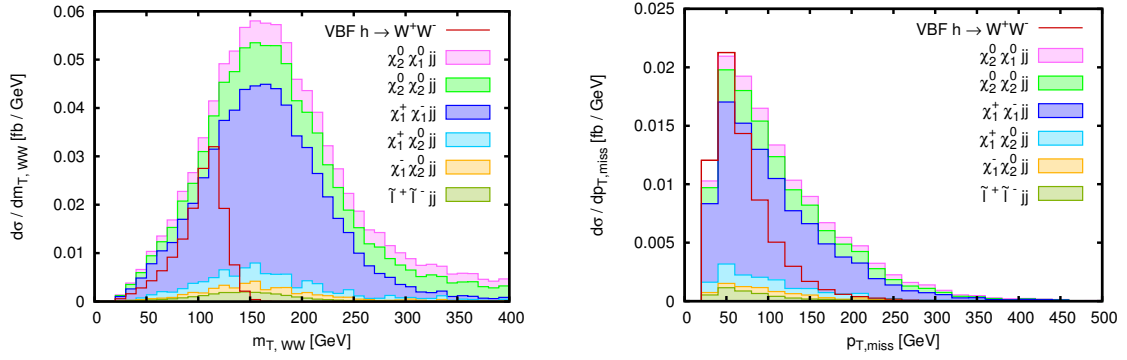


Figure 3.18: Distributions of  $m_T(WW)$  and  $\cancel{p}_T$  analogous to Fig. 3.12, but for the “light sleptons” scenario, including reducible SUSY background processes and relevant b-quark contributions. The cuts from Eqs. (3.39)–(3.41) and (3.43) have been applied.

The irreducible background processes shall be discussed first. The production cross sections for the processes with an electroweak gaugino pair plus jets remain unchanged with respect to the scenario SPS1amod. The effect on the decays of these SUSY particles on the other hand is very large. For the chargino process  $\chi_1^+ \chi_1^- jj$  including decays, but without any lepton cuts, the cross section increases by a factor of 8.3, which roughly equals  $\frac{1}{BR(\tau \rightarrow \ell \bar{\nu}_\ell \nu_\tau)^2}$ . Therefore the increase in the cross section arises indeed from the suppression of the leptonic tau decay. The  $\chi_2^0 \chi_1^0 jj$  cross section receives a much smaller enhancement, due to the large fraction of invisible  $\chi_2^0$  decays. The cross section for this process rises by a factor of 1.6 before taking into account lepton cuts. The combined production cross section of all slepton processes increases only slightly. However, the shares of the individual channels change significantly: the production of  $\tilde{e}_L$  and  $\tilde{\mu}_L$  pairs increases, while the cross section for the stau lepton pair production decreases significantly. Including decays, the cross section is roughly a factor of two larger than for the scenario SPS1amod, given that the sleptons of the first two generations now always decay into an electron or muon and that the staus play a minor role here.

With the new decay channels the kinematics and therefore the distributions change as well. This also results in different cut efficiencies. The directly produced electrons and muons in the chargino and next-to-lightest neutralino processes have larger transverse momenta and therefore a much bigger fraction of the events passes the basic cuts. On the other hand, the reconstructed transverse  $WW$  mass tends to be significantly higher, therefore the  $m_T(WW)$  cut is more efficient here. Finally, the cut on the missing transverse momentum does not reduce the SUSY contribution as much as in the scenario SPS1amod, since there are less invisible particles in the final state and the average missing transverse momentum in an event is therefore lower. The  $m_T(WW)$  and  $\cancel{p}_T$  distributions are shown in Figure 3.18. Altogether, the chargino contributions to the SUSY background with all cuts increase by a factor of 15 in the “light sleptons” scenario. The increase for the slepton processes is smaller, about a factor of three, and the next-to-lightest neutralino process increases by only roughly 30%.

At production level, the situation is similar for the reducible background processes: their cross sections hardly change. The effect on the decay and the resulting distribu-

Processes	basic + rapidity gap cuts Eqs. (3.39), (3.40)	+ $m_{inv}, \cancel{p}_T, \phi_{\ell\ell},$ $M_T(WW)$ , b-tag + (3.41), (3.43)–(3.45)	+ CJV on $j_{decay}$ + (3.46)
$\chi_1^+ \chi_1^- j j$	36.0 fb	1.09 fb	1.09 fb
$\chi_1^+ \chi_1^- j b/\bar{b}$	12.5 fb	0.14 fb	0.14 fb
$\chi_2^0 \chi_1^0 j j$	2.38 fb	0.103 fb	0.103 fb
$\chi_2^0 \chi_1^0 j b/\bar{b}$	0.72 fb	0.020 fb	0.020 fb
$\tilde{\ell}^+ \tilde{\ell}^- j j$	2.77 fb	0.082 fb	0.082 fb
$\chi_1^+ \chi_2^0 j j$	2.00 fb	0.133 fb	0.133 fb
$\chi_1^- \chi_2^0 j j$	0.97 fb	0.052 fb	0.051 fb
$\chi_2^0 \chi_2^0 j j$	4.92 fb	0.267 fb	0.267 fb
$\chi_2^0 \chi_2^0 j b/\bar{b}$	0.59 fb	0.023 fb	0.023 fb
$\Sigma B^{SUSY}$	62.9 fb	1.91 fb	1.91 fb
VBF $h \rightarrow WW$	2.91 fb	1.32 fb	1.32 fb
$S/B^{SUSY}$	0.046	0.69	0.69

Table 3.11: Total cross sections of the SUSY background processes dominant at low squark masses and the VBF  $h \rightarrow WW$  signal for the scenario with light sleptons.

tions on the other hand is very different. The soft jets from hadronic tau decays and the additional soft leptons from leptonic tau decays have been replaced by additional hard electrons and muons. While the tau decay products can be easily missed in the detector, the hard leptons can be observed very well. The class of processes which needs a tagging jet from a hadronic tau lepton or W boson (all processes with zero or one jet at production level) does not contribute to the SUSY background in the light slepton scenario, as these processes do not lead to two jets in the final state. The veto on additional jets from a heavy particle decay has no effect as well, given that there are no such jets. The process  $\chi_1^\pm \chi_2^0 j j$ , which is the largest contribution in the SPS1amod case is significantly reduced due to the additional hard leptons in the final state. The only process of the reducible background class which amounts to a significantly larger contribution in the “light sleptons” scenario is  $\chi_2^0 \chi_2^0 j j$  production. The fraction of events in which one of the neutralinos decays into two hard leptons, while the other one decays invisibly, leading to the requested two hard leptons in the final state, is quite large (almost 50%). For these events there are no additional visible particles which could be vetoed. Therefore the cross section rises by a factor of 4.5 with respect to the scenario SPS1amod.

In total, the signal to SUSY background ratio for the  $h \rightarrow WW$  channel is

$$S/B^{SUSY} = 0.69, \quad (3.54)$$

which is much smaller than the ratio  $S/B^{SUSY} = 1.9$  obtained in the scenario SPS1amod. All relevant cross sections can be found in Table 3.11.

Processes	basic + rapidity gap cuts Eqs. (3.39), (3.40)	+ $m_{inv}, \cancel{p}_T, \phi_{\ell\ell},$ $M_T(WW)$ , b-tag + (3.41), (3.43)–(3.45)	+ CJV on $j_{decay}$ + (3.46)
$\chi_1^+ \chi_1^- j j$	11.79 fb	0.266 fb	0.266 fb
$\chi_1^+ \chi_1^- j b/\bar{b}$	2.43 fb	0.040 fb	0.040 fb
$\chi_2^0 \chi_1^0 j j$	0.069 fb	0.001 fb	0.001 fb
$\chi_2^0 \chi_1^0 j b/\bar{b}$	0.473 fb	0.011 fb	0.011 fb
$\tilde{\ell}^+ \tilde{\ell}^- j j$	2.78 fb	0.086 fb	0.086 fb
$\chi_1^+ \chi_2^0 j j$	1.08 fb	0.058 fb	0.058 fb
$\chi_1^- \chi_2^0 j j$	0.47 fb	0.019 fb	0.019 fb
$\chi_2^0 \chi_2^0 j j$	0.48 fb	0.018 fb	0.018 fb
$\chi_2^0 \chi_2^0 j b/\bar{b}$	0.40 fb	0.014 fb	0.014 fb
$\sum B^{SUSY}$	19.97 fb	0.513 fb	0.513 fb
VBF $h \rightarrow WW$	4.50 fb	2.00 fb	2.00 fb
$S/B^{SUSY}$	0.23	3.9	3.9

Table 3.12: Total cross sections of the SUSY background processes dominant at low squark masses and the VBF  $h \rightarrow WW$  signal for the scenario with light sleptons but higher squark and gluino masses.

### 3.4.4.2 Higher Squark and Gluino Masses

The “light sleptons” scenario discussed in the last subsection showed that restricting the chargino and next-to-lightest neutralino decay channels by making the decay into a tau slepton kinematically unavailable can increase the SUSY contributions to the  $h \rightarrow WW$  background significantly. However, the squark and gluino masses have been chosen very light in that discussion.

Table 3.12 shows the cross sections for the dominant SUSY contributions in the “light sleptons with high  $m_{\tilde{q}}, m_{\tilde{g}}$ ” scenario. This scenario features higher squark masses for all three squark generations, with an average first and second generation squark mass of  $m_{\tilde{q}} \approx 1.1$  TeV, a light stop mass of  $m_{\tilde{t}_1} \approx 0.77$  TeV and a gluino mass of  $m_{\tilde{g}} \approx 1.2$  TeV. The larger stop mass leads also to a larger Higgs boson mass of  $m_h = 123$  GeV. This increases the  $h \rightarrow WW$  cross sections by roughly 50%, while the processes with charginos and neutralinos are reduced by a factor of at least two with respect to the low-squark-mass scenario. This behavior is expected considering the results from Section 3.4.3. Therefore the signal to SUSY background ratio increases significantly, yielding

$$S/B^{SUSY} = 3.9 \quad (3.55)$$

in the “light sleptons with high  $m_{\tilde{q}}, m_{\tilde{g}}$ ” scenario.

## 3.5 LHC Results for the $h \rightarrow \tau\tau$ Channel at 14 TeV

After discussing the SUSY background processes to the  $h \rightarrow WW$  channel in detail, this section focuses on the  $h \rightarrow \tau\tau$  signal process in VBF. Several characteristics of the signal process discussed in the last section are features of the VBF production mechanism and independent of the Higgs decay channel, e.g. the large rapidity separation between the tagging jets or the large  $m_{jj}$  mass. These aspects will be repeated only very briefly. On the other hand, some other background suppression techniques mentioned are specific to the  $h \rightarrow WW$  channel, namely the small azimuthal angle difference between the decay leptons and the rather small  $m_{\ell\ell}$ . They arise from the Higgs boson being a spin-0 particle in combination with the  $V - A$  coupling structure of the  $W$  boson. The latter is not present in the  $h \rightarrow \tau\tau$  case, therefore these two observables are not very powerful concerning background suppression.

Luckily, the  $h \rightarrow \tau\tau$  channel additionally has a feature which is missing in the  $h \rightarrow WW$  case: due to the small tau lepton mass it is possible to reconstruct the invariant Higgs boson mass, which will turn out to be a very powerful handle on the SUSY background processes.

In the following, the SUSY background processes to the  $h \rightarrow \tau\tau$  channel will be discussed for the base scenario SPS1amod and for the scenario which turned out to result in the largest contributions in the  $h \rightarrow WW$  case, the “light sleptons” scenario. The mass dependence will not be studied in detail, as the background will turn out to be very small already in the extremely conservative scenario SPS1amod. This is due to the possible Higgs boson mass reconstruction. However, the scenario with light sleptons and higher squark and gluino masses will be reviewed briefly for the 14 TeV LHC run in this section and for the 7 TeV LHC run in Section 3.6. The cuts used for SM background reduction are loosely based on the analysis in Ref. [102].

### 3.5.1 SPS1a-like Scenario

The first scenario in which the SUSY background to  $h \rightarrow \tau\tau$  is examined is the base scenario SPS1amod, which features very light squark masses and is very close to the mSUGRA scenario SPS1a. With the basic cuts

$$\begin{aligned}
 p_{T,j} &\geq 20 \text{ GeV} & p_{T,\ell} &\geq 10 \text{ GeV} \\
 |\eta_j| &\leq 4.5 & |\eta_\ell| &\leq 2.5 \\
 R_{jj} &\geq 0.8 & R_{\ell\ell} &\geq 0.6 \\
 R_{j\ell} &\geq 0.8, & &
 \end{aligned}
 \tag{3.56}$$

which mostly account for detector geometry and particle identification, the size of the SUSY background is very similar to the  $h \rightarrow WW$  channel: the SUSY background processes have much larger cross sections than the signal process, yielding

$$S/B^{SUSY} = 0.015 \tag{3.57}$$

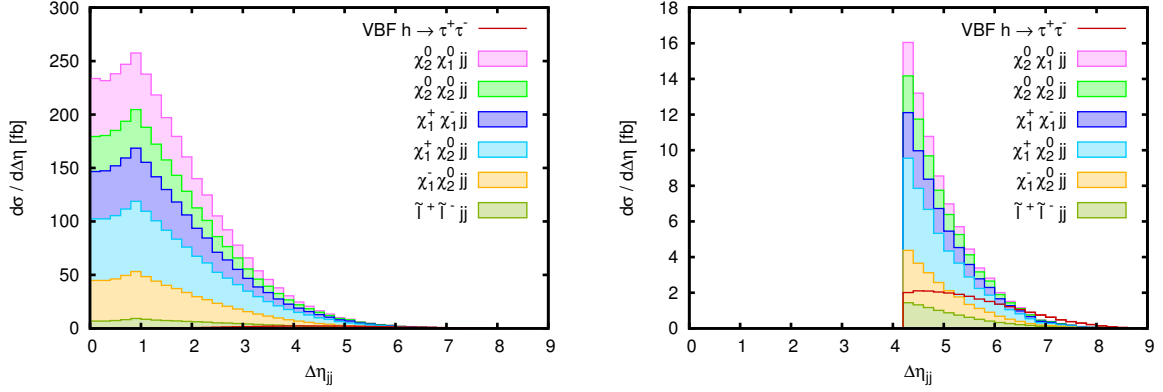


Figure 3.19: Rapidity separation for the dominant SUSY background contributions and the  $h \rightarrow \tau\tau$  signal with basic cuts, Eq. (3.56), (left) and additional  $\Delta\eta$  plus “leptons inside rapidity gap” cuts, Eq. (3.58) (right).

Processes	basic cuts Eq. (3.56)	+ rap. gap + (3.58)	+ $m_{inv},$ $p_T^{\min}$ + (3.59)	+ $m_{\tau\tau}$ + (3.64)	+ fake $\cancel{E}_T$ + (3.32)	+ CJV on $j_{decay}$ + (3.46)
$\chi_1^+ \chi_1^- j j$	64.13 fb	2.04 fb	1.35 fb	0.024 fb	0.025 fb	0.025 fb
$\chi_1^+ \chi_1^- j b/\bar{b}$	52.53 fb	0.46 fb	0.095 fb	0.002 fb	0.003 fb	0.003 fb
$\chi_2^0 \chi_1^0 j j$	109.2 fb	1.09 fb	0.96 fb	0.015 fb	0.015 fb	0.015 fb
$\chi_2^0 \chi_1^0 j b/\bar{b}$	12.88 fb	0.37 fb	0.122 fb	0.003 fb	0.003 fb	0.003 fb
$\tilde{\ell}^+ \tilde{\ell}^- j j$	26.35 fb	1.89 fb	0.61 fb	0.003 fb	0.003 fb	0.003 fb
$\chi_1^+ \chi_2^0 j j$	163.8 fb	5.16 fb	3.60 fb	0.086 fb	0.089 fb	0.060 fb
$\chi_1^- \chi_2^0 j j$	104.4 fb	2.81 fb	1.90 fb	0.047 fb	0.046 fb	0.033 fb
$\chi_2^0 \chi_2^0 j j$	76.15 fb	1.76 fb	1.44 fb	0.037 fb	0.036 fb	0.016 fb
$\chi_2^0 \chi_2^0 j b/\bar{b}$	9.22 fb	0.23 fb	0.080 fb	0.002 fb	0.002 fb	0.001 fb
$\sum B^{SUSY}$	618.7 fb	15.82 fb	10.16 fb	0.219 fb	0.222 fb	0.159 fb
VBF $h \rightarrow \tau\tau$	9.17 fb	4.94 fb	2.67 fb	2.46 fb	1.93 fb	1.93 fb
$S/B^{SUSY}$	0.015	0.31	0.26	11	8.7	12
$\sum$ further proc. (see Table 3.6)	374.9 fb	6.41 fb	5.21 fb	0.119 fb	0.115 fb	< 0.016 fb

Table 3.13: Total cross sections for the SUSY contributions and the signal process VBF  $h \rightarrow \tau\tau$  at various cut levels for the scenario SPS1amod, with b-quark contributions where relevant.

for the dominant<sup>8</sup> SUSY background contributions. All cross sections for the dominant reducible and irreducible SUSY processes are listed in Table 3.13 at different cut levels. The overall contribution from the sub-dominant processes given in Table 3.6 in the  $h \rightarrow WW$  analysis is listed as well.

As already mentioned, the observables involving the two jets in the event are similar for both signal channels  $h \rightarrow WW$  and  $h \rightarrow \tau\tau$ , therefore the cuts on the rapidity separation

$$\Delta\eta_{jj} \geq 4.2 \quad \eta_{j1} \cdot \eta_{j2} < 0 \quad \eta_{j,min} \leq \eta_\ell \leq \eta_{j,max} \quad (3.58)$$

(the  $\Delta\eta_{jj}$  distribution with and without these cuts are depicted in Figure 3.19) are comparable in their efficiency for both cases and improve the ratio  $S/B^{SUSY}$  by a factor of 20. The  $m_{jj}$  and  $p_{T,j}$  distributions show a similar behavior to the  $h \rightarrow WW$  channel as well.

The applied cut on  $m_{jj}$  is a part of the typical VBF cuts. Like in the  $h \rightarrow WW$  case it particularly reduces the slepton part of the SUSY background contribution. Another cut which is applied is a cut on the minimal amount of missing transverse momentum:

$$\cancel{p}_T \geq 40 \text{ GeV} \quad m_{jj} \geq 700 \text{ GeV} . \quad (3.59)$$

This cut improves the mass resolution of the tau pair, i.e. the Higgs boson mass reconstruction, and additionally suppresses the SM background contributions without neutrinos in the final state, e.g. processes with  $Z \rightarrow \ell\ell$  [102]. The value for the  $m_{jj}$  cut has been taken from Ref. [102].

A very powerful feature of the  $h \rightarrow \tau\tau$  channel in VBF is the possibility to reconstruct the invariant tau pair mass,  $m_{\tau\tau}$ , from its decay products. This  $m_{\tau\tau}$  corresponds to the Higgs boson mass  $m_h$ , which leads to a sharp peak in the  $m_{\tau\tau}^{\text{rec}}$  distribution. As background processes with two leptons in the final state which do not arise from a decay chain

$$X \rightarrow \tau^+\tau^- \rightarrow \ell_1^+\ell_2^-\nu_\tau\bar{\nu}_\tau\nu_1\bar{\nu}_2 \quad (3.60)$$

usually give a very flat  $m_{\tau\tau}^{\text{rec}}$  distribution, this allows for a very efficient background reduction. One dominant SM background for the  $h \rightarrow \tau\tau$  channel,  $Z \rightarrow \tau\tau$ , results in the same decay chain Eq. (3.60) as the signal. But as the Z boson mass is at  $m_Z = 91.1876 \text{ GeV}$  and the LEP Higgs mass bound is  $m_h > 114.4 \text{ GeV}$ , a quite good separation of this background is possible [102]. For a Higgs mass around 125 GeV the separation is even better.

The main problem of the mass reconstruction in the  $h \rightarrow WW$  and  $h \rightarrow \tau\tau$  channels is the existence of invisible neutrinos in the final state. The sole available information on their existence is the amount of missing momentum in the two transverse coordinates. Due to momentum conservation this corresponds to the sum of the momenta of all invisible particles. But neither the individual  $p_x$  and  $p_y$  values of the invisible particles

---

<sup>8</sup>Processes are attributed “dominant”, if their part on the total SUSY background is not negligible, once all analysis cuts have been applied.

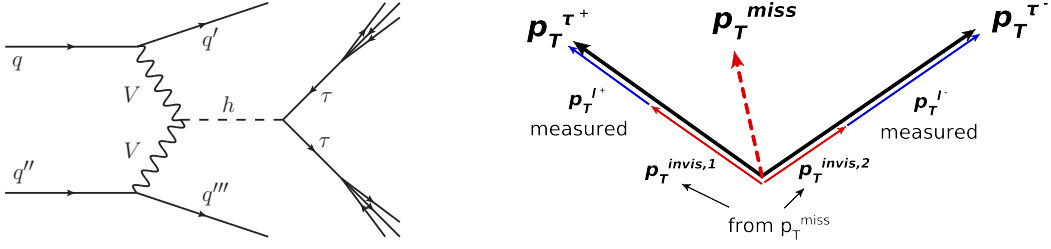


Figure 3.20: Sketch of the VBF  $h \rightarrow \tau\tau$  process (left) and geometrical approximation of the tau decay in the transverse plane (right).

nor any information on  $p_z$  is available. Therefore the mass reconstruction is not possible in the  $h \rightarrow WW$  case. For the  $h \rightarrow \tau\tau$  on the other hand a geometrical approximation is possible, given that the tau leptons being Higgs boson decay products are much lighter than the mother particle  $m_h \gg 2 \cdot m_\tau$ . This leads to highly boosted tau leptons, and to a good approximation the tau leptons and their decay products are collinear in the laboratory frame (sketched in the left part of Figure 3.20). Therefore the only unknown quantities are the tau momentum fractions carried by the visible leptons,  $x_\pm$ . As the signal process contains no invisible particles except for the neutrinos from the tau decay, this information can be obtained from a projection of the  $(\not{p}_x, \not{p}_y)$  vector onto the two vectors  $(p_x^{\ell^+}, p_y^{\ell^+})$  and  $(p_x^{\ell^-}, p_y^{\ell^-})$  of the visible leptons [102], as depicted in the right part of Figure 3.20:

$$\begin{aligned} x_+ &= \frac{p_T^{\ell^+}}{p_T^{\tau^+}} = \frac{p_x^{\ell^+} p_y^{\ell^-} - p_y^{\ell^+} p_x^{\ell^-}}{(p_x^{\ell^+} + \not{p}_x) p_y^{\ell^-} - (p_y^{\ell^+} + \not{p}_y) p_x^{\ell^-}} \\ x_- &= \frac{p_T^{\ell^-}}{p_T^{\tau^-}} = \frac{p_x^{\ell^+} p_y^{\ell^-} - p_y^{\ell^+} p_x^{\ell^-}}{(p_y^{\ell^-} + \not{p}_y) p_x^{\ell^+} - (p_x^{\ell^-} + \not{p}_x) p_y^{\ell^+}}. \end{aligned} \quad (3.61)$$

In Eq. (3.61) and in the following the tau rest mass has been neglected. The tau leptons as well as the electrons and muons are assumed to be on-shell. With

$$m_{\tau^+\tau^-}^2 = 2 \cdot p_\mu^{\tau^+} p^{\tau^- \mu} = \frac{2}{x_+ x_-} p_\mu^{\ell^+} p^{\ell^- \mu} = \frac{1}{x_+ x_-} m_{\ell^+\ell^-}^2 \quad (3.62)$$

the reconstructed tau pair mass can be written as

$$m_{\tau\tau}^{\text{rec}} = \frac{m_{\ell^+\ell^-}}{\sqrt{x_+ x_-}}, \quad x_\pm > 0. \quad (3.63)$$

Within this approximation, the cuts [102]

$$x_\pm \in [0, 1] \quad \cos \phi_{\ell\ell} \geq -0.9 \quad |m_{\tau\tau}^{\text{rec}} - m_h| \leq 15 \text{ GeV} \quad (3.64)$$

can be used for a very efficient background reduction. The first requirement restricts the lepton momentum fractions to the physically allowed region for the case of a true decay according to Eq. (3.60). For background processes where the two leptons and

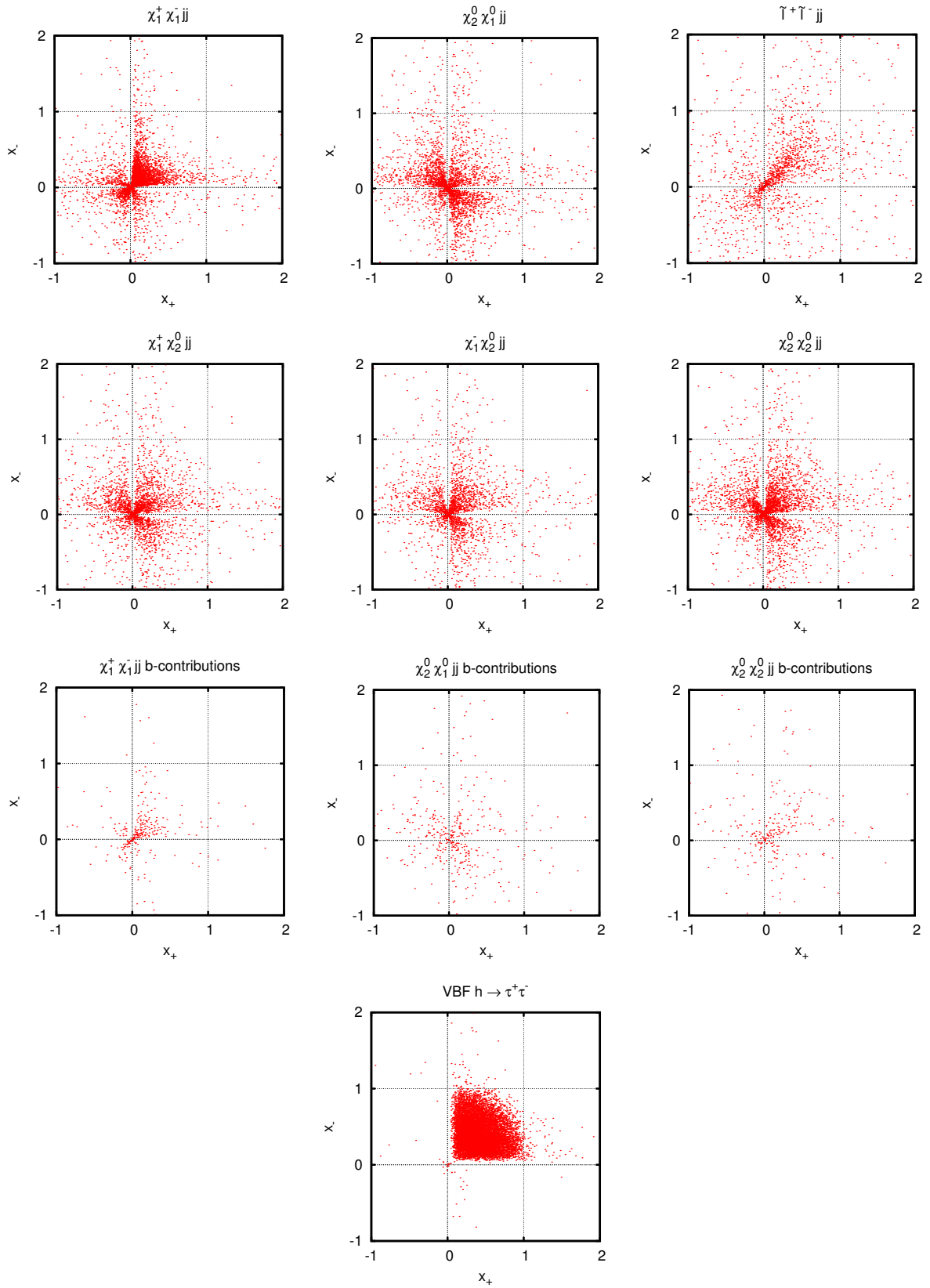


Figure 3.21: Tau momentum fractions for SUSY background processes and  $h \rightarrow \tau\tau$  signal with cuts from Eqs. (3.56), (3.58) and (3.59).

the missing energy do not stem (solely) from this decay chain, the  $x_{\pm}$  can also acquire values larger than one or smaller than zero. The second requirement, restricting the azimuthal angle difference between the lepton pair, discards events where the two leptons are emitted back-to-back in the laboratory frame, which makes the  $\cancel{p}_T$  projection impossible. With the third condition events are only considered if they give a reconstructed tau pair mass close to the expected Higgs boson mass. This cut efficiently reduces background contributions involving a  $Z \rightarrow \tau\tau$  decay.

In the SUSY background processes the leptons do not arise from a decay chain as given in Eq. (3.60). In addition, the processes lead to a large amount of missing energy in the detector, as the LSP is stable and therefore invisible in  $R$ -parity conserving SUSY models. Therefore they behave very differently than the signal with respect to the tau pair mass reconstruction. This is depicted in Figure 3.21, where scatter plots of events in the  $x_+ - x_-$  plane are shown for all dominant SUSY background processes (first three rows) and the signal process  $h \rightarrow \tau\tau$  (bottom plot) before applying the cuts from Eq. (3.64). For the signal process the momentum fractions are nicely located between zero and one, being the parameter range for which a mass reconstruction is possible. The situation is very different for the SUSY processes: for a large fraction of the events at least one of the  $x_{\pm}$  is outside the “allowed” region for a mass reconstruction. Therefore most of the events will be thrown away due to the first requirement of Eq. (3.64). Additionally, the physically allowed events of the SUSY processes tend to have very small  $x_{\pm}$ . Therefore the factor  $\frac{1}{\sqrt{x_+x_-}}$  in the mass reconstruction formula of Eq. (3.63) is usually much larger than for the signal, while the average invariant lepton pair mass in the SUSY processes is not smaller than in the signal process (see Figure 3.22). This leads to a too large  $m_{\tau\tau}^{\text{rec}}$  for most of the events, as can be seen in Figure 3.23. As a result, the “mass window” cut of Eq. (3.64) turns out to be very effective in suppressing the SUSY background as well. For the slepton processes the valid momentum fractions are slightly higher than for the other processes. But since the  $m_{\ell\ell}$  values are also quite large for this process, the numbers for  $m_{\tau\tau}^{\text{rec}}$  are again too high.

Altogether, the cuts from Eq. (3.64) reduce the SUSY background by a factor of almost 50, while the reduction in the signal cross section amounts to only 8%. Taking into account the limited missing energy resolution according to Eq. (3.32), the efficiency of the mass reconstruction cuts slightly reduces, as the sharp resonance of the signal process is broadened, which is depicted in Figure 3.23. But still the signal to SUSY background ratio is much better than in the  $h \rightarrow WW$  case, yielding

$$S/B^{\text{SUSY}} = 8.7, \quad (3.65)$$

while this ratio was  $S/B^{\text{SUSY}} = 1.3$  in the  $h \rightarrow WW$  analysis, imposing all cuts with the exception of the central jet veto. An additional cut on the missing transverse momentum, which improved the signal to background ratio further for the  $h \rightarrow WW$  signal, has no significant effect here, as the high- $\cancel{p}_T$  regions are already very much suppressed by the mass reconstruction cuts, as can be seen in Figure 3.24.

Finally, as in the  $h \rightarrow WW$  channel, the numbers of Table 3.13 show that the reducible background contributions are much larger than the irreducible background processes at this cut level. Therefore it seems advisable to apply the central jet veto from

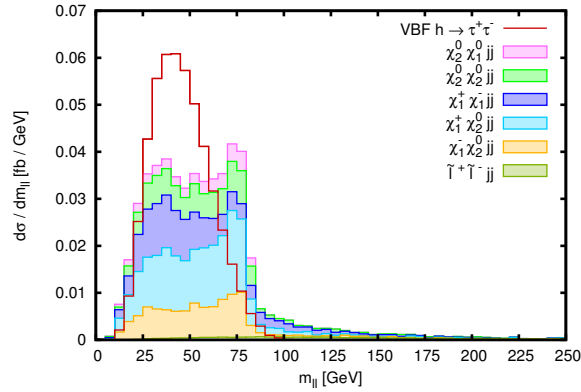


Figure 3.22: Invariant lepton pair mass with all cuts from Eqs. (3.56), (3.58), (3.59) and (3.64) except for the “mass window” cut from Eq. (3.64), for the dominant SUSY processes and the  $h \rightarrow \tau\tau$  signal.

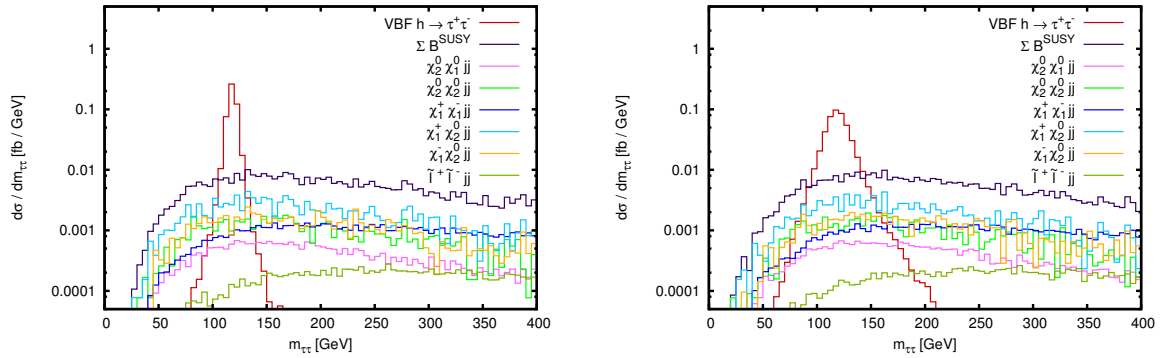


Figure 3.23: Reconstructed tau pair mass with all cuts from Eqs. (3.56), (3.58), (3.59) and (3.64) except for the “mass window” cut from Eq. (3.64), for the dominant SUSY processes and the  $h \rightarrow \tau\tau$  signal. The left panel is without detector effects, the plot on the right incorporates resolution effects according to Eq. (3.32).

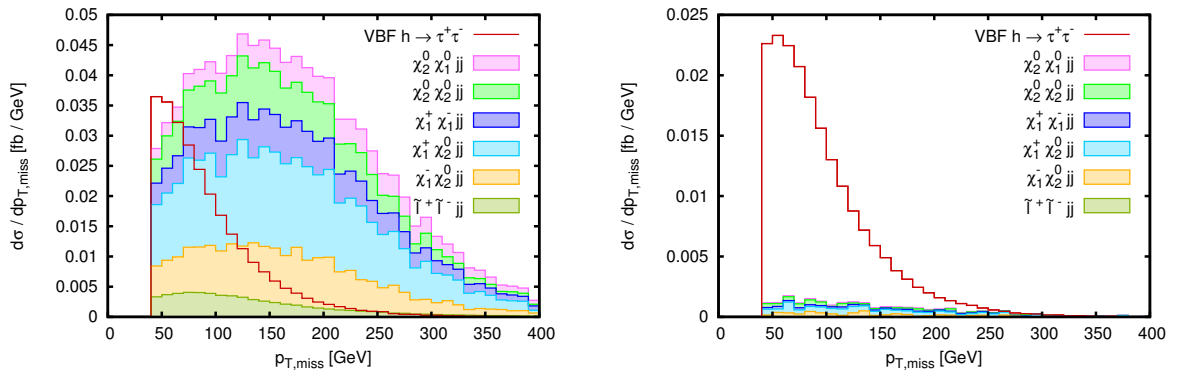


Figure 3.24: Missing transverse momentum distribution for the dominant SUSY processes and the  $h \rightarrow \tau\tau$  signal. In the left plot the cuts from Eqs. (3.56), (3.58) and (3.59) are applied, in the right plot the mass reconstruction cuts from Eq. (3.64) are included as well.

Eq. (3.46) ( $\eta_{j_{tag},min} < \eta_{j_{decay}} < \eta_{j_{tag},max}$ , with  $p_{T,j_{decay}} > 20$  GeV,  $|\eta_{j_{decay}}| < 4.5$ ) also in the  $h \rightarrow \tau\tau$  case. The veto on the additional jets from heavy particle decays improves the signal to SUSY background ratio by roughly 40%, giving

$$S/B^{SUSY} = 12. \quad (3.66)$$

### 3.5.2 Scenario with an Inverted Slepton Hierarchy

In the “light sleptons” scenario, introduced in Section 3.2.1, the  $h \rightarrow WW$  signal suffered from the by far largest SUSY background contributions of all discussed scenarios so far, with  $S/B^{SUSY} = 0.69$  for the full set of cuts. Therefore the SUSY background contributions in this scenario will now be discussed for the  $h \rightarrow \tau\tau$  channel as well.

The situation is in principle very similar to the shift from SPS1amod to “light sleptons” in the  $h \rightarrow WW$  case: the chargino cross section rises by more than an order of magnitude and the chargino process therefore dominates the SUSY background contribution. The cross sections of the other irreducible background processes also increase a bit. The reducible background processes, on the other hand, suffer from the scenario switch due to the occurring additional hard leptons, solely the cross sections of the  $\chi_2^0 \chi_2^0 jj$  process become larger due to the branching ratio shifts for the next-to-lightest neutralino.

Concerning the tau pair mass reconstruction, the tau momentum fractions for the dominant chargino process are now shifted to larger values (Figure 3.25 left), but as the invariant lepton pair mass increases as well (Figure 3.25 right) the resulting  $m_{\tau\tau}^{rec}$  is shifted to even higher values than in the scenario SPS1amod (see Figure 3.26 left).

Like in the  $h \rightarrow WW$  channel, the central jet veto on jets from a heavy particle decay has no effect on the SUSY background processes or on the signal process in the “light sleptons” scenario. Therefore the jet veto can be omitted and the final signal to SUSY background ratio is reached already after the mass reconstruction, incorporating the missing energy measurement uncertainties, yielding

$$S/B^{SUSY} = 4.3. \quad (3.67)$$

The reduction for  $S/B^{SUSY}$  due to the shift from SPS1amod to “light sleptons” is therefore of the same order as for the  $h \rightarrow WW$  channel. As the background is quite flat in the reconstructed tau pair mass (see Figure 3.26 left), it should be possible to subtract the remaining background quite well via a sideband analysis. All relevant cross sections for the “light sleptons” scenario are listed in Table 3.14.

For the higher squark masses in the “light sleptons with high  $m_{\tilde{q}}, m_{\tilde{g}}$ ” scenario defined in Section 3.2.1 the combined cross sections including all cuts decrease by a factor of roughly five to  $\sigma^{SUSY} = 0.093$  fb. The signal cross section decreases at the same time slightly to  $\sigma^{h \rightarrow \tau\tau} = 1.71$  fb, resulting in an increased signal to SUSY background ratio of

$$S/B^{SUSY} = 18. \quad (3.68)$$

The final  $m_{\tau\tau}^{rec}$  distribution for the higher squark masses is given in the right plot of Figure 3.26.

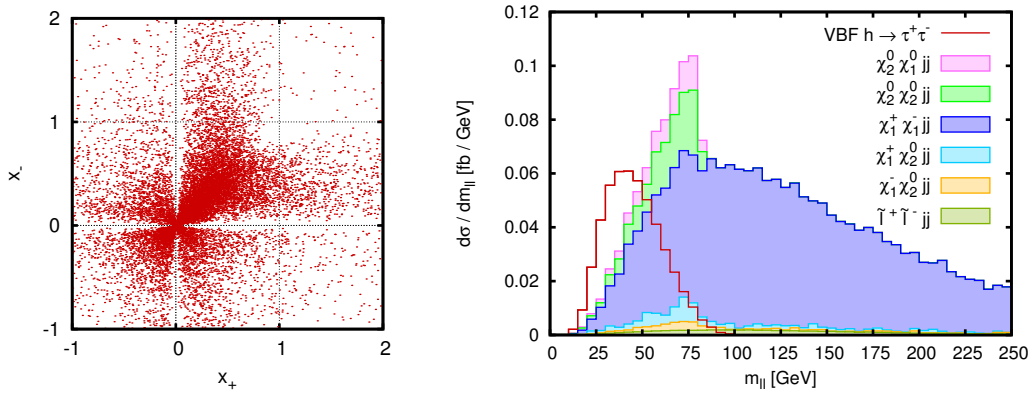


Figure 3.25: Left panel: tau momentum fractions for the chargino process, analogous to Figure 3.21, but for the scenario with light sleptons. Right panel: invariant lepton pair mass analogous to Figure 3.22, but for the scenario with light sleptons. Both distributions include the cuts from Eqs. (3.56), (3.58) and (3.59). The right plot additionally includes the first two cuts from Eq. (3.64).

Processes	basic + rapidity gap cuts Eqs. (3.56), (3.58)	+ $m_{inv}$ , $p_T^{\min}$ + (3.59)	+ $m_{\tau\tau}$ , fake $\cancel{E}_T$ + (3.64), (3.32)
$\chi_1^+ \chi_1^- jj$	59.1 fb	38.3 fb	0.272 fb
$\chi_1^+ \chi_1^- j b/\bar{b}$	18.7 fb	3.78 fb	0.027 fb
$\chi_2^0 \chi_1^0 jj$	2.54 fb	2.24 fb	0.029 fb
$\chi_2^0 \chi_1^0 j b/\bar{b}$	0.93 fb	0.30 fb	0.004 fb
$\tilde{\ell}^+ \tilde{\ell}^- jj$	4.27 fb	1.36 fb	0.011 fb
$\chi_1^+ \chi_2^0 jj$	2.95 fb	1.79 fb	0.030 fb
$\chi_1^- \chi_2^0 jj$	1.47 fb	0.86 fb	0.009 fb
$\chi_2^0 \chi_2^0 jj$	5.70 fb	4.35 fb	0.064 fb
$\chi_2^0 \chi_2^0 j b/\bar{b}$	0.80 fb	0.23 fb	0.005 fb
$\Sigma B^{SUSY}$	96.5 fb	46.0 fb	0.451 fb
VBF $h \rightarrow \tau\tau$	4.94 fb	2.67 fb	1.93 fb
$S/B^{SUSY}$	0.051	0.058	4.3

Table 3.14: Total cross sections for the SUSY contributions and the signal process VBF  $h \rightarrow \tau\tau$  at various cut levels for the “light sleptons” scenario, with b-quark contributions where relevant.

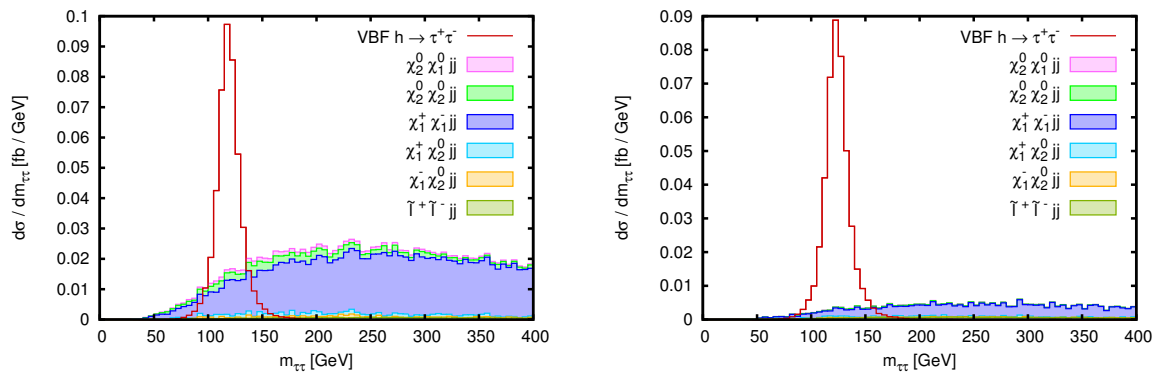


Figure 3.26: Reconstructed tau pair mass analogous to Figure 3.23. The left plot shows the “light sleptons” scenario, in the right plot the distributions in the “light sleptons with high  $m_{\tilde{\tau}}/m_{\tilde{g}}$ ” scenario are depicted. The cuts from Eqs. (3.56), (3.58), (3.59) and the first two cuts of Eq. (3.64) as well as the detector effects on the  $\cancel{p}_T$  measurement from Eq. (3.32) are taken into account in both plots.

### 3.6 LHC Results at 7 TeV Center-of-Mass Energy

Up to now, all results given have been calculated for the LHC running at 14 TeV center-of-mass energy, since the VBF channels have been assumed to be of more relevance at this energy due to their small cross sections. Therefore a detailed analysis of Higgs boson production in VBF will need at least  $30 \text{ fb}^{-1}$  of integrated luminosity at 14 TeV. However, due to the successful LHC run in the year 2011 at a center-of-mass energy of 7 TeV, the effect of the lower center-of-mass energy will be briefly discussed in this Section. The qualitative results should also hold for the energy of 8 TeV used in the 2012 run, with a slight tendency towards the 14 TeV results.

Three different scenarios will be discussed in the following, in more detail for the  $h \rightarrow WW$  channel and very briefly for the  $h \rightarrow \tau\tau$  channel, which always shows a smaller SUSY background after all cuts have been applied. The first scenario will be the conservative mSUGRA inspired “base” scenario of this whole analysis, SPS1amod. The second scenario will be one of the “light sleptons” scenarios with inverted mass hierarchy in the slepton sector, which led to larger SUSY background contributions at 14 TeV. The “light sleptons” will be discussed for larger squark masses of 1.1 TeV. The third scenario presented will be the “light sleptons with LHC-like Higgs” scenario, which has light first and second generation sleptons, first and second generation squark masses of 1.3 TeV, a light stop mass of 0.8 TeV and a Higgs boson mass  $m_h = 124.4 \text{ GeV}$  in the vicinity of the mass of the new particle observed at the LHC [19, 20].

#### 3.6.1 SPS1a-like Scenario

The results for the  $h \rightarrow WW$  channel in the SPS1amod scenario are given in Table 3.15 and in the left plot of Figure 3.27. The SUSY background processes have a much stronger dependence on the center-of-mass energy than the Higgs boson signal process

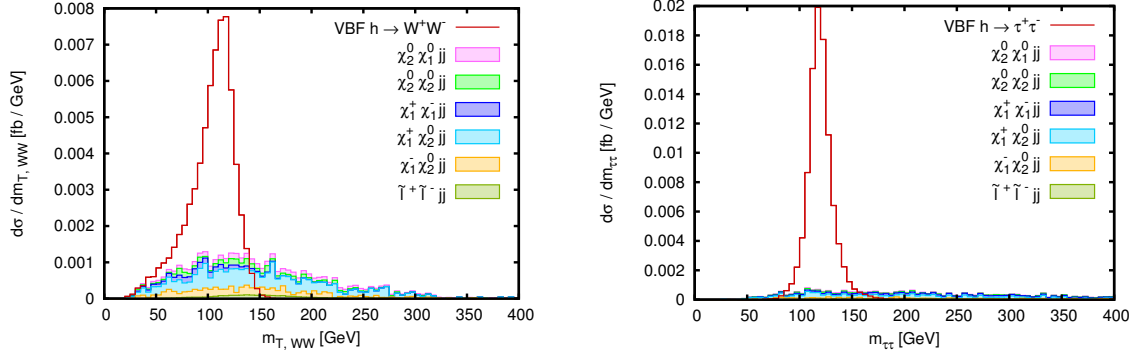


Figure 3.27: Left panel: Transverse  $WW$  mass distribution for the SUSY processes and the  $h \rightarrow WW$  signal, with all cuts from the  $h \rightarrow WW$  analysis except for the  $m_T(WW)$  cut. Right panel: Reconstructed tau pair mass distribution for the SUSY processes and the  $h \rightarrow \tau\tau$  signal, with all cuts from the  $h \rightarrow \tau\tau$  analysis except for the  $m_{\tau\tau}^{\text{rec}}$ -window cut. For both plots the scenario SPS1amod at 7 TeV center-of-mass energy is assumed and b-quark contributions are included where relevant.

Processes	basic + rapidity gap cuts Eqs. (3.39), (3.40)	+ $m_{\text{inv}}, \not{p}_T, \phi_{\ell\ell},$ $M_T(WW)$ , b-tag + (3.41), (3.43)–(3.45)	+ CJV on $j_{\text{decay}}$ + (3.46)
$\chi_1^+ \chi_1^- j j$	145 ab	9.9 ab	9.9 ab
$\chi_1^+ \chi_1^- j b/\bar{b}$	26 ab	0.6 ab	0.6 ab
$\chi_2^0 \chi_1^0 j j$	99 ab	8.9 ab	8.9 ab
$\chi_2^0 \chi_1^0 j b/\bar{b}$	24 ab	0.9 ab	0.9 ab
$\tilde{\ell}^+ \tilde{\ell}^- j j$	206 ab	4.4 ab	4.4 ab
$\chi_1^+ \chi_2^0 j j$	588 ab	53.7 ab	36.5 ab
$\chi_1^- \chi_2^0 j j$	246 ab	24.8 ab	16.5 ab
$\chi_2^0 \chi_2^0 j j$	158 ab	20.2 ab	8.8 ab
$\chi_2^0 \chi_2^0 j b/\bar{b}$	13 ab	0.6 ab	0.3 ab
$\sum B^{\text{SUSY}}$	1505 ab	124 ab	86.8 ab
VBF $h \rightarrow WW$	777 ab	316 ab	316 ab
$S/B^{\text{SUSY}}$	0.52	2.5	3.6

Table 3.15: Total cross sections of the SUSY background contributions and the VBF  $h \rightarrow WW$  signal for the scenario SPS1amod at 7 TeV center-of-mass energy.

due to the much heavier particles involved in the former processes. Hence the signal to SUSY background ratio for the  $h \rightarrow WW$  channel in VBF improves by roughly a factor of 2, giving

$$S/B^{SUSY} = 3.6 \quad (3.69)$$

for the processes of Table 3.15 with the full set of cuts.

For the  $h \rightarrow \tau\tau$  channel the situation is even better, for the same reasons as for 14 TeV center-of-mass energy. The signal cross section for all discussed cuts is  $\sigma^{h \rightarrow \tau\tau} = 398$  ab and the SUSY processes giving the dominant contribution account for  $\sigma^{SUSY} = 19.3$  ab, yielding

$$S/B^{SUSY} = 21. \quad (3.70)$$

The approximate reconstructions of the Higgs boson mass in both channels,  $m_T(WW)$  for the  $h \rightarrow WW$  channel and  $m_{\tau\tau}^{\text{rec}}$  for the  $h \rightarrow \tau\tau$  channel, respectively, are depicted in Figure 3.27. Both signals show a peak roughly at the Higgs boson mass of  $m_h = 118$  GeV. However, for the  $h \rightarrow WW$  case the peak is broader and slightly asymmetric, while the resonance from  $h \rightarrow \tau\tau$  is sharper and symmetric. Additionally, the background in the  $h \rightarrow \tau\tau$  channel is smaller and much flatter, giving the much better background suppression from Eq. (3.70) compared to Eq. (3.69). The shape of the  $m_T(WW)$  and  $m_{\tau\tau}^{\text{rec}}$  distributions is as expected from the 14 TeV analysis. The main difference is the larger relative difference in the size of signal and background contributions.

### 3.6.2 Light Sleptons with Higher Squark Masses

The “light sleptons with high  $m_{\tilde{q}}, m_{\tilde{g}}$ ” scenario features higher SUSY process cross sections due to the inverted slepton mass hierarchy together with squark masses which are in good agreement with the mid-2011 LHC SUSY searches [97, 98], being the most stringent ones during the completion of this analysis.

Like for the scenario SPS1amod, the signal to SUSY background ratios improve significantly for both Higgs boson channels when moving from 14 TeV center-of-mass energy to 7 TeV, yielding

$$S/B^{SUSY} = 8.1 \quad (3.71)$$

for the  $h \rightarrow WW$  channel, including all cuts. The central jet veto on jets from a heavy particle decay again has no effect, due to the missing hadronic decay products of the electroweak gauginos. The relevant cross sections are listed in Table 3.16.

For the  $h \rightarrow \tau\tau$  channel the final signal to SUSY background ratio in this scenario reads

$$S/B^{SUSY} = 45, \quad (3.72)$$

which is again much better than the corresponding result in the  $h \rightarrow WW$  channel. The signal cross section in this scenario amounts to  $\sigma^{h \rightarrow \tau\tau} = 340$  ab and the relevant SUSY processes yield a cross section of  $\sigma^{SUSY} = 7.6$  ab.

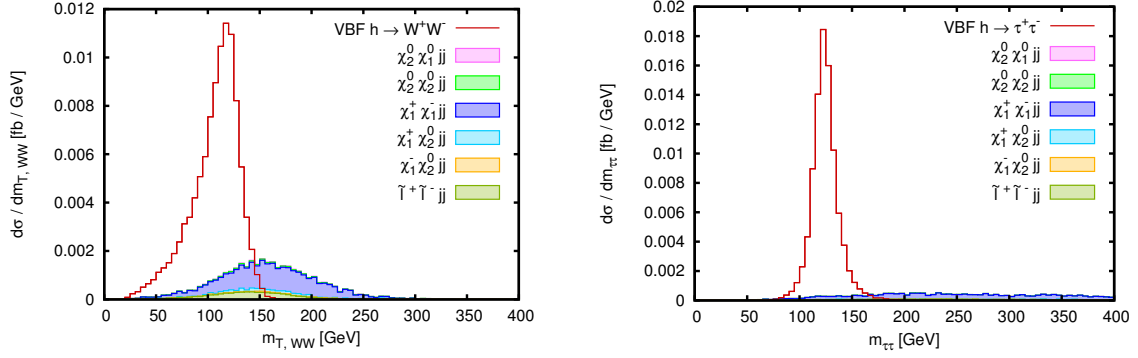


Figure 3.28: Left panel: Transverse  $WW$  mass distribution for the SUSY processes and the  $h \rightarrow WW$  signal, with all cuts from the  $h \rightarrow WW$  analysis except for the  $m_T(WW)$  cut. Right panel: Reconstructed tau pair mass distribution for the SUSY processes and the  $h \rightarrow \tau\tau$  signal, with all cuts from the  $h \rightarrow \tau\tau$  analysis except for the  $m_{\tau\tau}^{\text{rec}}$ -window cut. For both plots the scenario “light sleptons with high  $m_{\tilde{g}}, m_{\tilde{q}}$ ” at 7 TeV center-of-mass energy is assumed and b-quark contributions are included where relevant.

Processes	basic + rapidity gap cuts Eqs. (3.39), (3.40)	+ $m_{\text{inv}}, \cancel{p}_T, \phi_{\ell\ell},$ $M_T(WW)$ , b-tag + (3.41), (3.43)–(3.45)	+ CJV on $j_{\text{decay}}$ + (3.46)
$\chi_1^+ \chi_1^- j j$	1756 ab	35.0 ab	35.0 ab
$\chi_1^+ \chi_1^- j b/\bar{b}$	216 ab	2.2 ab	2.2 ab
$\chi_2^0 \chi_1^0 j j$	1.6 ab	0.03 ab	0.03 ab
$\chi_2^0 \chi_1^0 j b/\bar{b}$	43 ab	0.7 ab	0.7 ab
$\tilde{\ell}^+ \tilde{\ell}^- j j$	482 ab	13.4 ab	13.4 ab
$\chi_1^+ \chi_2^0 j j$	132 ab	3.8 ab	3.8 ab
$\chi_1^- \chi_2^0 j j$	48 ab	1.3 ab	1.3 ab
$\chi_2^0 \chi_2^0 j j$	32 ab	1.7 ab	1.7 ab
$\chi_2^0 \chi_2^0 j b/\bar{b}$	35 ab	0.8 ab	0.8 ab
$\sum B^{\text{SUSY}}$	2746 ab	58.9 ab	58.9 ab
VBF $h \rightarrow WW$	1193 ab	476 ab	476 ab
$S/B^{\text{SUSY}}$	0.44	8.1	8.1

Table 3.16: Total cross sections of the SUSY background contributions and the VBF  $h \rightarrow WW$  signal for the scenario with light sleptons and higher squark/gluino masses at 7 TeV center-of-mass energy.

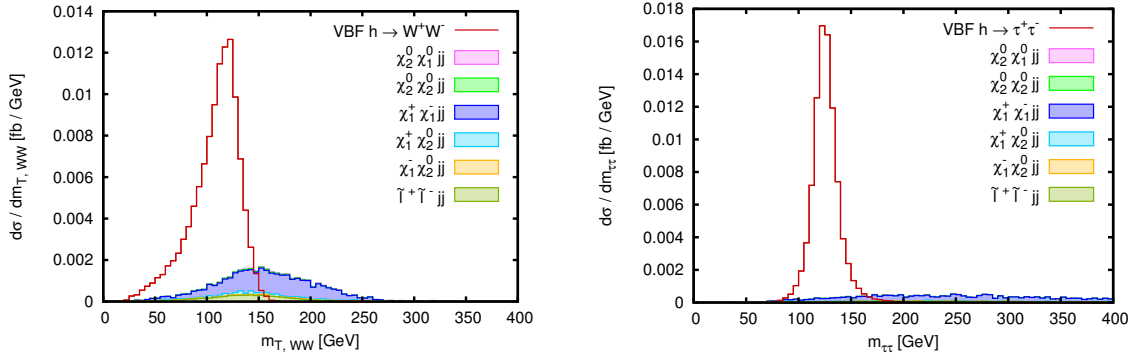


Figure 3.29: Left panel: Transverse  $WW$  mass distribution for the SUSY processes and the  $h \rightarrow WW$  signal, with all cuts from the  $h \rightarrow WW$  analysis except for the  $m_T(WW)$  cut. Right panel: Reconstructed tau pair mass distribution for the SUSY processes and the  $h \rightarrow \tau\tau$  signal, with all cuts from the  $h \rightarrow \tau\tau$  analysis except for the  $m_{\tau\tau}^{\text{rec}}$ -window cut. For both plots the scenario “light sleptons with LHC-like Higgs” at 7 TeV center-of-mass energy is assumed and b-quark contributions are included where relevant.

Figure 3.28 finally shows the  $m_T(WW)$  and  $m_{\tau\tau}^{\text{rec}}$  distributions, which approximate the Higgs boson mass in case of the signal processes, for the scenario with light sleptons and higher squark and gluino masses. The signal shapes are very similar to the ones from Figure 3.27, but the  $h \rightarrow WW$  cross section is larger due to the increased  $h \rightarrow WW$  branching ratio arising from the higher Higgs boson mass, while the  $h \rightarrow \tau\tau$  cross section is a little bit smaller in this case. Once again, the SUSY background shows a quite broad bump in the  $m_T(WW)$  distribution, centered around a slightly larger value for  $m_T(WW)$  compared to the SPS1amod scenario due to the harder leptons in the light sleptons scenario. The SUSY background contributions in the  $h \rightarrow \tau\tau$  channel are shifted to larger values as well. As before, the SUSY background is extremely flat, resulting once again in a good background suppression.

### 3.6.3 Scenario with a Higgs Boson Mass of about 125 GeV

Given the first hints for a Higgs boson of about 125 GeV end of 2011 [191, 192] (followed by the observation in mid-2012 [19, 20]), the scenario of the last section has been modified for a Higgs boson mass of  $m_h = 124.4$  GeV, which is in the vicinity of the new resonance. As discussed before, constructing the scenario “light sleptons with LHC-like Higgs” has been achieved in the same way as for the scenario SPS1amod2, with squark and gluino masses corresponding to  $\xi = 1.5$  (as defined in Section 3.2.1).

This gives an increased signal cross section of  $\sigma^{h \rightarrow WW} = 527$  ab for the  $h \rightarrow WW$  channel, with a SUSY background contribution of  $\sigma^{\text{SUSY}} = 63$  ab. The resulting ratio is

$$S/B^{\text{SUSY}} = 8.4. \quad (3.73)$$

The corresponding values for the  $h \rightarrow \tau\tau$  channel are  $\sigma^{h \rightarrow \tau\tau} = 329$  ab for the signal cross section,  $\sigma^{SUSY} = 7.5$  ab for the cross section of the SUSY processes, and

$$S/B^{SUSY} = 44 \quad (3.74)$$

for the signal to SUSY background ratio. Figure 3.29 shows the reconstructed Higgs boson mass distributions in the two channels. As already the signal to background ratios suggest, there is no significant difference to the scenario depicted in Figure 3.28.

## 3.7 Additional Aspects of SUSY Background Processes

Several aspects of the SUSY background to the Higgs boson searches in VBF have been discussed so far for many SUSY processes in several MSSM scenarios. Two additional general features of possible MSSM scenarios will be examined separately in this section, taking the chargino process  $\chi_1^+ \chi_1^- jj$  as an example: the impact of an almost massless LSP and the effect of a small mass splitting in a SUSY decay chain. The final topic considered in this analysis will be the influence of the central jet veto on additional QCD radiation. As mentioned before, the central jet veto of Eq. (3.46) is only applied on jets from heavy particle decays. As the two jet types cannot be distinguished in the experiment, the effect of the jet veto on the radiated QCD jets has to be estimated as well. This will be done for the  $h \rightarrow WW$  channel, using the processes  $\chi_1^+ \chi_1^- jj$  and  $\chi_2^0 \chi_1^0 jj$  as examples.

The following calculations are again carried out for a center-of-mass energy of 14 TeV. However, the results are not tied to this energy but hold for other collision energies as well.

### 3.7.1 Effect of a Light LSP

The first point addressed in this section concerns the question, whether the SUSY background increases substantially, when the available phase space for the decay leptons is larger than in the scenarios discussed in detail so far. This test is done for the  $\chi_1^+ \chi_1^- jj$  process, with the SPS1amod scenario as starting point. The enlarged lepton phase space is achieved by lowering the masses of the chargino decay products: the LSP is chosen almost massless, while the light stau mass is lowered to  $m_{\tilde{\tau}_1} = 100$  GeV. In order to keep the other characteristics of the scenario unchanged, these modifications have not been carried out by modifying the soft SUSY breaking parameters, but instead the masses of  $\chi_1^0$  and  $\tilde{\tau}_1$  have been set directly in the output of the spectrum generator `SuSpect` [135]. The altered file is then fed into `SDECAY` [137] and `FeynHiggs` [140–143] for the branching ratio calculations. While this is no genuine MSSM scenario anymore, it still can be used to investigate the implications of a light LSP.

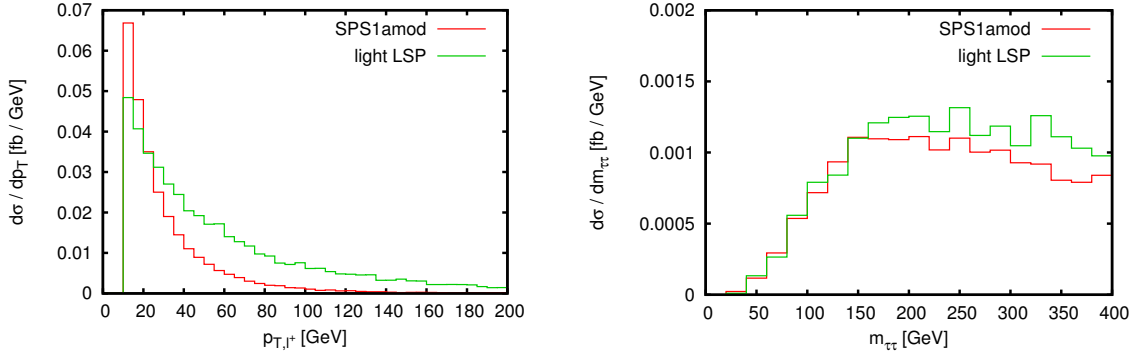


Figure 3.30: Left panel:  $p_{T,\ell^\pm}$  distribution of  $\chi_1^+ \chi_1^- jj$  with cuts (3.56)–(3.59). Right panel: reconstructed invariant tau pair mass with the additional cuts on  $x_i$  and  $\cos \phi_{\ell\ell}$  from Eq. (3.64).

In this scenario the chargino can decay in two possible ways

$$\begin{aligned} \chi_1^\pm &\rightarrow \tilde{\tau}_1^\pm \nu \rightarrow \tau^\pm \chi_1^0 \nu \rightarrow \ell^\pm \chi_1^0 \nu \bar{\nu} \nu \\ \chi_1^\pm &\rightarrow W^\pm \chi_1^0 \rightarrow \ell^\pm \chi_1^0 \nu, \end{aligned} \quad (3.75)$$

with roughly 50% branching ratio for each decay mode. With a chargino mass of  $m_{\chi_1^\pm} \approx 180$  GeV, at each decay step, except for the  $\tau$  decay, there is at least 80 GeV available for kinematics.

The scenario modifications indeed lead to harder leptons, as can be seen in Figure 3.30 (left). Therefore more events pass the transverse momentum cut and the cross section rises by up to a factor of 1.8, depending on the additionally applied cuts. For the final cuts of the  $h \rightarrow WW$  analysis the enhancement factor is 1.4. After the  $m_{\tau\tau}$  reconstruction, on the other hand, the effect is marginal, which can be seen in the right plot of Figure 3.30. This shows that the changes do not yield a more signal like ratio of lepton transverse momenta and the missing transverse momentum of the event.

### 3.7.2 Effect of Small Mass Differences in the SUSY Particle Decay Chain

After increasing the phase space in the SUSY decay chain it is also interesting to study the opposite case, i.e. reducing the mass difference between mother and daughter particles for one decay in the chain yielding a lepton. This test uses a modified version of the mSUGRA scenario SPS1a: the unified trilinear coupling  $A_0$  is changed from the SPS1a value  $A_0 = -100$  GeV to  $A_0 = -750$  GeV, which leads to a mass splitting of only 9 GeV between the light stau and the LSP. In this scenario the chargino decay into a light stau is dominant, which again results in the  $\chi_1^+ \chi_1^- jj$  process being a good test candidate.

The left plot of Figure 3.31 displays the lepton transverse momentum distribution. The lepton from the tau decay in the scenario with a small mass splitting has a very small

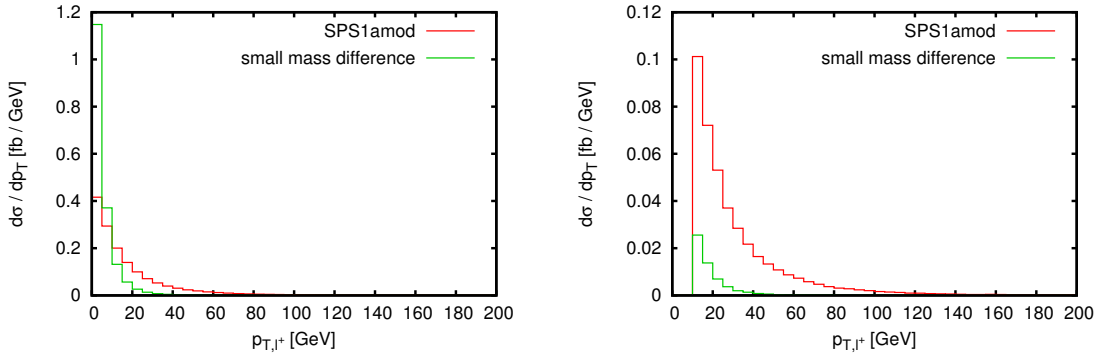


Figure 3.31:  $p_{T,\ell^+}$  distribution of  $\chi_1^+ \chi_1^- jj$  in a scenario with a small difference between the  $\tilde{\tau}_1$  and  $\chi_1^0$  mass. In the left plot, otherwise generated with the cuts from Eqs. (3.56)+(3.58), the cut on  $p_{T,\ell}$  is omitted.

transverse momentum, resulting in a very efficient  $p_T$  cut. Requiring  $p_{T,\ell} > 10$  GeV therefore removes most of the chargino contribution, as can be seen in the right part of Figure 3.31. The comparison with the SPS1amod scenario shows that decreasing the  $m_{\tilde{\tau}_1} - m_{\chi_1^0}$  difference from 36 GeV in the SPS1amod case to a difference of the order of 10 GeV leads to an extremely suppressed cross section, while increasing the difference, as it has been done for the light LSP scenario of Section 3.7.1, induces substantially smaller effects.

### 3.7.3 Effect of a Central Jet Veto on QCD Radiation in SUSY Background Processes

Up to now, for the central jet veto introduced in Section 3.4.1.2 and used from thereon, with the numerical values from Eq. (3.46), only additional jets from the decay of heavy particles have been considered. However, in the experiment additional jets always arise from QCD radiation as well. The effect of a jet veto on these jets has to be studied for two reasons: on the one hand, the two jet types cannot be separated in the experiment, therefore a jet veto always acts on all jets. On the other hand it has to be checked, whether the amount of jets from QCD radiation is different for the signal and SUSY background processes, which has an influence on the signal to SUSY background ratio.

The effect of a jet veto on QCD jets could be investigated for example in a parton-level study or a full simulation including parton-shower effects. Another possibility to estimate the effects of a jet veto on additional jets from QCD radiation, without using a parton shower, is the exponentiation model of Refs. [164, 165]. In this model, with the assumption that additional jets typically arise from QCD splittings, the veto probability of the jet veto can be estimated to

$$P_{veto} = 1 - e^{-\bar{n}}, \quad (3.76)$$

with

$$\bar{n} = \frac{\sigma(jjj)}{\sigma(jj)} \quad (3.77)$$

X	$\sigma(X + jj)$	$\sigma(X + jjj)$	$P_{\text{veto}}$
$\chi_1^+ \chi_1^-$	0.073 fb	0.044 fb	0.45
$\chi_2^0 \chi_1^0$	0.081 fb	0.109 fb	0.74
$h \rightarrow WW$	1.38 fb	0.139 fb	0.10

Table 3.17: Total cross sections and central jet veto probabilities for  $\chi_1^+ \chi_1^- jj(j)$ ,  $\chi_2^0 \chi_1^0 jj(j)$  and  $h \rightarrow WW$  with the cuts from Eqs. (3.39)–(3.41), (3.43)–(3.44). For the  $jjj$  case, the cross sections are within the veto region defined in Eq. (3.78).

giving the average multiplicity of additional jets and  $\sigma(jj)$  and  $\sigma(jjj)$  representing the cross sections of the desired process and of the process with one extra jet, respectively. The extra jet in the  $\sigma(jjj)$  cross section has to be located within the veto region.

The effect of the central jet veto on additional QCD jets will be discussed for the two processes  $\chi_1^+ \chi_1^- jj$  and  $\chi_2^0 \chi_1^0 jj$ . The additional jet in the corresponding three-jet processes  $\chi_1^+ \chi_1^- jjj$  and  $\chi_2^0 \chi_1^0 jjj$ , considering the scenario SPS1amod, typically arises from gluon radiation, therefore the effect of extra QCD radiation can be estimated in the exponentiation model. The three-jet contribution from gluino decays is small in this scenario. For the  $\chi_2^0 \chi_1^0 jjj$  process the same approximation as in the two-jet case has been used and only the  $\alpha_s^3 \alpha^2$  contributions have been considered. The effect of the jet veto on the SUSY processes will be compared to the change of the  $h \rightarrow WW$  signal processes. Additionally, the cross sections have been calculated using the  $h \rightarrow WW$  cuts from Eqs. (3.39)–(3.41) and Eqs. (3.43)–(3.44). The veto region for the additional jet is defined as

$$\begin{aligned}
 p_{T,j_{\text{veto}}} &\geq 20 \text{ GeV} & \eta_{j_{\text{tag},\text{min}}} &\leq \eta_{j_{\text{veto}}} \leq \eta_{j_{\text{tag},\text{max}}} \\
 R_{j_{\text{tag},i},j_{\text{veto}}} &\geq 0.8 & R_{j_{\text{veto},\ell}} &\geq 0.3,
 \end{aligned}
 \tag{3.78}$$

where the two hardest jets are required to be the tagging jets  $j_{\text{tag},i}$ , while the third jet  $j_{\text{veto}}$  serves as candidate for the jet veto. The two-jet and three-jet cross sections within these cuts as well as the resulting veto probabilities  $P_{\text{veto}}$  for the chargino, the next-to-lightest neutralino and the signal process are given in Table 3.17. The minor difference of the two-jet cross section of the  $h \rightarrow WW$  process with respect to the values in the previous sections (e.g. Table 3.2) is due to a different scale choice: The scales  $\mu_F = \mu_R = \min(p_{T,j_i})$  are reasonable choices both for the two-jet and three-jet case. As the results for the veto probabilities are certainly higher for the SUSY processes than for the  $h \rightarrow WW$  signal in VBF, it can be assumed that a central jet veto as it has been applied in the  $h \rightarrow WW$  analysis of Sections 3.4.1 and 3.6.1 would lead to a stronger SUSY background suppression than assumed there.

## 3.8 Conclusion

In this Chapter the SUSY induced background processes to the production of the light neutral Higgs boson in the MSSM via VBF have been studied in a leading-order parton-level analysis. Two Higgs boson decay modes have been considered:  $h \rightarrow WW$  and  $h \rightarrow \tau\tau$ , with subsequent leptonic decays of the tau leptons and W bosons. The dominant SUSY background contributions have been identified for an SPS1a-like scenario and several scenarios with partially changed characteristics, for example heavier SUSY particle masses or a different slepton mass hierarchy.

Among the SUSY processes that account for the irreducible background by matching the signal process signature exactly, the most relevant background contributions arise from  $\chi_1^+ \chi_1^- jj$  and  $\chi_2^0 \chi_1^0 jj$  production with subsequent decay of  $\chi_1^\pm$  and  $\chi_2^0$ . Smaller effects concerning the irreducible background emerge from  $\tilde{\ell}^+ \tilde{\ell}^- jj$  production. The dominant processes contributing to the reducible SUSY background are  $\chi_1^\pm \chi_2^0 jj$  and  $\chi_2^0 \chi_2^0 jj$  production. As the decay of the SUSY particles in these processes leads to additional jets or leptons in the detector, their events can in principle be vetoed. However, even after applying a central jet veto the contribution of the reducible background processes in the SPS1a-like scenario is twice as large as the irreducible background contribution, given that the extra particles can evade detection. Contributions with b-quarks in the final state have been analyzed separately: they add significantly to the SUSY background when only basic cuts are considered. Once all cuts are applied, including a b-jet veto, the impact of the b-quark contributions is much smaller than the non-b-quark contributions.

The dominant SUSY background processes in the  $h \rightarrow WW$  channel, assuming the SPS1a-like scenario, yield a ratio of  $S/B^{SUSY} = 1.9$  for the 14 TeV LHC after the application of all cuts. Therefore the SUSY background is under sufficient control. The investigation of the squark and gluino mass dependence with squark masses between 550 GeV and 1.6 TeV showed a reduction of the SUSY background of 70% for squark masses of 1.1 TeV with respect to the SPS1a values for the squark masses of 550 GeV. For squark masses above 1.1 TeV no further reduction of the SUSY background is observed. In addition to the SPS1a-like scenario a scenario with selectrons and smuons being the lightest sleptons has been discussed, both for light squark masses and squark masses of 1.1 TeV. In this scenario the SUSY background is significantly enhanced, even exceeding the signal cross section for the light squark case. For heavier squarks a ratio of  $S/B^{SUSY} = 3.9$  remains.

The SUSY background to the  $h \rightarrow \tau\tau$  signal process is much less troublesome: for this signal process the invariant tau pair mass, which corresponds to the Higgs boson mass, can be reconstructed within the collinear approximation of the tau lepton decays. As the correlation between the measured lepton momenta and the missing transverse energy components for the  $h \rightarrow \tau\tau$  signal and for the SUSY processes is not alike, the resulting reconstructed masses for the signal and SUSY processes are very different. This allows for a very efficient background reduction when a mass window cut around the Higgs boson mass is applied and the resulting SUSY background is more than

an order of magnitude smaller than the signal for the SPS1a-like scenario. Even for the scenario with light selectrons, smuons and very low squark and gluino masses the  $h \rightarrow \tau\tau$  signal is more than four times larger than the combined SUSY background processes.

For the LHC running at a center-of-mass energy of 7 TeV the signal to background ratio improves by roughly a factor of two as the SUSY processes suffer much more from the smaller collision energy than the signal process.

Finally, the effect of a central jet veto on additional jets from QCD radiation has been estimated for the  $h \rightarrow WW$  signal and the two SUSY background processes  $\chi_1^+ \chi_1^- jj$  and  $\chi_2^0 \chi_1^0 jj$ . This suggests that the jet veto is even more effective in the SUSY background reduction when moving from a LO parton-level analysis as described in this Chapter to a full simulation including parton-shower effects.

In conclusion, the SUSY induced background processes to VBF Higgs boson production with the two Higgs boson decay modes  $h \rightarrow WW$  and  $h \rightarrow \tau\tau$  have turned out to be under good control once the squark masses are chosen larger than approximately 1 TeV. Squark masses above this threshold have been already favored considering the mid-2011 analyses from ATLAS and CMS [97, 98]. The most recent LHC results [193–197] additionally exclude the lower mass ranges for charginos, neutralinos and sleptons, which restricts SUSY induced background contributions even further.

## CHAPTER 4

---

### New Physics Effects in Background Determination

---

The work described in this chapter has been published in *Phys. Lett. B717 (2012) 390-395* [198] and in the proceedings of the *24th Rencontres de Blois 2012* [199].

#### 4.1 Introduction

Besides showing up as direct background, another possible area in which BSM effects could interfere with measurements of SM or SM-like quantities is the determination of SM background contributions with data-driven techniques. As discussed in Chapter 2.3.2, these methods are widely used in LHC analyses, for example in Higgs boson searches [91–93].

One type of data-driven background determination is the use of background control regions. In this method, the background contribution in the signal region is normalized to the background contribution in a control region, which is assumed to be signal-free and largely dominated by the corresponding background process. New Physics effects can spoil this type of background determination in the following way: if the relative size of the BSM contribution in the control region is larger than in the signal region, the background in the signal region gets over-estimated, which would be interpreted as a lack of signal events.

In this chapter the possibility of a BSM physics influence on control regions is discussed using the Higgs boson search at the LHC as an example, in particular the  $H \rightarrow WW \rightarrow \ell\nu\ell\nu$  channel. The study is based on the LHC analyses for the Moriond meeting of

2012 from ATLAS [92] and CMS [93]. Within this data sample, most of the sensitivity on a SM-like Higgs boson arises from Higgs boson production via gluon-fusion,

$$gg \rightarrow H \rightarrow W^+W^- \rightarrow \ell^+\nu\ell^-\bar{\nu}. \quad (4.1)$$

A major irreducible background for this signal process is the production of a W boson pair, followed by a leptonic decay of the W bosons,

$$q\bar{q} \rightarrow W^+W^- \rightarrow \ell^+\nu\ell^-\bar{\nu}. \quad (4.2)$$

This substantial background is determined with the help of a control region, characterized by a large invariant mass  $m_{\ell\ell}$  of the two leptons in the final state. The signal region in contrast is located at quite low values of  $m_{\ell\ell}$ . As BSM physics processes are usually expected in hard events and therefore would end up preferably at large invariant masses, they could indeed compromise the  $WW$  background determination.

In fact the 2011 dataset from the LHC experiments showed a lack of events in the  $H \rightarrow WW$  channel compared to other channels and the SM expectation [200,201], while there was and still is a slight excess in the 7 TeV data of  $WW$  pair production [202,203]. A natural candidate for a BSM model with processes that could explain the measured data is the Minimal Supersymmetric Extension of the Standard Model. In particular processes that involve the production of charginos  $\chi_i^\pm$ , neutralinos  $\chi_i^0$  and sleptons  $\tilde{\ell}$  can give rise to the two leptons plus missing energy signature of  $WW$  production. Therefore the issue of BSM physics tampering with SM background determination is done using the MSSM as an example.

## 4.2 Analysis Setup

The analysis method in this study is similar to the one in Chapter 3 with some modifications specific to the question whether the SUSY processes can have an influence on the SM background determination. These modifications in the SUSY scenarios and the analysis tools will be discussed in the following. Afterwards, the event selection that defines the signal and the control region will be given.

### 4.2.1 SUSY Scenario

The MSSM phenomenology strongly depends on assumptions on the SUSY breaking sector (see Chapter 2.2). As no evidence for supersymmetry has been seen so far (see e.g. [193–197]), the SUSY breaking parameters can be chosen freely. However, the resulting scenario must not predict values for observables, such as event rates for SUSY processes, which are already ruled out by the LHC and by previous experiments.

As this study focuses on the Higgs data from early 2012, SUSY limits from the same time are relevant for setting up the MSSM scenario. Much effort has already been

devoted for the analysis in Chapter 3 to construct a scenario which gives rise to large dilepton signals at the LHC and at the same time avoids the mid-2011 LHC exclusions [96–98, 131]. The “light sleptons” scenario defined in Chapter 3.2.1 turned out to induce the largest dilepton signals and therefore served as a starting point. The main feature of the “light sleptons” scenario is that the tau sleptons are heavier than the light chargino, while the masses of selectrons and smuons lie between the light chargino mass and the lightest neutralino mass, which is the LSP. This constellation yields a slepton to lepton plus LSP branching ratio of one. The main chargino decay channel proceeds via a slepton and therefore yields a final-state lepton as well.

A few modifications have to be applied to match the experimental results from early 2012: exclusion limits in the squark and gluino sector [204–207] can be easily satisfied by increasing the soft-SUSY breaking terms controlling the squark and gluino masses. This does not affect the analysis at all, as only superpartners of electroweak gauge bosons, leptons and Higgs bosons are involved in the relevant processes. The parameters of the MSSM Higgs boson sector are set to values that lead to a SM-like Higgs boson with a mass of 124.7 GeV, which matches the experimental hints of a SM-Higgs-like boson within the early-2012 data [200, 201] (confirmed by LHC studies with more data [19, 20]). Furthermore, the ATLAS  $2\text{fb}^{-1}$  trilepton search [208] puts some constraints on the chargino mass, which can be fulfilled by modifying the soft-SUSY breaking parameters  $M_2$  and  $m_{H_u}$ .

However, there is a tension with the CMS trilepton analysis [209, 210], which became public a few weeks after the ATLAS study. It uses the full  $5\text{fb}^{-1}$  dataset of 2011 and puts stronger constraints on the light chargino mass if the predicted neutralino properties are taken literally. The main exclusion limits for the light chargino stem from generally highly correlated properties of the light chargino and the next-to-lightest neutralino within the MSSM. However, the occurrence of a next-to-lightest neutralino with a visible leptonic decay signature is not important for the BSM effect discussed here. While the  $\chi_1^\pm \chi_2^0$  production adds a small contribution to the dilepton plus missing energy signature of  $WW$  pair production, it mostly gives rise to a trilepton signal, which can be easily tagged and used for exclusion limits. Any general BSM scenario without such a trilepton source while fulfilling the other criteria described here still shows the same behavior concerning the  $WW$  background but is much harder to detect at the LHC.<sup>1</sup> This could be achieved for example by imposing a next-to-lightest neutralino which is much heavier than the light chargino. Such a scenario would typically lie outside the MSSM parameter range. Having in mind that the CMS trilepton search uses properties and assumptions which are not needed within this study, the tension will be ignored in the main part of the analysis. Possibilities to weaken this tension within the MSSM would be for example to allow a decay of the light chargino and the next-to-lightest neutralino equally into all three lepton generations or to increase the next-to-lightest neutralino and light chargino masses. The effect of these changes will be discussed briefly at the end of Section 4.3.

---

<sup>1</sup>The current exclusion limits for charginos from the two-lepton search [195] are in fact much weaker than from the trilepton analysis [194].

The scenario described so far will be called the “*base*” scenario in the subsequent parts of this chapter. With these parameters, the processes with dominant contributions to the  $WW$  production signature are

$$q \bar{q} \rightarrow \chi_1^+ \chi_1^- \rightarrow \ell^+ \ell'^- + \cancel{p}_T \quad (4.3)$$

$$q \bar{q} \rightarrow \tilde{\ell}^+ \tilde{\ell}^- \rightarrow \ell^+ \ell^- + \cancel{p}_T \quad (4.4)$$

$$q \bar{q} \rightarrow \chi_1^\pm \chi_2^0 \rightarrow \ell^\pm \ell'^+ \ell'^- + \cancel{p}_T . \quad (4.5)$$

From these processes, chargino pair production gives by far the largest contribution, followed by slepton pair production. The third process, the production of a next-to-lightest neutralino and a light chargino, is of minor importance with respect to the other two production modes. As discussed above, the main decay modes of the  $\chi_1^\pm \chi_2^0$  system produce a trilepton signal, and any model without such a trilepton source would be harder to exclude while having the same effect on the  $WW$  background.

Starting from the “*base*” scenario, the parameters which control the slepton, light chargino and lightest neutralino mass will be varied to study their influence on the  $WW$  background control region and the Higgs boson signal region. Within this class of models, a scenario with a 25% higher LSP mass and a 40% higher slepton mass, later on called “*worst case*” scenario, will be discussed in more detail. Results for a scenario with heavier charginos and next-to-lightest neutralinos will be given as well. Finally, the “*worst case*” scenario will also be discussed briefly for the case of charginos and next-to-lightest neutralinos decaying equally into all three slepton generations, which has been achieved by setting the soft SUSY breaking parameters of all three slepton generations to the same value. The full details on the MSSM scenarios under investigation can be found in Appendix A.

Finally, it should be kept in mind that these scenarios only serve as an example of more general New Physics models. As long as they exhibit the necessary features, namely significantly populating the background control region while leaving the signal region unaffected, the influence on the background determination would be comparable.

## 4.2.2 Analysis Tools

The technical setup of Monte-Carlo simulation tools used for the  $WW$  background study is very similar to the setup presented in Chapter 3. Again **Herwig++** [81] is used to perform the SUSY particle decays, here in version 2.5.2 [211]. In contrast to Chapter 3 there is no need to use an external parton-level event generator for the hard process, as **Herwig++** has the relevant production modes already built in. This has the advantage that spin correlations between production and decay are included [181]. For the  $q\bar{q} \rightarrow WW$  production process the next-to-leading-order QCD implementation provided by **Herwig++** has been used [212]. It is based on the calculation from [213], matched to parton showers via the **POWHEG** method [214, 215]. For SUSY particle pair production there is no public NLO QCD calculation available that could be interfaced to a parton-shower event generator. Therefore the leading-order matrix elements from

`Herwig++` are used [174, 175], scaled by an appropriate  $K$ -factor ( $K = 1.2$ ), which has been obtained with `Prospino2` [153]. As the experiments do their analyses exclusive in the number of jets, the information on additional jets from QCD radiation is necessary. The parton shower of `Herwig++` has been used to access this information.

This setup has been checked against a combination of `MadGraph 5.1.3` [73] and `Pythia 6.4` [179], which led to comparable results.

The influence of the  $gg \rightarrow WW$  contribution, which is formally a NNLO QCD contribution to  $q\bar{q} \rightarrow WW$ , has been assessed using `gg2WW` [216, 217], interfaced to `Herwig++` via Les Houches event files [180].

Analysis cuts, jet definition and histogram output have been performed with an adapted version of the FORTRAN program described in Chapter 3. The `Herwig++` results have been transferred to the analysis routine via Les Houches event files [180].

### 4.2.3 Event Selection

Both ATLAS [92] and CMS [93] have presented a study of the  $H \rightarrow WW \rightarrow 2\ell 2\nu$  channel with the full data set of 2011. Cuts and methods are largely taken from the ATLAS analysis, because they published the distributions relevant for this discussion in the transverse mass of the W boson pair [218]

$$m_T = \sqrt{(E_T^{\ell\ell} + E_T^{\text{miss}})^2 - |\mathbf{p}_T^{\ell\ell} + \mathbf{p}_T^{\text{miss}}|^2}, \quad \text{with } E_T^{\ell\ell} = \sqrt{|\mathbf{p}_T^{\ell\ell}|^2 + m_{\ell\ell}^2}, \quad E_T^{\text{miss}} = |\mathbf{p}_T^{\text{miss}}| \quad (4.6)$$

in the signal and control regions up to quite high values in  $m_T$ . This gives an opportunity to check if the effects of BSM physics could be identified in the experiment as an excess of particularly hard events. CMS performs a similar analysis, but they only show distributions of the invariant lepton pair mass  $m_{\ell\ell}$  and the azimuthal angle  $\Delta\phi_{\ell\ell}$  between the leptons. These distributions have turned out to be less illuminating concerning the  $H \rightarrow WW$  background determination. However, as the CMS cut selection is similar to the ATLAS one, the results should hold qualitatively for CMS as well.

As this analysis uses 2011 data from LHC it is performed for a center-of-mass energy of 7 TeV. The `POWHEG` event samples are calculated using the `CT10` parton distribution functions [219], while the leading-order SUSY calculations incorporate the `cteq611` PDFs [182]. Renormalization and factorization scales are set to the invariant mass of the W boson pair or the SUSY particle pair, respectively.

For the basic event selection two oppositely charged leptons  $\ell$  (electrons or muons) are required, where the harder lepton with respect to the transverse momentum  $p_T$  is labeled  $\ell_1$ , the softer one  $\ell_2$ . The following cuts are applied, largely taken from [92]:

$$\begin{aligned} p_{T,\ell_1} &> 25 \text{ GeV} & p_{T,\ell_2} &> 15 \text{ GeV} \\ m_{ee(\mu\mu)} &> 12 \text{ GeV} & m_{e\mu} &> 10 \text{ GeV} \\ |m_{ee(\mu\mu)} - M_Z| &> 15 \text{ GeV} & |\eta_\ell| &< 2.5 . \end{aligned} \quad (4.7)$$

The events are categorized according to the number of visible jets. Jets are clustered using the anti- $k_t$  algorithm [186] with distance parameter  $\Delta R = 0.4$  and the following requirements on the rapidity  $\eta_j$  and the transverse momentum  $p_{T,j}$ :

$$|\eta_j| < 4.5 \quad p_{T,j} > 25 \text{ GeV} . \quad (4.8)$$

Leptons that are within the  $R$ -separation  $\Delta R_{j\ell} < 0.3$  of a jet are counted as part of the jet. For the QCD background suppression in the  $H \rightarrow WW$  analysis the LHC experiments use the quantity

$$E_{T,rel}^{miss} = E_T^{miss} \cdot \sin(\min(\Delta\phi, \frac{\pi}{2})), \quad (4.9)$$

where  $E_T^{miss}$  is the missing transverse energy of the event and  $\Delta\phi$  is the azimuthal angle between the  $E_T^{miss}$  vector and the closest lepton or jet with  $p_T > 25 \text{ GeV}$ . The requirement is

$$E_{T,rel}^{miss} > 45 \text{ GeV for } \ell\ell = ee/\mu\mu \quad \text{and} \quad E_{T,rel}^{miss} > 25 \text{ GeV for } \ell\ell = e\mu . \quad (4.10)$$

The spin-0 nature of the Higgs boson is exploited by demanding [187]

$$\Delta\phi_{\ell\ell} < 1.8 . \quad (4.11)$$

The signal region in the 0-jet channel is furthermore restricted in the dilepton transverse momentum  $p_T^{\ell\ell}$

$$p_T^{ee(\mu\mu)} > 45 \text{ GeV} \quad p_T^{e\mu} > 30 \text{ GeV} \quad (4.12)$$

and [188]

$$m_{\ell\ell} < 50 \text{ GeV} . \quad (4.13)$$

For the 1-jet channel ATLAS uses cuts on the vectorial sum of the  $\mathbf{p}_T = (p_x, p_y)$  of jets, leptons and  $\mathbf{p}_T^{miss} = (\not{p}_x, \not{p}_y)$ , and on the  $\tau\tau$  invariant mass  $m_{\tau\tau}$ , calculated in the collinear approximation [220]

$$|\mathbf{p}_T^{l_1} + \mathbf{p}_T^{l_2} + \mathbf{p}_T^j + \mathbf{p}_T^{miss}| < 30 \text{ GeV} \quad |m_{\tau\tau} - M_Z| > 25 \text{ GeV} . \quad (4.14)$$

Events with identified b-jets are rejected, with an assumed b-tagging efficiency of 80% and a 6% mistag rate, taken from the ATLAS study. The  $WW$  control regions for the 0-jet and 1-jet bin are defined by omitting the  $\Delta\phi_{\ell\ell}$  and  $m_{\ell\ell}$  cuts of Eqs. (4.11) and (4.13) and requiring a minimal invariant lepton pair mass of

$$m_{\ell\ell} > 80 \text{ GeV} . \quad (4.15)$$

The 2-jet channel is not considered, as there is not enough statistics in the 2011 datasets from ATLAS and CMS for any conclusions in this channel.

Detector effects, efficiencies and hadronization effects have not been considered directly in the simulation. However, for the comparison with the ATLAS data from [92], these effects are estimated in the conversion of cross sections  $\sigma$  into expected number of events  $N$ : the  $WW$  event number prediction within the 0-jet control region for an integrated

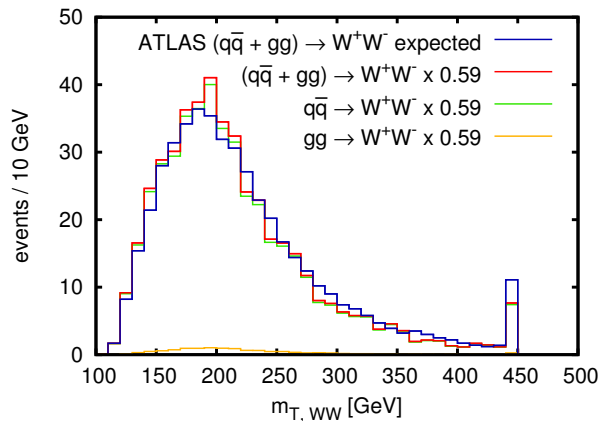


Figure 4.1: Event numbers of the rescaled  $q\bar{q} \rightarrow WW$  and  $gg \rightarrow WW$  contributions in the control region for the 0-jet channel. Additionally the expected event numbers for  $pp \rightarrow WW$  from the ATLAS study [92] are shown.

luminosity of  $4.7 \text{ fb}^{-1}$  (790 events) is normalized to the expected number of events from the ATLAS  $H \rightarrow WW$  study ( $465 \pm 3$  events). From this rescaling the overall efficiency for the evolution of showered parton-level events to reconstructed jets and leptons in the analysis is estimated to be 59%. For the rescaling the  $gg \rightarrow WW$  contribution is taken into account, which is also included in the  $pp \rightarrow WW$  background of the ATLAS study. This part is formally of next-to-next-to-leading order in QCD with respect to the  $q\bar{q} \rightarrow WW$  contribution and adds a few percent to the cross section [91]. The overall effect of the  $gg \rightarrow WW$  contribution on the  $WW$  background normalization is small and will therefore be neglected. The overlay of the rescaled  $m_T$  distribution in the 0-j control region with ATLAS data can be seen in Figure 4.1. The deviations can be attributed to the fact that the experimental efficiency improves for particles with higher energies, which corresponds to higher values of  $m_T$ . However, this uncertainty can be largely eliminated by comparing ratios of event numbers in the study. Still, the accuracy is sufficient for an approximate comparison with ATLAS data.

## 4.3 Results

At first, the effect of the SUSY processes on the  $WW$  background will be discussed for the “base” scenario. Afterwards the dependence on the slepton, LSP and chargino/next-to-lightest neutralino masses will be studied. From the mass dependence a “worst case” scenario is determined, for which the SUSY effects on the  $WW$  background will be quantified by means of a correction factor  $C$ . Finally, this factor  $C$  is also given for scenarios which weaken the tension with the CMS trilepton analysis [209, 210].

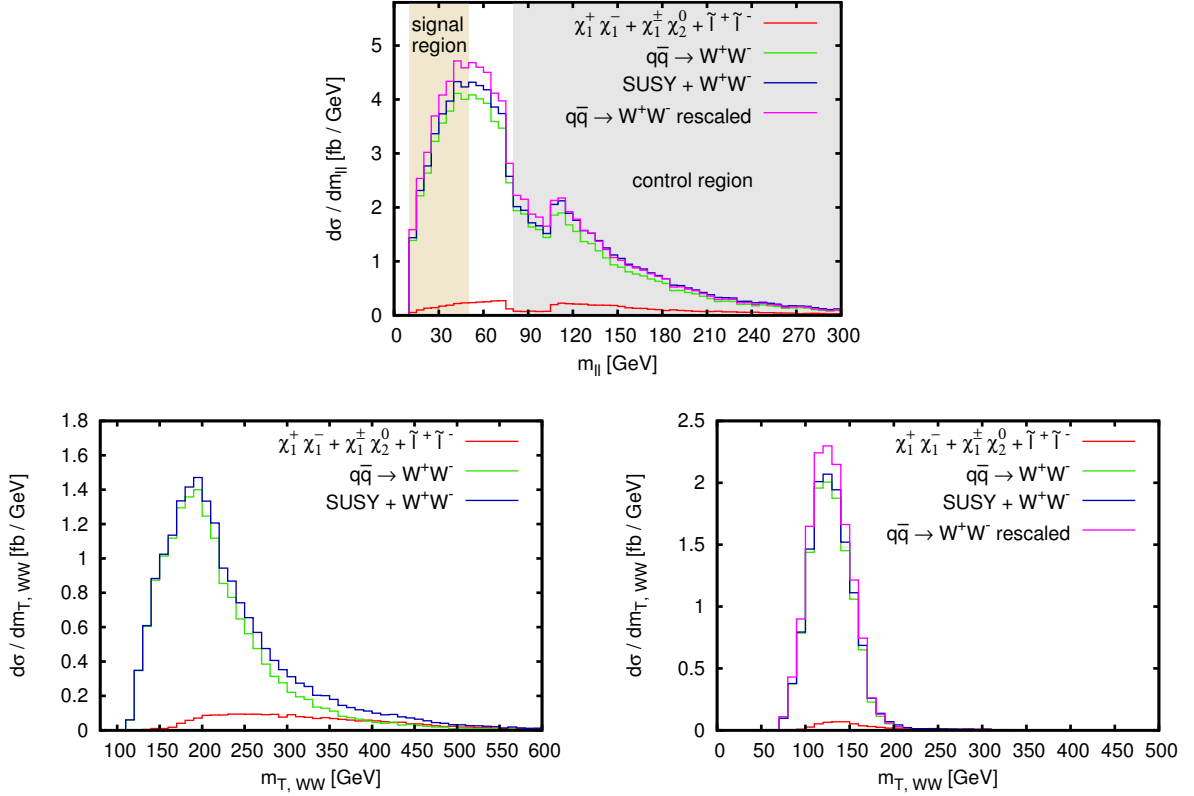


Figure 4.2: Invariant lepton pair mass  $m_{\ell\ell}$  (upper plot) and transverse mass  $m_T$  (lower row) distributions for the 0-jet channel in the “base” scenario. The  $m_{\ell\ell}$  distribution is calculated including the cuts of Eqs. (4.7)–(4.10) and (4.12). The lower left  $m_T$  plot of the control region additionally includes the  $m_{\ell\ell}$  cut of Eq. (4.15). The lower right  $m_T$  distribution of the signal region instead includes the  $m_{\ell\ell}$  cut of Eq. (4.13) and the  $\Delta\phi_{\ell\ell}$  of Eq. (4.11). All plots show the  $q\bar{q} \rightarrow WW$  distribution, the SUSY contributions and their sum. The  $m_{\ell\ell}$  plot and signal region  $m_T$  distribution also show the  $q\bar{q} \rightarrow WW$  result, rescaled by  $(\sigma_C^{WW} + \sigma_C^{SUSY})/\sigma_C^{WW}$ , extracted from the control region.

### 4.3.1 SUSY Background Contribution in the “Base” Scenario

As the 0-jet channel shows the best statistics it shall serve as a starting point for the analysis. The effects of the SUSY processes of Eqs. (4.3)–(4.5) on the  $WW$  background in the full  $m_{\ell\ell}$  range can be seen in the upper half of Figure 4.2. The signal region, located at  $m_{\ell\ell} < 50$  GeV, also includes a cut on  $\Delta\phi_{\ell\ell}$ , Eq. (4.11), which is not taken into account in this figure. In any case, the effect of this cut on the  $WW$  and SUSY processes is very small in the signal region.

Chargino pair production accounts for the largest part of the SUSY signal, especially in the control region, while slepton pair production has larger effects in the low  $m_{\ell\ell}$  region due to the assumed small slepton masses. As stated before, the production of a light chargino and the next-to-lightest neutralino has only a very small contribution and is therefore not important for the background determination.

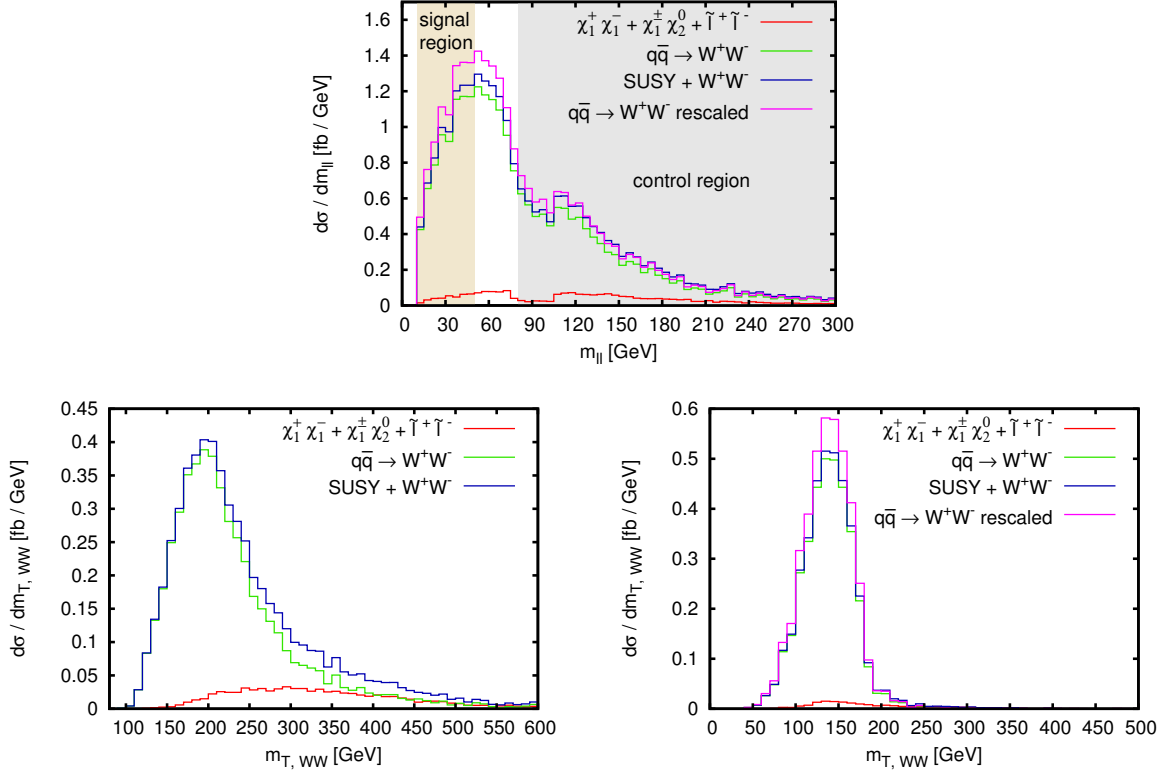


Figure 4.3: The same distributions as in Figure 4.2, but for the 1-jet channel instead of the 0-jet channel.

The relative contribution of the SUSY processes to the signal region is clearly much smaller than the contribution to the control region. Therefore this scenario is potentially dangerous for the data-driven estimation of the  $q\bar{q} \rightarrow WW$  background. From the description of the background determination with a control region in Chapter 2.3.2 follows, that the  $WW$  prediction in the signal region would be rescaled by

$$\frac{\sigma_C^{WW} + \sigma_C^{SUSY}}{\sigma_C^{WW}}, \quad (4.16)$$

if the BSM physics could not be identified. Here,  $\sigma_C^{WW}$  and  $\sigma_C^{SUSY}$  are the cross sections of the  $WW$  and BSM contributions in the control region. For the “base” scenario the  $WW$  prediction for the signal region is clearly too high. Furthermore, the effect on the shape of the  $m_{\ell\ell}$  and  $m_T$  distributions in the signal region is too small for a detection of the SUSY contamination (see lower row of Figure 4.2).

In contrast, a closer look at the transverse mass distribution can reveal the BSM physics effects of this scenario. As  $m_T$  is bounded from below by  $m_{\ell\ell}$  and additional missing transverse energy results in even larger values of  $m_T$ , BSM effects with large  $m_{\ell\ell}$  naturally lead to contributions at high  $m_T$  values. This is especially the case in theories with additional sources of missing energy like the MSSM. The lower right plot of Figure 4.2 shows an enhancement due to the SUSY contributions of more than 100% for  $m_T$  values exceeding 350-400 GeV. ATLAS measured 41 events with  $m_T > 350$  GeV,

with a total background expectation of 48 events, including a  $WW$  contribution of 31 events [92]. Therefore a factor of two increase in the “ $WW$  contribution” is already ruled out with current data.

With the analysis setup described earlier the 1-jet channel can be analyzed as well, though with larger theoretical uncertainties: the SUSY particle pair production processes are generated without jets at leading order and rescaled with a constant  $K$ -factor. Therefore the additional jets only have the leading-log accuracy of the parton shower. The  $WW$  production process on the other hand uses NLO matrix elements matched with the parton shower. Therefore the extra jet is formally of leading-order accuracy.

The situation in the 1-jet bin, depicted in Figure 4.3, is very similar to the 0-jet bin. However, the BSM effects in this channel are much less restricted due to smaller event rates. Therefore, the amount of BSM physics that can hide in the control region is determined by the contribution in the 0-jet channel and in the remainder of this chapter only the 0-jet channel will be considered.

### 4.3.2 Effects of Varying the Chargino, Slepton and LSP Mass

Most of the SUSY contributions arise from chargino pair production. Therefore the kinematics of the final state leptons and the amount of missing transverse momentum depend strongly on the masses of the chargino decay products. In order to determine this dependence, the variation of the soft SUSY breaking parameters  $M_1$ ,  $M_{eL}$  and  $M_{\mu L}$ , which govern the LSP and left-handed slepton masses, is studied in the following. The slepton mass variation also directly modifies the slepton pair production contributions to the signal and the control region. For the identification of a potentially dangerous scenario (regarding the normalization of the  $WW$  background with the help of a control region) the following constraints have to be fulfilled:

- The contribution to the signal region has to be as low as possible.
- The contribution to the control region has to be as large as possible, but still small enough to hide in the shape uncertainties of the control region.
- The part of the control region with high  $m_T$  is strongly constrained by the ATLAS data from early 2012. Therefore the BSM effect in this region has to be small.

With the prescription described in Section 4.2.3 the number of events shown in Figure 4.4 is calculated for a LSP mass of 99 GeV (left diagram) and 124 GeV (right diagram). For each plot the slepton mass is varied up to the chargino mass, bounded from below by the requirement that the lightest neutralino has to be the LSP. These event numbers have to be compared with the following values for the  $q\bar{q} \rightarrow WW$  prediction (Monte Carlo prediction as described in Section 4.2, scaled with the overall efficiency factor 0.59):

$$N_S^{WW} = 336 \quad N_C^{WW} = 454 \quad N_{m_T > 350 \text{ GeV}}^{WW} = 22 \quad N_{m_T > 440 \text{ GeV}}^{WW} = 7, \quad (4.17)$$

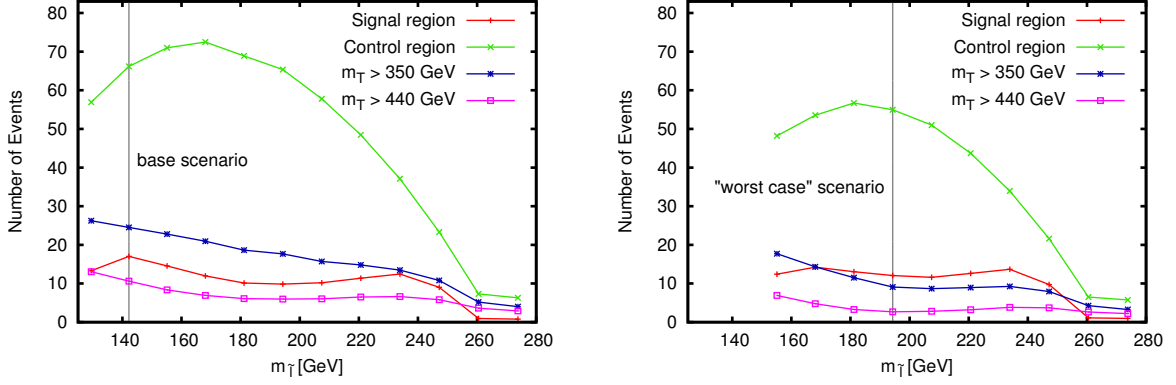


Figure 4.4: Event numbers of the SUSY contributions in the signal region, in the control region with  $m_T > 350$  GeV and  $m_T > 440$  GeV for varying slepton masses of the first two generations. The LSP mass is  $m_{\chi_1^0} = 99$  GeV in the left plot and  $m_{\chi_1^0} = 124$  GeV in the right plot. The discussed “base” and “worst case” scenarios are marked by the vertical line.

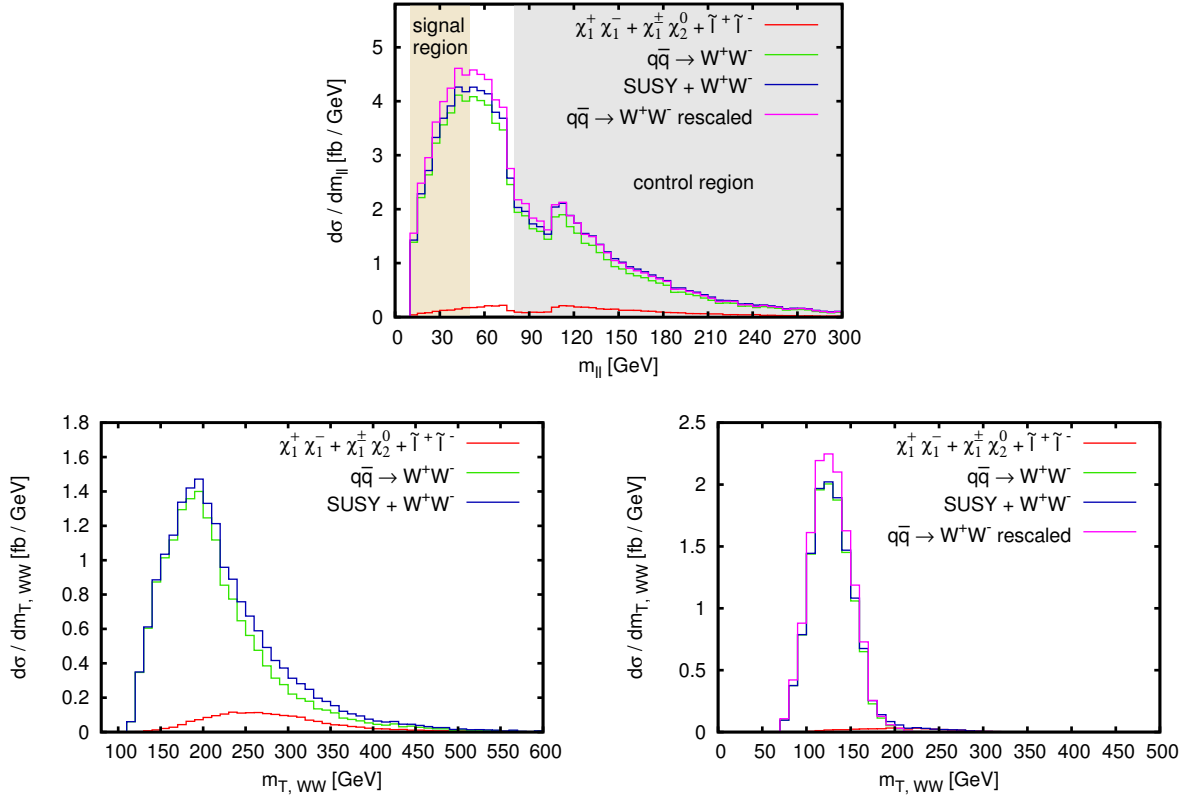


Figure 4.5: The same  $m_{\ell\ell}$  and  $m_T$  distributions in signal and control region as in Figure 4.2, but for the “worst case” scenario.

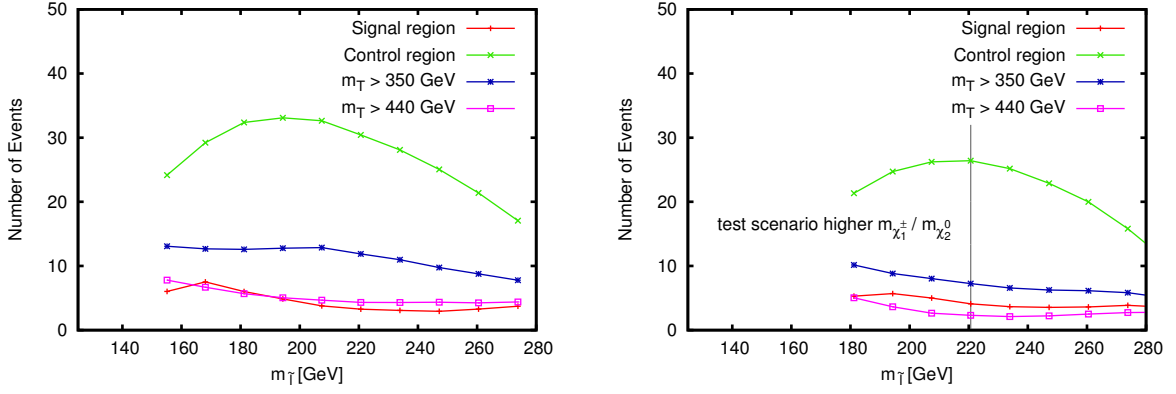


Figure 4.6: The same distributions as in Figure 4.4, but for a chargedino mass of  $m_{\chi_1^\pm} = 308$  GeV instead of  $m_{\chi_1^\pm} = 260$  GeV. The LSP mass is  $m_{\chi_1^0} = 124$  GeV in the left plot and  $m_{\chi_1^0} = 147$  GeV in the right plot. The discussed “test scenario higher  $m_{\chi_1^\pm}/m_{\chi_2^0}$ ” is marked by the vertical line.

or

$$N_{m_T > 350 \text{ GeV}}^{WW} = 31 \quad \text{and} \quad N_{m_T > 440 \text{ GeV}}^{WW} = 11 \quad (4.18)$$

as taken from the ATLAS  $m_T$  distribution [92]. Here,  $N_S^{WW}$  and  $N_C^{WW}$  are the number of expected events due to the  $WW$  production in the signal and control region, respectively. For the event numbers  $N_{m_T > 350 \text{ GeV}}^{WW}$  and  $N_{m_T > 440 \text{ GeV}}^{WW}$  only the high- $m_T$  tail of the control region is considered, with  $m_T > 350$  GeV and  $m_T > 440$  GeV, respectively. As already mentioned, the discrepancy between the ATLAS numbers and the Monte Carlo prediction of this analysis can be ascribed to higher efficiencies for high- $m_T$  events. However, the main results will be based on ratios of event rates or cross sections, which largely eliminates these uncertainties.

A slepton mass roughly in the middle between the LSP and chargedino masses gives the largest contribution to the control region. At the same time, the tail of the  $m_T$  distribution is significantly smaller than for lighter sleptons. Furthermore, the larger slepton mass shifts the slepton pair production contribution from the signal region to the control region. The increased LSP mass in the right plot of Figure 4.4 leads to less available kinetic energy for the decay products and therefore to smaller  $m_{\ell\ell}$ ,  $m_T$  and  $p_T^{miss}$ . This further reduces the contributions in the high- $m_T$  bin of the control region.

Taking the criteria as described above leads to a suitable scenario, labeled as “worst case” scenario. As can be seen in Figures 4.4 and 4.5, this scenario leads to a very small contribution in the high- $m_T$  tail of the control region, small enough so that it cannot be identified at the moment. Additionally, the contributions to the signal region are very small and therefore not noticeable, although they are at partially higher values of  $m_T$  than the  $WW$  background. At the same time the overall contribution to the control region is fairly large, suggesting a substantial effect on the  $WW$  background determination.

Of course not only the masses of the chargedino decay products, but also the chargedino mass itself has an impact on the contribution in the signal and in the  $WW$  control

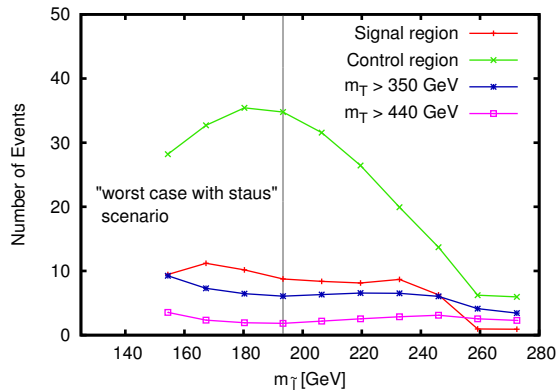


Figure 4.7: The same distributions as in the right plot of Figure 4.4, but for charginos and next-to-lightest neutralinos decaying equally into sleptons of all three generations. The discussed “worst case with staus” scenario is marked by the vertical line.

region, therefore larger chargino masses have also been considered as input (smaller masses are already ruled out by the LHC searches). Additionally, this reduces the tension with the CMS trilepton analysis [209,210]. The larger chargino mass reduces the chargino pair production cross section and therefore leads, as expected, to a reduction of the overall effect. Examples for a chargino mass of  $m_{\chi_1^\pm} = 308$  GeV instead of  $m_{\chi_1^\pm} = 260$  GeV are shown in Figure 4.6. The effect of the scenario labeled as “*test scenario higher  $m_{\chi_1^\pm}/m_{\chi_2^0}$* ” on the  $WW$  background will be briefly discussed at the end of this section as a representative for a scenario with higher chargino and next-to-lightest neutralino masses. Its contributions to the high- $m_T$  part of the control region and the signal region are even smaller than for the “worst case” scenario, while the overall control region contributions are large in the context of higher chargino and next-to-lightest neutralino masses.

As mentioned before, the tension with the CMS trilepton analysis can also be weakened by allowing the chargino and next-to-lightest neutralino to decay into all three slepton generations instead of a decay into sleptons and smuons only. This reduces the SUSY contribution to signal and control region, as can be seen in Figure 4.7. The scenario with the same chargino, next-to-lightest-neutralino, slepton and LSP masses as in the “worst case” scenario, but with comparable  $\chi_1^\pm$  and  $\chi_2^0$  decay fractions into all slepton generations will be discussed in more detail in Section 4.3.4. This scenario will be denoted as “*worst case with staus*” scenario.

### 4.3.3 SUSY Background Contribution in the “Worst Case” Scenario

Finally, the effect of the “worst case” scenario on the  $WW$  background prediction should be quantified by calculating the factor  $C$  by which the expected number of  $WW$  events in the signal region obtained from the normalization would have to be

corrected. The extrapolation from the number of events in the control region  $N_C$  to the number of events in the signal region  $N_S$  is done using [91]

$$N_S = \frac{N_{S,MC}^{WW}}{N_{C,MC}^{WW}} N_C = \alpha \cdot N_C. \quad (4.19)$$

Here,  $N_{S,MC}^{WW}$  and  $N_{C,MC}^{WW}$  are the Monte Carlo predictions for the number of  $WW$  events in the signal and the control region, respectively. Taking both Standard Model  $WW$  production  $N_C^{WW}$  and the BSM effects  $N_C^{SUSY}$  in the control region into account, this leads to a predicted number of background events in the signal region given by

$$N_S^{norm} = \alpha \cdot (N_C^{WW} + N_C^{SUSY}), \quad (4.20)$$

while the actual contribution is

$$N_S^{true} = N_S^{WW} + N_S^{SUSY}, \quad (4.21)$$

with  $N_S^{WW}$  and  $N_S^{SUSY}$  denoting the number of  $WW$  and SUSY events in the signal region, respectively. Therefore the predicted number of events would have to be reduced by

$$C = \frac{N_S^{true}}{N_S^{norm}} = \frac{\sigma_S^{WW} + \sigma_S^{SUSY}}{\sigma_C^{WW} + \sigma_C^{SUSY}} \cdot \frac{\sigma_C^{WW}}{\sigma_S^{WW}} \quad (4.22)$$

where the ratios of event numbers got replaced by the corresponding theoretical cross sections.

For this specific scenario the correction factor is

$$C = 0.924. \quad (4.23)$$

In the ATLAS analysis [92] the experimental data finally serves as an input to a statistical analysis, in which it is fitted to various signal hypotheses. These fits are then used to compute exclusion limits on the Higgs boson mass. For this analysis a selection cut of

$$0.75 \cdot m_H < m_T < m_H \quad (4.24)$$

on the transverse mass is applied. Within this  $m_T$  range the relative BSM contribution of the “worst case” scenario is even smaller, leading to a larger correction for the extraction of the  $WW$  background. In this case the number of  $WW$  events would have to be reduced by a factor of

$$C_{m_T\text{-cut}} = 0.897. \quad (4.25)$$

Since a SM Higgs signal is about 20% of the overall background, an overestimate of 10% in the (dominant)  $WW$  background would lead to a very large underestimate in the size of the extracted Higgs signal.

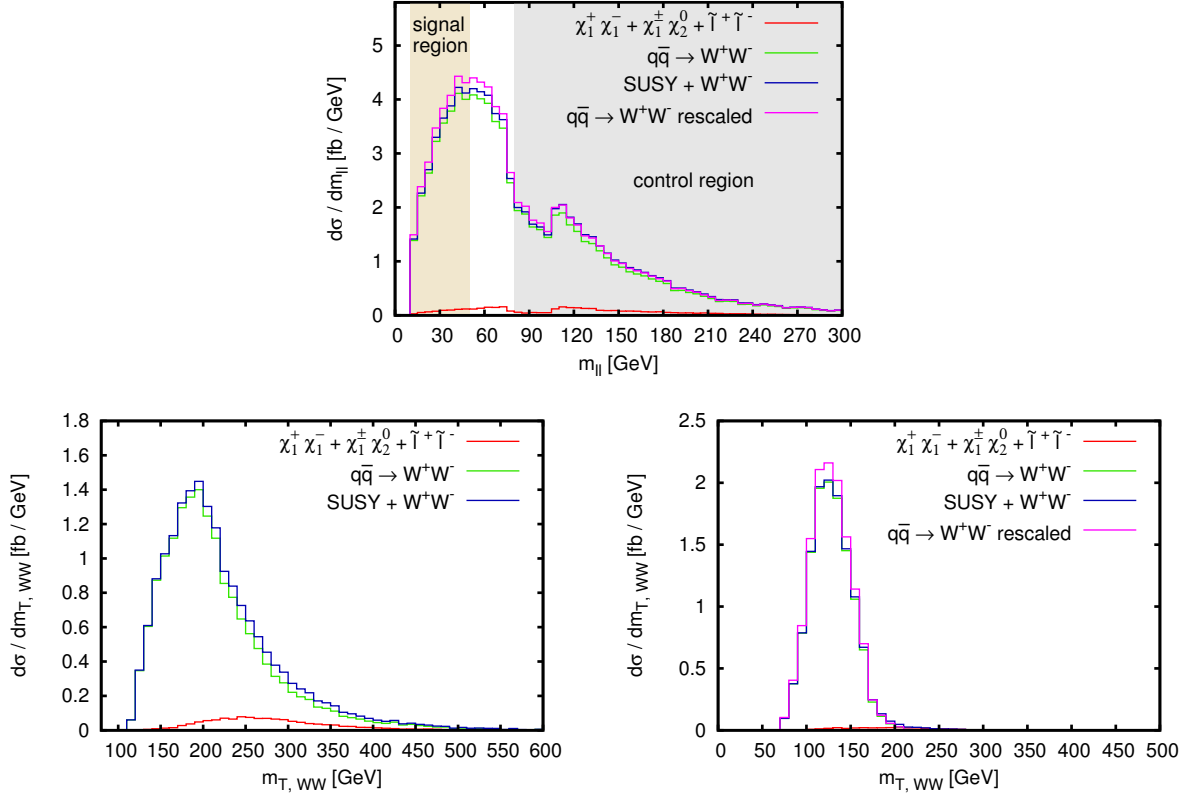


Figure 4.8: The same  $m_{\ell\ell}$  and  $m_T$  distributions in signal and control region as in Figure 4.2, but for the “worst case with staus” scenario.

#### 4.3.4 SUSY Background Contribution in Scenarios with Modified Chargino Parameters

Finally, two possible modifications of the “worst case” scenario will be discussed, which can reduce the tension with the  $5 \text{ fb}^{-1}$  CMS trilepton analysis [209, 210], as they lead to a smaller trilepton signal.

In the first scenario the stau masses are roughly of the same size as the selectron and smuon masses. Hence, the light chargino and the next-to-lightest neutralino have comparable branching ratios into all three slepton generations. Since only a small fraction of the staus leads to an electron or muon in the detector due to the involved tau lepton, this reduces the trilepton signal. Additionally, this leads to a reduction of the dilepton signal from the chargino pair production. Furthermore, the leptons from a tau decay are softer than the directly produced electrons and muons, and a larger fraction of them fails the lepton- $p_T$  cuts. The reduced SUSY contribution to the  $WW$  background can be seen by comparing the  $m_{\ell\ell}$  and  $m_T$  distributions in Figure 4.8 with the ones of the normal “worst case” scenario in Figure 4.5. The reduction for the  $m_T$  distribution in the control region is quite constant over the whole range, while the signal region contributions in the modified scenario are reduced and shifted towards smaller  $m_T$  values. The shape of the  $m_{\ell\ell}$  distribution remains essentially unchanged,

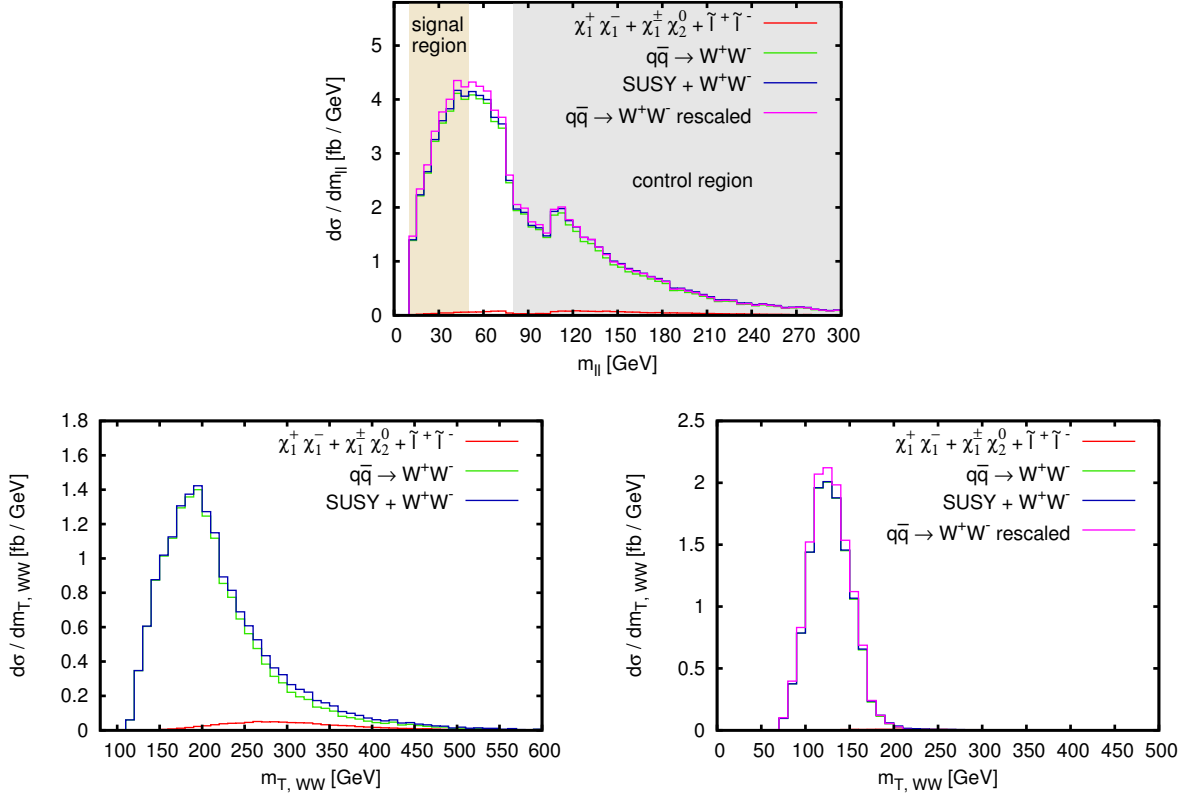


Figure 4.9: The same  $m_{\ell\ell}$  and  $m_T$  distributions in signal and control region as in Figure 4.2, but for the “test scenario higher  $m_{\chi_1^\pm}/m_{\chi_2^0}$ ”.

with only a slight enhancement in the low- $m_{\ell\ell}$  region.

The effect on the  $WW$  background in the “worst case with staus” scenario is reduced by 35–40% with respect to the “worst case” scenario. The background correction factors are

$$C = 0.953 \quad (4.26)$$

without a cut on  $m_T$  in the signal region and

$$C_{m_T\text{-cut}} = 0.934 \quad (4.27)$$

including the cut of Eq. (4.24).

In the “test scenario higher  $m_{\chi_1^\pm}/m_{\chi_2^0}$ ” the masses of the light chargino and the next-to-lightest neutralino are increased from 260 GeV for the “worst case” scenario to roughly 308 GeV. The slepton and LSP masses are changed accordingly to keep the contribution in the high- $m_T$  tail of the control region small. As for the “worst case with staus” scenario these modifications reduce the trilepton signal from  $\chi_1^\pm \chi_2^0$  production and the dilepton signal from  $\chi_1^+ \chi_1^-$  production. The slepton contributions are reduced accordingly, due to the higher slepton masses. The effect of these changes is shown in Figure 4.9. The reduction of the SUSY contribution is enlarged compared to the scenario discussed above. Due to the heavier SUSY particles the low- $m_T$  and low- $m_{\ell\ell}$

regions suffer even more. Especially the signal region, which generally resides at low  $m_{\ell\ell}$  and low  $m_T$ , receives a large reduction.

Since the SUSY contributions to the signal region are extremely small in this scenario, the BSM effect on the  $WW$  background determination is still roughly 55% of the effect in the “worst case” scenario, although the cross section reduction in the control region would suggest an even smaller effect. The corresponding correction factors are

$$C = 0.957 \tag{4.28}$$

without the  $m_T$  cut of Eq. (4.24) and

$$C_{m_T\text{-cut}} = 0.946 \tag{4.29}$$

including it. Due to the very small SUSY contribution in the signal region, the effect of the  $m_T$  cut is smaller than for the other scenarios.

## 4.4 Conclusion

Data driven methods for background determination are widely used at the LHC. Especially at hadron colliders, backgrounds stemming from processes involving quarks and gluons are usually huge. Therefore, the known precision in perturbative calculations of the relevant processes is often not sufficient to completely determine them from Monte Carlo predictions. Additionally, modeling background contributions largely induced by mis-measurements, for example the  $W$ +jets background for the  $H \rightarrow WW$  search [92], where a jet could be misidentified as a lepton, greatly relies on data-driven methods. However, those data-driven methods are only valid if, apart from the searched signal events, no other New Physics contribution exists that would affect the background determination.

This Chapter presented a study on the impact of New Physics contributions on the estimate of the SM background to the  $H \rightarrow WW \rightarrow \ell\bar{\nu}\ell\nu$  search, based on the early-2012 analyses from ATLAS and CMS. A major background for the  $H \rightarrow WW$  search channel is  $WW$  production, which is estimated by means of a control region: The number of events is measured in a high  $m_{\ell\ell}$  region, where no signal events are expected. This measurement is then extrapolated to the softer signal region, using predictions from a SM Monte Carlo for the shape of the  $WW$  distributions. This prescription faces general problems with New Physics effects, which usually occur at high energy scales. Therefore they can naturally enhance the number of events in hard control regions while the contribution in a softer signal region is much smaller. This can lead to an overestimate of the background in the signal region, which would be interpreted as a reduced signal rate.

The  $WW$  background determination in the early-2012  $H \rightarrow WW$  analyses have been discussed in several scenarios within the MSSM. In the first one, the BSM physics contributions cause two effects in the  $WW$  control region. Besides an overall enhancement

of event rates a noticeable change in the shape of the  $m_T$  distribution occurs: the enhancement in the high- $m_T$  tail is much larger than for smaller  $m_T$  values. In the second example the shape changes of distributions are less prominent and could indeed have been missed in the early-2012  $H \rightarrow WW$  analyses. Two additional scenarios have been analyzed, with heavier charginos and next-to-lightest neutralinos and with a modified chargino decay pattern. Both scenarios are harder to exclude in searches, but their effect on the  $WW$  background determination is reduced as well.

The MSSM scenarios described above are just examples of BSM physics which might affect the background determination via control regions, in this case for the  $WW$  background in the  $H \rightarrow WW$  search. Certainly, more recent Higgs boson search analyses [19, 20] and SUSY searches [193–197] did not confirm any of these scenarios. Instead, a new SM-Higgs-like boson has been discovered, where also the  $H \rightarrow WW$  signal strength is compatible with a SM Higgs boson [111, 221]. However, such potential BSM contamination should be kept in mind when interpreting the Higgs boson search data and coupling measurements within BSM scenarios: resulting errors on the measured quantities may be larger than in a pure SM analysis. Especially when aiming for high precision, for example in Higgs boson coupling measurements, even small effects could affect the experimental results.

---

## Multiboson Production with Semileptonic Decays

---

### 5.1 Introduction

Many important processes at hadron colliders involve the production of electroweak bosons: as the  $W$  and  $Z$  bosons obtain their mass due to electroweak symmetry breaking, the  $H \rightarrow ZZ$  and  $H \rightarrow W^+W^-$  channels play an important role in the Higgs boson analyses at the LHC. Their couplings to the Higgs boson,  $HZZ$  and  $HW^+W^-$ , are of particular interest, since the prediction arising from the Higgs mechanism of  $HVV \propto m_V$  has to be confirmed. Moreover, scrutinizing the non-abelian structure of the electroweak symmetry group by testing the triple and quartic gauge boson self couplings is another major task at the LHC. The high center-of-mass energy of the LHC allows for precision measurements of the triple gauge boson couplings and first direct measurements of the quartic couplings. Furthermore, the investigation of the gauge boson self couplings may reveal hints of New Physics at higher scales, beyond the currently available energies in collider experiments. The low-energy effects of these new particles and interactions can be parametrized in a model-independent way by anomalous triple (aTGC) and quartic (aQGC) gauge boson couplings [222, 223].

Certainly, the produced  $W$  and  $Z$  bosons are not directly measurable in the detector due to their short lifetimes. Instead, they are reconstructed from their decay products, which can either be leptons (plus missing energy in case of the  $W$  boson) or hadronic jets. Due to the enormous hadronic activity at a hadron collider, most of the analyses for the bosonic Higgs search channels and multiboson production only consider the leptonic decay modes of the vector bosons. The final-state leptons from the vector boson decay can be detected and measured quite well. Additionally, a signal with several isolated leptons has to face a much lower background than a multi-jet signal.

However, the restriction to fully leptonic decays leads to a significant limitation of the achievable event rates, especially when the production of two or three vector bosons is considered: while most of the  $W$  and  $Z$  bosons decay into a quark-antiquark pair,

$$BR(W \rightarrow \sum q\bar{q}') \approx BR(Z \rightarrow \sum q\bar{q}) = \mathcal{O}(70\%), \quad (5.1)$$

the branching ratios into final states with charged leptons ( $\ell \in \{e, \mu, \tau\}$ ) are much smaller, in particular for the  $Z$  boson,

$$BR(W^+ \rightarrow \sum \ell^+ \nu) = \mathcal{O}(30\%) \quad \text{and} \quad BR(Z \rightarrow \sum \ell^+ \ell^-) = \mathcal{O}(10\%). \quad (5.2)$$

In case of the  $W$  boson the hadronic decay has the additional advantage over the leptonic decay that both decay products are visible, allowing for the reconstruction of the invariant  $W$  boson mass from the decay products. For the  $Z$  boson decay the invariant mass can be reconstructed from the decay products in both decay modes.

The increase in the cross section makes the study of semileptonic decay modes, i.e. with one vector boson decaying hadronically while the other ones decay leptonically, particularly interesting. The fact that the jets from on-shell vector boson decay can be identified by their invariant mass is important to suppress the large background in the semileptonic case due to jets from pure QCD processes. Therefore, the semileptonic Higgs boson search channels are better suited for the search of an additional heavy Higgs boson, with a Higgs boson mass above the  $2m_W/2m_Z$  threshold. In this case both vector bosons coming from the Higgs decay are usually on shell.

First LHC analyses focusing on semileptonic vector boson decays are available in the  $H \rightarrow WW$  [224, 225] and  $H \rightarrow ZZ$  [226–228] channels. For diboson searches in the context of aTGC first studies exist on the combined  $WW + WZ$  channel with semileptonic decays [229, 230]. Finally, the channel  $WW\gamma + WZ\gamma$  with semileptonic decays has been analyzed recently by CMS [231] and limits on aQGC have been derived.

In the past the development of publicly available parton-level Monte Carlo programs with predictions for diboson and triboson production (plus jets) including decays focused on the fully leptonic decay modes. Most of the processes implemented in VBFNLO [145–147], MCFM [232], MC@NLO [233], POWHEG-BOX [234] and gg2VV [235] solely allow for leptonic decays of the vector bosons. There are a few exceptions, namely  $VV$  production in MCFM ( $V \in \{W, Z\}$ ) and a very recent implementation of  $W^+W^-jj$  production in VBF in the POWHEG-BOX [236], which allow for the calculation of semileptonic final states.

The goal of the work described in this chapter is the implementation of semileptonic decay modes into VBFNLO. This program can calculate cross sections and distributions for several processes at hadron colliders, including diboson, triboson and diboson plus two jets in VBF production [146]. Anomalous triple and quartic gauge boson couplings are available in all these processes [237, 238].

The main focus of the semileptonic decay implementation will be on  $VVjj$  production in VBF, since this process class is interesting for several reasons. The investigation of vector boson scattering [239] can contribute to the solution of the puzzle, whether

the newly discovered boson [19, 20] is in fact the Higgs boson responsible for EWSB. In this case it should unitarize the vector boson scattering amplitude at high energies. Additionally, these channels are very promising for aQGC studies. Last but not least,  $VVjj$  in VBF is important for VBF Higgs boson searches in the bosonic decay channels  $H \rightarrow WW$  and  $H \rightarrow ZZ$  with subsequent semileptonic decays, since it contains the Higgs signal as well as the continuum background. Further processes of VBFNLO have also been extended by semileptonic decays: the pure Higgs signal process in VBF now includes the case of one hadronically decaying vector boson. Finally, semileptonic decay modes have been implemented into  $VV$  production and one exemplary triboson process,  $WWZ$  production, as well. The aTGC and aQGC implementation of VBFNLO is available for all calculations with semileptonic final states.

## 5.2 Implementation of Semileptonic Vector Boson Decays in VBFNLO

VBFNLO [145–147] is the parton-level Monte Carlo program which has been chosen for the implementation of the semileptonic vector boson decays. This section covers a brief introduction into VBFNLO, discussing the processes of interest and the organization of the matrix element calculation in the fully leptonic case. Afterwards the details of the implementation of semileptonic vector boson decays and the performed tests and checks will be presented.

### 5.2.1 Overview and Process List

The parton-level Monte Carlo program VBFNLO calculates cross sections and distributions at NLO QCD for many processes involving electroweak bosons. All processes include the fully leptonic decay of the vector bosons. Diboson production plus two jets in VBF, in particular the processes

$$pp \rightarrow W^+W^- jj \rightarrow \ell_1^+ \nu_{\ell_1} \ell_2^- \bar{\nu}_{\ell_2} jj \quad (5.3)$$

$$pp \rightarrow W^\pm W^\pm jj \rightarrow \ell_1^\pm \bar{\nu}_{\ell_1} \ell_2^\pm \bar{\nu}_{\ell_2} jj \quad (5.4)$$

$$pp \rightarrow W^\pm Z jj \rightarrow \ell_1^\pm \bar{\nu}_{\ell_1} \ell_2^\pm \ell_2^- jj \quad (5.5)$$

$$pp \rightarrow ZZ jj \rightarrow \ell_1^+ \ell_1^- \ell_2^+ \ell_2^- jj, \quad (5.6)$$

is important for studies of weak boson scattering, the measurement of triple and quartic gauge boson self couplings as well as for the background estimation to Higgs boson production in vector boson fusion. The current implementation of these processes does not only include doubly resonant contributions, one exemplary Feynman diagram is depicted in the left part of Figure 5.1. Additionally, singly and non-resonant contributions (second and third diagram of Figure 5.1) that contribute to the same leptonic final state are included. Contributions with virtual photons instead of Z bosons are

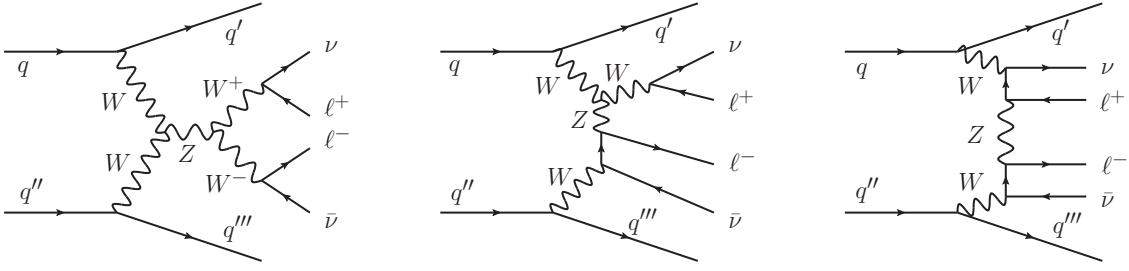


Figure 5.1: Representative Feynman diagrams for  $W^+W^-jj$  production in VBF. The left diagram shows an example of a doubly resonant contribution, the middle and right diagrams are part of the singly and non-resonant contributions.

considered as well. The processes are therefore not defined by their intermediate states, but by specifying the final state and neglecting QCD contributions at LO. However, only the t-channel and u-channel contributions of electroweak  $VVjj$  production are included in the “VBF” processes of VBFNLO. The s-channel contributions<sup>1</sup> and the interference terms between t-channel and u-channel are small in the phase space regions where VBF processes are searched for at the LHC and can therefore be neglected [240]. The small interference effects due to identical leptons in the final state are neglected in all VBFNLO processes [146]. More details on the implementation of the  $VVjj$  processes with leptonic decays can be found in the corresponding original publications [240–243].

For the semileptonic versions of the processes from Eqs. (5.3)–(5.6) the decay products of one vector boson will be replaced by a  $q\bar{q}'$  pair, not only in the case of a real vector boson decay, but also for all non-resonant contributions. The substitution of a  $\ell_i \nu_i$  pair with a  $q\bar{q}'$  pair will be called “hadronic W boson decay”, the interchange of a  $\ell^+ \ell^-$  pair with a  $q\bar{q}$  pair will be denoted as “hadronic Z boson decay”. This leads to the following  $VVjj$  production processes in VBF with semileptonic decays,

$$pp \rightarrow W^+W^- jj \rightarrow q\bar{q}' \ell^- \bar{\nu}_\ell jj \quad (5.7)$$

$$pp \rightarrow W^+W^- jj \rightarrow \ell^+ \nu_\ell q\bar{q}' jj \quad (5.8)$$

$$pp \rightarrow W^\pm W^\pm jj \rightarrow \ell^\pm \bar{\nu}_\ell q\bar{q}' jj \quad (5.9)$$

$$pp \rightarrow W^\pm Z jj \rightarrow q\bar{q}' \ell^+ \ell^- jj \quad (5.10)$$

$$pp \rightarrow W^\pm Z jj \rightarrow \ell^\pm \bar{\nu}_\ell q\bar{q} jj \quad (5.11)$$

$$pp \rightarrow ZZ jj \rightarrow \ell^+ \ell^- q\bar{q} jj, \quad (5.12)$$

which have been implemented into VBFNLO.

Since the  $\mathcal{O}(\alpha_s)$  corrections of the fully leptonic process do not affect the leptons and neutrinos from the vector boson decays, the hadronic decays obtained with the prescription described above are at leading order in the perturbative expansion. The NLO QCD corrections occurring in the fully leptonic processes and in the semileptonic processes will be denoted as “NLO QCD corrections of the production process”. NLO

<sup>1</sup>The classification into s-channel, t-channel and u-channel refers to the production mode of the final-state quark pair.

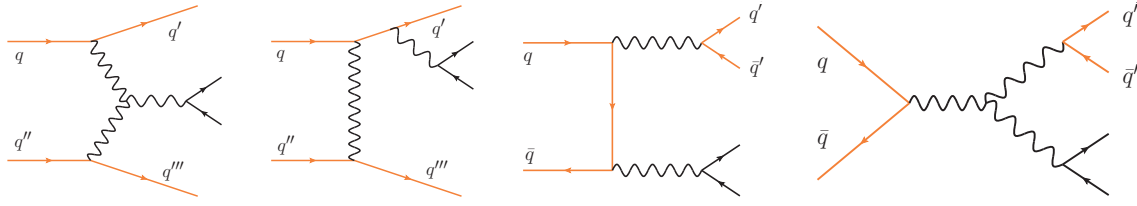


Figure 5.2: Representative Feynman diagrams for  $Vjj$  production with leptonic vector boson decay. The first and second graphs show examples of t-channel contributions, while the third and fourth graphs show the corresponding diagrams with an s-channel production of the final-state quark pair.

QCD corrections affecting the quark line of the hadronic vector boson decay (“NLO decay”) and corrections connecting this quark line and the partons already present in the fully leptonic decay processes will be discussed in Section 5.2.2.4.

The diboson production processes without additional jets at leading order,

$$pp \rightarrow W^+W^- \rightarrow \ell_1^+ \nu_{\ell_1} \ell_2^- \bar{\nu}_{\ell_2} \quad (5.13)$$

$$pp \rightarrow W^\pm Z \rightarrow \ell_1^\pm \bar{\nu}_{\ell_1} \ell_2^\pm \ell_2^- \quad (5.14)$$

$$pp \rightarrow ZZ \rightarrow \ell_1^+ \ell_1^- \ell_2^+ \ell_2^-, \quad (5.15)$$

are available as well, including the  $gg$ -initiated processes, which are formally of next-to-next-to-leading order with respect to the  $q\bar{q}$  initiated processes. As for the other processes, also singly resonant contributions leading to the same leptonic final state are considered. The diboson processes with semileptonic decays,

$$pp \rightarrow W^+W^- \rightarrow q\bar{q}' \ell^- \bar{\nu}_\ell \quad (5.16)$$

$$pp \rightarrow W^+W^- \rightarrow \ell^+ \nu_\ell q\bar{q}' \quad (5.17)$$

$$pp \rightarrow W^\pm Z \rightarrow q\bar{q}' \ell^+ \ell^- \quad (5.18)$$

$$pp \rightarrow W^\pm Z \rightarrow \ell^\pm \bar{\nu}_\ell q\bar{q} \quad (5.19)$$

$$pp \rightarrow ZZ \rightarrow \ell^+ \ell^- q\bar{q}, \quad (5.20)$$

are of interest for testing the triple gauge couplings. Additionally, for the sake of the implementation itself, they are a good starting point for the semileptonic decay implementation, since they are the simplest processes for which semileptonic vector boson decays are possible. Finally, diboson production with semileptonic decays yields the s-channel contributions to electroweak  $Vjj$  production at LO. As for  $VVjj$  production, the t-channel contributions are already available in VBFNLO, denoted as “single vector boson production plus two jets in VBF” (shown in the first two diagrams of Figure 5.2). The s-channel contributions, depicted in the last two diagrams of Figure 5.2, are negligible once cuts designed for vector boson fusion analyses are applied. They become important once more inclusive cuts are used. With the inclusion of all semileptonic  $VV$  production processes the s-channel graphs to  $Vjj$  production in VBF can now be calculated within VBFNLO. By treating the s-channel and t-channel contributions as separate processes the interference effects between s-channel and t-channel are still

missing, but they are small for VBF processes [244] and thus can be neglected. The “full”  $Zjj$  production at LO with leptonic decays at  $\mathcal{O}(\alpha^4 \alpha_s^0)$  in VBFNLO then consists of the “VBF process”  $Zjj$ ,  $W^\pm Z$  production with a hadronically decaying  $W^\pm$ , and  $ZZ$  production with one  $Z$  decaying into a  $q\bar{q}'$  pair. The full electroweak production of  $W^\pm jj$  is carried out similarly by calculating  $W^\pm jj$  in VBF and  $W^+W^-$  plus  $W^\pm Z$  with semileptonic decays. For  $Vjj$  production at NLO QCD some minor contributions of the “s-channel part” are still missing, since the semileptonic  $VV$  processes obtained by the replacement of a  $\ell_i \nu_i$  or a  $\ell^+ \ell^-$  pair with a  $q\bar{q}'$  pair do not include the QCD corrections connected to the decay quarks. An approximate inclusion of NLO QCD effects in the hadronic decay will be discussed in Section 5.2.2.4.

The triboson production processes are a much larger class. Like  $VVjj$  production in VBF they have contributions with quartic vector boson vertices and are therefore used for studies of aQGC [231, 245]. VBFNLO has the full set of possible triboson processes with leptonic decays available, including all processes with final-state photons. Semileptonic decays have been implemented exemplary for one of these processes, namely  $W^+W^-Z$  production [246],

$$pp \rightarrow W^+W^-Z \rightarrow \ell_1^+ \nu_{\ell_1} \ell_2^- \bar{\nu}_{\ell_2} \ell_3^+ \ell_3^- . \quad (5.21)$$

Again, all off-shell effects contributing to the same leptonic final state are included. This process with leptonic decays leads to three processes with semileptonic decays,

$$pp \rightarrow W^+W^-Z \rightarrow q\bar{q}' \ell_1^- \bar{\nu}_{\ell_1} \ell_2^+ \ell_2^- \quad (5.22)$$

$$pp \rightarrow W^+W^-Z \rightarrow \ell_1^+ \nu_{\ell_1} q\bar{q}' \ell_2^+ \ell_2^- \quad (5.23)$$

$$pp \rightarrow W^+W^-Z \rightarrow \ell_1^+ \nu_{\ell_1} \ell_2^- \bar{\nu}_{\ell_2} q\bar{q}' . \quad (5.24)$$

The  $WWZ$  production process serves only as an example process. Several other triboson processes, namely  $WWW$ ,  $ZZW$ ,  $ZZZ$ ,  $WW\gamma$ ,  $WZ\gamma$  and  $ZZ\gamma$  production, have important semileptonic decay channels as well: on the one hand for the vector boson self coupling studies, and on the other hand providing the missing s-channel contributions for the  $VVjj$  production processes from Eqs. (5.3)–(5.6).

Finally, semileptonic decays have also been implemented for the pure Higgs boson signal processes [144] in VBF with decays into  $W$  and  $Z$  bosons

$$pp \rightarrow H jj \rightarrow W^+W^- jj \rightarrow \ell_1^+ \nu_{\ell_1} \ell_2^- \bar{\nu}_{\ell_2} jj \quad (5.25)$$

$$pp \rightarrow H jj \rightarrow ZZ jj \rightarrow \ell_1^+ \ell_1^- \ell_2^+ \ell_2^- jj , \quad (5.26)$$

which yields the processes

$$pp \rightarrow H jj \rightarrow W^+W^- jj \rightarrow q\bar{q}' \ell^- \bar{\nu}_\ell jj \quad (5.27)$$

$$pp \rightarrow H jj \rightarrow W^+W^- jj \rightarrow \ell^+ \nu_\ell q\bar{q}' jj \quad (5.28)$$

$$pp \rightarrow H jj \rightarrow ZZ jj \rightarrow q\bar{q} \ell^+ \ell^- jj \quad (5.29)$$

$$(5.30)$$

with semileptonic decay modes. As already mentioned before, these channels are particularly interesting for Higgs boson masses larger than the threshold of a decay into on-shell vector bosons of  $2 \cdot m_V$ .

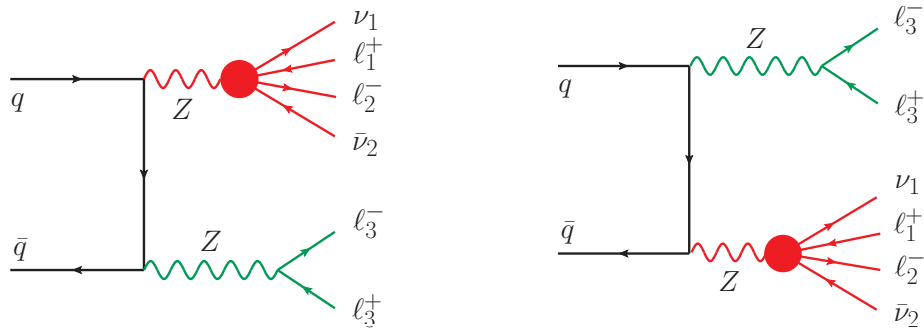


Figure 5.3: Illustration of “leptonic tensors” (red and green) in  $WWZ$  production. The big blob in the red leptonic tensor represents all possible subdiagrams that contribute to  $Z \rightarrow \ell_1^+ \nu_1 \ell_2^- \bar{\nu}_2$ .

The structure of the matrix element calculation for the already existing processes with fully leptonic decays is very well suited for the implementation of the semileptonic decays, since the leptonic and the hadronic parts of the calculation are carried out separately. The leptonic part of the calculation consists of several “leptonic tensors” [240], which are off-shell currents representing the subamplitudes from the vector bosons attached to the quark lines decaying into the final-state leptons. The propagator factors of the attached vector bosons are included in the leptonic tensors. Examples of such leptonic tensors in  $WWZ$  production are depicted in Figure 5.3. The red leptonic tensor there consists of all subamplitudes contributing to

$$Z \rightarrow \ell_1^+ \nu_1 \ell_2^- \bar{\nu}_2. \quad (5.31)$$

For the processes with fully leptonic decays the introduction of the leptonic tensors leads to an enormous speed-up. The subamplitudes encoded in the tensors occur several times in different Feynman diagrams and different subprocesses, but have to be calculated only once per phase space point. They facilitate the implementation of semileptonic decays as well, since the only parts of the matrix element calculation which have to be altered are the leptonic tensors. This holds both for the LO and the NLO decay, given that graphs with a color-connection between production and decay can be neglected. More details will be given in Section 5.2.2.4. There is no necessity of redundant changes in several parts of the matrix elements. Additionally, the part affected by NLO corrections to the production process does not have to be modified and these NLO corrections can be taken from the fully leptonic process. Certainly, once the leptonic tensors are modified, they are no longer restricted to vector bosons and leptons as constituents. For the sake of simplicity, the name “leptonic tensors” will still be kept for the processes with semileptonic decays.

## 5.2.2 Implementation Details

Major modifications due to the semileptonic decay implementation at leading order occur in the leptonic tensors. However, a few other points have to be taken into

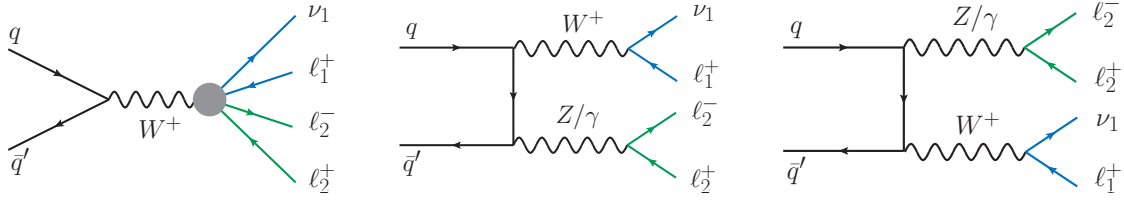


Figure 5.4: Feynman Diagrams of  $W^+Z$  production at LO. The leptonic tensor depicted in the left diagram contains all subamplitudes contributing to  $W^+ \rightarrow \ell_1^+ \nu_1 \ell_2^+ \ell_2^-$ . The leptonic tensors of the second and third diagram only include the resonant decay of one vector boson. The “ $W^+$  decay products” are marked in blue, the “ $Z/\gamma$  decay products” are marked in green.

account in order to get a numerically stable result. NLO corrections to the hadronic decay and the approximation used in the semileptonic decay implementation will be discussed briefly.

### 5.2.2.1 Modified Leptonic Tensors for Semileptonic LO Decays

The leptonic tensors for the semileptonic case are based on the implementations of Refs. [237, 238], which include anomalous triple and quartic gauge boson couplings for the fully leptonic process. Additionally, all new diagrams that have to be included for the semileptonic case are implemented using the gauge boson vertex expressions from Refs. [237, 238], including the anomalous couplings. Thus they are supported for all processes with semileptonic decays. The necessary modifications will be discussed in the following, taking the process of  $W^+Z$  production of Eq. (5.14) for the leptonic case and Eqs. (5.18) and (5.19) for the semileptonic case as an example. The topologies occurring in this process are depicted in Figure 5.4. Here, the only leptonic tensor including both doubly and singly resonant contributions is

$$W^+ \rightarrow \ell_1^+ \nu_{\ell_1} \ell_2^+ \ell_2^-, \quad (5.32)$$

which is shown in the left part of Figure 5.4. Therefore the modifications due to the hadronic decay of one vector boson are discussed by means of this leptonic tensor. All quarks and leptons emerging in the leptonic tensors are considered being massless.

For the resonant contributions the transition from leptonic to semileptonic decays, shown in Figure 5.5, is simple. For the hadronic W boson decay the amplitude calculation is almost unchanged, since the coupling of W bosons to quarks and leptons/neutrinos (with a coupling constant  $GF$ ) is the same. The only difference that has to be taken into account is the additional factor  $C = 3$  from summing over the colors of the final-state quarks, which does not occur for the colorless leptons/neutrinos. For the hadronic  $Z/\gamma$  decay also the couplings have to change, since Z bosons and photons couple differently to leptons ( $GZL/GAL$ ), up-type quarks ( $GZU/GAU$ ), and down-type quarks ( $GZD/GAD$ ), respectively.

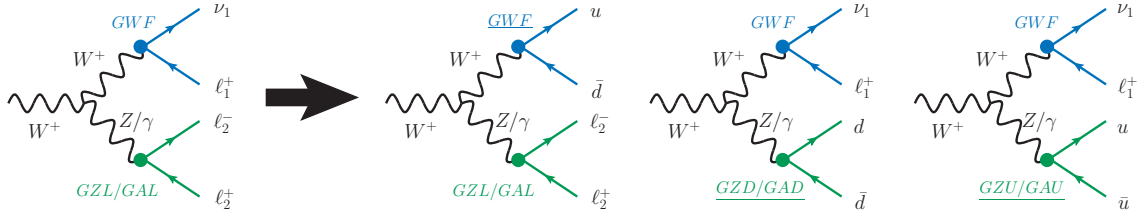


Figure 5.5: Left plot: Feynman diagram of the doubly resonant contributions for the leptonic tensor from Eq. (5.32), with fully leptonic decays. The same is shown additionally for the case of a “hadronic  $W^+$  decay” and a “hadronic  $Z/\gamma$  decay” into  $d\bar{d}$  and  $u\bar{u}$ , respectively.

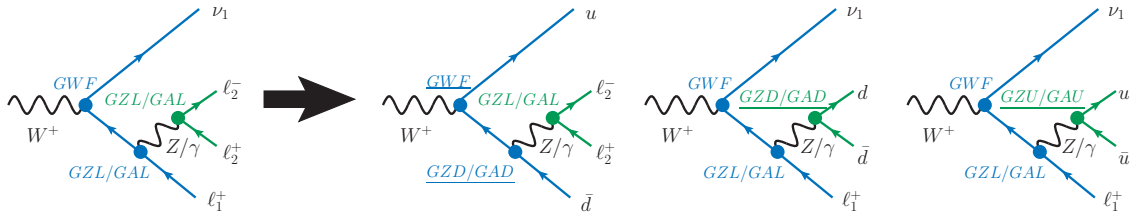


Figure 5.6: Feynman diagram of the singly resonant contributions of Eq. (5.32) which contain a  $Zff$  coupling along the fermion line of the “hadronic  $W^+$  decay products”. The diagrams depict the following cases: fully leptonic decays, “hadronic  $W^+$  decay” and “hadronic  $Z/\gamma$  decay” into  $d\bar{d}$  and  $u\bar{u}$ , respectively.

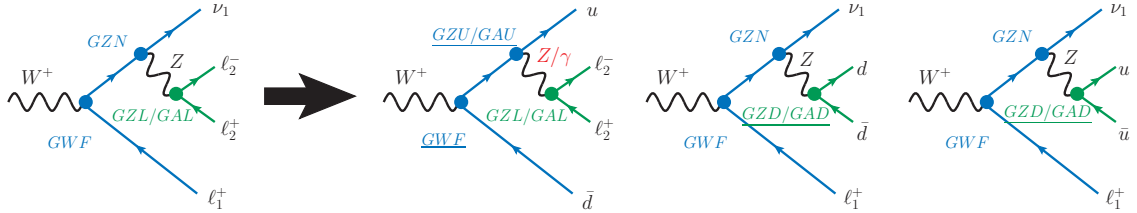


Figure 5.7: Feynman diagram of the singly resonant contributions of Eq. (5.32) which do not contain a  $\gamma$  contribution in the leptonic case due to the missing  $GAN$  coupling in the SM. The diagrams depict the following cases: fully leptonic decays, “hadronic  $W^+$  decay” and “hadronic  $Z/\gamma$  decay” into  $d\bar{d}$  and  $u\bar{u}$ , respectively.

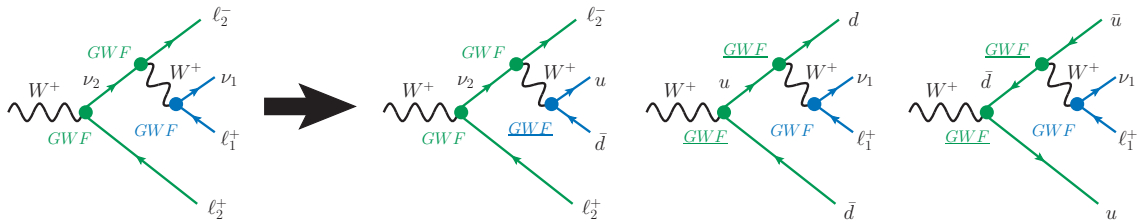


Figure 5.8: Feynman diagram of the singly resonant contributions of Eq. (5.32) which contain two  $GWF$  couplings along the fermion line of the “hadronic  $Z/\gamma$  decay products”. The diagrams depict the following cases: fully leptonic decays, “hadronic  $W^+$  decay” and “hadronic  $Z/\gamma$  decay” into  $d\bar{d}$  and  $u\bar{u}$ , respectively.

The implementation of semileptonic decays for the single and non-resonant contributions implies further modifications. Firstly, Z bosons and virtual photons also occur in the “hadronic W boson decay” and their couplings have to be modified accordingly (see Figure 5.6). Additionally, new Feynman diagrams have to be considered, since a coupling of  $u\bar{u}\text{-}\gamma$  ( $GAU$ ) is possible while the corresponding leptonic vertex  $\nu\bar{\nu}\text{-}\gamma$  ( $GAN$ ) does not exist. Therefore some topologies, which were only possible with Z bosons as internal particles in the leptonic case are now allowed for internal photons as well (see Figure 5.7). Finally, for the hadronic Z boson decay with an  $u\bar{u}$  pair as final-state quarks the orientation of the quark line in diagrams with two  $GW$  couplings along the quark line has to be flipped, since the weak isospin quantum number of the lepton in the original calculation and the u-quark differ in their sign (see Figure 5.8).

The changes discussed so far are the only ones necessary for the matrix element calculation with semileptonic decays into a specific  $\ell^+\nu/\ell^+\ell^-$  and  $q\bar{q}'$  pair. For hadronic decays into all relevant light quark combinations an additional factor of two has to be applied for the case of a hadronic W boson decay, since a  $W^+$  ( $W^-$ ) can decay into  $u\bar{d}$  ( $d\bar{u}$ ) and  $c\bar{s}$  ( $s\bar{c}$ ). The result for the hadronic Z boson decay consists of two times the  $Z/\gamma \rightarrow u\bar{u}$  contribution and two or three times the  $Z/\gamma \rightarrow d\bar{d}$  contribution, depending on whether b-quarks in the final state should be allowed. The desired vector boson decay products can be selected in the VBFNLO input file.

Many further small changes to VBFNLO are necessary for the successful run of semileptonic decay processes, e.g. in the process initialization, in the phase space, in the jet and cut definition and for event and histogram output. The list of changes to the VBFNLO functions due to the implementation of semileptonic decays is given in Appendix B.

### 5.2.2.2 Virtual Photon Contributions in the “Hadronic Z Boson Decay”

All diboson and triboson processes with semileptonic decays have well-defined cross sections at LO in production and decay if two visible jets with non-vanishing transverse momenta are required, except for the processes with leptonic  $Z/\gamma$  decays. For these processes additional cuts on the leptons of the  $Z/\gamma$  decays are needed in order to avoid singularities in the  $\gamma \rightarrow \ell^+\ell^-$  decay, since the leptons are considered being massless. The cross sections of the VBF processes with semileptonic decays and a leptonically decaying W boson are finite if four visible jets are being requested. In case of a leptonically decaying  $Z/\gamma$  again additional cuts on its decay products are needed.

When the NLO QCD corrections of the production process are taken into account these requirements are no longer sufficient. Singularities in the calculation of NLO QCD corrections which already appear in the fully leptonic case are treated by the implementation of the Catani-Seymour dipole subtraction method [247]. As mentioned before, these parts of the calculation can be taken directly from the existing implementation of the fully leptonic processes. However, additional problems arise for the semileptonic decay processes in two different domains. On the one hand, collinear singularities can occur due to a virtual photon splitting in two massless quarks. This leads to unstable results in all processes with a hadronic  $Z/\gamma$  decay if the contributions

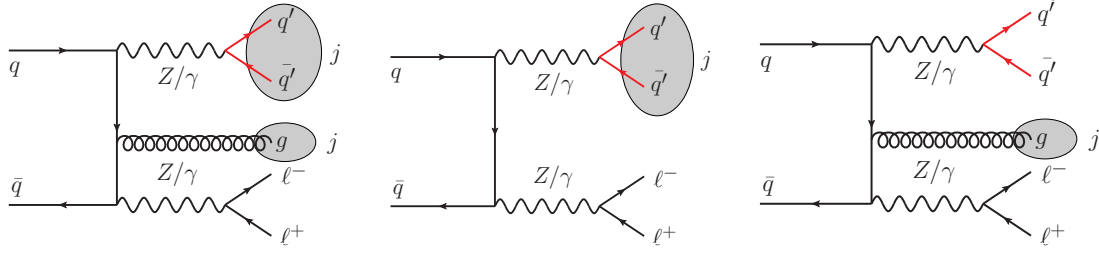


Figure 5.9: Possibly divergent configurations in  $ZZ$  production with semileptonic decays due to a  $\gamma \rightarrow q\bar{q}$  decay. A grey blob marks a single visible jet.

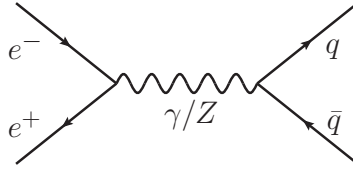


Figure 5.10: Feynman diagram for  $e^+e^- \rightarrow \text{hadrons}$ .

from photons with low  $Q^2$  are not eliminated. On the other hand contributions with t-channel photon exchange can lead to collinear singularities in the VBF processes. The former issue will be discussed in the following, the latter one will be handled in Section 5.2.2.3.

For the semileptonic decay processes the contributions with only one jet for the diboson and triboson processes and three jets for the  $VVjj$  processes in VBF are interesting as well, since they allow for both decay quarks to be collimated in one jet. This is in particular interesting for analyses with boosted kinematics [248]. For these selection criteria the problems with virtual photon decays and t-channel photons set in already at LO. However, the strategies leading to finite cross sections are the same and no additional divergences arise.

In the following, the problems arising from the decay of a virtual photon into a massless  $q\bar{q}$  pair in the “hadronic Z decay” will be discussed by means of the  $ZZ$  production process with semileptonic decays. When two visible jets are demanded the real-emission contribution of the NLO production process is problematic. Since there are three partons in the final state, the two jets from the  $Z/\gamma$  decay can cluster into one jet while the parton from the real emission provides the other jet. The  $Z/\gamma$  itself can be significantly boosted, providing the necessary  $p_T$  for the jet cut, while the virtuality  $Q_\gamma^2$  of the  $\gamma$  contribution is not restricted, leading to a divergence for  $Q_\gamma^2 \rightarrow 0$ . The same situation occurs at LO if only one visible jet is requested. In the real-emission configuration of the one-jet case the jet(s) from the hadronic decay can even end up completely untagged. All three situations are depicted in Figure 5.9.

In reality the divergence in the  $\gamma \rightarrow q\bar{q}$  decay is regularized by finite meson masses, with two times the mass of the neutral pion as lower bound. Since neither quark masses, nor the subsequent hadronization into mesons are taken into account in the parton-level Monte Carlo, the divergence has to be regularized in a different way. One

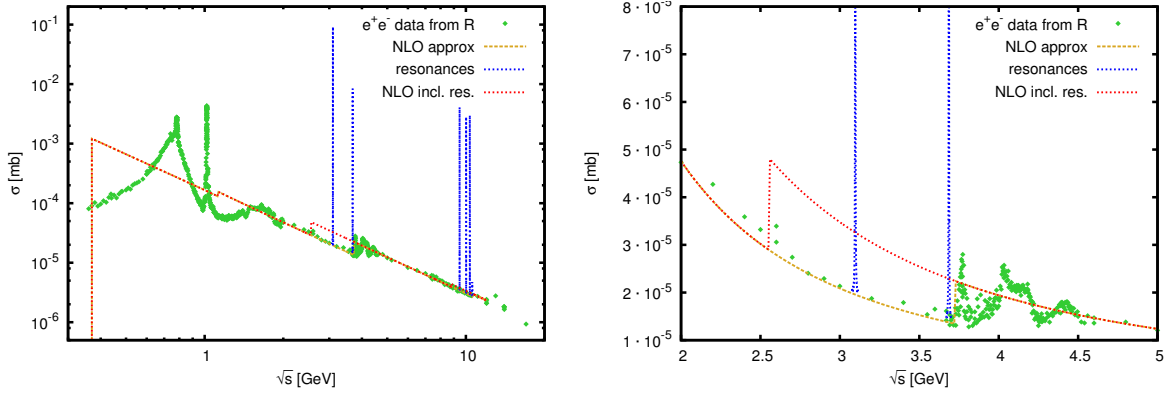


Figure 5.11: Cross section of  $e^+e^- \rightarrow \text{hadrons}$  as a function of the center-of-mass energy. The left figure displays the whole energy range of interest for the virtual photon decay, while the right figure shows the threshold region of the charm quark.

possible solution is the restriction to the phase space region of on-shell vector boson production by introducing a cut on the invariant jet (pair) mass. Another solution is the introduction of individual cutoffs on  $Q_\gamma^2$ , depending on the quark flavor of the hadronic decay. This method will be discussed in the following. The kinematics of the  $\gamma \rightarrow q\bar{q}$  decay around the  $q\bar{q}$  thresholds will certainly not be described well, given that the neglected mass effects play a crucial role for the kinematics there. However, these details are not important here, since the  $Z/\gamma$  decay products of the low- $Q^2$  region will be anyway clustered into a single jet or remain completely undetected. Therefore it is sufficient to describe the rates of the low  $Q_\gamma^2$  regime near thresholds in a reasonable way.

The hadronic  $Z/\gamma$  decay part of  $ZZ$  production with semileptonic decays and the process  $e^+e^- \rightarrow \text{hadrons}$  [249] are very much alike, which can be seen in the comparison of Figure 5.9 and Figure 5.10. Furthermore,  $e^+e^- \rightarrow \text{hadrons}$  has been measured very well in the energy regime up to  $\approx 10$  GeV, especially around the  $q\bar{q}$  threshold regions. Therefore this process can be used for the determination of the  $Q_\gamma^2$  thresholds at which a certain quark flavor should be included into the hadronic final state of the  $Z/\gamma$  decay. A graph showing the measured cross sections of  $e^+e^- \rightarrow \text{hadrons}$  in the relevant energy range is depicted in the left plot of Figure 5.11. A compilation of all experimental results can be found in Ref. [250]. Additionally, the experimental data is available at <http://pdg.lbl.gov/current/xsect/>.

The process  $e^+e^- \rightarrow \text{hadrons}$  is usually discussed by means of the observable [249]

$$R(s) = \frac{\sigma_{e^+e^- \rightarrow \text{hadrons}}(s)}{\sigma_{e^+e^- \rightarrow \mu^+\mu^-}(s)} = R_{\text{EW}}(s)(1 + \delta_{\text{QCD}}(s)). \quad (5.33)$$

For the relevant center-of-mass energy range  $\sqrt{s} \ll M_Z$  the  $Z$  boson contribution can be neglected. Therefore  $R_{\text{EW}}$ , the electroweak prediction of  $R$ , reads

$$R_{\text{EW}}(s) = 3 \sum_{q(s)} e_q^2, \quad (5.34)$$

	resonances	$\sqrt{s_1}$	$\sqrt{s_2}$
b-quark	$\Upsilon(1S), \Upsilon(2S), \Upsilon(3S), \Upsilon(4S)$	10.58 GeV	10.58 GeV
c-quark	$J/\psi, \psi(2S)$	3.73 GeV	4.50 GeV
s-quark	–	1.00 GeV	1.85 GeV
u+d-quark	–	0.36 GeV	1.00 GeV

Table 5.1: Narrow resonances and “threshold regions”  $[\sqrt{s_1}, \sqrt{s_2}]$  considered in the quark threshold determination. For the  $b\bar{b}$  threshold  $\sqrt{s_1} = \sqrt{s_2}$ , since the experimental data shows a rather clean step at 10.58 GeV.

where  $e_q$  is the electric charge of quark  $q$  and finite-quark-mass effects have been neglected. The sum over quark flavors in Eq. (5.34) includes all active quarks at the given energy  $\sqrt{s}$ , i.e.  $\sqrt{s} > 2 \cdot m_q$ . The quark mass thresholds are therefore encoded in  $R_{\text{EW}}$ . The QCD corrections to  $R$  at NLO QCD,  $\delta_{\text{QCD}}(s)$ , and the cross section of the process  $e^+e^- \rightarrow \mu^+\mu^-$  are given by

$$\delta_{\text{QCD}}(s) = \frac{\alpha_s(s)}{\pi} \quad (5.35)$$

$$\sigma_{e^+e^- \rightarrow \mu^+\mu^-}(s) = \frac{4}{3} \frac{\pi \alpha^2}{s}. \quad (5.36)$$

Thus, using the Equations (5.33)–(5.36), the NLO approximation of the cross section for  $e^+e^- \rightarrow \text{hadrons}$  can be written as

$$\sigma_{\text{NLO}}(s) = \frac{4\pi\alpha^2}{s} \left( \sum_{q(s)} e_q^2 \right) \left( 1 + \frac{\alpha_s(s)}{\pi} \right). \quad (5.37)$$

Certainly, the NLO QCD approximation to  $\sigma_{e^+e^- \rightarrow \text{hadrons}}$  described so far does not include any resonance effects around the thresholds. However, the contribution of a resonance  $i$  can be described by [250]

$$R_{\text{res},i}(s) = \frac{9}{\alpha^2} \frac{s \Gamma_{ee,i} \Gamma_{\text{tot},i} s/M_i^2}{(s - M_i^2)^2 + M_i^2 \Gamma_{\text{tot},i}^2}, \quad (5.38)$$

assuming a Breit-Wigner shape for the resonances. Here  $\Gamma_{ee,i}$  and  $\Gamma_{\text{tot},i}$  are the physical partial decay width into electrons and the total width of the resonance, respectively, and  $M_i$  denotes its mass. All resonance parameters are taken from the PDG review [249]. As mentioned before, the kinematics of the resonance contributions is not important. The event rate information of the resonance contributions can be included into the NLO prediction by lowering the corresponding quark mass threshold  $s_f$  accordingly.

With the elements described above the  $Q_f^2$  threshold for the inclusion of a quark of flavor  $f$  into the  $Z/\gamma \rightarrow q\bar{q}$  decay, is determined from the corresponding energy threshold  $s_f$  of  $e^+e^- \rightarrow \text{hadrons}$  in the following way: The starting point for the quark threshold is the lower boundary  $\sqrt{s_1}$  of the corresponding threshold region. This boundary is defined

decay quark	minimal $Q_\gamma$
b-quark	8.77 GeV
c-quark	2.56 GeV
s-quark	1.13 GeV
u+d-quark	0.373 GeV

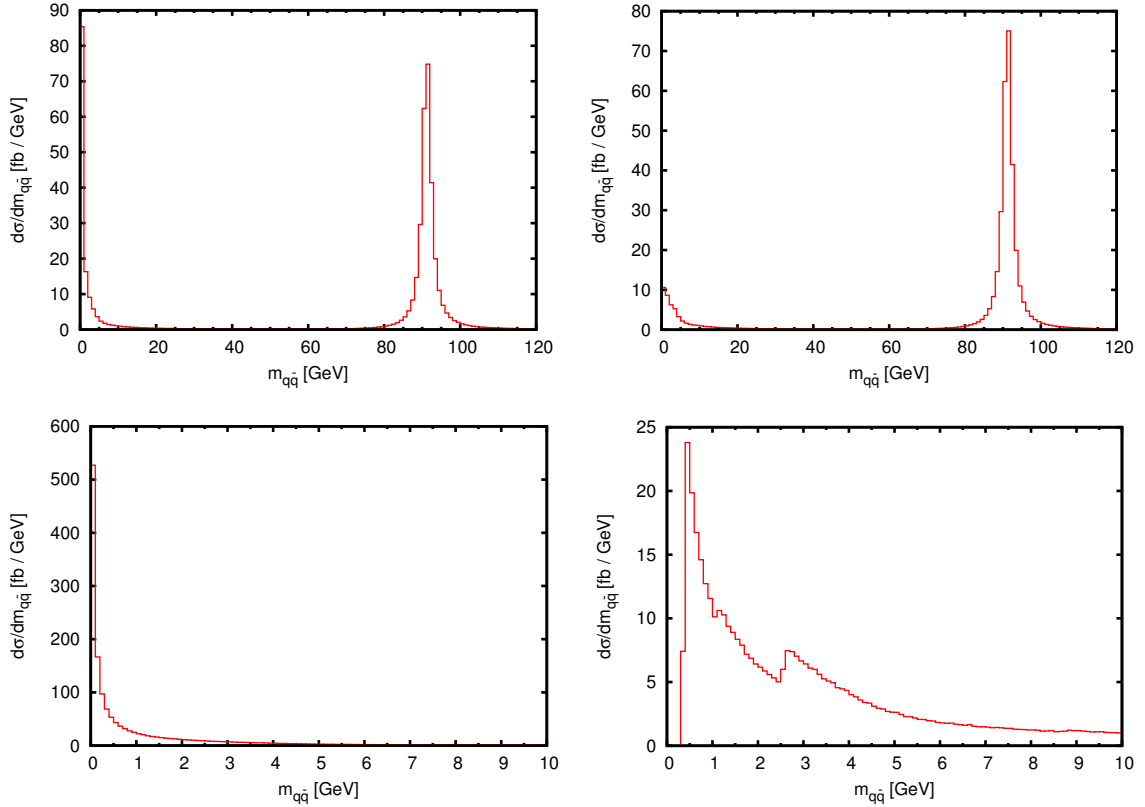
Table 5.2:  $Q_\gamma$  thresholds used in the  $Z/\gamma \rightarrow q\bar{q}$  calculation.

Figure 5.12: Invariant mass distribution of the  $q\bar{q}$  pair in  $pp \rightarrow ZZ$  production with semileptonic decays. In the left plots no cut on the virtuality of the hadronically decaying photon is applied (except for a small cut that ensures a finite result). The right plots incorporate the thresholds from Table 5.2. Upper and lower row differ only by the mass range. The following cuts have been applied:  $p_T^j > 20$  GeV,  $|\eta_j| < 4.5$ ,  $\Delta R_{jj} > 0.4$ ,  $p_T^\ell > 10$  GeV,  $|\eta_\ell| < 2.5$ ,  $m_{\ell\ell} > 15$  GeV,  $\Delta R_{\ell\ell} > 0.4$ ,  $\Delta R_{j\ell} > 0.4$ . The calculation is carried out at LO for a center-of-mass energy of 8 TeV. The different peak heights for small invariant masses in the upper and lower row arise solely from a different binning.

as the energy, at which the impact of the quark of flavor  $f$  onto the measured cross section becomes noticeable, neglecting any sharp resonances. The upper boundary  $\sqrt{s}_2$  of the threshold region denotes the energy at which the measured cross section again matches the NLO approximation of  $\sigma_{e^+e^- \rightarrow \text{hadrons}}$  from Eq. (5.37), denoted as  $\sigma_{\text{NLO}}$ . The quark threshold is then modified by taking into account two contributions that are not described by  $\sigma_{\text{NLO}}$ : the narrow resonances and the threshold effects, which lead to the difference between  $\sigma_{\text{NLO}}$  and the experimental cross sections in the threshold region. This prescription is realized by solving

$$\int_{\sqrt{s}_f}^{\sqrt{s}_1} d\sqrt{s} \sigma_{\text{NLO}}^f(\sqrt{s}) = \sum_i \int d\sqrt{s} \left( R_{\text{res},i}(\sqrt{s}) \cdot \sigma_{e^+e^- \rightarrow \mu^+\mu^-}(\sqrt{s}) \right) + \int_{\sqrt{s}_1}^{\sqrt{s}_2} d\sqrt{s} \left( \sigma_{\text{exp}}(\sqrt{s}) - \sigma_{\text{NLO}}(\sqrt{s}) \right) \quad (5.39)$$

for  $\sqrt{s}_f$ . The left-hand side describes the changes to the quark threshold, the first term of the right-hand side represents the narrow resonances and the last term represents the correction due to the threshold effects. Here,  $\sigma_{\text{exp}}(\sqrt{s})$  is the interpolated curve based on the measured cross sections. The contribution of a quark  $f$  to  $e^+e^- \rightarrow \text{hadrons}$  is given by the expression  $\sigma_{\text{NLO}}^f$ .

Table 5.1 lists the narrow resonances considered for each quark flavor. Broader resonances, e.g.  $\phi(1020)$  in case of the s-quark threshold, are included in the experimental data. The energy range  $[\sqrt{s}_1, \sqrt{s}_2]$  considered in the threshold determination of a certain quark flavor is given in the table as well. The calculation has been carried out with **Mathematica 8.0**, using the program package **RunDec** [251] for the running of  $\alpha_s$ , with  $\alpha_s(M_Z) = 0.1184$  [252]. For  $\sqrt{s} < 1$  GeV, where QCD approaches the non-perturbative regime, the value  $\alpha_s(1 \text{ GeV})$  has been used. Figure 5.11 shows the experimental cross section data for  $e^+e^- \rightarrow \text{hadrons}$ , the Breit-Wigner approximation of the additional narrow resonances and the NLO QCD approximation, with and without the inclusion of the narrow resonance contributions. The left plot includes all quark thresholds, while the right plot displays the charm-quark threshold region.

The effect of the inclusion of the thresholds from Table 5.2 into the  $Z/\gamma \rightarrow q\bar{q}$  decay of  $ZZ$  production with semileptonic decays is shown in Figure 5.12. The invariant mass distributions of the two quarks from the  $Z/\gamma$  decay are generated by a LO calculation. At least one jet of  $p_T > 20$  GeV is demanded, which corresponds to the middle plot of Figure 5.9. The distributions in the left plots are calculated without a lower bound on the photon virtuality.<sup>2</sup> The steep increase due to the divergence for  $m_{q\bar{q}} \rightarrow 0$  is clearly visible. Once the quark thresholds are included (right plots), the divergence is gone and the numerical stability of the code improves significantly. In the lower right plot the charm and strange quark thresholds are clearly visible.

However, interfacing VBFNLO with a parton-shower Monte Carlo may cause problems for semileptonic decay processes, since the low  $Q_\gamma^2$  threshold for u-quark and d-quark of

<sup>2</sup>A very small cut of  $Q^2 > 0.0001 \text{ GeV}^2$  has been used for numerical stability.

0.37 GeV is in a regime where the parton-shower is no longer applicable. Events with  $m_{q\bar{q}} < 2 \cdot m_q$  may be dismissed as well by the parton shower. Therefore a user-definable low- $Q^2$  cut has been included, which can be used to cut this cumbersome contribution.

### 5.2.2.3 Treatment of t-channel Photon Contributions in the VBF Processes

The VBF processes  $W^+W^-jj$ ,  $W^\pm Zjj$  and  $ZZjj$  include contributions with a t-channel photon exchange. These contributions can become divergent in the real-emission part of the NLO production for the fully leptonic and semileptonic decay channels. When only three visible jets are demanded in the semileptonic case the problems arise already at leading order. Figure 5.13 shows an exemplary Feynman graph with a photon in the t-channel for each divergent contribution of both decay channels. The real-emission contribution is assumed to emerge from the upper quark line. For a QCD radiation off the lower quark line the situation is equivalent. The numerical results discussed in this context have been calculated for a high Higgs boson mass,  $m_H = 600$  GeV, and a rather large jet distance parameter,  $\Delta R_{jj} = 0.8$ , in order to enhance the fraction of events with boosted kinematics, where both decay jets form a single jet. The typical VBF cuts are applied ( $\Delta\eta_{jj} > 4$ ,  $\eta_1 \cdot \eta_2 < 0$ ,  $m_{jj} > 600$  GeV), including the requirement that the leptons should fall inside the rapidity gap of the tagging jets. For the fully leptonic processes the two jets with largest transverse momentum have been selected as tagging jets, while for the semileptonic processes the two jets with largest rapidity separation have been chosen. More details on defining tagging jets in semileptonic decay processes will follow in Section 5.3.1.

The divergence due to t-channel photon exchange in the VBF processes with fully leptonic decays has been analyzed in Ref. [244]. The method to circumvent the numerical evaluation of the divergent contribution described there has been applied to all VBF processes with t-channel photons implemented in **VBFNLO**. A collinear  $q \rightarrow q\gamma$  divergence arises in the real-emission diagram of Figure 5.13 (upper left plot) if the two partons from the upper quark line form two visible jets: in that case there are no restrictions on the  $p_T$  of the final-state quark from the lower quark line and therefore the momentum transfer of the radiated photon is not constrained. This contribution can be interpreted as QED correction to another process, namely  $p\gamma \rightarrow W^+W^-jj$ , i.e. the collinear divergence is absorbed into the NLO definition of the photon distribution inside a proton. Therefore the t-channel photon contributions with a momentum transfer below  $Q_\gamma^2 = 4 \text{ GeV}^2$  are not calculated as a part of  $pp \rightarrow W^+W^-jj$  production in VBF, but are counted towards  $p\gamma \rightarrow W^+W^-jj$ , which is not included in **VBFNLO**. For the phase space region relevant in VBF studies the missing part is very small and can be neglected [244]. The impact of the low- $Q_\gamma^2$  contribution is estimated by lowering the cut on the photon virtuality from  $Q_\gamma^2 > 4 \text{ GeV}^2$  to  $Q_\gamma^2 > 0.1 \text{ GeV}^2$ . The effect of this change on the  $pp \rightarrow W^+W^-jj \rightarrow \ell_1^+ \nu_1 \ell_2^- \bar{\nu}_2 jj$  cross section with VBF cuts, depicted in Table 5.3, is indeed very small.

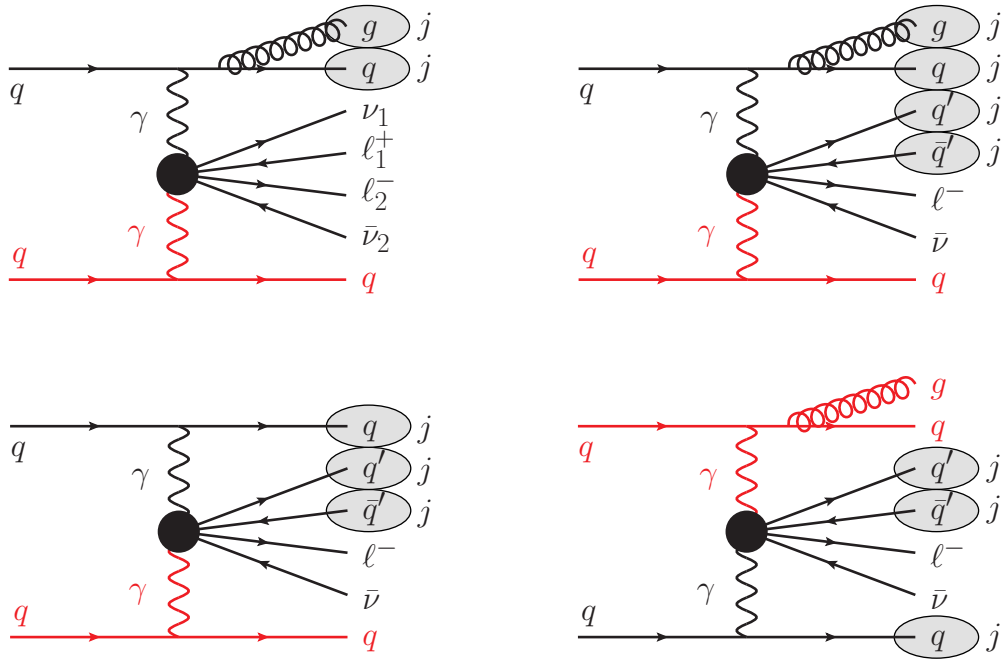


Figure 5.13: Feynman diagrams for t-channel photon contributions with collinear singularity in  $W^+W^-jj$  production via VBF. The upper left plot is for the fully leptonic decay, the upper right plot for the semileptonic decay with 4 jets required, the lower plots are for the semileptonic decays with three jets required. Identified jets are marked with a gray ellipse. The parts exhibiting the divergence are highlighted in red.

	minimal number of jets	$m_{j(j)}^V$ not restricted	$ m_{j(j)}^V - m_V  < 20 \text{ GeV}$
$W^+W^-jj \rightarrow \ell_1^+ \nu_1 \ell_2^- \bar{\nu}_2 jj$	2	0.02 %	–
$W^+W^-jj \rightarrow q\bar{q}\ell^-\bar{\nu}jj$	4	0.91 %	0.06 %
$W^+W^-jj \rightarrow q\bar{q}\ell^-\bar{\nu}jj$	4 (3)	0.84 %	0.05 %
$W^+W^-jj \rightarrow q\bar{q}\ell^-\bar{\nu}jj$	3	4.7 %	0.05 %
$ZZjj \rightarrow \ell_1^+ \ell_1^- \ell_2^+ \ell_2^- jj$	2	0.015 %	–
$ZZjj \rightarrow q\bar{q}\ell^+\ell^-jj$	3	0.040 %	0.006 %

Table 5.3: Relative changes in the cross section of NLO  $VVjj$  production in VBF due to lowering the cut on the virtuality of the t-channel photon from  $Q_\gamma^2 > 4 \text{ GeV}^2$  to  $Q_\gamma^2 > 0.1 \text{ GeV}^2$ . The reconstructed invariant vector boson mass is denoted by  $m_{j(j)}^V$ . Typical VBF cuts on the tagging jets have been applied ( $\Delta\eta_{jj} > 4$ ,  $m_{jj} > 600 \text{ GeV}$ ). The minimal jet number “4 (3)” denotes the case where in general four jets are required. However, if both  $V$  decay products form a single jet, then three visible jets are sufficient to pass the cuts.

	minimal number of jets	$m_{j(j)}^V$ not restricted	$ m_{j(j)}^V - m_V  < 20 \text{ GeV}$
$W^+W^- jj \rightarrow q\bar{q} \ell^- \bar{\nu} jj$	4	33.3 fb	25.3 fb
$W^+W^- jj \rightarrow q\bar{q} \ell^- \bar{\nu} jj$	4 (3)	41.8 fb	33.1 fb
$W^+W^- jj \rightarrow q\bar{q} \ell^- \bar{\nu} jj$	3	55.8 fb	33.2 fb

Table 5.4: Cross sections of NLO  $W^+W^-jj$  production in VBF with semileptonic decay of the vector bosons for different numbers of required jets in the final state. The minimal jet number of 4 (3) denotes the case where three jets are only allowed if the  $V$  decay products form a single jet.

Naturally, this configuration occurs for the semileptonic decays with four identified jets as well (upper right plot Figure 5.13) with, however, a substantially larger effect. This can be attributed to the fact that the two additional jets enhance the possibility that events with a soft t-channel photon pass the VBF cuts. Once an invariant jet pair mass close to the mass of the vector boson  $m_V$  is requested the possibility of a decay jet serving as tagging jet is reduced and the size of the t-channel photon effect is as small as for the fully leptonic decay.

In the three-jet case, which is important for VBF analyses with boosted kinematics, the divergence arises already at leading order (lower left plot of Figure 5.13). This has a substantially larger impact on the cross section as can be seen in Table 5.3. Still, the cross section of the low- $Q_\gamma^2$  fraction is small with respect to the other contributions. In this case even NNLO corrections to  $p\gamma \rightarrow W^+W^-jj$  arise in the real-emission part of the calculation, which is depicted in the lower right plot of Figure 5.13. These contributions are again cut off by the requirement  $Q_\gamma^2 > 4 \text{ GeV}^2$ . However, once the existence of a jet (pair) with an invariant mass close to the mass  $m_V$  of the decayed vector boson is required, the low- $Q_\gamma^2$  contribution in the three-jet case is of the same order as it is for four jets.

The additional divergences in the three-jet case (lower row of Figure 5.13) can be avoided by demanding that three jets are only allowed if the two quarks from the hadronic decay form a single jet. This restriction is justified since these events form the phenomenologically interesting part of the three-jet contribution. Once a cut is applied restricting the invariant jet (pair) mass to a region around the mass of the decayed vector boson, the cross sections of both jet selection criteria approach each other. Corresponding numbers are listed in Table 5.4.

Qualitatively the situation for  $ZZjj$  production in VBF is very similar to the  $W^+W^-jj$  case: without a restriction on the invariant jet (pair) mass for the hadronically decaying boson the effect is larger than for the fully leptonic decay. Once this restriction is applied, the change of the cross section due to the lower  $Q_\gamma^2$  cut approaches the level of the leptonic case. However, the overall effect is much smaller: resonant  $ZZjj$  production is dominated by t-channel  $W$  exchange, since there exists no triple neutral

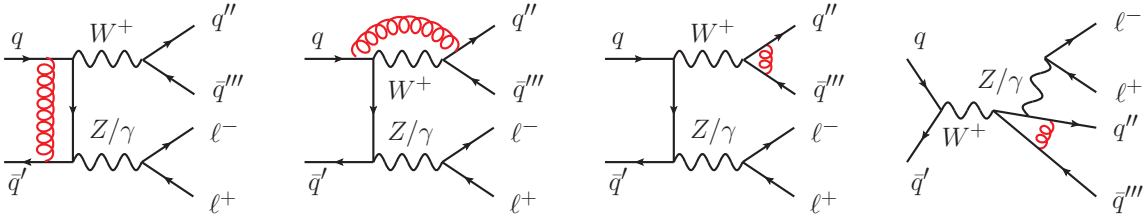


Figure 5.14: Exemplary one-loop Feynman diagrams of different categories for  $W^+Z$  production. From left to right: corrections to quark line from production process, corrections connecting quark lines from production and decay and corrections of the vector boson decay, both for on-shell and off-shell contributions.

gauge boson couplings the  $Z$  boson radiation off a t-channel  $Z/\gamma$  is forbidden and the VBF cuts suppress the  $Z/\gamma$  radiation directly from the quark lines.

#### 5.2.2.4 NLO Corrections to the Hadronic Decay

The virtual part of NLO QCD corrections to processes with semileptonic decays can be separated into three classes of corrections, which are depicted in Figure 5.14, taking  $W^+Z$  production as an example. The first type of corrections consists of diagrams with loops along the quark line(s) of the production process. These corrections are already part of the fully leptonic processes and their implementation can be directly used for the semileptonic case as well. The implementation of NLO QCD effects for the production process naturally also includes the effects of real-emission contributions with radiation from the corresponding quark lines.

Contributions from Feynman graphs with loops connecting the quark lines from production and decay of the vector bosons are very small or even absent due to color structures and/or kinematic features, depending on the particular process. For diboson and triboson production with semileptonic decays no interference with the Born diagrams is possible. Interference of the virtual part with the tree-level diagrams of electroweak  $Vjj$  production in VBF and with  $\mathcal{O}(\alpha_s^2\alpha^2)$  contributions to  $Vjj$  production with leptonic decays exist, but they are color suppressed and small [158, 253]. For the VBF processes with semileptonic decays again contributions from the interference of one-loop diagrams and the considered Born diagrams are forbidden by color algebra, since interference effects between t-channel and u-channel diagrams are not taken into account. In summary, one-loop corrections connecting production and decay of the vector bosons do not contribute to the semileptonic processes within the approximations used in VBFNLO. Therefore the NLO corrections of the production and decay part of the calculation can be treated independently.

The Feynman diagrams of the  $VVjj$  and  $VV(V)$  production processes with semileptonic decays can be split into the ones where the  $q\bar{q}$  pair stems from resonant production and decay of a vector boson (e.g. third diagram of Figure 5.14) and the ones where

the  $q\bar{q}$  pair arises from off-shell effects (e.g. fourth diagram of Figure 5.14 for  $W^+Z$  production or third diagram of Figure 5.1 in case of  $W^+W^-jj$  production in VBF).

The NLO corrections of the hadronic vector boson decay are known [254] and quite small, they yield a  $K$ -factor of

$$K_{V \rightarrow q\bar{q}} = \left(1 + \frac{\alpha_s}{\pi}\right) \approx 1.038. \quad (5.40)$$

These NLO contributions, which include vertex corrections and the corresponding real-emission diagrams, are the only ones that play a role for the hadronic decay in the processes with resonant vector boson production. They are the same NLO QCD corrections as for  $R$  in  $e^+e^- \rightarrow$  hadrons, since the hadronic  $\gamma \rightarrow q\bar{q}$  decay is the only part of that calculation which receives corrections at NLO in QCD. The NLO QCD corrections of the off-shell contributions on the other hand are more involved. For diboson production the virtual contributions include up to box-type graphs (right plot of Figure 5.14), for triboson production and for the VBF processes even pentagons are possible. However, the by far largest contribution of the considered processes arises from the resonant production. For example for  $WWZ$  production the off-shell diagrams add merely a few per-cent to the cross section. Therefore the approximation of applying a factor of

$$\left(1 + \frac{\alpha_s(Q^2)}{\pi}\right) \quad (5.41)$$

onto the whole cross section, similarly to  $e^+e^- \rightarrow$  hadrons or the hadronic vector boson decay, is justified. This describes the NLO effects on the true hadronic vector boson decay very well, while the quite small off-shell effects are most certainly not described accurately. However, the overall impact of this error is small. Effects of cuts on the additional radiation off the jets from the hadronic decay in the NLO case on the other hand cannot be investigated with this prescription. The scale of the strong coupling constant in Eq. (5.41) is taken as the invariant mass of the decaying vector boson, analogous to  $e^+e^- \rightarrow$  hadrons. Likewise, for the photon contributions with  $Q^2 < 1$  GeV the scale is fixed at 1 GeV. The inclusion of the factor denoted in Eq. (5.41) in the cross section calculation is optional and can be switched on via the VBFNLO input files.

### 5.2.3 Tests and Comparisons

Most of the changes due to the semileptonic decay implementation in VBFNLO are inside the leptonic tensors. Therefore comparisons with MadGraph-generated [72] matrix elements and leptonic tensors constitute the largest part of the performed checks. In addition, checks at the level of total cross sections and comparisons with MCFM [232] have been performed.

### 5.2.3.1 Pointwise Tests of Leptonic Tensors and Matrix Element Calculation

The original leptonic tensors consist of HELAS [255] calls generated by MadGraph [72]. For the implementation of anomalous gauge boson couplings [237, 238] these have been already modified by exchanging the HELAS calls for the gauge boson vertices with versions incorporating the anomalous couplings. The anomalous couplings part of the semileptonic decay tensors has been checked already extensively for the processes with fully leptonic decays. Since the changes due to the semileptonic decay implementation do not affect the subroutine calls with anomalous gauge boson couplings it is sufficient to test the new implementation for the Standard Model case, i.e. with all anomalous couplings set to zero.

For the rather simple processes of diboson production the complete Standard Model matrix element with semileptonic decays has been generated with MadGraph as well. Both implementations agree very well, the relative difference of the matrix elements squared for randomly chosen phase space points is usually below  $10^{-10}$ .

For the more complicated processes of triboson production and diboson plus two jets production in VBF a different approach has been used, since the matrix element generation is more cumbersome there, introducing new possible error sources. Therefore not the entire matrix element has been generated using MadGraph, but instead only the “semileptonic tensors” for the standard model case. The relative difference of the “semileptonic tensors” for randomly chosen phase space points, defined as

$$\sum_{a,b} \left| \frac{\mathcal{T}_{ab}^{\text{VBFNLO}}}{\mathcal{T}_{ab}^{\text{MG}}} - 1 \right|, \quad (5.42)$$

where  $\mathcal{T}_{ab}^{\text{VBFNLO/MG}}$  denote the “semileptonic tensors”, is again between  $10^{-15}$  and  $10^{-10}$ . The full matrix elements squared for both leptonic tensors again agree nicely, with a relative difference usually between  $10^{-12}$  and  $10^{-8}$ .

### 5.2.3.2 Checks and Comparisons of Integrated Cross Sections

At the level of integrated cross sections internal checks as well as comparisons with MCFM have been carried out. All results of this subsection have been obtained with the following input parameters:

$$\begin{aligned} M_Z &= 91.1876 \text{ GeV} & G_F &= 1.16637 \cdot 10^{-5} \text{ GeV}^{-2} \\ M_W &= 80.398 \text{ GeV} & \mu_F = \mu_R &= 80.0 \text{ GeV}. \end{aligned} \quad (5.43)$$

For the widths of W and Z boson the values

$$\Gamma_W = 2.097673 \text{ GeV} \quad \text{and} \quad \Gamma_Z = 2.508420 \text{ GeV} \quad (5.44)$$

obtained from a calculation by VBFNLO have been used. The results have been generated for a 14 TeV LHC using the cteq611 [182] and CT10 [219] parton distribution functions

	$W^\pm \rightarrow \ell\nu$	$W^+ \rightarrow u\bar{d}$		$W^- \rightarrow d\bar{u}$	
	$\sigma_{\text{lep}}$	$\sigma_{W^+, \text{had}}$	$\frac{\sigma_{W^+, \text{had}}}{\sigma_{\text{lep}}}$	$\sigma_{W^-, \text{had}}$	$\frac{\sigma_{W^-, \text{had}}}{\sigma_{\text{lep}}}$
$W^+W^-$	828.5 (2) fb	2484.9 (7) fb	3.00	2485.1 (7) fb	3.00
$W^+W^-jj$	24.81 (4) fb	74.28 (11) fb	2.99	74.31 (11) fb	3.00
$W^+W^+jj$	5.532 (4) fb	16.59 (1) fb	3.00	—	—

Table 5.5: Cross sections of  $W^+W^-$ ,  $W^+W^-jj$  and  $W^+W^+jj$  production at LO with fully leptonic and semileptonic decay of the vector bosons without cuts on the final-state particles.

	$W^\pm/Z \rightarrow \ell\nu/\ell\ell$	$W^+ \rightarrow u\bar{d}$		$W^- \rightarrow d\bar{u}$	
	$\sigma_{\text{lep}}$	$\sigma_{W^+, \text{had}}$	$\frac{\sigma_{W^+, \text{had}}}{\sigma_{\text{lep}}}$	$\sigma_{W^-, \text{had}}$	$\frac{\sigma_{W^-, \text{had}}}{\sigma_{\text{lep}}}$
$W^+Z$	54.97 (6) fb	159.9 (1) fb	2.91	—	—
$W^-Z$	35.06 (4) fb	101.5 (1) fb	2.90	—	—
$W^+Zjj$	0.943 (1) fb	2.818 (3) fb	2.99	—	—
$W^-Zjj$	0.533 (1) fb	1.592 (1) fb	2.99	—	—
$W^+W^Z$	49.06 (7) ab	146.8 (2) ab	2.99	146.6 (2) ab	2.99

Table 5.6: Cross sections of LO  $W^\pm Z$ ,  $W^\pm Zjj$  and  $WWZ$  production with fully leptonic decay and semileptonic decay of one of the W bosons with equal cuts on all final-state quarks, leptons and neutrinos ( $p_T > 10$  GeV,  $|\eta| < 4.5$ ,  $\Delta R_{ij} > 0.4$ ).

			$W^\pm \rightarrow \ell\nu$	$W^+ \rightarrow 2 \cdot u\bar{d}$	$W^- \rightarrow 2 \cdot d\bar{u}$
$W^+W^-$	VBFNLO	LO	446.0 (1) fb	2436 (1) fb	2572 (1) fb
$W^+W^-$	MCFM	LO	445.9 (2) fb	2439 (1) fb	2574 (1) fb
$W^+W^-$	VBFNLO	NLO	767.1 (2) fb	4872 (1) fb	4971 (1) fb
$W^+W^-$	MCFM	NLO	767.4 (3) fb	4862 (2) fb	4960 (2) fb
			$W^\pm/Z \rightarrow \ell\nu/\ell\ell$	$Z \rightarrow 2 \cdot u\bar{u}$	$Z \rightarrow 3 \cdot d\bar{d}$
$W^+Z$	VBFNLO	LO	27.88 (1) fb	234.5 (1) fb	444.2 (2) fb
$W^+Z$	MCFM	LO	27.79 (2) fb	236.3 (1) fb	442.2 (2) fb

Table 5.7: Cross sections of  $W^+W^-$  production at LO and NLO and  $W^+Z$  production at LO with fully leptonic and semileptonic decay of the vector bosons for VBFNLO and MCFM. The following cuts on jets and leptons have been used:  $p_{T,j} > 20$  GeV,  $|\eta_j| < 4.5$ ,  $p_{T,\ell} > 10$  GeV,  $|\eta_\ell| < 2.5$ ,  $\Delta R_{ij} > 0.4$ ,  $m_{Z/\gamma} > 15$  GeV.

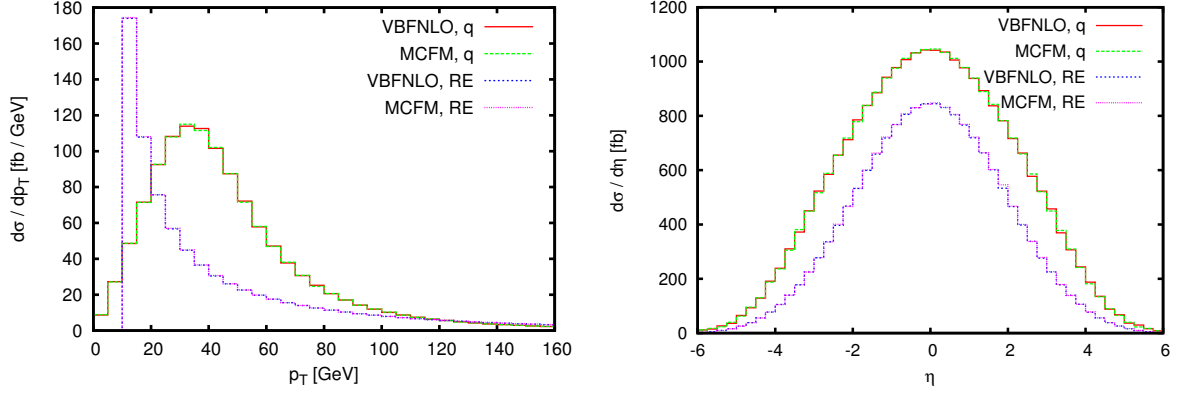


Figure 5.15: Comparison of VBFNLO and MCFM for  $W^+W^-$  production at NLO with hadronic decay of the  $W^+$ . The following cuts on the leptons have been applied:  $p_{T,\ell} > 10$  GeV,  $|\eta_\ell| < 2.5$ . No clustering of the partons has been used.  $p_T$  (left) and  $\eta$  (right) distributions are shown for the up-type quark from the  $W^+$  decay (denoted as “q”) and the extra parton from the real emission (denoted as “RE”). For the distributions of this parton only the contribution with  $p_T > 10$  GeV is considered.

for the LO and NLO calculations, respectively. For the processes with fully leptonic decay each vector boson decays in a different lepton generation. For the hadronic vector boson decays only one quark generation is considered in the numerical results shown below. Initial-state b-quarks and NLO effects in the hadronic decay are excluded. The NNLO contributions from the  $gg$  initial state in  $W^+W^-$  production are not taken into account. The applied cuts for each comparison are given in the respective table captions.

Several plausibility checks have been performed within VBFNLO. At leading order the  $pp \rightarrow WW$  and  $pp \rightarrow W^\pm W^\pm jj$  in VBF processes are well-defined even without any jet and lepton cuts, except for the soft t-channel photon contribution of  $W^+W^-jj$  production. As mentioned before, this contribution is regularized by a cut on the momentum transfer of the photon. Since the coupling of the W boson to fermions is universal and the off-shell effects containing couplings of  $Z/\gamma$  to the fermions are small, the integrated cross sections of the fully leptonic and the semileptonic process without cuts should differ quite precisely by a factor of three, due to the decay quarks carrying color. As can be seen in Table 5.5 this is the case, which additionally proves that the non-resonant contributions are indeed small. The same holds in the case of finite but equal cuts for jets, leptons and neutrinos. Here the hadronic W decay of the processes with W and Z boson production ( $W^\pm Z$ ,  $W^\pm Zjj$  and  $W^+W^-Z$ ) can be checked as well. These results are listed in Table 5.6 and match the expectations nicely. Solely the process  $W^\pm Z$  shows some discrepancies, which is due to large  $Z/\gamma$  interference effects in this process. With an additional cut on the invariant mass of the leptonic  $Z/\gamma$  decay products of  $m_{Z/\gamma} > 60$  GeV, which essentially removes the photon contribution,  $\frac{\sigma_{W^\pm, \text{had}}}{\sigma_{\text{lep}}} = 3.00$  is recovered.

The real-emission contribution of the NLO calculation contains the real-emission matrix elements as well as the Born matrix elements, where the latter ones are part of the

Catani-Seymour dipoles [247]. Therefore the cancellation of the infrared divergences would no longer work if the fully leptonic and semileptonic tensors would have been used inconsistently in the two matrix elements. This has not been observed for any of the processes with semileptonic decays.

Finally, the diboson production processes have been checked against MCFM [232], where good agreement has been found in distributions and total cross sections, both for the leptonic and the semileptonic processes at LO and NLO. However, for the semileptonic decay modes of  $W^+Z$  production MCFM did not produce stable results. All cross sections of this comparison can be found in Table 5.7. Here two quark generations are considered in the hadronic  $W$  decay. The hadronic  $Z/\gamma$  decay includes three generations of down-type quarks and two generations of up-type quarks. The small differences of a few per-mil in the NLO cross sections for the processes with semileptonic decays can be attributed to the clustering of partons and the usage of pseudorapidity for the calculation of  $\Delta R_{j\ell}$  in MCFM. Without enforcing a minimal number of jets and without the  $\Delta R_{j\ell}$  cut the cross sections and distributions agree perfectly: both programs give a cross section of  $\sigma = 5973(2)$  fb. Exemplary  $p_T$  and  $\eta$  distributions for this case are depicted in Figure 5.15 for the quark from the  $W$  decay and the additional radiation in  $W^+W^-$  production at NLO.

## 5.3 Phenomenological Aspects

This section illustrates two important issues which have to be taken into account in phenomenological studies of processes with semileptonic decays. On the one hand the tagging-jet definition in the VBF processes should be modified with respect to the fully leptonic case. On the other hand the interpretation of  $K$ -factors for the semileptonic processes needs special attention. Finally, the key features of the anomalous couplings implementation shall be briefly discussed since the investigation of the gauge boson self couplings is a major application of vector boson production with semileptonic decays.

### 5.3.1 Tagging-Jet Definitions

Higgs boson searches and vector boson scattering studies in the VBF channels largely depend on the two forward/backward “tagging” jets appearing in these processes. Rapidity separations between jets as large as in the VBF processes are very uncommon for QCD processes. This allows for a very efficient background reduction, which is crucial given that the cross sections of these electroweak processes are much smaller than the cross sections of the QCD background processes.

For the processes with fully leptonic decays of the vector bosons the tagging jets are usually defined as the two hardest jets of an event. Since there are no other jets at leading order in true VBF events and jets from additional radiation are usually softer this works well. However, for processes with semileptonic decays this definition is too

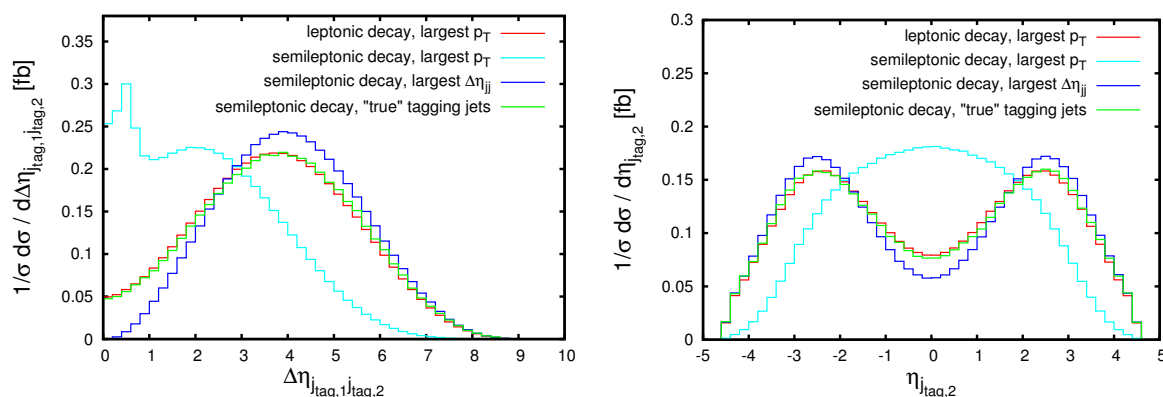


Figure 5.16: Rapidity separation of both tagging jets and rapidity of the softer tagging jet for  $W^+W^-jj$  production at LO with fully leptonic and semileptonic decays for different tagging-jet choices. The following cuts are used:  $p_{T,j} > 20$  GeV,  $|\eta_j| < 4.5$ ,  $p_{T,\ell} > 10$  GeV,  $|\eta_\ell| < 2.5$  and  $\Delta R_{ij} > 0.4$ .

simple since there are additional jets in the event from the vector boson decay. For a sizable fraction of the VBF contribution taking the hardest jets as tagging jets will no longer select the “true tagging jets” exhibiting the large rapidity gap. This is especially the case for vector bosons from a heavy “Higgs boson” decay. Decay products of highly boosted vector bosons usually have large transverse momenta as well.

This situation is illustrated in Figure 5.16 for the process  $W^+W^-jj$  in VBF. The left plot shows the rapidity separation between the two tagging jets, the right plot displays the rapidity of the second hardest tagging jet. For the process with fully leptonic decay the typical VBF shape is apparent, with rather forward/backward jets and a large rapidity separation. With semileptonic decay and the same tagging-jet definition as in the fully leptonic case the VBF shape gets heavily distorted. The shape can be restored by selecting the two jets with largest rapidity separation as tagging jets (see Figure 5.16). While this works quite well for the signal process, the reduction of the background is much worse, since a large rapidity separation between rather soft jets arises much more frequently than for two fairly hard jets. Additionally, already at NLO QCD this prescription would often pick the additional radiation as one of the tagging jets. Therefore other tagging-jet definitions have been proposed and two of them have been included in the semileptonic decay implementation discussed here.

The first tagging-jet definition for processes with semileptonic decays has been proposed in Ref. [256] for the search of a heavy Higgs boson in the  $WW$  channel with semileptonic decays. The authors suggest to separate the phase space in  $\eta$  explicitly into the central region with  $|\eta| < \eta_c$  and the forward/backward region with  $|\eta| > \eta_c$ . The tagging jets are then defined as the hardest jet of the forward and backward region, respectively:

$$\left. \begin{array}{l} |\eta_{j_{\text{tag},1}}| > \eta_c \\ \left\{ \begin{array}{ll} \eta_{j_{\text{tag},2}} > \eta_c & \text{if } \eta_{j_{\text{tag},1}} < \eta_c \\ \eta_{j_{\text{tag},2}} < -\eta_c & \text{if } \eta_{j_{\text{tag},1}} > \eta_c \end{array} \right\} \end{array} \right\} \text{ and } p_{T,j_{\text{tag},1}} > p_{T,j_i} \text{ for } \eta_{j_i} > \eta_c$$

$$\text{and } p_{T,j_{\text{tag},2}} > p_{T,j_k} \text{ for } \eta_{j_{\text{tag},2}} \cdot \eta_{j_k} > 0. \quad (5.45)$$

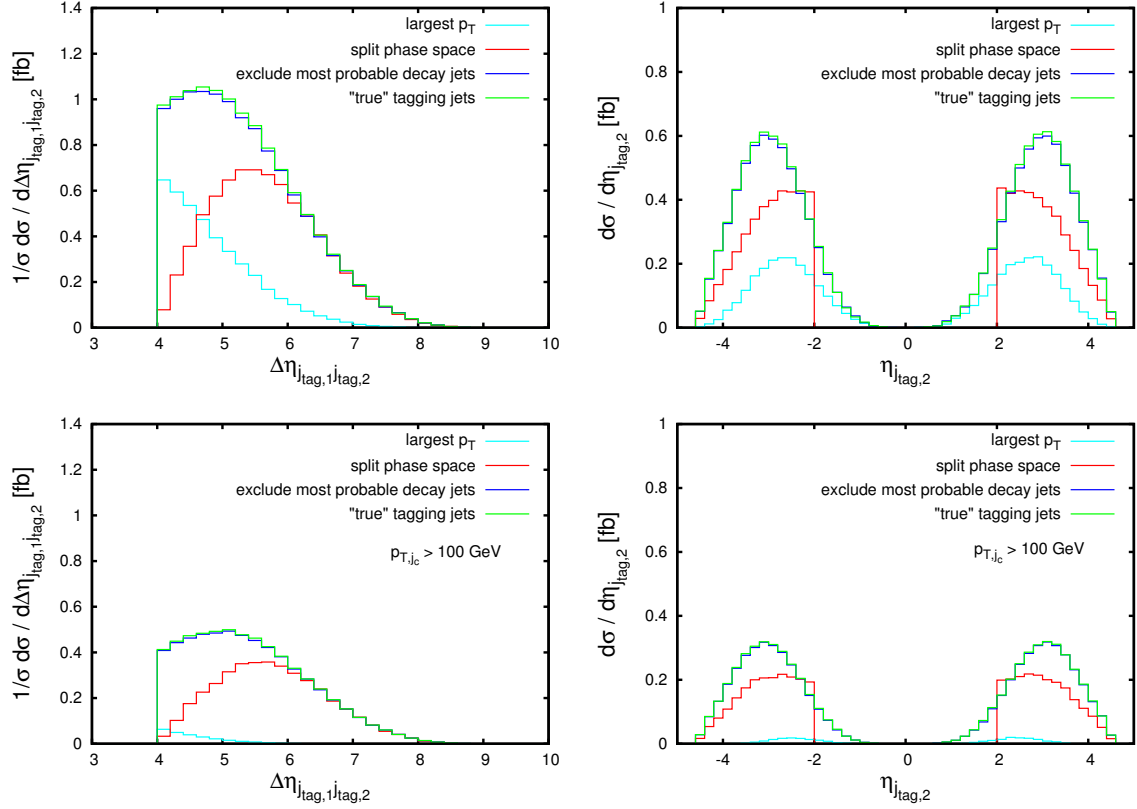


Figure 5.17: Rapidity separation of both tagging jets and rapidity of the softer tagging jet for  $W^+W^-jj$  production at LO with semileptonic decays of the vector bosons for different tagging-jet choices. The distributions of the upper row are calculated for the following “basic + VBF” cuts:  $p_{T,j} > 30$  GeV,  $|\eta_j| < 4.5$ ,  $p_{T,\ell} > 15$  GeV,  $|\eta_\ell| < 2.5$ ,  $\Delta R_{ij} > 0.4$ ,  $|\eta_{j_{tag,1}} - \eta_{j_{tag,2}}| > 4$ ,  $m_{j_{tag,1}j_{tag,2}} > 600$  GeV,  $\eta_{j_{tag,1}} \cdot \eta_{j_{tag,2}} < 0$ . The two lower plots additionally require a central jet with  $p_T > 100$  GeV.

Since the decay products of the vector bosons usually reside in the central region, the jets from the boson decay do not interfere substantially with the tagging-jet selection. This tagging jet choice is dubbed “split phase space” in the following.

For the  $H \rightarrow WW$  VBF channel in the semileptonic Higgs boson search of Ref. [224] another approach has been used. There at first two candidate jets from the hadronic W boson decay are identified by demanding an invariant jet pair mass within the vicinity of the W boson mass. These two jets are then excluded from the tagging-jet selection and the two hardest of the remaining jets are identified as tagging jets. A slightly modified version of this tagging-jet definition has been included into VBFNLO for the semileptonic decay processes. Here, no fixed mass window for the jet pair mass is demanded. Instead, the two jets which have an invariant mass closest to the mass of the hadronically decaying vector boson are excluded from being a tagging-jet candidate. This option is called “exclude most probable decay jets” in the upcoming figures.

In Figure 5.17 the performance of the two new tagging jet choices is compared to the

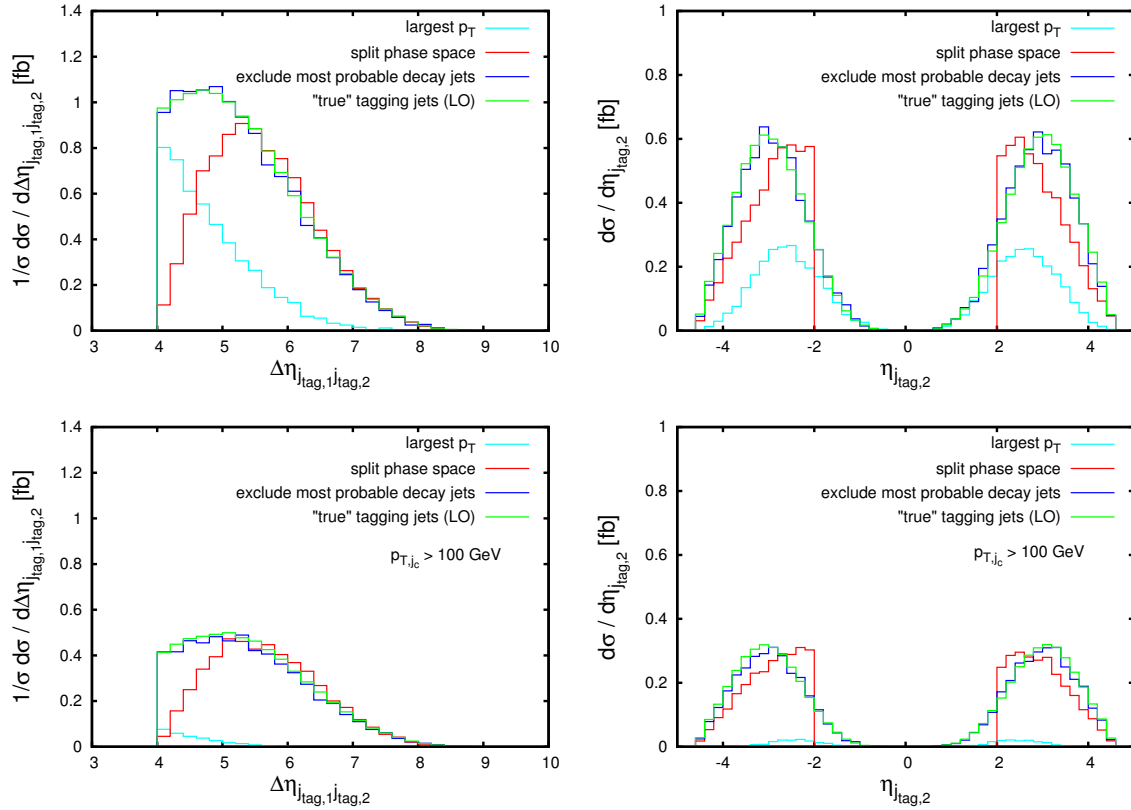


Figure 5.18: The same rapidity separation and rapidity distributions as in Figure 5.17 for different tagging-jet choices, but at NLO QCD accuracy for the production process. The “true” tagging jet curve is still at LO, since this choice is no longer well-defined at NLO.

traditional tagging-jet definition for  $W^+W^-jj$  production in VBF at leading order, with the assumed existence of a heavy Higgs boson of  $m_H = 600$  GeV. Additionally, the case where the two quarks from the VBF production process are chosen as tagging jets is shown. The latter choice is certainly not available in an experiment, but only within Monte Carlo calculations. This choice resembles the situation of the fully leptonic case at parton level in a leading-order calculation. It is only included here as a measure of the performance of the different tagging-jet definitions. For  $M_W$ ,  $M_Z$  and  $G_F$  the values from Eq. (5.43) have been used. The basic cuts include  $p_{T,j} > 30$  GeV,  $|\eta_j| < 4.5$ ,  $p_{T,\ell} > 15$  GeV,  $|\eta_\ell| < 2.5$  and  $\Delta R_{ij} > 0.4$ . Additionally, typical VBF cuts for the two tagging jets

$$|\eta_{j_{tag,1}} - \eta_{j_{tag,2}}| > 4 \quad , \quad m_{j_{tag,1}j_{tag,2}} > 600 \text{ GeV} \quad \text{and} \quad \eta_{j_{tag,1}} \cdot \eta_{j_{tag,2}} < 0 \quad (5.46)$$

have been applied. The rapidity value which separates the central from the forward/backward region is set to  $\eta_c = 2$ , which again yields a minimal rapidity separation of 4 for the “split phase space” tagging-jet definition of Eq. (5.45).

The upper row of Figure 5.17 shows the rapidity separation of the tagging jets and the rapidity of the softer tagging jet for the different tagging-jet choices. Choosing the two

hardest jets as tagging jets results in a VBF contribution which only amounts to roughly 1/3 of the contribution for the case of the “perfect” tagging-jet algorithm. Both “new” tagging-jet choices perform much better. The explicit phase space separation yields about 2/3 of the full contribution, while the definition with the mass reconstruction is extremely close to the “true” tagging jets case. In an actual experiment, however, the latter definition will not yield these perfect results since the mass reconstruction in reality has a noticeable uncertainty and there are naturally more than the two tagging jets and the two jets from the boson decay in an event. Therefore also other jet combinations may feature invariant masses close to  $m_V$ . Additionally, the prescription based on the mass reconstruction will not be optimal for contributions arising from a light Higgs boson, given that one of the vector bosons from the Higgs boson decay has to be off shell for  $m_H < 2 \cdot m_V$ .

When a hard central jet is required in addition, which is useful in the heavy Higgs boson search [256], the efficiency of the “hardest jets as tagging jets” case becomes even worse. Here a value of

$$p_{T,j_c} > 100 \text{ GeV} \quad \text{with} \quad |\eta_{j_c}| < 2 \quad (5.47)$$

has been chosen. In this case it is very unlikely that the two quarks from the VBF signature both have larger transverse momenta than the hard central jet. Therefore only a few per-cent of the VBF events survive in the scenario described above, while the other two tagging-jet definitions perform reasonably well. Their efficiencies are roughly the same as without the requirement of a hard central jet, which can be seen in the lower row of Figure 5.17.

In Figure 5.18 the same distributions as in Figure 5.17 are shown, but this time for  $WWjj$  production in VBF at next-to-leading order. Solely the curve for the “true” tagging jets is still at LO, since this choice is no longer well-defined at NLO. The comparison of these two figures shows, that the “exclude most probable decay jets” choice for the tagging jets yields a much more stable result concerning the NLO corrections than the “split phase space” option. The latter tagging-jet choice is influenced by the additional jet activity in the real emission contribution, which may also indicate sizable parton-shower effects for this tagging jet definition. The impact of the additional jet in the real-emission part of the calculation onto the semileptonic decay processes will be discussed in more detail in the next subsection.

### 5.3.2 Interpretation of Inclusive NLO Cross Sections for the Semileptonic Processes

In the discussion of scattering processes the cross sections of particular processes are usually considered as inclusive in the number of jets, i.e. the cross section of  $pp \rightarrow W^+W^-jj$  also includes contributions with one or more additional visible jets in the final state from initial-state radiation. The additional jets can be assessed in calculations for example by interfacing the partonic process with the minimal number of required jets to a parton shower, which generates the additional radiation with leading-log accuracy.

	fully leptonic decay	semileptonic decay	
		$ m_{jj} - m_V  < \infty$	$ m_{jj} - m_V  < 20 \text{ GeV}$
$W^+W^-$	1.50	1.97	1.59
$ZZ$	1.42	1.71	1.48
$W^-W^-jj$	1.00	1.49	1.23
$ZZjj$	0.97	1.41	1.22
$W^+W^-Z$	1.53	1.80	1.53

Table 5.8: Comparison of  $K$ -factors  $K = \frac{\sigma_{NLO}}{\sigma_{LO}}$  for several processes with fully leptonic and semileptonic decay of the vector bosons. For the semileptonic case of  $W^+W^-$  production the  $W^+$  decays hadronically. For  $W^+W^-Z$  production the  $Z \rightarrow q\bar{q}$  mode is shown. The  $K$ -factors for the semileptonic decay processes are shown with and without a restriction on the invariant mass of one jet pair. The following cuts on jets and leptons have been used:  $p_{T,j} > 30 \text{ GeV}$ ,  $|\eta_j| < 4.5$ ,  $p_{T,\ell} > 15 \text{ GeV}$ ,  $|\eta_\ell| < 2.5$ ,  $\Delta R_{ij} > 0.4$ ,  $m_{\ell_i^+\ell_j^-} > 15 \text{ GeV}$ . For the tagging jets in the VBF processes the definition of Eq. (5.45) has been used.

Additional jets also come into play in the calculation of higher-order corrected cross sections. Each additional order in perturbation theory introduces the possibility of emitting one additional parton, which can lead to an additional jet in the final state. These additional jets can influence the higher-order corrected cross section substantially, if the LO process already contains jets and the corresponding cross section is defined within a set of jet cuts. Since the cuts for the inclusive cross section are the same for the LO calculation and all parts of the NLO calculation, in the real-emission contribution only  $n - 1$  out of the possible  $n$  jets have to pass the cuts.

For the production of multiple vector bosons this leads to a larger factor  $K = \sigma_{NLO}/\sigma_{LO}$  for the semileptonic decay case with respect to the fully leptonic decay case. The  $K$ -factors for both cases are listed in Table 5.8. For the processes with semileptonic decays one of the jets from the hadronic decay may fail the jet cuts if the jet from the real emission is hard enough to pass the cuts. Additionally, the real-emission parton and a quark from the hadronic decay can form a single jet which is hard enough to pass the cuts, while the vector boson decay quark alone would fail them. Therefore the cuts for the real-emission kinematics are less stringent than for the Born kinematics, which gives rise to the large  $K$ -factor, in particular when no constraints are applied on the reconstructed mass of the hadronically decaying vector boson. In contrast, for the leptonic decay case there is no “backup” lepton in the QCD real-emission kinematics which would satisfy the cuts if the lepton from the vector boson decay does not meet the criteria.

The enhancement of the  $K$ -factor in the semileptonic case can be reduced by demanding at least one jet pair in the final state with an invariant mass compatible with the mass

of the hadronically decaying vector boson,

$$|m_{j_i j_k} - m_V| < 20 \text{ GeV}. \quad (5.48)$$

This requirement in particular reduces the fraction of the real-emission contribution where one of the vector boson decay quarks fails the cuts and instead the jet from the real emission survives. Since the invariant mass of one decay quark and the real-emission parton usually does not fall in the range defined by Eq. (5.48), they fail this criterion. For the diboson and triboson processes the  $K$ -factor with the invariant mass restriction is of the same order as in the fully leptonic case. For the VBF processes, which feature additional jets already in the fully leptonic case at LO, the  $K$ -factor is reduced by introducing the restriction of Eq. (5.48). However, the additional jets still allow for some additional combinations of the real-emission kinematics to pass the cuts, yielding higher  $K$ -factors than for fully leptonic vector boson decays.

### 5.3.3 Anomalous Gauge Boson Couplings

One of the major applications of  $VVjj$  production in VBF, diboson and triboson production is the study of the triple and quartic gauge boson couplings. With the assumption of New Physics above a high energy scale  $\Lambda$ , outside the energy range up to which current experiments are sensitive on, the low-energy effects of the new degrees of freedom would manifest themselves in modified interactions between Standard Model particles. With the restriction on gauge boson self couplings these effects can be parametrized by the effective Lagrangian

$$\mathcal{L}_{\text{eff}} = \mathcal{L}_{\text{SM}} + \sum_i \frac{f_i}{\Lambda^2} \mathcal{O}_i + \sum_j \frac{f_j}{\Lambda^4} \mathcal{L}_j + \mathcal{O}\left(\frac{c_i}{\Lambda^6}\right) \quad (5.49)$$

Below the scale  $\Lambda$  only the first orders of this  $\frac{1}{\Lambda}$  expansion significantly affect observables. Higher-order terms are therefore neglected. The dimension-6 operators  $\mathcal{O}_i$  modify triple gauge couplings and are therefore probed best in diboson production. The dimension-8 operators  $\mathcal{L}_j$  only modify quartic and higher couplings at tree level. Thus they should be examined in vector boson scattering or in triboson production.

The anomalous couplings implementation of Refs. [237, 238], which is used for the semileptonic decay processes of VBFNLO, includes the following operators:

- The  $CP$ -even operators  $\mathcal{O}_W$ ,  $\mathcal{O}_B$ ,  $\mathcal{O}_{WWW}$ ,  $\mathcal{O}_{WW}$  and  $\mathcal{O}_{BB}$  from Ref. [257] are implemented as well as their  $CP$ -odd counterparts  $\mathcal{O}_{\tilde{W}}$ ,  $\mathcal{O}_{\tilde{B}}$ ,  $\mathcal{O}_{\tilde{WWW}}$ ,  $\mathcal{O}_{\tilde{WW}}$  and  $\mathcal{O}_{\tilde{BB}}$ . Two of the additional  $CP$ -odd operators  $\mathcal{O}_{D\tilde{W}}$  and  $\mathcal{O}_{B\tilde{W}}$  are available as well.
- The complete list of dimension-8 operators from Ref. [223] is included:  $\mathcal{L}_{S,0}$ ,  $\mathcal{L}_{S,1}$ ,  $\mathcal{L}_{M,0}$ – $\mathcal{L}_{M,7}$ ,  $\mathcal{L}_{T,0}$ – $\mathcal{L}_{T,9}$ .

The conversion into parametrizations used by other Monte Carlo programs like WHIZARD [74, 258] and MadGraph/MadEvent [73, 259] or the LEP2-parametrization of  $WW\gamma\gamma$  and  $ZZ\gamma\gamma$  [249] is summarized in Ref. [260].

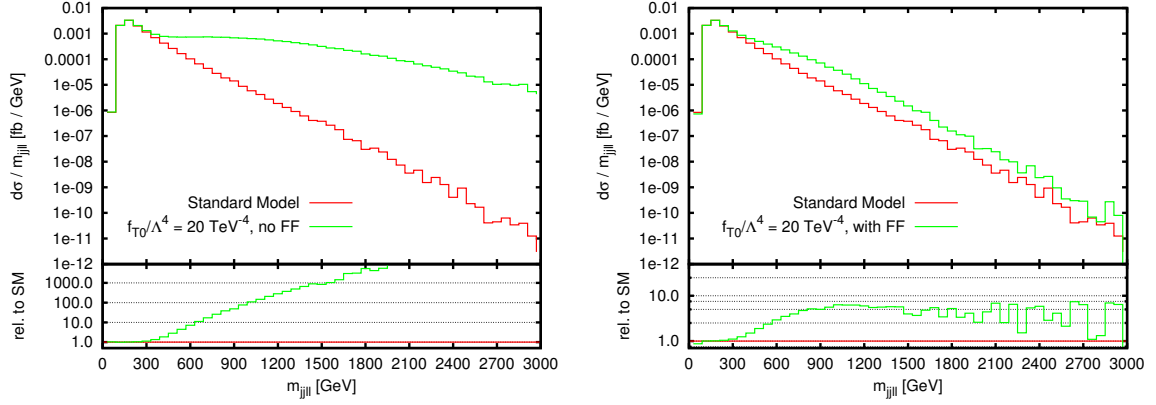


Figure 5.19: Invariant mass of both leptons and the decay jet candidates in  $ZZjj$  production with semileptonic decays, corresponding to  $m_{ZZ}$ , including the operator  $\mathcal{L}_{T,0}$  with  $\frac{f_{T,0}}{\Lambda^4} = 20 \text{ TeV}^{-4}$ . In the left plot no form factor is applied, the right plot includes a dipole form factor with  $n = 4$  and  $\Lambda_{FF} = 2.9 \text{ TeV}$  to preserve unitarity at high energies.

The invariant mass distributions of  $ZZjj$  production via VBF shown in Figure 5.19 have been obtained using

$$\mathcal{L}_{T,0} = \text{Tr} [\hat{W}_{\mu\nu} \hat{W}^{\mu\nu}] \times \text{Tr} [\hat{W}_{\alpha\beta} \hat{W}^{\alpha\beta}] \quad (5.50)$$

with  $\hat{W}_{\mu\nu}$  defined as

$$\hat{W}_{\mu\nu} = \frac{i}{2} g \sigma^i W_{\mu\nu}^i \quad (5.51)$$

and a coupling constant

$$\frac{f_{T,0}}{\Lambda^4} = 20 \text{ TeV}^{-4}. \quad (5.52)$$

The left part of the figure shows the invariant mass of the  $jj\ell^+\ell^-$  system, where the two jets arise from the hadronic decay of one  $Z$  boson, while the lepton pair stems from the leptonically decaying  $Z$  boson. Therefore this invariant mass corresponds to the partonic energy available in the quartic gauge boson vertex. The deviation from the Standard Model is large at high energies, while the low-energy region is almost unaffected by the modified couplings.

This  $m_{jj\ell^+\ell^-}$  curve with an anomalous quartic gauge boson coupling also shows one of the major problems arising in anomalous coupling studies at a hadron collider, especially for the inclusion of dimension-8 operators. The nominal energy which can be reached at the LHC running with its design energy is 14 TeV. However, contributions at high energies are extremely suppressed, since the probability of partons colliding with an energy close to the energy of the whole proton is very small. Therefore most of the LHC sensitivity on anomalous couplings arises at much lower energies than the maximal energy. This causes problems in the comparison of measured rates with theoretical predictions calculated with the effective Lagrangian of Eq. (5.49). For coupling strengths  $\frac{f_i}{\Lambda^4}$  with values leading to measurable deviations at rather low energies tree-level unitarity at the maximal LHC energy is usually no longer fulfilled.

With the assumption of coupling strengths  $f_i$  of  $\mathcal{O}(1)$  the energy regime at which unitarity breaks down [261, 262] is larger than the New Physics scale  $\Lambda$ . Thus it is no longer valid to neglect the higher-order terms of the expansion in Eq. (5.49), since they become similarly important as the terms included in the anomalous couplings implementation. Therefore measures have to be taken in order to exclude the energy regions which are physically not meaningful from sensitivity analyses of anomalous couplings. One way to achieve this is the inclusion of appropriate experimental cuts. However, for processes with neutrinos in the final state the partonic energy in the quartic vertex is not accessible. In processes with one W boson in the final state choosing the semileptonic decay mode over the fully leptonic one can give a handle on the partonic center-of-mass energy if the W boson decays hadronically. Another method ensuring unitarity is the projection of the unitarity violating amplitudes onto the unitarity circle, as it is done in the  $K$ -matrix method [258]. In the anomalous couplings implementation of VBFNLO unitarity at high energies is preserved by means of a dipole form factor,

$$\mathcal{F}(s) = \frac{1}{\left(1 + \frac{s}{\Lambda_{FF}^2}\right)^n}, \quad (5.53)$$

introducing two new parameters, the characteristic energy scale of the form factor  $\Lambda_{FF}$  and the exponent  $n$ . The form factor is included into the calculation by replacing the coupling constants  $f_i$  of the new operators with

$$f_i \rightarrow \mathcal{F}(s) \cdot f_i, \quad (5.54)$$

which leads to a damping of the anomalous contributions to the scattering amplitude at high energies, ensuring unitarity for appropriate choices of  $\Lambda_{FF}$  and  $n$ . For the determination of  $\Lambda_{FF}$  and  $n$  depending on the coupling constant choices a FORTRAN program [263] has been developed, which is based on a partial wave analysis in on-shell vector boson scattering. Here the operator  $\mathcal{L}_{T,0}$  with the coupling strength of Eq. (5.52) leads to unitarity violation at 1.0–1.8 TeV center-of-mass energy, depending on the considered vector bosons. In on-shell  $ZZ \rightarrow ZZ$  scattering a form factor with

$$\Lambda_{FF} = 2.9 \text{ TeV} \quad \text{and} \quad n = 4 \quad (5.55)$$

ensures tree-level unitarity up to 14 TeV. As can be seen in the right part of Figure 5.19 this form factor choice also leads to a physical high-energy behavior of  $ZZ jj$  production in VBF.

## 5.4 Conclusion

While the fully leptonic decay mode of vector bosons in processes with more than one vector boson yields a very clean signal, the small branching ratios of  $W$  and  $Z$  bosons into leptons limit the achievable rates at experiments. Therefore semileptonic decay modes, with one of the vector bosons decaying hadronically, are being considered both in Higgs boson searches and in anomalous gauge boson coupling studies. These experimental studies depend on precise theoretical predictions for the semileptonic decay channels.

Therefore in this work semileptonic decay modes have been implemented into the parton-level program `VBFNLO`. This program already provided predictions at NLO QCD for many processes with fully leptonic vector boson decays. The process list includes several diboson plus two jets production processes in VBF as well as diboson and triboson production. Anomalous triple and quartic gauge boson couplings induced by additional dimension-6 and dimension-8 operators in the Lagrangian are available both for the fully leptonic and the semileptonic case.

The main modifications of the matrix element calculation in the transition to semileptonic decays include changes of the vector boson couplings to the final-state fermions and additional diagrams in the off-shell contributions. These new diagrams are absent in the leptonic case due to the non-existing photon-neutrino coupling. NLO QCD effects in the hadronic decay are included in the approximation of an on-shell vector boson decay.

For semileptonic decays with the  $Z/\gamma$  decaying hadronically an infrared divergence occurs due to the additional jet in the real-emission contribution of the NLO QCD calculation. In this case the virtual photon may become soft. This divergence arises already at leading order when the two quarks from the  $Z/\gamma$  decay are allowed to form a single jet and it is regularized by individual thresholds for each quark flavor. They can be determined from experimental data of the process  $e^+e^-$  to hadrons, given that this process has the same decay structure of the intermediate particle as the hadronic  $Z/\gamma$  decay. For the case that only one jet from the hadronic decay is requested the treatment of collinear divergences due to photons in the t-channel of VBF processes has to be extended. The resulting numerical impact on the cross section is estimated to be small if a reconstruction of the invariant mass of the hadronically decaying vector boson is performed.

For the VBF processes several tagging-jet definitions have been discussed, since taking the two jets with highest transverse momentum, which is widely used in processes with fully leptonic decays, quite often selects at least one of the vector boson decay jets in the semileptonic case. Two tagging-jet choices have been implemented, one featuring an explicit phase space splitting, the other one based on the reconstruction of the vector boson mass, which both perform reasonably well.

With the inclusion of NLO corrections to the production part of the multiboson production processes a significantly rising  $K$ -factor is observed after switching from fully

leptonic to semileptonic decays of the vector bosons. The reason for this enhancement lies in the real-emission contribution, which is less restricted by cuts in the semileptonic decay case. If the decay jets are required to be compatible with the mass of their mother particle, the enhancement is significantly smaller.

The new implementation of semileptonic decays allows for the precise calculation of signal and background processes in the heavy Higgs boson searches at the LHC. Additionally, vector boson self coupling studies are supported by the implementation of anomalous triple and quartic gauge boson coupling models. Since these models can lead to unphysical behavior in the PDF-suppressed high-energy tails a dipole form factor can be included in VBFNLO calculations. The form factor parameters can be obtained from a partial-wave analysis of on-shell vector boson scattering.

# CHAPTER 6

---

## Summary

---

In this thesis several aspects of electroweak processes at the Large Hadron Collider have been studied. The symmetry breaking mechanism of the electroweak sector receives a lot of attention at the moment, since the LHC is expected to provide insight into this mechanism and indeed discovered a very promising SM-like Higgs boson candidate [19, 20]. On the other hand, a lot of effort on the theoretical and the experimental side is put into scrutinizing possible new physics phenomena.

The first part of this work discussed one possible overlap of Higgs boson and SUSY searches, given that for Higgs boson searches in a SUSY theory backgrounds from SUSY particle production have to be considered, even if the Higgs boson itself is assumed to be SM-like. Therefore, the SUSY background to the search for a SM-like Higgs boson in the MSSM has been investigated for several MSSM scenarios at center-of-mass energies of 7 and 14 TeV. Two decay modes of Higgs boson production in vector boson fusion have been considered, the decay into a  $W^+W^-$  pair and a  $\tau^+\tau^-$  pair. While substantial background from SUSY particle production has been found in some scenarios with light SUSY particles, the background turned out to be under good control for SUSY particles masses above the current exclusion limits from the LHC.

A domain in which BSM effects could interfere with measurements of quantities which are not directly associated to these BSM effects is data-driven background determination. This has been studied for the case of charginos, neutralinos and sleptons interfering with the determination of the continuum  $WW$  background in the  $h \rightarrow WW$  Higgs boson search channel. For the early-2012 LHC studies [92, 93] it has been shown that a significant influence of the BSM effects would have been possible. However, more recent data disfavors this hypothesis. Nevertheless, such effects should be taken into account in the error estimation of data-driven background determination techniques.

In order to obtain as much information from the LHC experiments as possible it is mandatory to exploit as many signatures as possible. In the case of vector boson self coupling studies as well as analyses of Higgs boson decays into vector bosons this implies, that not only the fully leptonic vector boson decays should be investigated, but also semileptonic decays, i.e. with one hadronically decaying vector boson. Precise theoretical predictions for the semileptonic decays in multiboson production are essential for corresponding experimental analyses. Therefore they have been implemented into a parton-level Monte Carlo program, which had the fully leptonic decay mode already implemented for a variety of processes involving electroweak bosons. Since one of the main motivations for the study of multiboson production processes is their sensitivity on the structure of triple and quartic gauge boson vertices, anomalous gauge boson couplings have been included in the new implementation of processes with semileptonic decays. It has been shown that several issues had to be solved in the transition from fully leptonic to semileptonic vector boson decays. Besides the changes to the matrix element, further measures had to be taken in order to get well-defined cross sections at NLO QCD. Additionally, the definition of tagging jets in vector boson fusion processes had to be adapted to the new final states.

# APPENDIX A

---

## SUSY Spectra

---

### A.1 Scenarios for “SUSY Background to Neutral MSSM Higgs Boson Searches”

This section summarizes all relevant input parameters as well as the important masses and branching ratios for the MSSM scenarios discussed in Chapter 3.

The Standard Model input parameters in the spectrum calculator for all scenarios are

$$\begin{aligned}\alpha_{em}^{-1}(M_Z) &= 127.934 & G_F &= 1.16639 \cdot 10^{-5} \text{ GeV}^{-2} \\ \alpha_s(M_Z) &= 0.1172 & M_Z &= 91.187 \text{ GeV} \\ M_b(M_b) &= 4.25 \text{ GeV} & M_t &= 172.5 \text{ GeV},\end{aligned}\tag{A.1}$$

with the top quark mass value from [264].

Except for the scenario SPS1aslope, all scenarios are based on the mSUGRA scenario SPS1a [122], which has the following input parameters at the GUT scale (approximately  $10^{16}$  GeV):

$$M_0 = 100 \text{ GeV}, \quad M_{1/2} = 250 \text{ GeV}, \quad A_0 = -100 \text{ GeV}, \quad \tan \beta = 10, \quad \mu > 0.\tag{A.2}$$

After the RGE running down to the SUSY scale  $Q = 1 \text{ TeV}$  using `SuSpect` [135], the following SUSY breaking parameters are obtained:

$$\begin{aligned}
M_1 &= 103.1 \text{ GeV} & M_{eL} = M_{\mu L} &= 194.4 \text{ GeV} \\
M_2 &= 192.9 \text{ GeV} & M_{eR} = M_{\mu R} &= 135.8 \text{ GeV} \\
M_3 &= 567.8 \text{ GeV} & M_{\tau L} &= 193.6 \text{ GeV} \\
A_t &= -490.9 \text{ GeV} & M_{\tau R} &= 133.4 \text{ GeV} \\
A_b &= -763.3 \text{ GeV} & M_{q_1L} = M_{q_2L} &= 526.5 \text{ GeV} \\
A_\tau &= -249.4 \text{ GeV} & M_{uR} = M_{cR} &= 508.0 \text{ GeV} \\
A_u = A_c &= -657.1 \text{ GeV} & M_{dR} = M_{sR} &= 505.8 \text{ GeV} \\
A_d = A_s &= -821.7 \text{ GeV} & M_{q_3L} &= 480.7 \text{ GeV} \\
A_e = A_\mu &= -251.1 \text{ GeV} & M_{tR} &= 408.3 \text{ GeV} \\
M_{H_d}^2 &= 32598 \text{ GeV}^2 & M_{bR} &= 502.8 \text{ GeV} \\
M_{H_u}^2 &= -112336 \text{ GeV}^2 & \tan \beta(M_Z) &= 10.0.
\end{aligned} \tag{A.3}$$

The trilinear stop coupling is modified to match the relations of the  $m_h^{\text{max}}$  scenario [129],

$$A_t = -733 \text{ GeV}. \tag{A.4}$$

These parameters are then fed into `SUSYHIT 1.3` [135–138] and `FeynHiggs 2.6.5` [140–143], generating the SLHA file [133, 134] for the base scenario “SPS1amod”. Relevant masses and branching ratios for this scenario can be found in the Tables A.1 and A.2.

For the scenario “SPS1amod2” additionally the parameters  $M_{q_3L}$  and  $M_{tR}$  are increased and  $A_t$  is further modified to again match the  $m_h^{\text{max}}$  scenario:

$$M_{q_3L} = 881 \text{ GeV} \tag{A.5}$$

$$M_{tR} = 808 \text{ GeV} \tag{A.6}$$

$$A_t = -1833 \text{ GeV}. \tag{A.7}$$

This leads to higher stop masses and a higher Higgs boson mass of  $m_h = 124.1 \text{ GeV}$  compared to  $m_h = 118.2 \text{ GeV}$ .

To study the squark and gluino mass dependence, starting with SPS1amod, the parameters that contribute significantly to the squark masses of the first two generations,  $M_{q_1L}$ ,  $M_{q_2L}$ ,  $M_{uR}$ ,  $M_{dR}$ ,  $M_{cR}$  and  $M_{sR}$ , are modified by a factor

$$(1 + \xi) \quad \text{with} \quad 0 \leq \xi \leq 2. \tag{A.8}$$

As the SUSY cascade decays of squarks and the gluino substantially depend on whether the gluino is heavier or lighter than the squarks, the mass hierarchy of the base scenario SPS1amod is preserved by varying the gluino mass parameter  $M_3$  by the same factor. Since gluinos heavier than squarks usually produce cascades with more jets than expected for the VBF Higgs processes, the mass hierarchy of SPS1amod will give more important SUSY backgrounds anyway. The example scenario with  $\xi = 1$  is given in the Tables A.1 and A.2.

The b-quark contributions discussed in this analysis depend on the masses of stops and sbottoms instead of squarks of the first two generations. Therefore the corresponding soft SUSY breaking parameters  $M_{q_3L}$ ,  $M_{tR}$ ,  $M_{bR}$ ,  $A_t$ ,  $A_b$  and  $M_3$  are varied by a factor

$$(1 + \rho) \quad \text{with} \quad 0 \leq \rho \leq 1. \quad (\text{A.9})$$

Again resulting masses and branching ratios for one example value,  $\rho = 1$ , are listed in the Tables A.1 and A.2.

For the scenario ‘‘SPS1aslope’’ the initial mSUGRA conditions are modified to

$$M_0 = -A_0 = 130 \text{ GeV}, \quad M_{1/2} = 2.5 \cdot M_0, \quad (\text{A.10})$$

and again  $M_{q_3L}$ ,  $M_{tR}$  and  $A_t$  are modified like for SPS1amod2, which gives about 30% higher SUSY masses as SPS1amod and a Higgs boson mass of  $m_h = 124.1 \text{ GeV}$ . More details are shown in Tables A.1 and A.2.

In order to study the effect of a modified slepton hierarchy, where both staus are heavy while all sleptons of the first two generations are light, i.e.

$$m_{\chi_1^0} < m_{\tilde{e}_L} = m_{\tilde{\mu}_L} \approx m_{\tilde{e}_R} = m_{\tilde{\mu}_R} < m_{\{\chi_1^\pm/\chi_2^0\}} < m_{\tilde{\tau}_{1/2}}, \quad (\text{A.11})$$

the following parameters of the scenario SPS1amod have been modified:

$$M_{eL} = M_{\mu L} = 134.4 \text{ GeV} \quad (\text{A.12})$$

$$M_{\tau L} = 393.6 \text{ GeV} \quad (\text{A.13})$$

$$M_{\tau R} = 333.4 \text{ GeV}. \quad (\text{A.14})$$

These parameters leave the Higgs boson mass unchanged at  $m_h = 118.2 \text{ GeV}$ . As can be seen in Tables A.1 and A.2 a light chargino predominantly produces an electron or muon in its decay chain in this ‘‘light sleptons’’ scenario.

The light sleptons scenario has also been analyzed for higher squark and gluino masses. Therefore the parameters  $M_{q_1L}$ ,  $M_{q_2L}$ ,  $M_{uR}$ ,  $M_{dR}$ ,  $M_{cR}$ ,  $M_{sR}$ ,  $M_{q_3L}$ ,  $M_{tR}$ ,  $M_{bR}$ ,  $A_t$ ,  $A_b$  and  $M_3$  have been multiplied by a factor of two. This corresponds to  $\xi = 1$  for the masses of the squarks of the first two generations and the gluino, and to  $\rho = 1$  for the stops and sbottoms. With increasing stop masses the Higgs boson mass is shifted to a value of  $m_h = 123 \text{ GeV}$ .

The scenario with an almost massless LSP is constructed by modifying the physical sparticle masses of SPS1amod. Afterwards the widths and branching ratios are recalculated using SDECAY [137]. Two masses are changed:

$$m_{\tilde{\tau}_1} = 100 \text{ GeV} \quad (\text{A.15})$$

$$m_{\chi_1^0} = 1 \text{ GeV}. \quad (\text{A.16})$$

This gives a mass difference between mother and daughter particles of at least  $\approx 80 \text{ GeV}$  at each decay step in the possible decay chains of the light chargino:

$$\begin{aligned} \chi_1^\pm &\rightarrow \tilde{\tau}^\pm \nu \rightarrow \tau^\pm \chi_1^0 \nu, \\ \chi_1^\pm &\rightarrow W^\pm \chi_1^0 \rightarrow \ell^\pm \chi_1^0 \nu. \end{aligned} \quad (\text{A.17})$$

Finally a scenario close to SPS1a(mod), but with a small mass difference between  $\tilde{\tau}_1$  and  $\chi_1^0$  (decay products within the decay chain of the light charginos) is constructed by setting

$$A_0 = -750 \text{ GeV} \tag{A.18}$$

instead of  $A_0 = -100 \text{ GeV}$ . This gives SUSY particle masses very similar to SPS1amod, except for the stop, sbottom and stau sector. The most relevant change for the analysis is the modified mass of the light stau:

$$m_{\tilde{\tau}_1} = 108.4 \text{ GeV} . \tag{A.19}$$

	SPS1amod	$\xi = 1.0$	$\rho = 1.0$	SPS1a-slope	light sleptons
$m_{\tilde{u}_L} = m_{\tilde{c}_L}$	560.2 GeV	1090.9 GeV	576.1 GeV	713.7 GeV	560.1 GeV
$m_{\tilde{d}_L} = m_{\tilde{s}_L}$	565.6 GeV	1093.7 GeV	581.6 GeV	717.9 GeV	565.6 GeV
$m_{\tilde{u}_R} = m_{\tilde{c}_R}$	543.9 GeV	1055.4 GeV	559.6 GeV	691.4 GeV	543.9 GeV
$m_{\tilde{d}_R} = m_{\tilde{s}_R}$	543.6 GeV	1052.0 GeV	559.3 GeV	690.0 GeV	543.6 GeV
$m_{\tilde{b}_1}$	518.2 GeV	533.5 GeV	1003.6 GeV	685.8 GeV	518.2 GeV
$m_{\tilde{b}_2}$	544.9 GeV	560.4 GeV	1047.2 GeV	852.5 GeV	544.9 GeV
$m_{\tilde{t}_1}$	346.3 GeV	365.6 GeV	768.3 GeV	665.4 GeV	346.2 GeV
$m_{\tilde{t}_2}$	608.4 GeV	620.3 GeV	1060.0 GeV	976.1 GeV	608.4 GeV
$m_{\tilde{g}}$	607.6 GeV	1165.8 GeV	1140.7 GeV	783.6 GeV	607.6 GeV
$m_{\chi_1^+}$	181.1 GeV	183.8 GeV	182.0 GeV	244.6 GeV	180.2 GeV
$m_{\chi_2^0}$	181.6 GeV	184.4 GeV	182.5 GeV	244.9 GeV	180.8 GeV
$m_{\chi_1^0}$	97.5 GeV	98.1 GeV	97.6 GeV	129.9 GeV	97.1 GeV
$m_{\tilde{e}_L} = m_{\tilde{\mu}_L}$	199.7 GeV	199.6 GeV	199.6 GeV	256.1 GeV	141.9 GeV
$m_{\tilde{e}_R} = m_{\tilde{\mu}_R}$	142.6 GeV	142.6 GeV	142.7 GeV	181.7 GeV	142.6 GeV
$m_{\tilde{\tau}_1}$	133.0 GeV	133.1 GeV	132.8 GeV	172.9 GeV	334.8 GeV
$m_{\tilde{\tau}_2}$	203.9 GeV	203.8 GeV	204.1 GeV	259.1 GeV	397.4 GeV
$m_{\tilde{\nu}_e} = m_{\tilde{\nu}_\mu}$	183.8 GeV	183.8 GeV	183.8 GeV	244.1 GeV	118.6 GeV
$m_{\tilde{\nu}_\tau}$	183.0 GeV	183.0 GeV	183.0 GeV	243.0 GeV	388.5 GeV
$m_h$	118.2 GeV	118.4 GeV	122.7 GeV	124.0 GeV	118.2 GeV

Table A.1: Particle masses in the scenarios SPS1amod, with higher first and second generation squark masses ( $\xi = 1.0$ ), with higher stop masses ( $\rho = 1.0$ ), SPS1a-slope and with light selectrons and smuons.

	SPS1amod	$\xi = 1.0$	$\rho = 1.0$	SPS1a-slope	light sleptons
$BR(\tilde{u}_L \rightarrow \chi_1^+ d)$	65.0 %	62.9 %	65.1 %	65.1 %	65.0 %
$BR(\tilde{u}_L \rightarrow \chi_2^0 u)$	31.8 %	30.7 %	31.9 %	32.1 %	31.8 %
$BR(\tilde{u}_L \rightarrow \chi_1^0 u)$	0.7 %	0.6 %	0.7 %	1.0 %	0.7 %
$BR(\tilde{u}_R \rightarrow \chi_1^0 u)$	98.6 %	97.7 %	98.7 %	99.3 %	98.6 %
$BR(\tilde{t}_1 \rightarrow \chi_1^+ b)$	80.7 %	74.9 %	21.1 %	44.1 %	80.7 %
$BR(\tilde{b}_1 \rightarrow \chi_1^0 b)$	3.1 %	3.1 %	1.0 %	70.2 %	3.1 %
$BR(\tilde{b}_1 \rightarrow \chi_2^0 b)$	21.4 %	22.1 %	12.0 %	6.0 %	21.4 %
$BR(\tilde{b}_2 \rightarrow \chi_1^0 b)$	14.0 %	13.0 %	29.5 %	0.7 %	14.0 %
$BR(\tilde{b}_2 \rightarrow \chi_2^0 b)$	11.1 %	9.9 %	1.2 %	12.2 %	11.1 %
$BR(\chi_1^+ \rightarrow \tilde{\tau}_1^+ \nu_\tau)$	95.8 %	93.3 %	95.6 %	74.4 %	0.0 %
$BR(\chi_1^+ \rightarrow \ell^+ \tilde{\nu}_\ell)$	0.0 %	0.0 %	0.0 %	0.1 %	71.4 %
$BR(\chi_1^+ \rightarrow \tilde{\ell}_L^+ \nu_\ell)$	0.0 %	0.0 %	0.0 %	0.0 %	28.5 %
$BR(\chi_1^+ \rightarrow W^+ \chi_1^0)$	4.2 %	6.7 %	4.4 %	25.5 %	0.1 %
$BR(\chi_2^0 \rightarrow \tilde{\ell}_R^\pm \ell^\mp)$	11.9 %	12.3 %	10.6 %	8.1 %	0.4 %
$BR(\chi_2^0 \rightarrow \tilde{\ell}_L^\pm \ell^\mp)$	0.0 %	0.0 %	0.0 %	0.0 %	36.4 %
$BR(\chi_2^0 \rightarrow \tilde{\tau}_1^\pm \tau^\mp)$	88.1 %	87.0 %	89.4 %	87.3 %	0.0 %
$BR(\chi_2^0 \rightarrow \tilde{\nu}_\ell \bar{\nu}_\ell)$	0.0 %	0.2 %	0.0 %	0.3 %	63.2 %
$BR(\chi_2^0 \rightarrow \tilde{\nu}_\tau \bar{\nu}_\tau)$	0.0 %	0.5 %	0.0 %	0.8 %	0.0 %
$BR(\chi_2^0 \rightarrow \chi_1^0 Z)$	0.0 %	0.0 %	0.0 %	3.5 %	0.0 %
$BR(\tilde{\ell}_L^\pm \rightarrow \chi_1^0 \ell^\pm)$	63.7%	70.7%	66.1%	87.8%	100.0%
$BR(\tilde{\ell}_L^\pm \rightarrow \chi_1^\pm \nu_\ell)$	23.3%	18.8%	21.8%	8.0%	0.0%
$BR(\tilde{\ell}_R^\pm \rightarrow \chi_1^0 \ell^\pm)$	100.0%	100.0%	100.0%	100.0%	100.0%
$BR(\tilde{\tau}_1 \rightarrow \chi_1^0 \tau^\pm)$	100.0%	100.0%	100.0%	100.0%	94.0%
$BR(\tilde{\tau}_2 \rightarrow \chi_1^0 \tau^\pm)$	64.8%	70.4%	66.6%	85.8%	12.6%
$BR(\tilde{\tau}_2 \rightarrow \chi_1^\pm \nu_\tau)$	22.5%	19.0%	21.4%	9.3%	54.7%
$BR(h \rightarrow W^+ W^-)$	8.2%	8.3%	12.6%	15.1%	8.2%
$BR(h \rightarrow \tau^+ \tau^-)$	7.4%	7.4%	7.0%	6.7%	7.4%

Table A.2: Branching ratios in the scenarios SPS1amod, with higher first and second generation squark masses ( $\xi = 1.0$ ), with higher stop masses ( $\rho = 1.0$ ), SPS1a-slope and with light selectrons and smuons. Here,  $\tilde{\ell}^{(\sim)}$  means the combined (s)electron and (s)muon channel. The branching ratios of the  $\tilde{d}$  decays are comparable to those listed for  $\tilde{u}$  decays.

## A.2 Scenarios for “New Physics Effects in Background Determination”

The “base” scenario discussed in Chapter 4 (published in [198]) is determined by the soft SUSY breaking parameters

$$\begin{aligned}
M_1 &= 103.1 \text{ GeV} & M_{eL} = M_{\mu L} &= 134.4 \text{ GeV} \\
M_2 &= 270.1 \text{ GeV} & M_{eR} = M_{\mu R} &= 135.8 \text{ GeV} \\
M_3 &= 1703.7 \text{ GeV} & M_{\tau L} &= 393.6 \text{ GeV} \\
A_t &= -2194.8 \text{ GeV} & M_{\tau R} &= 333.4 \text{ GeV} \\
A_b &= -1907.2 \text{ GeV} & M_{q_1L} = M_{q_2L} &= 1579.8 \text{ GeV} \\
A_\tau &= -249.4 \text{ GeV} & M_{uR} = M_{cR} &= 1524.3 \text{ GeV} \\
A_u = A_c &= -655.5 \text{ GeV} & M_{dR} = M_{sR} &= 1517.7 \text{ GeV} \\
A_d = A_s &= -821.8 \text{ GeV} & M_{q_3L} &= 1201.4 \text{ GeV} \\
A_e = A_\mu &= -251.1 \text{ GeV} & M_{tR} &= 1019.4 \text{ GeV} \\
M_{H_d}^2 &= 32609 \text{ GeV}^2 & M_{bR} &= 1257.2 \text{ GeV} \\
M_{H_u}^2 &= -169877 \text{ GeV}^2 & \tan \beta(M_Z) &= 10.0
\end{aligned} \tag{A.20}$$

at the scale  $Q = 1 \text{ TeV}$  and the following Standard Model parameters, with the top mass from [265]:

$$\begin{aligned}
\alpha_{em}^{-1}(M_Z) &= 127.934 & G_F &= 1.16639 \cdot 10^{-5} \text{ GeV}^{-2} \\
\alpha_s(M_Z) &= 0.1172 & M_Z &= 91.187 \text{ GeV} \\
M_b(M_b) &= 4.25 \text{ GeV} & M_t &= 173.2 \text{ GeV} .
\end{aligned} \tag{A.21}$$

These parameters are fed into SUSYHIT [135–138] for the calculation of the SUSY particle masses and branching ratios. The SLHA output file is then used as input for FeynHiggs 2.8.6 [140–143] in order to get precise Higgs boson mass values. The resulting scenario exhibits the following features:

- The squark masses of all three generations and the gluino mass ( $m_{\tilde{q}} \approx 1581 \text{ GeV}$ ,  $m_{\tilde{t}_1} = 934 \text{ GeV}$ ,  $m_{\tilde{b}_1} = 1232 \text{ GeV}$ ,  $m_{\tilde{g}} = 1725 \text{ GeV}$ ) are above early 2012 exclusion limits [204–207].
- The trilinear coupling  $A_t$  is adjusted according to the maximal mixing scenario [129], which yields a Higgs boson mass of  $m_h = 124.7 \text{ GeV}$ , which is in the vicinity of the early-2012 experimental hints of a Higgs boson [200, 201]. The discovery of a SM-Higgs like boson in this mass range was confirmed by later analyses [19, 20].
- The wino mass parameter  $M_2$  and the Higgs mass parameter  $m_{H_u}$  are chosen to give chargino masses outside the exclusion limits of the ATLAS  $2 \text{ fb}^{-1}$  trilepton search [208]. The discussion of the  $5 \text{ fb}^{-1}$  CMS trilepton analysis [209, 210] can be found in Chapter 4.2.
- The stau lepton masses are larger than the light chargino mass ( $m_{\tilde{\tau}_1} = 334 \text{ GeV}$ ), which is a specific feature of the considered scenarios.

- The mass parameters for the left-handed sleptons of the first two generations  $M_{eL}$  and  $M_{\mu L}$  are chosen such that the chargino decay into selectrons and smuons is the dominant decay mode.

The soft SUSY breaking parameters of the “worst case” scenario are the same as in the “base” scenario, except for

$$\begin{aligned} M_1 &= 128.9 \text{ GeV} & M_{eR} = M_{\mu R} &= 190.1 \text{ GeV} \\ M_{eL} = M_{\mu L} &= 188.2 \text{ GeV} . \end{aligned} \tag{A.22}$$

The “test scenario higher  $m_{\chi_1^\pm}/m_{\chi_2^0}$ ” differs from the “base” scenario in the following parameters:

$$\begin{aligned} M_1 &= 154.6 \text{ GeV} & M_{eL} = M_{\mu L} &= 215.0 \text{ GeV} \\ M_2 &= 328.0 \text{ GeV} & M_{eR} = M_{\mu R} &= 217.2 \text{ GeV} . \end{aligned} \tag{A.23}$$

Finally, the “worst case with staus” scenario is altered with respect to the “worst case” scenario by setting

$$M_{eL} = M_{\mu L} = M_{\tau L} = M_{eR} = M_{\mu R} = M_{\tau R} = 188.2 \text{ GeV} . \tag{A.24}$$

The relevant masses and branching ratios of all these scenarios are listed in Table A.3.

	“base” scenario	“worst case” scenario	“test scenario higher $m_{\chi_1^\pm}/m_{\chi_2^0}$ ”	“worst case with staus” scenario
$m_{\chi_1^0}$	98.9 GeV	124.1 GeV	149.2 GeV	124.1 GeV
$m_{\chi_1^+}$	260.0 GeV	260.3 GeV	308.2 GeV	260.3 GeV
$m_{\chi_2^0}$	260.3 GeV	260.7 GeV	309.0 GeV	260.7 GeV
$m_{\tilde{e}_L} = m_{\tilde{\mu}_L}$	141.8 GeV	193.5 GeV	219.7 GeV	193.5 GeV
$m_{\tilde{e}_R} = m_{\tilde{\mu}_R}$	142.6 GeV	195.0 GeV	221.6 GeV	193.2 GeV
$m_{\tilde{\tau}_1}$	334.4 GeV	334.4 GeV	334.4 GeV	172.9 GeV
$m_{\tilde{\tau}_2}$	397.7 GeV	397.7 GeV	397.7 GeV	211.9 GeV
$BR(\chi_1^+ \rightarrow \ell^+ \tilde{\nu}_\ell)$	58.0 %	60.4 %	57.2 %	39.7 %
$BR(\chi_1^+ \rightarrow \tilde{\ell}_L^+ \nu_\ell)$	41.0 %	37.7 %	38.7 %	24.8 %
$BR(\chi_1^+ \rightarrow \tau^+ \tilde{\nu}_\tau)$	0.0 %	0.0 %	0.0 %	20.0 %
$BR(\chi_1^+ \rightarrow \tilde{\tau}_1^+ \nu_\tau)$	0.0 %	0.0 %	0.0 %	11.1 %
$BR(\chi_1^+ \rightarrow \tilde{\tau}_2^+ \nu_\tau)$	0.0 %	0.0 %	0.0 %	3.1 %
$BR(\chi_1^+ \rightarrow W^+ \chi_1^0)$	1.0 %	1.9 %	4.1 %	1.3 %
$BR(\chi_2^0 \rightarrow \tilde{\ell}_{L,R}^\pm \ell^\mp)$	47.7 %	45.1 %	48.3 %	29.6 %
$BR(\chi_2^0 \rightarrow \tilde{\nu}_\ell \bar{\nu}_\ell)$	51.4 %	53.2 %	47.5 %	35.0 %
$BR(\chi_2^0 \rightarrow \tilde{\tau}_{1,2}^\pm \tau^\mp)$	0.0 %	0.0 %	0.0 %	16.8 %
$BR(\chi_2^0 \rightarrow \tilde{\nu}_\tau \bar{\nu}_\tau)$	0.0 %	0.0 %	0.0 %	17.5 %
$BR(\chi_2^0 \rightarrow \chi_1^0 Z)$	0.2 %	0.3 %	0.5 %	0.2 %
$BR(\chi_2^0 \rightarrow \chi_1^0 h_0)$	0.7 %	1.4 %	3.7 %	0.9 %
$BR(\tilde{\ell}_{L,R}^\pm \rightarrow \chi_1^0 \ell^\pm)$	100.0 %	100.0 %	100.0 %	100.0%
$BR(\tilde{\tau}_{1,2}^\pm \rightarrow \chi_1^0 \tau^\pm)$		not important		100.0%

Table A.3: Masses and branching ratios of interest for the scenarios discussed in Chapter 4. Here,  $\tilde{\ell}$  and  $\ell$  mean the combined selectron/smuon and electron/muon channel, respectively. For completeness, the mass and the branching ratios of the  $\chi_2^0$  are also given, though they are not important for the results.



# APPENDIX B

---

## List of VBFNLO Changes for the Semileptonic Decay Implementation

---

This appendix briefly summarizes the necessary changes to VBFNLO in order to implement semileptonic decays into already existing processes with fully leptonic vector boson decays. This list of changes is intended to assist future implementations of semileptonic decays in further processes.

**Leptonic Tensors:** The main changes for the implementation of semileptonic decays occur in the functions containing the “leptonic tensors”, as already described in Section 5.2. The new tensors are based on the ones from the anomalous couplings implementation of Refs. [237, 238], which are used for the Standard Model case as well. In order to minimize redundant code, all four possibilities of a hadronic decay ( $W^+ \rightarrow u\bar{d}$ ,  $W^- \rightarrow d\bar{u}$ ,  $Z/\gamma \rightarrow u\bar{u}$  and  $Z/\gamma \rightarrow d\bar{d}$ ) are included in one function. While originally the  $Z/\gamma$  couplings to fermions of the fermion lines connected to different vector bosons use the same variables, they are now separated and the couplings are set in the subroutine `coup1_haddecay` to the appropriate values (leptonic or hadronic) at the initialization stage of the program.

**Matrix Element Routines:** The matrix element routines of the considered processes have to be modified both for the Born and the real emission kinematics. The new leptonic tensors have to be called. Additionally, for the case of a hadronic  $Z/\gamma$  decay into up and down-type quarks both cases have to be initialized (via `Ztoun/Ztod`). Furthermore, the color factor, the individual quark thresholds for the  $Z/\gamma$  decay and the  $K$ -factor for the NLO decay have to be included, which is outsourced to the func-

tions `hadDecayFactor_W/Z`. Finally, the final-state particle ID for the Les Houches event output has to be set in case a summation over quark flavors is requested.

**utilities/process.inc:** The new process-IDs for semileptonic decays are introduced in the file `process.inc`. These new IDs have to be included in several case statements next to the IDs for the corresponding leptonic processes in the files

`utilities/statistics.F`, `utilities/scales.F`, `utilities/ptilde.F`,  
`utilities/parameters.F`, `utilities/process.F`, `phasespace/phasespace.F`,  
`amplitudes/amplitudes.F`

and subroutines

`InitCouplings`, `anomal_formfactor`, `printnfl`, `read_anomVcouplings`.

Additionally, the file `src/procinfo.dat`, which contains a description of all processes, has to be extended.

**utilities/process.F.in:** Additional changes in the subroutines `InitProcess` and `proc_assignment` account for the different number of final-state leptons and jets. The new routine `quark_assignment` checks the input of final-state quarks. The routines `symmetry_factor` and `lepton_gen`, which calculate the symmetry factor in the case of identical leptons in the final state and the final-state lepton-IDs for the event output, respectively, have to be modified as well. Finally, `printFinalProc`, which generates the process output at the end of the VBFNLO run, has to be adapted to the semileptonic case.

**Event Output (utilities/leshouches.F.in):** This file contains the main routines for the Les Houches event output. Since the vector boson decay products switch from being leptons to being quarks a few modifications have to be executed. In the routine `kf_leptons` the output of the final-state particles has to be adapted to the new situation. Since the hadronic vector boson decay products now carry color charge, this has to be considered in the routine `fillColorless`. Additionally, the routines `fillColoredPartons` within the matrix element routines, which set the color flow of the partons of the production process have to be extended in order to include the new process-IDs.

**Cuts (utilities/cuts.F):** Several changes are made to the routines generating the phase space cuts in order to include the new cuts and tagging-jet definitions. In particular, each new process has to be included in the definitions of the variables `vbprocess`, `semileptonic` and `zdecay_had`. The cut on `QSQAMIN_ZDEC`, which is included for compatibility with parton-shower programs, is carried out in the routine `phasespace`.

---

## Bibliography

---

- [1] H. Fritzsch, M. Gell-Mann, and H. Leutwyler, *Advantages of the Color Octet Gluon Picture*. *Phys.Lett.* **B47** (1973) 365–368.
- [2] H. D. Politzer, *Reliable Perturbative Results for Strong Interactions?* *Phys.Rev.Lett.* **30** (1973) 1346–1349.
- [3] D. Gross and F. Wilczek, *Ultraviolet Behavior of Nonabelian Gauge Theories*. *Phys.Rev.Lett.* **30** (1973) 1343–1346.
- [4] S. Glashow, *Partial Symmetries of Weak Interactions*. *Nucl.Phys.* **22** (1961) 579–588.
- [5] S. Weinberg, *A Model of Leptons*. *Phys.Rev.Lett.* **19** (1967) 1264–1266.
- [6] A. Salam, *Weak and Electromagnetic Interactions*. *Conf.Proc.* **C680519** (1968) 367–377.
- [7] P. W. Higgs, *Broken symmetries, massless particles and gauge fields*. *Phys.Lett.* **12** (1964) 132–133.
- [8] P. W. Higgs, *Broken Symmetries and the Masses of Gauge Bosons*. *Phys.Rev.Lett.* **13** (1964) 508–509.
- [9] F. Englert and R. Brout, *Broken Symmetry and the Mass of Gauge Vector Mesons*. *Phys.Rev.Lett.* **13** (1964) 321–323.
- [10] G. Guralnik, C. Hagen, and T. Kibble, *Global Conservation Laws and Massless Particles*. *Phys.Rev.Lett.* **13** (1964) 585–587.
- [11] N. Cabibbo, *Unitary Symmetry and Leptonic Decays*. *Phys.Rev.Lett.* **10** (1963) 531–533.

- [12] M. Kobayashi and T. Maskawa, *CP Violation in the Renormalizable Theory of Weak Interaction*. *Prog.Theor.Phys.* **49** (1973) 652–657.
- [13] **CDF Collaboration**, F. Abe *et al.*, *Observation of top quark production in  $\bar{p}p$  collisions*. *Phys.Rev.Lett.* **74** (1995) 2626–2631, [arXiv:hep-ex/9503002 \[hep-ex\]](#).
- [14] **D0 Collaboration**, S. Abachi *et al.*, *Observation of the top quark*. *Phys.Rev.Lett.* **74** (1995) 2632–2637, [arXiv:hep-ex/9503003 \[hep-ex\]](#).
- [15] **UA1 Collaboration**, G. Arnison *et al.*, *Experimental Observation of Isolated Large Transverse Energy Electrons with Associated Missing Energy at  $s^{**}(1/2) = 540\text{-GeV}$* . *Phys.Lett.* **B122** (1983) 103–116.
- [16] **UA2 Collaboration**, M. Banner *et al.*, *Observation of Single Isolated Electrons of High Transverse Momentum in Events with Missing Transverse Energy at the CERN anti-p p Collider*. *Phys.Lett.* **B122** (1983) 476–485.
- [17] H. Flacher, M. Goebel, J. Haller, A. Hocker, K. Monig, *et al.*, *Revisiting the Global Electroweak Fit of the Standard Model and Beyond with Gfitter*. *Eur.Phys.J.* **C60** (2009) 543–583, [arXiv:0811.0009 \[hep-ph\]](#).
- [18] **NA48 Collaboration**, V. Fanti *et al.*, *A New measurement of direct CP violation in two pion decays of the neutral kaon*. *Phys.Lett.* **B465** (1999) 335–348, [arXiv:hep-ex/9909022 \[hep-ex\]](#).
- [19] **ATLAS Collaboration**, G. Aad *et al.*, *Observation of a new particle in the search for the Standard Model Higgs boson with the ATLAS detector at the LHC*. *Phys.Lett.* **B716** (2012) 1–29, [arXiv:1207.7214 \[hep-ex\]](#).
- [20] **CMS Collaboration**, S. Chatrchyan *et al.*, *Observation of a new boson at a mass of 125 GeV with the CMS experiment at the LHC*. *Phys.Lett.* **B716** (2012) 30–61, [arXiv:1207.7235 \[hep-ex\]](#).
- [21] H. Babcock, *On the Rotation of the Andromeda Nebula*. Lick Observatory bulletins. University of California, Berkeley, 1938.
- [22] F. Zwicky, *Die Rotverschiebung von extragalaktischen Nebeln*. *Helv.Phys.Acta* **6** (1933) 110–127.
- [23] V. C. Rubin and J. Ford, W. Kent, *Rotation of the Andromeda Nebula from a Spectroscopic Survey of Emission Regions*. *Astrophys.J.* **159** (1970) 379–403.
- [24] D. Volkov and V. Akulov, *Is the Neutrino a Goldstone Particle?* *Phys.Lett.* **B46** (1973) 109–110.
- [25] J. Wess and B. Zumino, *Supergauge Transformations in Four-Dimensions*. *Nucl.Phys.* **B70** (1974) 39–50.
- [26] P. Fayet, *Supersymmetry and Weak, Electromagnetic and Strong Interactions*. *Phys.Lett.* **B64** (1976) 159.

- [27] P. Fayet, *Spontaneously Broken Supersymmetric Theories of Weak, Electromagnetic and Strong Interactions*. *Phys.Lett.* **B69** (1977) 489.
- [28] H. P. Nilles, *Supersymmetry, Supergravity and Particle Physics*. *Phys.Rept.* **110** (1984) 1–162.
- [29] H. E. Haber and G. L. Kane, *The Search for Supersymmetry: Probing Physics Beyond the Standard Model*. *Phys.Rept.* **117** (1985) 75–263.
- [30] M. Sohnius, *Introducing Supersymmetry*. *Phys.Rept.* **128** (1985) 39–204.
- [31] J. Gunion and H. E. Haber, *Higgs Bosons in Supersymmetric Models. 1*. *Nucl.Phys.* **B272** (1986) 1.
- [32] J. Gunion and H. E. Haber, *Erratum to: Higgs bosons in supersymmetric models (I): [Nucl. Phys. {B272} (1986) 1]*. *Nucl.Phys.* **B402** (1993) 567–568.
- [33] J. Gunion and H. E. Haber, *Higgs Bosons in Supersymmetric Models. 2. Implications for Phenomenology*. *Nucl.Phys.* **B278** (1986) 449.
- [34] S. P. Martin, *A Supersymmetry primer*. [arXiv:hep-ph/9709356](https://arxiv.org/abs/hep-ph/9709356) [[hep-ph](#)].
- [35] P. Fayet, *Relations Between the Masses of the Superpartners of Leptons and Quarks, the Goldstino Couplings and the Neutral Currents*. *Phys.Lett.* **B84** (1979) 416.
- [36] G. R. Farrar and P. Fayet, *Phenomenology of the Production, Decay, and Detection of New Hadronic States Associated with Supersymmetry*. *Phys.Lett.* **B76** (1978) 575–579.
- [37] E. Witten, *Dynamical Breaking of Supersymmetry*. *Nucl.Phys.* **B188** (1981) 513.
- [38] A. Lahanas and D. V. Nanopoulos, *The Road to No Scale Supergravity*. *Phys.Rept.* **145** (1987) 1.
- [39] S. Dimopoulos and H. Georgi, *Softly Broken Supersymmetry and SU(5)*. *Nucl.Phys.* **B193** (1981) 150.
- [40] N. Sakai, *Naturalness in Supersymmetric Guts*. *Z.Phys.* **C11** (1981) 153.
- [41] M. Baak, A. Blondel, R. Caputo, T. Corbett, C. Degrande, O. Eboli, J. Erler, B. Feigl, *et al.*, *Study of Electroweak Interactions at the Energy Frontier*. [arXiv:1310.6708](https://arxiv.org/abs/1310.6708) [[hep-ph](#)].
- [42] E. Sudarshan and R. Marshak, *Chirality invariance and the universal Fermi interaction*. *Phys.Rev.* **109** (1958) 1860–1860.
- [43] R. Feynman and M. Gell-Mann, *Theory of Fermi interaction*. *Phys.Rev.* **109** (1958) 193–198.
- [44] C.-N. Yang and R. L. Mills, *Conservation of Isotopic Spin and Isotopic Gauge Invariance*. *Phys.Rev.* **96** (1954) 191–195.

- [45] A. Djouadi, *The Anatomy of electro-weak symmetry breaking. I: The Higgs boson in the standard model.* *Phys.Rept.* **457** (2008) 1–216, [arXiv:hep-ph/0503172 \[hep-ph\]](#).
- [46] U. Amaldi, W. de Boer, and H. Furstenau, *Comparison of grand unified theories with electroweak and strong coupling constants measured at LEP.* *Phys.Lett.* **B260** (1991) 447–455.
- [47] W. de Boer and C. Sander, *Global electroweak fits and gauge coupling unification.* *Phys.Lett.* **B585** (2004) 276–286, [arXiv:hep-ph/0307049 \[hep-ph\]](#).
- [48] **Super-Kamiokande**, H. Nishino *et al.*, *Search for Nucleon Decay into Charged Anti-lepton plus Meson in Super-Kamiokande I and II.* *Phys.Rev.* **D85** (2012) 112001, [arXiv:1203.4030 \[hep-ex\]](#).
- [49] A. Djouadi, *The Anatomy of electro-weak symmetry breaking. II. The Higgs bosons in the minimal supersymmetric model.* *Phys.Rept.* **459** (2008) 1–241, [arXiv:hep-ph/0503173 \[hep-ph\]](#).
- [50] G. Giudice and R. Rattazzi, *Theories with gauge mediated supersymmetry breaking.* *Phys.Rept.* **322** (1999) 419–499, [arXiv:hep-ph/9801271 \[hep-ph\]](#).
- [51] A. H. Chamseddine, R. L. Arnowitt, and P. Nath, *Locally Supersymmetric Grand Unification.* *Phys.Rev.Lett.* **49** (1982) 970.
- [52] R. Barbieri, S. Ferrara, and C. A. Savoy, *Gauge Models with Spontaneously Broken Local Supersymmetry.* *Phys.Lett.* **B119** (1982) 343.
- [53] L. E. Ibanez, *Locally Supersymmetric SU(5) Grand Unification.* *Phys.Lett.* **B118** (1982) 73.
- [54] L. J. Hall, J. D. Lykken, and S. Weinberg, *Supergravity as the Messenger of Supersymmetry Breaking.* *Phys.Rev.* **D27** (1983) 2359–2378.
- [55] N. Ohta, *Grand Unified Theories Based on Local Supersymmetry.* *Prog.Theor.Phys.* **70** (1983) 542.
- [56] L. Girardello and M. T. Grisaru, *Soft Breaking of Supersymmetry.* *Nucl.Phys.* **B194** (1982) 65.
- [57] **MSSM Working Group**, A. Djouadi *et al.*, *The Minimal supersymmetric standard model: Group summary report.* [arXiv:hep-ph/9901246 \[hep-ph\]](#).
- [58] S. L. Adler and W. A. Bardeen, *Absence of higher order corrections in the anomalous axial vector divergence equation.* *Phys.Rev.* **182** (1969) 1517–1536.
- [59] J. Bell and R. Jackiw, *A PCAC puzzle:  $\pi^0 \rightarrow \gamma\gamma$  in the sigma model.* *Nuovo Cim.* **A60** (1969) 47–61.
- [60] J. R. Ellis, G. Ridolfi, and F. Zwirner, *Radiative corrections to the masses of supersymmetric Higgs bosons.* *Phys.Lett.* **B257** (1991) 83–91.

- [61] Y. Okada, M. Yamaguchi, and T. Yanagida, *Upper bound of the lightest Higgs boson mass in the minimal supersymmetric standard model*. *Prog.Theor.Phys.* **85** (1991) 1–6.
- [62] H. E. Haber and R. Hempfling, *Can the mass of the lightest Higgs boson of the minimal supersymmetric model be larger than  $m(Z)$ ?* *Phys.Rev.Lett.* **66** (1991) 1815–1818.
- [63] P. H. Chankowski, S. Pokorski, and J. Rosiek, *Charged and neutral supersymmetric Higgs boson masses: Complete one loop analysis*. *Phys.Lett.* **B274** (1992) 191–198.
- [64] A. Brignole, *Radiative corrections to the supersymmetric neutral Higgs boson masses*. *Phys.Lett.* **B281** (1992) 284–294.
- [65] A. Dabelstein, *The One loop renormalization of the MSSM Higgs sector and its application to the neutral scalar Higgs masses*. *Z.Phys.* **C67** (1995) 495–512, [arXiv:hep-ph/9409375 \[hep-ph\]](#).
- [66] S. Heinemeyer, *MSSM Higgs physics at higher orders*. *Int.J.Mod.Phys.* **A21** (2006) 2659–2772, [arXiv:hep-ph/0407244 \[hep-ph\]](#).
- [67] G. Degrandi, P. Slavich, and F. Zwirner, *On the neutral Higgs boson masses in the MSSM for arbitrary stop mixing*. *Nucl.Phys.* **B611** (2001) 403–422, [arXiv:hep-ph/0105096 \[hep-ph\]](#).
- [68] P. Kant, R. Harlander, L. Mihaila, and M. Steinhauser, *Light MSSM Higgs boson mass to three-loop accuracy*. *JHEP* **1008** (2010) 104, [arXiv:1005.5709 \[hep-ph\]](#).
- [69] **ALEPH Collaboration, CDF Collaboration, D0 Collaboration, DELPHI Collaboration, L3 Collaboration, OPAL Collaboration, SLD Collaboration, LEP Electroweak Working Group, Tevatron Electroweak Working Group, SLD Electroweak and Heavy Flavour Groups**, *Precision Electroweak Measurements and Constraints on the Standard Model*. [arXiv:1012.2367 \[hep-ex\]](#).
- [70] **LEP Working Group for Higgs boson searches, ALEPH Collaboration, DELPHI Collaboration, L3 Collaboration, OPAL Collaboration**, R. Barate *et al.*, *Search for the standard model Higgs boson at LEP*. *Phys.Lett.* **B565** (2003) 61–75, [arXiv:hep-ex/0306033 \[hep-ex\]](#).
- [71] J. C. Collins, D. E. Soper, and G. F. Sterman, *Factorization of Hard Processes in QCD*. *Adv.Ser.Direct.High Energy Phys.* **5** (1988) 1–91, [arXiv:hep-ph/0409313 \[hep-ph\]](#).
- [72] J. Alwall, P. Demin, S. de Visscher, R. Frederix, M. Herquet, *et al.*, *MadGraph/MadEvent v4: The New Web Generation*. *JHEP* **0709** (2007) 028, [arXiv:0706.2334 \[hep-ph\]](#).

- [73] J. Alwall, M. Herquet, F. Maltoni, O. Mattelaer, and T. Stelzer, *MadGraph 5 : Going Beyond*. *JHEP* **1106** (2011) 128, [arXiv:1106.0522 \[hep-ph\]](#).
- [74] W. Kilian, T. Ohl, and J. Reuter, *WHIZARD: Simulating Multi-Particle Processes at LHC and ILC*. *Eur.Phys.J.* **C71** (2011) 1742, [arXiv:0708.4233 \[hep-ph\]](#).
- [75] M. Moretti, T. Ohl, and J. Reuter, *O'Mega: An Optimizing matrix element generator*. [arXiv:hep-ph/0102195 \[hep-ph\]](#).
- [76] T. Gleisberg, S. Hoeche, F. Krauss, M. Schonherr, S. Schumann, *et al.*, *Event generation with SHERPA 1.1*. *JHEP* **0902** (2009) 007, [arXiv:0811.4622 \[hep-ph\]](#).
- [77] F. Krauss, R. Kuhn, and G. Soff, *AMEGIC++ 1.0: A Matrix element generator in C++*. *JHEP* **0202** (2002) 044, [arXiv:hep-ph/0109036 \[hep-ph\]](#).
- [78] V. Hirschi, R. Frederix, S. Frixione, M. V. Garzelli, F. Maltoni, *et al.*, *Automation of one-loop QCD corrections*. *JHEP* **1105** (2011) 044, [arXiv:1103.0621 \[hep-ph\]](#).
- [79] G. Cullen, N. Greiner, G. Heinrich, G. Luisoni, P. Mastrolia, *et al.*, *Automated One-Loop Calculations with GoSam*. *Eur.Phys.J.* **C72** (2012) 1889, [arXiv:1111.2034 \[hep-ph\]](#).
- [80] B. Webber, *A QCD Model for Jet Fragmentation Including Soft Gluon Interference*. *Nucl.Phys.* **B238** (1984) 492.
- [81] M. Bahr, S. Gieseke, M. Gigg, D. Grellscheid, K. Hamilton, *et al.*, *Herwig++ Physics and Manual*. *Eur.Phys.J.* **C58** (2008) 639–707, [arXiv:0803.0883 \[hep-ph\]](#).
- [82] B. Andersson, G. Gustafson, G. Ingelman, and T. Sjostrand, *Parton Fragmentation and String Dynamics*. *Phys.Rept.* **97** (1983) 31–145.
- [83] T. Sjostrand, S. Mrenna, and P. Z. Skands, *A Brief Introduction to PYTHIA 8.1*. *Comput.Phys.Commun.* **178** (2008) 852–867, [arXiv:0710.3820 \[hep-ph\]](#).
- [84] M. Bengtsson and T. Sjostrand, *A Comparative Study of Coherent and Noncoherent Parton Shower Evolution*. *Nucl.Phys.* **B289** (1987) 810.
- [85] G. Marchesini and B. Webber, *Monte Carlo Simulation of General Hard Processes with Coherent QCD Radiation*. *Nucl.Phys.* **B310** (1988) 461.
- [86] T. Sjostrand and M. van Zijl, *A Multiple Interaction Model for the Event Structure in Hadron Collisions*. *Phys.Rev.* **D36** (1987) 2019.
- [87] **ATLAS Collaboration**, *Differential cross sections of the Higgs boson measured in the diphoton decay channel using 8 TeV pp collisions*. ATLAS-CONF-2013-072, CERN, Geneva, Jul, 2013.

- [88] C. Sander, *Data Driven Background Estimation*. Talk at SFB Block Meeting, SFB 676-B2, U. Hamburg, 2012.  
[www.desy.de/~csander/Talks/120223\\_SFB\\_DataDrivenBackgrounds.pdf](http://www.desy.de/~csander/Talks/120223_SFB_DataDrivenBackgrounds.pdf).
- [89] **CMS Collaboration**, *Performance of Methods for Data-Driven Background Estimation in SUSY Searches*. CMS-PAS-SUS-10-001, CERN, 2010. Geneva, 2010.
- [90] **ATLAS Collaboration**, *Data-driven estimation of the background to charged Higgs boson searches using hadronically-decaying tau final states in ATLAS*. ATLAS-CONF-2011-051, CERN, Geneva, Apr, 2011.
- [91] S. Dittmaier, C. Mariotti, G. Passarino, R. Tanaka, *et al.*, *Handbook of LHC Higgs Cross Sections: 2. Differential Distributions*. [arXiv:1201.3084](https://arxiv.org/abs/1201.3084) [[hep-ph](#)].
- [92] **ATLAS Collaboration**, *Search for the Standard Model Higgs boson in the  $H \rightarrow WW \rightarrow l\nu l\nu$  decay mode with  $4.7 \text{ fb}^{-1}$  of ATLAS data at  $\sqrt{s} = 7 \text{ TeV}$* . ATLAS-CONF-2012-012, CERN, Geneva, Mar, 2012.
- [93] **CMS Collaboration**, S. Chatrchyan *et al.*, *Search for the standard model Higgs boson decaying to a  $W$  pair in the fully leptonic final state in  $pp$  collisions at  $\sqrt{s} = 7 \text{ TeV}$* . *Phys.Lett.* **B710** (2012) 91–113, [arXiv:1202.1489](https://arxiv.org/abs/1202.1489) [[hep-ex](#)].
- [94] **CMS Collaboration**, *A search using multivariate techniques for a standard model Higgs boson decaying into two photons*. CMS-PAS-HIG-12-001, CERN, Geneva, 2012.
- [95] **CMS Collaboration**, S. Chatrchyan *et al.*, *Measurement of the Inclusive  $W$  and  $Z$  Production Cross Sections in  $pp$  Collisions at  $\sqrt{s} = 7 \text{ TeV}$* . *JHEP* **1110** (2011) 132, [arXiv:1107.4789](https://arxiv.org/abs/1107.4789) [[hep-ex](#)].
- [96] **CMS Collaboration**, S. Chatrchyan *et al.*, *Search for Physics Beyond the Standard Model in Opposite-Sign Dilepton Events at  $\sqrt{s} = 7 \text{ TeV}$* . *JHEP* **1106** (2011) 026, [arXiv:1103.1348](https://arxiv.org/abs/1103.1348) [[hep-ex](#)].
- [97] **ATLAS Collaboration**, G. Aad *et al.*, *Search for squarks and gluinos using final states with jets and missing transverse momentum with the ATLAS detector in  $\sqrt{s} = 7 \text{ TeV}$  proton-proton collisions*. *Phys.Lett.* **B710** (2012) 67–85, [arXiv:1109.6572](https://arxiv.org/abs/1109.6572) [[hep-ex](#)].
- [98] **CMS Collaboration**, S. Chatrchyan *et al.*, *Search for Supersymmetry at the LHC in Events with Jets and Missing Transverse Energy*. *Phys.Rev.Lett.* **107** (2011) 221804, [arXiv:1109.2352](https://arxiv.org/abs/1109.2352) [[hep-ex](#)].
- [99] B. Feigl, H. Rzehak, and D. Zeppenfeld, *SUSY Background to Neutral MSSM Higgs Boson Searches*. *Eur.Phys.J.* **C72** (2012) 1903, [arXiv:1108.1110](https://arxiv.org/abs/1108.1110) [[hep-ph](#)].

- [100] B. Feigl, H. Rzehak, and D. Zeppenfeld, *Erratum to: SUSY Background to Neutral MSSM Higgs Boson Searches*. *Eur.Phys.J.* **C73** (2013) 2564, [arXiv:1108.1110 \[hep-ph\]](#).
- [101] P. Bechtle, K. Desch, M. Uhlenbrock, and P. Wienemann, *Constraining SUSY models with Fittino using measurements before, with and beyond the LHC*. *Eur.Phys.J.* **C66** (2010) 215–259, [arXiv:0907.2589 \[hep-ph\]](#).
- [102] **ATLAS Collaboration**, G. Aad *et al.*, *Expected Performance of the ATLAS Experiment - Detector, Trigger and Physics*. [arXiv:0901.0512 \[hep-ex\]](#).
- [103] **CMS Collaboration**, G. Bayatian *et al.*, *CMS technical design report, volume II: Physics performance*. *J.Phys.* **G34** (2007) 995–1579.
- [104] D. L. Rainwater and D. Zeppenfeld, *Searching for  $H \rightarrow \gamma\gamma$  in weak boson fusion at the LHC*. *JHEP* **9712** (1997) 005, [arXiv:hep-ph/9712271 \[hep-ph\]](#).
- [105] D. L. Rainwater, D. Zeppenfeld, and K. Hagiwara, *Searching for  $H \rightarrow \tau^+\tau^-$  in weak boson fusion at the CERN LHC*. *Phys.Rev.* **D59** (1998) 014037, [arXiv:hep-ph/9808468 \[hep-ph\]](#).
- [106] D. L. Rainwater and D. Zeppenfeld, *Observing  $H \rightarrow W^*W^* \rightarrow e^\pm\mu^\mp p_{T,miss}$  in weak boson fusion with dual forward jet tagging at the CERN LHC*. *Phys.Rev.* **D60** (1999) 113004, [arXiv:hep-ph/9906218 \[hep-ph\]](#).
- [107] T. Plehn, D. L. Rainwater, and D. Zeppenfeld, *Probing the MSSM Higgs sector via weak boson fusion at the LHC*. *Phys.Lett.* **B454** (1999) 297–303, [arXiv:hep-ph/9902434 \[hep-ph\]](#).
- [108] N. Kauer, T. Plehn, D. L. Rainwater, and D. Zeppenfeld,  *$H \rightarrow W^+W^-$  as the discovery mode for a light Higgs boson*. *Phys.Lett.* **B503** (2001) 113–120, [arXiv:hep-ph/0012351 \[hep-ph\]](#).
- [109] **LHC Higgs Cross Section Working Group**, S. Dittmaier *et al.*, *Handbook of LHC Higgs Cross Sections: 1. Inclusive Observables*. [arXiv:1101.0593 \[hep-ph\]](#).
- [110] **CMS Collaboration**, *Update of the search for the Standard Model Higgs boson decaying into  $WW$  in the vector boson fusion production channel*. CMS-PAS-HIG-13-022, CERN, Geneva, 2013.
- [111] **ATLAS Collaboration**, *Measurements of the properties of the Higgs-like boson in the  $WW^{(*)} \rightarrow l\nu l\nu$  decay channel with the ATLAS detector using 25  $fb^{-1}$  of proton-proton collision data*. ATLAS-CONF-2013-030, CERN, Geneva, Mar, 2013.
- [112] **ATLAS Collaboration**, G. Aad *et al.*, *Measurements of Higgs boson production and couplings in diboson final states with the ATLAS detector at the LHC*. *Phys.Lett.* **B** (2013), [arXiv:1307.1427 \[hep-ex\]](#).

- [113] M. Dührssen, S. Heinemeyer, H. Logan, D. Rainwater, G. Weiglein, *et al.*, *Extracting Higgs boson couplings from CERN LHC data*. *Phys.Rev.* **D70** (2004) 113009, [arXiv:hep-ph/0406323](#) [hep-ph].
- [114] H. Baer, V. Barger, and G. Shaughnessy, *SUSY backgrounds to Standard Model calibration processes at the LHC*. *Phys.Rev.* **D78** (2008) 095009, [arXiv:0806.3745](#) [hep-ph].
- [115] A. Datta, A. Djouadi, M. Guchait, and F. Moortgat, *Detection of mssm higgs bosons from supersymmetric particle cascade decays at the LHC*. *Nucl.Phys.* **B681** (2004) 31–64, [arXiv:hep-ph/0303095](#) [hep-ph].
- [116] M. Consonni, *Higgs searches in SUSY cascade with the ATLAS detector*. *Nucl.Phys.Proc.Suppl.* **177-178** (2008) 271–272.
- [117] **ATLAS Collaboration**, *ATLAS searches for MSSM Higgs bosons decaying into SUSY cascades*. ATL-PHYS-PUB-2009-079, ATL-COM-PHYS-2009-086, CERN, Geneva, Mar, 2009.
- [118] **CMS Collaboration**, S. Chatrchyan *et al.*, *Search for Neutral MSSM Higgs Bosons Decaying to Tau Pairs in pp Collisions at  $\sqrt{s} = 7$  TeV*. *Phys.Rev.Lett.* **106** (2011) 231801, [arXiv:1104.1619](#) [hep-ex].
- [119] **ATLAS Collaboration**, G. Aad *et al.*, *Search for neutral MSSM Higgs bosons decaying to  $\tau^+ \tau^-$  pairs in proton-proton collisions at  $\sqrt{s} = 7$  TeV with the ATLAS detector*. *Phys.Lett.* **B705** (2011) 174–192, [arXiv:1107.5003](#) [hep-ex].
- [120] **ATLAS Collaboration**, G. Aad *et al.*, *Search for the neutral Higgs bosons of the Minimal Supersymmetric Standard Model in pp collisions at  $\sqrt{s} = 7$  TeV with the ATLAS detector*. *JHEP* **1302** (2013) 095, [arXiv:1211.6956](#) [hep-ex].
- [121] **CMS Collaboration**, S. Chatrchyan *et al.*, *Search for a Higgs boson decaying into a b-quark pair and produced in association with b quarks in proton-proton collisions at 7 TeV*. *Phys.Lett.* **B722** (2013) 207–232, [arXiv:1302.2892](#) [hep-ex].
- [122] B. Allanach, M. Battaglia, G. Blair, M. S. Carena, A. De Roeck, *et al.*, *The Snowmass points and slopes: Benchmarks for SUSY searches*. *Eur.Phys.J.* **C25** (2002) 113–123, [arXiv:hep-ph/0202233](#) [hep-ph].
- [123] H. P. Nilles, *Dynamically Broken Supergravity and the Hierarchy Problem*. *Phys.Lett.* **B115** (1982) 193.
- [124] H. P. Nilles, *Supergravity Generates Hierarchies*. *Nucl.Phys.* **B217** (1983) 366.
- [125] **LEPSUSYWG, ALEPH, DELPHI, L3 and OPAL experiments**, *Interpretation of the results in Minimal SUGRA*. LEPSUSYWG/02-06.2, CERN, Geneva, 2002. <http://lepsusy.web.cern.ch/lepsusy/Welcome.html>.

- [126] **CDF Collaboration**, T. Aaltonen *et al.*, *Inclusive Search for Squark and Gluino Production in  $p\bar{p}$  Collisions at  $\sqrt{s} = 1.96$ -TeV*. *Phys.Rev.Lett.* **102** (2009) 121801, [arXiv:0811.2512](#) [[hep-ex](#)].
- [127] **D0 Collaboration**, V. Abazov *et al.*, *Search for squarks and gluinos in events with jets and missing transverse energy using  $2.1 \text{ fb}^{-1}$  of  $p\bar{p}$  collision data at  $\sqrt{s} = 1.96$ - TeV*. *Phys.Lett.* **B660** (2008) 449–457, [arXiv:0712.3805](#) [[hep-ex](#)].
- [128] **D0 Collaboration**, V. Abazov *et al.*, *Search for associated production of charginos and neutralinos in the trilepton final state using  $2.3 \text{ fb}^{-1}$  of data*. *Phys.Lett.* **B680** (2009) 34–43, [arXiv:0901.0646](#) [[hep-ex](#)].
- [129] M. S. Carena, S. Heinemeyer, C. E. M. Wagner, and G. Weiglein, *Suggestions for improved benchmark scenarios for Higgs boson searches at LEP-2*. [arXiv:hep-ph/9912223](#).
- [130] **ATLAS Collaboration**, G. Aad *et al.*, *Search for squarks and gluinos using final states with jets and missing transverse momentum with the ATLAS detector in  $\sqrt{s} = 7$  TeV proton-proton collisions*. *Phys.Lett.* **B701** (2011) 186–203, [arXiv:1102.5290](#) [[hep-ex](#)].
- [131] **ATLAS Collaboration**, G. Aad *et al.*, *Search for supersymmetric particles in events with lepton pairs and large missing transverse momentum in  $\sqrt{s} = 7$  TeV proton-proton collisions with the ATLAS experiment*. *Eur.Phys.J.* **C71** (2011) 1682, [arXiv:1103.6214](#) [[hep-ex](#)].
- [132] **CMS Collaboration**, S. Chatrchyan *et al.*, *Search for New Physics with Jets and Missing Transverse Momentum in  $pp$  collisions at  $\sqrt{s} = 7$  TeV*. *JHEP* **1108** (2011) 155, [arXiv:1106.4503](#) [[hep-ex](#)].
- [133] P. Z. Skands, B. Allanach, H. Baer, C. Balazs, G. Belanger, *et al.*, *SUSY Les Houches accord: Interfacing SUSY spectrum calculators, decay packages, and event generators*. *JHEP* **0407** (2004) 036, [arXiv:hep-ph/0311123](#) [[hep-ph](#)].
- [134] B. Allanach, C. Balazs, G. Belanger, M. Bernhardt, F. Boudjema, *et al.*, *SUSY Les Houches Accord 2*. *Comput.Phys.Commun.* **180** (2009) 8–25, [arXiv:0801.0045](#) [[hep-ph](#)].
- [135] A. Djouadi, J.-L. Kneur, and G. Moultaka, *SuSpect: A Fortran code for the supersymmetric and Higgs particle spectrum in the MSSM*. *Comput.Phys.Commun.* **176** (2007) 426–455, [arXiv:hep-ph/0211331](#).
- [136] A. Djouadi, M. M. Muhlleitner, and M. Spira, *Decays of supersymmetric particles: The Program SUSY-HIT (SUSpect-SdecaY-Hdecay-InTerface)*. *Acta Phys.Polon.* **B38** (2007) 635–644, [arXiv:hep-ph/0609292](#).
- [137] M. Muhlleitner, A. Djouadi, and Y. Mambrini, *SDECAY: A Fortran code for the decays of the supersymmetric particles in the MSSM*. *Comput.Phys.Commun.* **168** (2005) 46–70, [arXiv:hep-ph/0311167](#).

- [138] A. Djouadi, J. Kalinowski, and M. Spira, *HDECAY: A Program for Higgs boson decays in the standard model and its supersymmetric extension*. *Comput.Phys.Commun.* **108** (1998) 56–74, [arXiv:hep-ph/9704448](#).
- [139] W. Porod, *SPheno, a program for calculating supersymmetric spectra, SUSY particle decays and SUSY particle production at  $e^+e^-$  colliders*. *Comput.Phys.Commun.* **153** (2003) 275–315, [arXiv:hep-ph/0301101](#) [[hep-ph](#)].
- [140] S. Heinemeyer, W. Hollik, and G. Weiglein, *FeynHiggs: A Program for the calculation of the masses of the neutral CP even Higgs bosons in the MSSM*. *Comput.Phys.Commun.* **124** (2000) 76–89, [arXiv:hep-ph/9812320](#).
- [141] S. Heinemeyer, W. Hollik, and G. Weiglein, *The Masses of the neutral CP - even Higgs bosons in the MSSM: Accurate analysis at the two loop level*. *Eur.Phys.J.* **C9** (1999) 343–366, [arXiv:hep-ph/9812472](#).
- [142] G. Degrandi, S. Heinemeyer, W. Hollik, P. Slavich, and G. Weiglein, *Towards high precision predictions for the MSSM Higgs sector*. *Eur.Phys.J.* **C28** (2003) 133–143, [arXiv:hep-ph/0212020](#).
- [143] M. Frank, T. Hahn, S. Heinemeyer, W. Hollik, H. Rzehak, and G. Weiglein, *The Higgs Boson Masses and Mixings of the Complex MSSM in the Feynman-Diagrammatic Approach*. *JHEP* **0702** (2007) 047, [arXiv:hep-ph/0611326](#).
- [144] T. Figy, C. Oleari, and D. Zeppenfeld, *Next-to-leading order jet distributions for Higgs boson production via weak boson fusion*. *Phys.Rev.* **D68** (2003) 073005, [arXiv:hep-ph/0306109](#) [[hep-ph](#)].
- [145] K. Arnold, M. Bahr, G. Bozzi, F. Campanario, C. Englert, *et al.*, *VBFNLO: A Parton level Monte Carlo for processes with electroweak bosons*. *Comput.Phys.Commun.* **180** (2009) 1661–1670, [arXiv:0811.4559](#) [[hep-ph](#)].
- [146] K. Arnold, J. Bellm, G. Bozzi, M. Brieg, F. Campanario, *et al.*, *VBFNLO: A Parton Level Monte Carlo for Processes with Electroweak Bosons – Manual for Version 2.5.0*. [arXiv:1107.4038](#) [[hep-ph](#)].
- [147] K. Arnold, J. Bellm, G. Bozzi, F. Campanario, C. Englert, *et al.*, *Release Note – Vbfno-2.6.0*. [arXiv:1207.4975](#) [[hep-ph](#)].
- [148] V. Del Duca, W. Kilgore, C. Oleari, C. Schmidt, and D. Zeppenfeld, *Gluon fusion contributions to  $H + 2$  jet production*. *Nucl.Phys.* **B616** (2001) 367–399, [arXiv:hep-ph/0108030](#) [[hep-ph](#)].
- [149] A. Bredenstein, K. Hagiwara, and B. Jager, *Mixed QCD-electroweak contributions to Higgs-plus-dijet production at the LHC*. *Phys.Rev.* **D77** (2008) 073004, [arXiv:0801.4231](#) [[hep-ph](#)].

- [150] J. Andersen, T. Binoth, G. Heinrich, and J. Smillie, *Loop induced interference effects in Higgs Boson plus two jet production at the LHC*. *JHEP* **0802** (2008) 057, [arXiv:0709.3513 \[hep-ph\]](#).
- [151] C. Uhlemann and N. Kauer, *Narrow-width approximation accuracy*. *Nucl.Phys.* **B814** (2009) 195–211, [arXiv:0807.4112 \[hep-ph\]](#).
- [152] W. Beenakker, R. Hopker, M. Spira, and P. Zerwas, *Squark and gluino production at hadron colliders*. *Nucl.Phys.* **B492** (1997) 51–103, [arXiv:hep-ph/9610490 \[hep-ph\]](#).
- [153] W. Beenakker, M. Klasen, M. Kramer, T. Plehn, M. Spira, *et al.*, *The Production of charginos / neutralinos and sleptons at hadron colliders*. *Phys.Rev.Lett.* **83** (1999) 3780–3783, [arXiv:hep-ph/9906298 \[hep-ph\]](#).
- [154] T. Han, G. Valencia, and S. Willenbrock, *Structure function approach to vector boson scattering in  $p p$  collisions*. *Phys.Rev.Lett.* **69** (1992) 3274–3277, [arXiv:hep-ph/9206246 \[hep-ph\]](#).
- [155] M. Spira, *QCD effects in Higgs physics*. *Fortsch.Phys.* **46** (1998) 203–284, [arXiv:hep-ph/9705337 \[hep-ph\]](#).
- [156] E. L. Berger and J. M. Campbell, *Higgs boson production in weak boson fusion at next-to-leading order*. *Phys.Rev.* **D70** (2004) 073011, [arXiv:hep-ph/0403194 \[hep-ph\]](#).
- [157] M. Ciccolini, A. Denner, and S. Dittmaier, *Strong and electroweak corrections to the production of Higgs + 2jets via weak interactions at the LHC*. *Phys.Rev.Lett.* **99** (2007) 161803, [arXiv:0707.0381 \[hep-ph\]](#).
- [158] M. Ciccolini, A. Denner, and S. Dittmaier, *Electroweak and QCD corrections to Higgs production via vector-boson fusion at the LHC*. *Phys.Rev.* **D77** (2008) 013002, [arXiv:0710.4749 \[hep-ph\]](#).
- [159] T. Figy, S. Palmer, and G. Weiglein, *Higgs Production via Weak Boson Fusion in the Standard Model and the MSSM*. *JHEP* **1202** (2012) 105, [arXiv:1012.4789 \[hep-ph\]](#).
- [160] A. Djouadi and M. Spira, *SUSY - QCD corrections to Higgs boson production at hadron colliders*. *Phys.Rev.* **D62** (2000) 014004, [arXiv:hep-ph/9912476 \[hep-ph\]](#).
- [161] W. Hollik, T. Plehn, M. Rauch, and H. Rzehak, *Supersymmetric Higgs Bosons in Weak Boson Fusion*. *Phys.Rev.Lett.* **102** (2009) 091802, [arXiv:0804.2676 \[hep-ph\]](#).
- [162] P. Bolzoni, F. Maltoni, S.-O. Moch, and M. Zaro, *Higgs production via vector-boson fusion at NNLO in QCD*. *Phys.Rev.Lett.* **105** (2010) 011801, [arXiv:1003.4451 \[hep-ph\]](#).

- [163] R. V. Harlander, J. Vollinga, and M. M. Weber, *Gluon-Induced Weak Boson Fusion*. *Phys.Rev.* **D77** (2008) 053010, [arXiv:0801.3355 \[hep-ph\]](#).
- [164] D. L. Rainwater, R. Szalapski, and D. Zeppenfeld, *Probing color singlet exchange in  $Z + two\ jet$  events at the CERN LHC*. *Phys.Rev.* **D54** (1996) 6680–6689, [arXiv:hep-ph/9605444 \[hep-ph\]](#).
- [165] D. L. Rainwater, D. Summers, and D. Zeppenfeld, *Multi - jet structure of high  $E_T$  hadronic collisions*. *Phys.Rev.* **D55** (1997) 5681–5684, [arXiv:hep-ph/9612320 \[hep-ph\]](#).
- [166] **ATLAS Collaboration**, D. W. Miller, *First measurement of jets and missing transverse energy with the ATLAS calorimeter at  $\sqrt{s} = 900\ GeV$  and  $\sqrt{s} = 7\ TeV$* . ATL-PHYS-PROC-2010-049, CERN, Geneva, Jul, 2010.
- [167] **ATLAS Collaboration**, G. Aad *et al.*, *Measurements of underlying-event properties using neutral and charged particles in  $pp$  collisions at 900 GeV and 7 TeV with the ATLAS detector at the LHC*. *Eur.Phys.J.* **C71** (2011) 1636, [arXiv:1103.1816 \[hep-ex\]](#).
- [168] **CDF Collaboration**, T. Aaltonen *et al.*, *Studying the Underlying Event in Drell-Yan and High Transverse Momentum Jet Production at the Tevatron*. *Phys.Rev.* **D82** (2010) 034001, [arXiv:1003.3146 \[hep-ex\]](#).
- [169] M. Cacciari, G. P. Salam, and S. Sapeta, *On the characterisation of the underlying event*. *JHEP* **1004** (2010) 065, [arXiv:0912.4926 \[hep-ph\]](#).
- [170] **ATLAS Collaboration**, *The underlying event in jet events at 7 TeV with the ATLAS experiment*. ATLAS-CONF-2012-164, CERN, Geneva, Dec, 2012.
- [171] A. Pukhov, E. Boos, M. Dubinin, V. Edneral, V. Ilyin, *et al.*, *CompHEP: A Package for evaluation of Feynman diagrams and integration over multiparticle phase space*. [arXiv:hep-ph/9908288 \[hep-ph\]](#).
- [172] A. Pukhov, *CalcHEP 2.3: MSSM, structure functions, event generation, batchs, and generation of matrix elements for other packages*. [arXiv:hep-ph/0412191 \[hep-ph\]](#).
- [173] **CompHEP Collaboration**, E. Boos *et al.*, *CompHEP 4.4: Automatic computations from Lagrangians to events*. *Nucl.Instrum.Meth.* **A534** (2004) 250–259, [arXiv:hep-ph/0403113 \[hep-ph\]](#).
- [174] M. Gigg and P. Richardson, *Simulation of beyond standard model physics in Herwig++*. *Eur.Phys.J.* **C51** (2007) 989–1008, [arXiv:hep-ph/0703199 \[HEP-PH\]](#).
- [175] M. Gigg and P. Richardson, *Simulation of Finite Width Effects in Physics Beyond the Standard Model*. [arXiv:0805.3037 \[hep-ph\]](#).
- [176] N. Desai and P. Z. Skands, *Supersymmetry and Generic BSM Models in PYTHIA 8*. *Eur.Phys.J.* **C72** (2012) 2238, [arXiv:1109.5852 \[hep-ph\]](#).

- [177] G. Corcella, I. Knowles, G. Marchesini, S. Moretti, K. Odagiri, *et al.*, *HERWIG 6: An Event generator for hadron emission reactions with interfering gluons (including supersymmetric processes)*. *JHEP* **0101** (2001) 010, [arXiv:hep-ph/0011363 \[hep-ph\]](#).
- [178] S. Moretti, K. Odagiri, P. Richardson, M. H. Seymour, and B. R. Webber, *Implementation of supersymmetric processes in the HERWIG event generator*. *JHEP* **0204** (2002) 028, [arXiv:hep-ph/0204123 \[hep-ph\]](#).
- [179] T. Sjostrand, S. Mrenna, and P. Z. Skands, *PYTHIA 6.4 Physics and Manual*. *JHEP* **0605** (2006) 026, [arXiv:hep-ph/0603175 \[hep-ph\]](#).
- [180] J. Alwall, A. Ballestrero, P. Bartalini, S. Belov, E. Boos, *et al.*, *A Standard format for Les Houches event files*. *Comput.Phys.Commun.* **176** (2007) 300–304, [arXiv:hep-ph/0609017 \[hep-ph\]](#).
- [181] P. Richardson, *Spin correlations in Monte Carlo simulations*. *JHEP* **0111** (2001) 029, [arXiv:hep-ph/0110108 \[hep-ph\]](#).
- [182] J. Pumplin, D. Stump, J. Huston, H. Lai, P. M. Nadolsky, *et al.*, *New generation of parton distributions with uncertainties from global QCD analysis*. *JHEP* **0207** (2002) 012, [arXiv:hep-ph/0201195 \[hep-ph\]](#).
- [183] *RootSimple v.1.00 can be obtained from the following URL* .  
<https://herwig.hepforge.org/trac/wiki/RootSimple>.
- [184] I. Antcheva, M. Ballintijn, B. Bellenot, M. Biskup, R. Brun, *et al.*, *ROOT: A C++ framework for petabyte data storage, statistical analysis and visualization*. *Comput.Phys.Commun.* **180** (2009) 2499–2512.
- [185] J. Alwall, P. Artoisenet, S. de Visscher, C. Duhr, R. Frederix, *et al.*, *New Developments in MadGraph/MadEvent*. *AIP Conf.Proc.* **1078** (2009) 84–89, [arXiv:0809.2410 \[hep-ph\]](#).
- [186] M. Cacciari, G. P. Salam, and G. Soyez, *The Anti- $k(t)$  jet clustering algorithm*. *JHEP* **0804** (2008) 063, [arXiv:0802.1189 \[hep-ph\]](#).
- [187] M. Dittmar and H. K. Dreiner, *How to find a Higgs boson with a mass between 155-GeV - 180-GeV at the LHC*. *Phys.Rev.* **D55** (1997) 167–172, [arXiv:hep-ph/9608317 \[hep-ph\]](#).
- [188] V. D. Barger, G. Bhattacharya, T. Han, and B. A. Kniehl, *Intermediate mass Higgs boson at hadron supercolliders*. *Phys.Rev.* **D43** (1991) 779–788.
- [189] **CMS Collaboration**, *Algorithms for  $b$  Jet identification in CMS* .  
CMS-PAS-BTV-09-001, (2009).
- [190] **CMS Collaboration**, *Commissioning of  $b$ -jet identification with  $pp$  collisions at  $\sqrt{s} = 7$  TeV* . CMS-PAS-BTV-10-001, (2010).

- [191] **ATLAS Collaboration**, *Combination of Higgs Boson Searches with up to 4.9 fb<sup>-1</sup> of pp Collisions Data Taken at a center-of-mass energy of 7 TeV with the ATLAS Experiment at the LHC*. ATLAS-CONF-2011-163, (2011).
- [192] **CMS Collaboration**, *Combination of SM Higgs Searches*. CMS-PAS-HIG-11-032, (2011).
- [193] **ATLAS Collaboration**, *Search for squarks and gluinos with the ATLAS detector in final states with jets and missing transverse momentum and 20.3 fb<sup>-1</sup> of  $\sqrt{s} = 8$  TeV proton-proton collision data*. ATLAS-CONF-2013-047, CERN, Geneva, May, 2013.
- [194] **ATLAS Collaboration**, *Search for direct production of charginos and neutralinos in events with three leptons and missing transverse momentum in 21 fb<sup>-1</sup> of pp collisions at  $\sqrt{s} = 8$  TeV with the ATLAS detector*. ATLAS-CONF-2013-035, CERN, Geneva, Mar, 2013.
- [195] **ATLAS Collaboration**, *Search for direct-slepton and direct-chargino production in final states with two opposite-sign leptons, missing transverse momentum and no jets in 20/fb of pp collisions at  $\sqrt{s} = 8$  TeV with the ATLAS detector*. ATLAS-CONF-2013-049, CERN, Geneva, May, 2013.
- [196] **CMS Collaboration**, *Search for Supersymmetry in pp collisions at 8 TeV in events with a single lepton, multiple jets and b-tags*. CMS-PAS-SUS-13-007, CERN, Geneva, 2013.
- [197] **CMS Collaboration**, *Search for electroweak production of charginos, neutralinos, and sleptons using leptonic final states in pp collisions at 8 TeV*. CMS-PAS-SUS-13-006, CERN, Geneva, 2013.
- [198] B. Feigl, H. Rzehak, and D. Zeppenfeld, *New Physics Backgrounds to the  $H \rightarrow WW$  Search at the LHC?* *Phys.Lett.* **B717** (2012) 390–395, [arXiv:1205.3468 \[hep-ph\]](#).
- [199] B. Feigl, H. Rzehak, and D. Zeppenfeld, *SUSY confronts LHC results – LHC results confront SUSY?*, In the proceedings of “24th Rencontres de Blois 2012 – Particle Physics and Cosmology”. May 27 – June 1, 2012, Blois, France.
- [200] **ATLAS Collaboration**, *An update to the combined search for the Standard Model Higgs boson with the ATLAS detector at the LHC using up to 4.9 fb<sup>-1</sup> of pp collision data at  $\sqrt{s} = 7$  TeV*. ATLAS-CONF-2012-019, CERN, Geneva, Mar, 2012.
- [201] **CMS Collaboration**, *Combination of SM, SM<sub>4</sub>, FP Higgs boson searches*. CMS-PAS-HIG-12-008, CERN, Geneva, 2012.
- [202] **ATLAS Collaboration**, G. Aad *et al.*, *Measurement of the WW cross section in  $\sqrt{s} = 7$  TeV pp collisions with the ATLAS detector and limits on anomalous gauge couplings*. *Phys.Lett.* **B712** (2012) 289–308, [arXiv:1203.6232 \[hep-ex\]](#).

- [203] **CMS Collaboration**, S. Chatrchyan *et al.*, *Measurement of the  $W+W^-$  cross section in  $pp$  collisions at  $\sqrt{s} = 7$  TeV and limits on anomalous  $WW$  gamma and  $WWZ$  couplings.* [arXiv:1306.1126](#) [[hep-ex](#)].
- [204] **ATLAS Collaboration**, *Search for squarks and gluinos using final states with jets and missing transverse momentum with the ATLAS detector in  $\sqrt{s} = 7$  TeV proton-proton collisions*. ATLAS-CONF-2012-033, 2012.
- [205] **CMS Collaboration**, *Search for supersymmetry with the razor variables at CMS*. CMS-PAS-SUS-12-005, CERN, Geneva, 2012.
- [206] **ATLAS Collaboration**, G. Aad *et al.*, *Search for scalar top quark pair production in natural gauge mediated supersymmetry models with the ATLAS detector in  $pp$  collisions at  $\sqrt{s} = 7$  TeV.* *Phys.Lett.* **B715** (2012) 44–60, [arXiv:1204.6736](#) [[hep-ex](#)].
- [207] **ATLAS Collaboration**, G. Aad *et al.*, *Search for scalar bottom pair production with the ATLAS detector in  $pp$  Collisions at  $\sqrt{s} = 7$  TeV.* *Phys.Rev.Lett.* **108** (2012) 181802, [arXiv:1112.3832](#) [[hep-ex](#)].
- [208] **ATLAS Collaboration**, G. Aad *et al.*, *Search for supersymmetry in events with three leptons and missing transverse momentum in  $\sqrt{s} = 7$  TeV  $pp$  collisions with the ATLAS detector.* *Phys.Rev.Lett.* **108** (2012) 261804, [arXiv:1204.5638](#) [[hep-ex](#)].
- [209] **CMS Collaboration**, S. Chatrchyan *et al.*, *Search for anomalous production of multilepton events in  $pp$  collisions at  $\sqrt{s} = 7$  TeV.* *JHEP* **1206** (2012) 169, [arXiv:1204.5341](#) [[hep-ex](#)].
- [210] **CMS Collaboration**, *Interpretation of Searches for Supersymmetry*. CMS-PAS-SUS-11-016, CERN, Geneva, 2012.
- [211] S. Gieseke, D. Grellscheid, K. Hamilton, A. Papaefstathiou, S. Platzer, *et al.*, *Herwig++ 2.5 Release Note.* [arXiv:1102.1672](#) [[hep-ph](#)].
- [212] K. Hamilton, *A positive-weight next-to-leading order simulation of weak boson pair production.* *JHEP* **1101** (2011) 009, [arXiv:1009.5391](#) [[hep-ph](#)].
- [213] S. Frixione, *A Next-to-leading order calculation of the cross-section for the production of  $W+ W^-$  pairs in hadronic collisions.* *Nucl.Phys.* **B410** (1993) 280–324.
- [214] P. Nason, *A New method for combining NLO QCD with shower Monte Carlo algorithms.* *JHEP* **0411** (2004) 040, [arXiv:hep-ph/0409146](#) [[hep-ph](#)].
- [215] S. Frixione, P. Nason, and C. Oleari, *Matching NLO QCD computations with Parton Shower simulations: the POWHEG method.* *JHEP* **0711** (2007) 070, [arXiv:0709.2092](#) [[hep-ph](#)].

- [216] T. Binoth, M. Ciccolini, N. Kauer, and M. Kramer, *Gluon-induced  $WW$  background to Higgs boson searches at the LHC*. *JHEP* **0503** (2005) 065, [arXiv:hep-ph/0503094](#) [[hep-ph](#)].
- [217] T. Binoth, M. Ciccolini, N. Kauer, and M. Kramer, *Gluon-induced  $W$ -boson pair production at the LHC*. *JHEP* **0612** (2006) 046, [arXiv:hep-ph/0611170](#) [[hep-ph](#)].
- [218] A. J. Barr, B. Gripaios, and C. G. Lester, *Measuring the Higgs boson mass in dileptonic  $W$ -boson decays at hadron colliders*. *JHEP* **0907** (2009) 072, [arXiv:0902.4864](#) [[hep-ph](#)].
- [219] H.-L. Lai, M. Guzzi, J. Huston, Z. Li, P. M. Nadolsky, *et al.*, *New parton distributions for collider physics*. *Phys.Rev.* **D82** (2010) 074024, [arXiv:1007.2241](#) [[hep-ph](#)].
- [220] R. K. Ellis, I. Hinchliffe, M. Soldate, and J. van der Bij, *Higgs Decay to  $\tau+\tau$ : A Possible Signature of Intermediate Mass Higgs Bosons at the SSC*. *Nucl.Phys.* **B297** (1988) 221.
- [221] **CMS Collaboration**, *Evidence for a particle decaying to  $W+W^-$  in the fully leptonic final state in a standard model Higgs boson search in  $pp$  collisions at the LHC*. CMS-PAS-HIG-13-003, CERN, Geneva, 2013.
- [222] W. Buchmuller and D. Wyler, *Effective Lagrangian Analysis of New Interactions and Flavor Conservation*. *Nucl.Phys.* **B268** (1986) 621.
- [223] O. Eboli, M. Gonzalez-Garcia, and J. Mizukoshi,  *$pp \rightarrow jje^\pm\mu^\pm\nu\nu$  and  $jje^\pm\mu^\pm\nu\nu$  at  $O(\alpha(em)^6)$  and  $O(\alpha(em)^4\alpha(s)^2)$  for the study of the quartic electroweak gauge boson vertex at CERN LHC*. *Phys.Rev.* **D74** (2006) 073005, [arXiv:hep-ph/0606118](#) [[hep-ph](#)].
- [224] **ATLAS Collaboration**, G. Aad *et al.*, *Search for the Higgs boson in the  $H \rightarrow WW \rightarrow l\nu jj$  decay channel at  $\sqrt{s} = 7$  TeV with the ATLAS detector*. *Phys.Lett.* **B718** (2012) 391–410, [arXiv:1206.6074](#) [[hep-ex](#)].
- [225] **CMS Collaboration**, *Search for a Standard Model-like Higgs boson decaying into  $WW$  to  $l\nu q\bar{q}$  in  $pp$  collisions at  $\sqrt{s} = 8$  TeV*. CMS-PAS-HIG-13-008, CERN, Geneva, 2013.
- [226] **ATLAS Collaboration**, G. Aad *et al.*, *Search for a standard model Higgs boson in the mass range 200 - 600-GeV in the  $H \rightarrow ZZ \rightarrow \ell^+\ell^-q\bar{q}$  decay channel with the ATLAS detector*. *Phys.Lett.* **B717** (2012) 70–88, [arXiv:1206.2443](#) [[hep-ex](#)].
- [227] **ATLAS Collaboration**, *Study of the channel  $H \rightarrow Z^*Z \rightarrow \ell^+\ell^-q\bar{q}$  in the mass range 120-180 GeV with the ATLAS Detector at  $\sqrt{s}=7$  TeV*. ATLAS-CONF-2012-163, CERN, Geneva, Nov, 2012.

- [228] **CMS Collaboration**, *Search for a standard model like Higgs boson in the decay channel  $H$  to  $ZZ$  to  $l+l- q qbar$  at CMS*. CMS-PAS-HIG-12-024, CERN, Geneva, 2013.
- [229] **ATLAS Collaboration**, *Measurement of the combined  $WW$  and  $WZ$  production cross section in the semileptonic final state in proton-proton collisions at  $\sqrt{s} = 7$  TeV with the ATLAS detector*. ATLAS-CONF-2012-157, CERN, Geneva, Nov, 2012.
- [230] **CMS Collaboration**, S. Chatrchyan *et al.*, *Measurement of the sum of  $WW$  and  $WZ$  production with  $W$ +dijet events in  $pp$  collisions at  $\sqrt{s} = 7$  TeV*. *Eur.Phys.J.* **C73** (2013) 2283, [arXiv:1210.7544](#) [[hep-ex](#)].
- [231] **CMS Collaboration**, *A Search for  $WW\gamma$  and  $WZ\gamma$  production in  $pp$  Collisions at  $\sqrt{s} = 8$  TeV*. CMS-PAS-SMP-13-009, CERN, Geneva, 2013.
- [232] J. M. Campbell, R. K. Ellis, and C. Williams, *Vector boson pair production at the LHC*. *JHEP* **1107** (2011) 018, [arXiv:1105.0020](#) [[hep-ph](#)].
- [233] S. Frixione, F. Stoeckli, P. Torrielli, B. R. Webber, and C. D. White, *The MCaNLO 4.0 Event Generator*. [arXiv:1010.0819](#) [[hep-ph](#)].
- [234] S. Alioli, P. Nason, C. Oleari, and E. Re, *A general framework for implementing NLO calculations in shower Monte Carlo programs: the POWHEG BOX*. *JHEP* **1006** (2010) 043, [arXiv:1002.2581](#) [[hep-ph](#)].
- [235] N. Kauer and G. Passarino, *Inadequacy of zero-width approximation for a light Higgs boson signal*. *JHEP* **1208** (2012) 116, [arXiv:1206.4803](#) [[hep-ph](#)].
- [236] B. Jager and G. Zanderighi, *Electroweak  $W+W$ - $jj$  production at NLO in QCD matched with parton shower in the POWHEG-BOX*. *JHEP* **1304** (2013) 024, [arXiv:1301.1695](#) [[hep-ph](#)].
- [237] B. Feigl, *Anomale Vier-Vektorboson-Kopplungen bei der Produktion von drei Vektorbosonen am LHC*. diploma thesis, ITP, KIT, 2009.  
[http://www.itp.kit.edu/prep/diploma/PSFiles/Diplom\\_Feigl.pdf](http://www.itp.kit.edu/prep/diploma/PSFiles/Diplom_Feigl.pdf).
- [238] O. Schlimpert, *Anomale Kopplungen bei der Streuung schwacher Eichbosonen*. diploma thesis, ITP, KIT, 2013.  
[http://www.itp.kit.edu/prep/diploma/PSFiles/Diplom\\_Schlimpert.pdf](http://www.itp.kit.edu/prep/diploma/PSFiles/Diplom_Schlimpert.pdf).
- [239] M. S. Chanowitz and M. K. Gaillard, *The TeV Physics of Strongly Interacting  $W$ 's and  $Z$ 's*. *Nucl.Phys.* **B261** (1985) 379.
- [240] B. Jager, C. Oleari, and D. Zeppenfeld, *Next-to-leading order QCD corrections to  $W+W$ - production via vector-boson fusion*. *JHEP* **0607** (2006) 015, [arXiv:hep-ph/0603177](#) [[hep-ph](#)].

- [241] B. Jager, C. Oleari, and D. Zeppenfeld, *Next-to-leading order QCD corrections to Z boson pair production via vector-boson fusion*. *Phys.Rev.* **D73** (2006) 113006, [arXiv:hep-ph/0604200 \[hep-ph\]](#).
- [242] G. Bozzi, B. Jager, C. Oleari, and D. Zeppenfeld, *Next-to-leading order QCD corrections to  $W^+ Z$  and  $W^- Z$  production via vector-boson fusion*. *Phys.Rev.* **D75** (2007) 073004, [arXiv:hep-ph/0701105 \[hep-ph\]](#).
- [243] B. Jager, C. Oleari, and D. Zeppenfeld, *Next-to-leading order QCD corrections to  $W^+ W^+ jj$  and  $W^- W^- jj$  production via weak-boson fusion*. *Phys.Rev.* **D80** (2009) 034022, [arXiv:0907.0580 \[hep-ph\]](#).
- [244] C. Oleari and D. Zeppenfeld, *QCD corrections to electroweak  $\nu(l) jj$  and  $l^+ l^- jj$  production*. *Phys.Rev.* **D69** (2004) 093004, [arXiv:hep-ph/0310156 \[hep-ph\]](#).
- [245] **ATLAS Collaboration**, *Studies of Vector Boson Scattering And Triboson Production with an Upgraded ATLAS Detector at a High-Luminosity LHC*. ATL-PHYS-PUB-2013-006, CERN, Geneva, Jun, 2013.
- [246] V. Hankele and D. Zeppenfeld, *QCD corrections to hadronic WWZ production with leptonic decays*. *Phys.Lett.* **B661** (2008) 103–108, [arXiv:0712.3544 \[hep-ph\]](#).
- [247] S. Catani and M. Seymour, *A General algorithm for calculating jet cross-sections in NLO QCD*. *Nucl.Phys.* **B485** (1997) 291–419, [arXiv:hep-ph/9605323 \[hep-ph\]](#).
- [248] A. Abdesselam, E. B. Kuutmann, U. Bitenc, G. Brooijmans, J. Butterworth, *et al.*, *Boosted objects: A Probe of beyond the Standard Model physics*. *Eur.Phys.J.* **C71** (2011) 1661, [arXiv:1012.5412 \[hep-ph\]](#).
- [249] **Particle Data Group**, J. Beringer *et al.*, *Review of Particle Physics (RPP)*. *Phys.Rev.* **D86** (2012) 010001.
- [250] V. Ezhela, S. Lugovsky, and O. Zenin, *Hadronic part of the muon  $g-2$  estimated on the  $\sigma_{total}^{2003}(e^+e^- \rightarrow \text{hadrons})$  evaluated data compilation*. [arXiv:hep-ph/0312114 \[hep-ph\]](#).
- [251] K. Chetyrkin, J. H. Kuhn, and M. Steinhauser, *RunDec: A Mathematica package for running and decoupling of the strong coupling and quark masses*. *Comput.Phys.Commun.* **133** (2000) 43–65, [arXiv:hep-ph/0004189 \[hep-ph\]](#).
- [252] S. Bethke, *World Summary of  $\alpha_s$  (2012)*. *Nucl.Phys.Proc.Suppl.* **234** (2013) 229–234, [arXiv:1210.0325 \[hep-ex\]](#).
- [253] S. Dittmaier, A. Huss, and C. Speckner, *Weak radiative corrections to dijet production at hadron colliders*. *JHEP* **1211** (2012) 095, [arXiv:1210.0438 \[hep-ph\]](#).

- [254] D. Albert, W. J. Marciano, D. Wyler, and Z. Parsa, *Decays of Intermediate Vector Bosons, Radiative Corrections and QCD Jets*. *Nucl.Phys.* **B166** (1980) 460.
- [255] H. Murayama, I. Watanabe, and K. Hagiwara, *HELAS: HELicity amplitude subroutines for Feynman diagram evaluations*. KEK-91-11, KEK, 1992.
- [256] K. Iordanidis and D. Zeppenfeld, *Searching for a heavy Higgs boson via the  $H \rightarrow$  lepton neutrino jet jet mode at the CERN LHC*. *Phys.Rev.* **D57** (1998) 3072–3083, [arXiv:hep-ph/9709506](#) [hep-ph].
- [257] K. Hagiwara, S. Ishihara, R. Szalapski, and D. Zeppenfeld, *Low-energy effects of new interactions in the electroweak boson sector*. *Phys.Rev.* **D48** (1993) 2182–2203.
- [258] A. Alboteanu, W. Kilian, and J. Reuter, *Resonances and Unitarity in Weak Boson Scattering at the LHC*. *JHEP* **0811** (2008) 010, [arXiv:0806.4145](#) [hep-ph].
- [259] O. Eboli and M. Gonzalez-Garcia, *Anomalous quartic electroweak gauge-boson interactions* ., 2013.  
<http://feynrules.irmp.ucl.ac.be/wiki/AnomalousGaugeCoupling>.
- [260] C. Degrande, O. Eboli, B. Feigl, B. Jager, W. Kilian, *et al.*, *Monte Carlo tools for studies of non-standard electroweak gauge boson interactions in multi-boson processes: A Snowmass White Paper*. [arXiv:1309.7890](#) [hep-ph].
- [261] U. Baur and D. Zeppenfeld, *Unitarity Constraints on the Electroweak Three Vector Boson Vertices*. *Phys.Lett.* **B201** (1988) 383.
- [262] G. Gounaris, J. Layssac, J. Paschalis, and F. Renard, *Unitarity constraints for new physics induced by dim-6 operators*. *Z.Phys.* **C66** (1995) 619–632, [arXiv:hep-ph/9409260](#) [hep-ph].
- [263] C. Englert, B. Feigl, J. Frank, M. Rauch, O. Schlimpert, and F. Schissler, *Dipole Form Factor Calculation Tool for Anomalous Couplings in VBFNLO* ., ITP, KIT, 2013.  
[www.itp.kit.edu/~vbfnlweb/wiki/doku.php?id=download:formfactor](http://www.itp.kit.edu/~vbfnlweb/wiki/doku.php?id=download:formfactor).
- [264] **Tevatron Electroweak Working Group, CDF Collaboration, D0 Collaboration**, E. Brubaker *et al.*, *Combination of CDF and D0 results on the mass of the top quark*. [arXiv:hep-ex/0603039](#) [hep-ex].
- [265] **Tevatron Electroweak Working Group, for the CDF and D0 Collaborations**, *Combination of CDF and D0 results on the mass of the top quark using up to 5.8 fb<sup>-1</sup> of data*. [arXiv:1107.5255](#) [hep-ex].

---

## Acknowledgments

---

First of all, my special thanks go to Prof. Dieter Zeppenfeld, for accepting me as a PhD student and the opportunity to work on several interesting topics in the phenomenology of elementary particle physics. I am very grateful for many illuminating discussions, his advice and his constant interest in my work. Furthermore, I acknowledge the possibility to attend several schools and the Pheno conference in Pittsburgh.

I appreciate Prof. Margarete Mühlleitners agreement on being the second referee of this thesis.

I sincerely thank Heidi Rzehak for her advice, many illuminating discussions, for answering many (sometimes stupid) questions and the pleasant atmosphere in general in the collaboration on the SUSY topics.

I am very thankful to Johannes Bellm, Christian Hangst, Eva Popena, Christian Röhr, Heidi Rzehak and Franziska Schissler for the careful proof-reading of the many pages of this thesis.

Many discussions in the recent years led to new insights on the topics of this work. For these I am very grateful to Johannes Bellm, Stefan Gieseke, Christian Hangst, Prof. Margarete Mühlleitner, Sophy Palmer, Dr. Eva Popena, Christian Röhr and Franziska Schissler and in particular to Michael Rauch, who answered many questions with a never-ending patience.

I thank my colleagues Johannes Bellm, Thomas Hermann, Jens Hoff, Peter Marquard, Simon Plätzer and Christian Röhr for the nice teamwork in the administration of the ITP/TTP institute cluster.

For the pleasant atmosphere at the institute, with the substantial contribution from many coffee/tea breaks and several pieces of fine cake, I thank all present and former members of the ITP, in particular my office colleagues Hamzeh Alavirad, Johannes Bellm, Christian Hangst, Eva Popena and Kathrin Walz.

The funding support for this thesis by the BMBF is greatly acknowledged.

All meine Freunde haben die Studiumszeit und die Promotion ganz wesentlich geprägt und sehr unterhaltsam gemacht. Dafür bin ich zutiefst dankbar. Insbesondere hat mich Simon Wendel überhaupt erst auf das ITP aufmerksam gemacht.

Meinen Eltern und meinem Bruder danke ich für die Unterstützung während des gesamten Studiums (und natürlich auch davor), die es überhaupt erst möglich gemacht haben, diese Arbeit zu bewerkstelligen.

Zu guter Letzt danke ich Eva von ganzem Herzen für ihre Liebe, ihre Ermutigungen, ihre Unterstützung während der ganzen Doktorarbeitszeit, ihre wunderbare Art und dass sie ihr Leben mit mir teilt.